Integrin $\alpha_{IIb}\beta_3$: From platelet membrane to biomimetic models

A thesis submitted to Dublin City University for the award of PhD

By

Vincent Gaul B.Sc, M.Sc

School of Chemical Sciences,
Dublin City University,
Glasnevin,
Dublin 9.

Supervisors: Tia Keyes (DCU) and Niamh Moran (RCSI)

March 2016

Declaration

I hereby certify that this material, which I now submit for assessment on the programme of study leading to the award of Ph.D is entirely my own work, that I have exercised reasonable care to ensure that the work is original, and does not to the best of my knowledge breach any law of copyright, and has not been taken from the work of others save and to the extent that such work has been cited and acknowledged within the text of my work.

Signed: _____ (Candidate) ID No.: _____ Date: _____

Acknowledgements

Firstly, I would like to express my gratitude to my supervisor Prof. Tia Keyes for her support, knowledge and assistance throughout my Ph.D. I would also like to thank my co-supervisor Prof. Niamh Moran for her time and expertise during the process. In addition, I want to thank Prof. Robert Forster and Prof. Barry Lentz for their invaluable knowledge. Without their help I would not have been able to complete my work. I would also like to express my thanks to all DCU, RCSI, and UNC Chapel Hill lab members, both past and present, that I had the pleasure to work with over past few years, as well as support and technical staff who helped me throughout.

I would also like to express my thank you to my mother, father, my brothers David and Robert, and my sister Caroline, as well as my friends who still don't know what I do. Finally, I would like to give a special thank you to Lorraine, who has has moved from one side of the city and back again for me, supported me through late nights and busy weekends, and has always been there for me. Thank you.

"*What I cannot create, I do not understand*"

- Richard Feynman

Table of Contents

Glossary of Abbreviations

AA	Arachidonic Acid
AAU	Arbitrary Absorbance Units
ABP	Actin-Binding Protein
ACD	Acid Citrate Dextrose
ACF	Autocorrelation Function
ADMIDAS	Adjacent to the Metal Ion-Dependent Adhesion Site
ADP	Adenosine Diphosphate
AFM	Atomic Force Microscopy
APTMS	(3-Aminopropyl)trimethoxysilane
ATP	Adenosine Triphosphate
cAMP	Cyclic Adenosine Monophosphate
cGMP	Cyclic Guanosine Monophosphate
CH	Cholesterol
CMC	Critical Micelle Concentration
DAG	Diglyceride
DLS	Dynamic Light Scattering
DMF	Dimethylformamide
DMPC	1,2-dimyristoyl-sn-glycero-3-phosphocholine
DMPG	1,2-dimyristoyl-sn-glycero-3-phosphorylglycerol
DOPC	1,2-dioleoyl-sn-glycero-3-phosphocholine
DOPE	1,2-dioleoyl-sn-glycero-3-phosphoethanolamine
DOPS	1,2-dioleoyl-sn-glycero-3-phospho-L-serine
DPPE	1,2-dipalmitoyl-sn-glycero-3-phosphoethanolamine
DTT	Dithiothreitol
ECM	Extracellular Matrix
FACS	Fluorescence-Activated Cell Sorting
FCS	Fluorescence Correlation Spectroscopy
Fg	Fibrinogen
FITC	Fluorescein Isothiocyanate
FLCS	Fluorescence Lifetime Correlation Spectroscopy
FLIM	Fluorescence Lifetime Imaging Microscopy
FRAP	Fluorescence Recovery After Photobleaching
FRET	Förster Resonance Energy Transfer
FSC	Forward Scatter
GA	Glutaraldehyde
GDP	Guanosine Diphosphate
GPCR	G Protein-Coupled Receptor
GTP	Guanosine Triphosphate

GUV	Giant Unilamellar Vesicle
HEPES	4-(2-hydroxyethyl)-1-piperazineethanesulfonic acid
I-EGF	Integrin-induced Epidermal Growth Factor
IP3	Inositol Trisphosphate
ITO	Indium Tin Oxide
LB	Langmuir Blodgett
LUV	Large Unilamellar Vesicle
MCS	Multichannel Scaler
MIDAS	Metal Ion-Dependent Adhesion Site
MLCK	Myosin Light Chain Kinase
MLV	Multilamellar Veiscle
OgFg	Oregon Green Fibrinogen
PBS	Phosphate-Buffered Saline
PC	Phosphocholine
PDGF	Platelet Derived Growth Factor
PDMS	Polydimethylsiloxane
PE	Phosphoethanolamine
PEG	Polyethylene Glycol
PGI2	Prostacyclin
PIP2	Phosphatidylinositol 4,5-bisphosphate
PKC	Protein Kinase C
PLA	Phospholipase A
PLC	Phospholipase C
PLL	Poly-L-lysine
POPC	1-palmitoyl-2-oleoyl-sn-glycero-3-phosphocholine
POPC	1-palmitoyl-2-oleoyl-sn-glycero-3-phosphocholine
POPE	1-palmitoyl-2-oleoyl-sn-glycero-3-phosphoethanolamine
POPG	1-palmitoyl-2-oleoyl-sn-glycero-3-phosphorylglycerol
POPS	1-palmitoyl-2-oleoyl-sn-glycero-3-phospho-L-serine
POPS	1-palmitoyl-2-oleoyl-sn-glycero-3-phospho-L-serine
PS	Phosphoserine
PSI	Plexin Semaphorin Integrin
SLB	Supported Lipid Bilayer
SM	Sphingomyelin
SPAD	Single-Photon Avalanche Diode
SSC	Side Scatter
STED	Stimulated Emission Depletion
STM	Scanning Tunnelling Microscopy
SUV	Small Unilamellar Vesicle
TCSPC	Time-Correlated Single Photon Counting
THD	Talin Head Domain
THF	Tetrahydrofuran
TIRFM	Total Internal Reflection Fluorescence Microscopy

TR	Thromboxane Receptor
TRAP	Trombin Receptor Activating Peptide
TxA2	Thromboxane A2
VASP	Vasodilator-Stimulated Phosphoprotein
VPP	Vesicle Prep Pro
vWF	von Willebrand Factor

Glossary of Units

cm	Centimetre
Da	Dalton
°C	Degrees Celcius
g	Gram
Hz	Hertz
K	Kelvin
kDa	Kilodalton
L	Litre
m	Metre
µg	Microgram
µl	Microliter
µm	Micrometre
$\mu m^2/s$	Micrometres squared per second
µM	Micromolar
µm	Microsecond
mg	Milligram
ml	Millilitre
mm	Millimetre
mM	Millimolar
mN	Millinewtons
ms	Millisecond
M	Molar
nm	Nanometre
nm	Nanosecond
RPM	Revolutions per minute
s	second
V	Volt
v/v	Volume per volume
w/v	Weight per volume
w/w	Weight per weight

Glossary of Figures

Glossary of Tables

Publications and Presentations

Peer reviewed publications

Gaul, V. *et al*. The Lateral Diffusion and Fibrinogen Induced Clustering of Platelet Integrin αIIbβ3 Reconstituted into Physiologically Mimetic GUVs. Integr. Biol. 7, 402–411 (2015).

Basit, H., Gaul, V., Maher, S., Forster, R. & Keyes, T. Aqueous-filled polymer microcavity arrays: versatile and stable lipid bilayer platforms offering high lateral mobility to incorporated membrane proteins. Analyst 3012–3018 (2015)

Poster presentations

The Lateral Diffusion and Fibrinogen Induced Clustering of Platelet Integrin $\alpha_{IIb}\beta_3$ Reconstituted into Physiologically Mimetic GUVs - SNAL ITN 4th Workshop on biomaterials and their interactions with biological and model membranes, Salou, Spain, 2015

Integrin Insertion into Biologically-Relevant Lipid Vesicles - BioPIC BioPhotonics & Imaging Conference, Dublin, Ireland, 2013

DTT and Mn^{2+}-Mediated Activation of $\alpha_{IIb}\beta_3$ in Platelets - Young Life Scientists Ireland Symposium, Dublin, Ireland, 2011

Abstract

The cell membrane is complex mixture of phospholipids, sphingolipids, sterols and proteins that combine to provide a semi-permeable barrier between the extracellular and intracellular environments, while also providing a functional role in cell-signalling, cell adhesion, and membrane transport. This complexity means that it is often better to study both the lipid and protein constituents of the cell membrane using artificial membrane models. Here, the transmembrane protein integrin $\alpha_{IIb}\beta_3$ was used as a model protein to be reconstituted into physiologically-relevant artificial lipid systems. $\alpha_{IIb}\beta_3$ is an integral membrane protein found in platelets and is a key mediator of thrombosis. Upon activation $\alpha_{IIb}\beta_3$ undergoes significant conformational rearrangement, clustering, and ligand-binding to enable complex bidirectional signalling. It is this structural rearrangement, aggregation and ligand binding that was the key focus of this project.

In chapter 2, and before reconstitution into artificial lipid models, $\alpha_{IIb}\beta_3$ was first studied in its native environment, the platelet. Here, DTT and Mn^{2+} were used to induce the activated form of $\alpha_{IIb}\beta_3$. It was found that both activators lead to structural changes in the integrin protein and varying degrees of platelet aggregation, without the full range of response normally associated with physiological agonists. Chapter 3 focused on the production of $\alpha_{IIb}\beta_3$-reconstituted liposomes. It was found that integrin-ligand binding lead to a reduction in $\alpha_{IIb}\beta_3$ mobility, as well as integrin clustering. $\alpha_{IIb}\beta_3$ was also found to preferentially excluded from cholesterol rich regions of lipid vesicles. Chapter 4 focused on the insertion of $\alpha_{IIb}\beta_3$ into a novel, cavity-spanning, lipid bilayer. Here, it was possible to determine $\alpha_{IIb}\beta_3$ diffusion co-efficients and induce protein aggregation. Finally, in chapter 5, cytoskeletal mimics were incorporated alongside a supported lipid bilayer in order to better imitate the conditions encountered by the cell membrane.

1. The Cell Membrane and Artificial Models

1.1. The Cell Membrane

At its most basic level, the cell membrane is a fluid lipid bilayer composed of constituent phospholipids, glycolipids, and cholesterols, interspersed with a range of proteins with varying biological roles. Cell membranes are semi-permeable membranes that enclose the cell cytoplasm to separate the cell from its outside environment. Over the years, a number of models have been proposed to explain how lipid molecules organise themselves in cell membranes. The first membrane model, proposed by Danielli *et al.* in 1935, built on the knowledge that lipids organise themselves into bilayers and suggested that a protein layer is tightly associated to the polar heads of lipids in the membrane.[1] This was further expanded on in 1972 when Singer and Nicolson put forward the "fluid mosaic model". In it, the cell membrane was described as a bilayer consisting of a homogenous mixture of diffusing macromolecules (lipids, proteins, glycoproteins, etc).[2] Since then this model has evolved and expanded to better describe the composition and organisation of the cell membrane. The biggest change in the model is the that this membrane is no longer thought to a homogenous mixture, but rather the various lipids and proteins are compartmentalised in heterogeneous phases, or domains. These domains are dynamic, restless, and cooperative molecular assemblies, which constantly form and disband within the plasma membrane over various timescales.[3] Of particular interest is the separation of lipids into the liquid disordered phase and liquid ordered phase. As the name suggests, the liquid ordered phase is a rigid and well-organised region, rich in sphingolipids and sterols. These nanoscale detergent resistant phases are often referred to as lipid rafts. It is believed these rafts function to serve as platforms for proteins that are involved in cell signalling.[4,5] In addition to these liquid disordered and liquid ordered phases, membrane invaginations, adhesive structures, and lectin-glycoprotein lattices are some of the features that have been added to the original fluid mosaic model.[6]

The dominant components of cell membranes are phospholipids. Phospholipids are amphiphiles and contain a hydrophilic headgroup and a hydrophobic tail composed

of two fatty acid chains. These chains may be saturated or unsaturated and are covalently linked to a phosphate group via a glycerol backbone. To the phosphate group, a simple molecule such as choline, serine, glycerol or ethanolamine is attached to form the headgroup. The amphipathic nature of phospholipids gives rise to their structural role. When exposed to an aqueous environment they readily self-assemble into bilayers with the hydrophilic heads orientated outwards and the hydrophobic tails buried within the interior.[7] Pure phospholipids have an intrinsic phase transition temperature, the temperature at which the phospholipid changes from a freely diffusing liquid phase to a rigid solid or gel phase. The temperature at which this occurs is dependent on the structure of the phospholipid. Longer fatty acid chain lengths exhibit higher phase transition temperatures, owing to increased Van der Waals interaction along their tails, and thus decreased lipid mobility. As well as the effect of chain length on phase transition temperature, the degree of unsaturation of the tails also influences the phase behaviour. The more double bonds present in the tail, the lower phase transition temperature. This is due to the fact that unsaturated tails interrupt the "packing" of phospholipids in the bilayer resulting in greater lipid mobility.[8]

Sphingolipids, like phospholipids, are composed of a polar head group and non-polar tail group. They have a long chain sphingoid base, generally 18 carbons in length. In the case of more complex sphingolipids they can form an amide-link to a long chain fatty acid.[9] The sphingolipid sphingomyelin, which is used throughout this thesis, is also composed of a phosphocholine or phosphoethanolamine head group. Owing to their long, largely saturated acyl chains, sphingolipids pack tightly in a bilayer, allowing for very little lateral movement. They are predominantly found in the outer leaflet of cell membranes and contribute to the stability of the bilayer.[9] As well as its role in signal transduction, sphingolipids plays an important role in the formation of lipid rafts.

The most well-known of the water insoluble sterols, cholesterol has a hydrophobic rigid ring structure with a short hydrocarbon tail. Cholesterol also has a polar hydroxyl group meaning it is also amphipathic in nature. In bilayers, the hydrophobic

ring of cholesterol positions itself adjacent to fatty acid tails of phospholipids, while the hydroxyl group of cholesterol forms hydrogen bonds with polar phospholipid head groups. Cholesterol has quite contrasting roles in the cell membrane, in that its rigidity decreases the mobility of phospholipid hydrocarbon tails, but its structure also serves to interfere with close packing of fatty acid tails. As such, cholesterol serves as a buffer between extremes of fluidity in the cell membrane. As previously mentioned, cholesterol also has an important role in the formation of lipid rafts. It associates primarily with lipids that feature long saturated fatty acyl chains, such as sphingomyelin. This non-random clustering forms the ordered raft domains that may have roles in membrane trafficking, cell-signalling and endocytosis.[10]

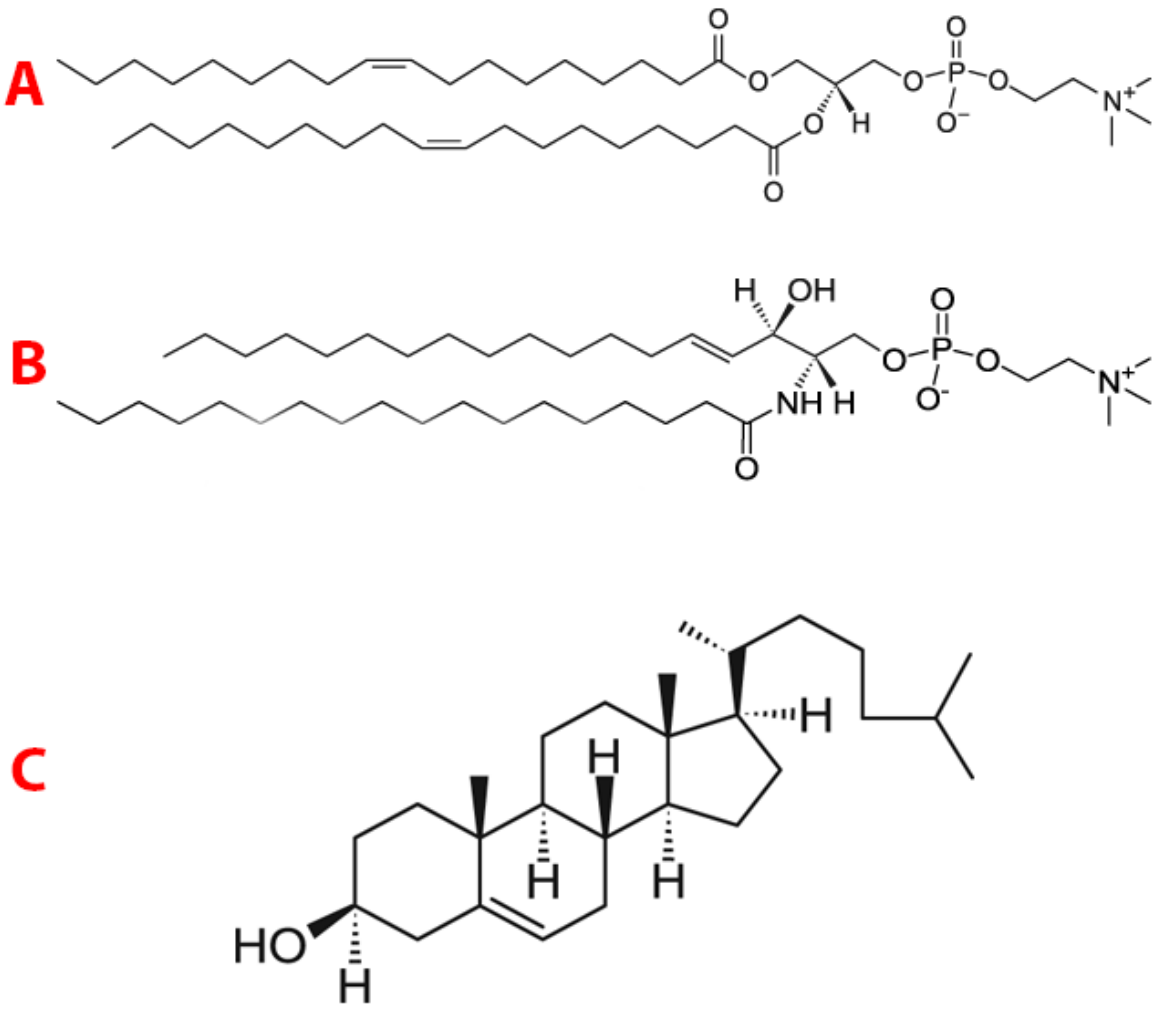

Figure 1: Examples of the main components of the lipid membrane. A) A phospholipid (DOPC). Phospholipids make up the bulk of the lipid membrane. Phospholipids consist of a hydrophilic headgroup and a hydrophobic tail composed of two fatty acid chains. These chains may be saturated or unsaturated and are covalently linked to a phosphate group via a glycerol backbone. To phosphate group, a simple molecule such as choline, serine, glycerol or ethanolamine is attached to form the headgroup. B) A sphingolipid (spingomylein). Sphingolipids are also composed of a polar head group and non-polar tail group. They have a long chain sphingolipid base and, in the case in the case of more complex sphingolipids, can form an amide-link to a long chain fatty acid. C) A sterol (cholesterol). Cholesterol has a hydrophobic rigid ring structure with a short hydrocarbon tail. Cholesterol also has a polar hydroxyl group meaning it is also amphipathic in nature.

While the basic structure of the cell membrane is provided by the aforementioned lipid constituents, membrane proteins perform the majority of the specific functions of membranes. The different classifications of membrane protein are summarised in Figure 2. Membrane proteins enable the cell to interact with the extracellular

environment and allows for a cell's characteristic functional properties. Due to this specificity, the proteins found within the cell membrane are numerous and diverse. Membrane bound proteins are typically classified as either integral; in which a portion of the protein is embedded within the bilayer, or peripheral, where the protein interacts with the exterior of the membrane or through binding via one of its constituents. For example, transmembrane proteins are integral proteins which extend through the lipid bilayer. Like the lipids themselves, transmembrane proteins are amphipathic and contain both hydrophilic and hydrophobic regions, the hydrophobic, spanning portion of such proteins are typically either α-helical or β-barrel structures. Other integral membrane proteins do not span through the bilayer but rather interact with a lipid monolayer of the cell membrane. This interaction may be through the hydrophobic face of an alpha helix or via covalent attachment to the lipid chains for example. This may occur on either the extracellular or intracellular side of the lipid bilayer. Finally, peripheral proteins do not interact directly with the lipid bilayer but rather act through membrane associated intermediates. Again these proteins may be found both extracellularly or intracellularly.[11] This thesis primarily focuses on a membrane protein $\alpha_{IIb}\beta_3$. $\alpha_{IIb}\beta_3$ is member of the integrin family of transmembrane receptors. Integrins are receptors found ubiquitously in metazoan cells. They facilitate cell migration and extracellular matrix assembly and are involved in a wide range of activities, including immune response, cell proliferation and apoptosis.[12] Like all 24 members of the integrin family, $\alpha_{IIb}\beta_3$ is a heterodimer of an alpha and beta subunit that spans the platelet plasma membrane once.[13] $\alpha_{IIb}\beta_3$ is found solely within the platelet lipid membrane, and numbers 50,000 to 80,000 copies per platelet making it the most abundant receptor on the cell fragment's surface. It's main role is in thrombosis where it undergoes significant conformational rearrangement, inducing complex bidirectional signalling and protein recruitment leading to platelet activation.[14]

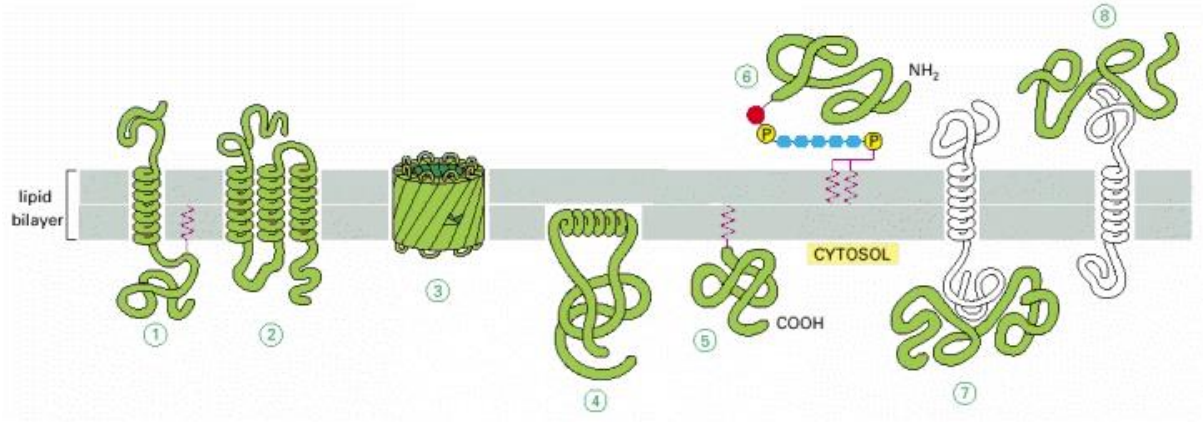

Figure 2: Different types of membrane proteins. Transmembrane proteins may extend across the lipid bilayer as single a single alpha helix (1), multiple alpha helices (2), or as rolled beta-sheets (3). Some membrane proteins are anchored to the cytosolic surface by an amphipathic alpha helix that partitions into the cytosolic monolayer of the lipid bilayer through the hydrophobic face of the helix (4). Others are membrane attached via a covalently attached lipid chain in the cytosolic monolayer (5). Some may be membrane attached via an oligosaccharide linker, to phosphatidylinositol in the non-cytosolic monolayer (6). Finally, peripheral membrane proteins interact with the lipid membrane via non-covalent interactions with other membrane proteins intracellularly (7), or extracellularly (8). Imaged from "Molecular Biology of the Cell".[11]

This thesis focuses on the lipid bilayer and transmembrane components of the platelet membrane. While the lipid composition of the platelet is discussed here, many of the membrane proteins are discussed in chapter 2. Within the literature, a number of different studies exist on the platelet lipid composition.[15–17] These are summarised in Table 1. Of the phospholipids, the majority have a phosphatidylcholine (PC) headgroup. The second most common headgroup is phosphatidylethanolamine (PE), while the third most common headgroup is phosphatidylserine (PS). All reports also agree that sphingomyelin (SM) is the primary sphingolipid found in platelets. This PC dominant lipid makeup is in contrast to some other cells; for example, in erythrocytes, PC, PE, and SM are found in almost equal parts.[15] Data also exists on the chain length of these lipid components. Owen *et al*. state that 20:4, 18:0, 18:1, and 16:0 fatty acids dominate the lipid make up of the platelet.[15] Hamid *et al*. highlights the same fatty acids types as well as 22:1. They later go on to breakdown this further: The relative majority of PC lipids are 16:0 fatty acids. The relative majority of PE lipids are 20:4 and 22:1 fatty acids. The relative majority of PS lipids are 18:0 fatty acids.[16] This breakdown of fatty acid content is also in agreement with Marcus *et al.*[17] Turning attention to the sterol composition in

platelets, phospholipids outnumber cholesterol 1.75 to 1 (mol/mol) according to Owen *et al.*[15] Hamid *et al.* give the ratio in weight, stating that the ratio is 4.42 to 1 (mg/mg).[16] Given that cholesterol has a molecular weight of 386 g/mol, and taking DOPC as a model phospholipid with a molecular weight of 786 g/ml we can approximate that phospholipids are twice the molecular weight of cholesterol. Taking this into account we can say that ratio of phospholipids to cholesterol is approximately 2.2 to 1, roughly in line with Owen's work. Similarly, Marcus *et al.* found a ratio of approximately 2 phospholipids for every 1 cholesterol molecule. For comparison, they state that liver plasma membranes have an approximate molar ratio of 3.8 to 1, erythrocytes have an approximate molar ratio of 1.1 to 1, and brain myelin has an approximate molar ratio of 0.76 to 1 (phospholipid:cholesterol).[17]

Table 1: The lipid composition of the platelet. The literature is in broad agreement with the breakdown of lipid components within the platelet. PC-based phospholipids make up the bulk of the lipids, followed by PE and PS containing phospholipids. SM is also a major lipid component of the cell. Phospholipids outnumber cholesterol approximately 2 to 1.

	Owen *et al.*[15]	**Hamid *et al.*[16]**	**Marcus *et al.*[17]**
Lipid type	Approximate % of phosphorus containing lipids in platelets		
PC	40	39	39
PE	28	26	26
PS	9	9	10
SM	19	18	18
	Approximate phospholipid to cholesterol ratio (mol/mol)		
PL:CH	1.75	2.2	2

1.2. Biomimetic Models

As previously described, the cell membrane is a complex and dynamic mixture of lipids and proteins interacting with one another. Due to this complexity, it is often desirable to create biomimetic models of the lipid membrane where constituents can be included or excluded at will. To this end, a range of biomimetic systems have been used within the the literature but they can generally be divided into two categories: lipid vesicles, and supported lipid bilayers (SLBs). Lipid vesicles (also known as liposomes) are free-standing, quasi-spherical, structures formed from an enclosed lipid bilayer. SLBs are planar lipid bilayers formed above a solid substrate such as glass or mica. Both lipid vesicles and SLBs may be formed from a wide range of techniques each with their own advantages and disadvantages.[1] In this thesis we sought to produce both vesicle-based (chapter 3) and SLB-based biomimetic models (chapter 4). One of the key goals of the project was to expand on the existing work within the literature by utilising more physiologically-relevant lipid compositions in order to more accurately mimic the cell membrane. Indeed, one of the striking features of existing models is reliance on unary or binary lipid compositions. Here, we explored more complex lipid mixtures including a composition adopted from the Lentz group at the University of North Carolina at Chapel Hill; known as nature's own, and various domain-forming lipid compositions.

While purely lipid models have their role, biomimetic systems are particularly powerful when membrane proteins are reconstituted within the lipid bilayer. This allows for the study of said protein in controlled isolation, away from the complexity of the cell membranes and any exogenous agents. For example, drug interactions, ligand binding, and diffusional studies may be carried out on reconstituted proteins, away from the multitude of other membrane constituents that would otherwise complicate such measurements. Given that we wanted to insert membrane proteins into our biomimetic models we needed to explore and understand various reconstitution techniques. A search of the literature shows that a number of general strategies may be used:

Perhaps the simplest method of membrane protein reconstitution is the spontaneous insertion of proteins into preformed unilamellar vesicles. A number of membrane proteins have been bilayer inserted via this method, such as cytochrome c oxidase, cytochrome b5, bacteriorhodopsin, and F_0F_1-ATPase.[18] Such reconstitution appears to more successful where impurities are introduced into the lipid (eg short chain myristic acids or cholesterol).[19] An additional factor that appears to influences direct incorporation is vesicles size, where insertion occurred preferentially in liposomes with a small diameter (approximately 20 nm).[18]

Organic solvents have also been successfully used to reconstitute membrane proteins in artificial lipid bilayers. Based on reverse phase evaporation, a method utilised to prepare large unilamellar and multilamellar vesicles[20], membrane proteins are added to the lipid-solvent mixture before the solvent is evaporated and the vesicles formed from the dried protein and lipid film. This protocol has been used to successfully insert a wide range of membrane proteins into liposomes, such as rhodopsin[21], bacteriorhodopsin[22], acetylcholine receptor (AcChR)[23], and cytochrome c oxidase.[24] The biggest and most obvious drawback to this insertion protocol is the usage of harsh organic solvents in direct contact with often delicate and easily denatured membrane proteins.

A rather crude approach to membrane protein insertion is the use of mechanical means to reconstitute the protein. Such mechanical means are routinely used to produce Small Unilamellar Vesicles (SUVs) or Large Unilamellar Vesicles (LUVs) from a lipid-buffer solution.[25] Sonication of such a mixture in the presence of membrane protein is one such method to incorporate transmembrane proteins into SUVs, although this method is obviously hindered by protein inactivation during the sonication process.[18] A slight modification to this protocol utilises a freeze thaw cycle to reduce the sonication time. Here, preformed vesicles are mixed with the membrane protein of choice before undergoing the freeze-thaw step before a short sonication phase. This technique has been used to reconstitute erythrocytes D-glucose transporter into lipid vesicles.[26]

By far the most common and successful method of membrane protein reconstitution utilises detergent-mediated reconstitution. In its simplest form, this approach begins with the creation of a lipid-protein-detergent mixture, followed by the removal of said detergent to leave behind a lipid-protein assembly. The exact protocol of reconstitution may vary between choice of protein and choice of detergent. Some groups use preformed SUVs[27] or LUVs[28] as the target for reconstitution. Others have used a solubilised lipid suspension as the lipid source rather than preformed lipid vesicles.[29–31] It is also possible to directly target preformed GUVs during the insertion process,[32,33] although this is harder to scale up and also runs the risk of vesicle destruction. In all cases, the end result is the formation of membrane protein reconstituted lipid vesicles, or proteoliposomes.

In similar fashion, detergent-mediated reconstitution can also be used to form membrane protein inserted SLBs. This can be achieved via the deformation of proteoliposomes to form a supported planar bilayer.[34] Alternatively, detergent-mediated insertion of membrane proteins into an SLB can be achieved *in situ*. In this case a preformed SLB may be created by whatever means before being partially solubilised by a detergent. By carefully controlling the detergent concentration, the SLB can be weakened to allow for membrane protein insertion without bilayer destruction. Subsequently, the detergent may be removed to leave behind an SLB containing properly inserted transmembrane proteins.[35]

To achieve this solubilisation process a wide range of detergents have been used, including, but not limited to, triton x-100[30], β-OG[27], CHAPS[36], and octyl-POE[33]. While some groups have sought to use minimal detergent concentrations to simply bring preformed lipid vesicles to the onset of solubilisation, other groups have sought to fully solubilise the lipid vesicles to allow for protein insertion. There is no general consensus on what detergent to use in the solubilisation process where the main concern is minimising protein aggregation and any other deleterious effects to the membrane protein. To this end, Rigaud and Lévy have proposed that glycosylated detergents (such as β-OG or dodecylmaltoside), polyoxyethylenic detergents (such as triton x-100 or $C_{12}E_8$), as well as ionic detergents (such as cholate) all be explored

as possible candidates for membrane protein insertion.[37] Interestingly, Müller *et al.* reported that lipid composition influenced detergent choice. In the reconstitution of $\alpha_{IIb}\beta_3$ they reported that triton-x 100-mediated insertion into DMPC and DMPC/DMPG vesicles was successful, while triton-x 100-mediated insertion into POPC/POPS vesicles was unsuccessful. On the other hand, β-OG-mediated insertion into DMPC and DMPC/DMPG vesicles was unsuccessful, yet β-OG-mediated insertion into POPC/POPS was successful (although not as successful as triton-x 100 and DMPC or DMPC/DMPG). However, it must be noted that the detergents were removed via different means in this case, where triton x-100 was removed by detergent adsorbent beads, and β-OG removed be extensive dialysis.[34] Thus it is unclear whether the differing observations are as a result of detergent choice or means of detergent removal. To date there is no definitive guide for membrane protein reconstitution, where most successful insertions appear to have been achieved through a trial and error process. In this thesis both triton x-100 and β-OG were explored in the detergent-mediated reconstitution process.

Whatever the means of formation of the lipid-protein-detergent mixture, the detergent must subsequently be removed from the micellar solution, allowing formation of closed lipid bilayers in which the proteins are incorporated. Once again the strategies for this step are wide ranging. Perhaps the simplest way detergent removal may be achieved is via dilution. Whilst not capable of completely removing detergent from the solution, dilution with a detergent-free buffer can reduce the initial surfactant below its critical micelle concentration, (CMC). The CMC is defined as the concentration at which detergent monomers form micellar aggregates[18], and reduction of detergent concentration below its CMC allows for the spontaneous formation of closed proteoliposomes. Practically speaking, this particular technique is limited to use with detergents with high CMCs such as cholate or β-OG and even so will normally require some later concentration step in order to obtain a solution with a workable protein concentration. As well as this, because the detergent is not actually removed from the solution, residual surfactants may influence downstream experiments. This particular method has been used to reconstitute sarcoplasmic reticulum Ca^{2+} ATPase and cytochrome oxidase[38], as well as bovine rhodopsin.[39]

Dialysis is a common and effective method for removing detergent from the solution. Here the lipid-protein-detergent mixture is dialysed against a detergent-free buffer. Only the detergent monomers diffuse through the dialysis tubing leaving behind a closed proteoliposome assembly. Again this method of detergent removal is best suited to remove detergents with high CMCs. It is also more difficult to reproduce and control the rate of dialysis, is relatively time consuming, and may leave trace amounts of surfactant behind. On the other-hand it is a simple, low-cost, and low-maintenance method of detergent removal.[37] Dialysis has been used in the insertion of many membrane proteins including, but not limited to, SNARE proteins[27], bovine rhodopsin[39], and spinach aquaporin SoPIP2;1.[40] Dialysis was one of the detergent removal processes utilised in this thesis, specifically for the removal of the detergent β-OG.

Perhaps the most common method of detergent removal is the use of detergent-adsorbent beads such Bio-Beads SM-2 or Amberlite XAD. The key advantage of this method is that detergent-adsorbent beads can be used regardless of the detergents CMC. The beads may be added directly to the lipid-protein-detergent solution, may be added to the outside of a dialysis bag to speed up the transfer process or may be used on a filtration column. Other major advantages of adsorbent beads is that the rate of surfactant removal can be controlled by varying the concentration of beads added, the fact that the beads ensure full detergent removal, as well as its high rate of reproducibility.[37] Detergent-adsorbent beads have been used for surfactant removal in the reconstitution process of platelet integrin $\alpha_{IIb}\beta_3$[30], the lactose transporter LacS[41], and the porin OmpF[33], amongst many others. In this thesis Bio-Beads were routinely used for the removal of triton x-100 after protein insertion.

Therefore, in summary, one of the key goals of this project was to explore these reconstitution techniques in order to insert membrane proteins into both liposome and SLB models, while maintaining the biological relevance of the lipid environment.

1.3. $\alpha_{IIb}\beta_3$ reconstitution

While a number of membrane proteins were explored by the group, the primary model protein used for reconstitution in this thesis was platelet integrin $\alpha_{IIb}\beta_3$. Prior to this work, there existed a number of relevant studies where $\alpha_{IIb}\beta_3$ had been reconstituted in a number of different artificial lipid systems. The first mention of $\alpha_{IIb}\beta_3$ reconstitution in lipid vesicles is found in work by Parise and Philips where $\alpha_{IIb}\beta_3$ was added to variety of egg yolk PC and bovine brain PS compositions in the presence of octyl glucoside. The lipid-protein-detergent solution was well mixed before a brief sonication period. To remove the detergent, the mixture was dialysed against a detergent-free buffer. It was found that a using a mixture of 30 % PC and 70 % PS (mol/mol) lead to the highest degree of integrin reconstitution and that the vast majority of integrin was orientated with its extracellular domain on the outside of the lipid vesicles as determined by cryoelectron microscopy.[42]

More in-depth work was done by Müller *et al.* where $\alpha_{IIb}\beta_3$ was incorporated into lipid vesicles using two different reconstitution methods, several detergents, and differing lipid compositions. All of these criteria reportedly influenced success of the $\alpha_{IIb}\beta_3$ insertion process as examined via cryoelectron microscopy. For example, using triton x-100 and bio-beads SM-2 to insert $\alpha_{IIb}\beta_3$ into POPC/POPS vesicles did not result in successful reconstitution. However, changing the lipid composition to DMPC or DMPC/DMPG (1:1) did result in successful reconstitution. Intriguingly, changing the detergent to octyl glucoside and the removal method to dialysis lead to almost the exact opposite result. Here, DMPC or DMPG vesicles could not be $\alpha_{IIb}\beta_3$-reconstituted, while POPC/POPS vesicles could be $\alpha_{IIb}\beta_3$-reconstituted. In this case the protocol and the ratio of POPC/POPS was almost exactly the same as the earlier work by Parise and Philips (30/70 versus 25/75) although interestingly this update reported the $\alpha_{IIb}\beta_3$ insertion as “partial” as well as stating that “incorporation was not homogeneous” suggesting that $\alpha_{IIb}\beta_3$ had a tendency to aggregate under these conditions. They did not further expand on why these results differed with choice of detergent and lipid composition. This work also highlighted the fact that colocation

of lipid and integrin was not a reliable measure of correct incorporation but instead a sign that $\alpha_{IIb}\beta_3$ had a tendency to strongly adhere to the lipid, an association that could not be removed by sucrose-gradient centrifugation.[34] In hindsight this perhaps brings into question the earlier work Parise and Philips where they had concluded that $\alpha_{IIb}\beta_3$ was fully reconstituted in their PC/PS mix.[42] Following the Müller reconstitution process the group went on to form a DMPC/DMPG SLB above a quartz substrate. Here they performed Total Internal Reflection Fluorescence Microscopy (TIRFM) and found that the bilayer inserted integrin was capable of binding both fibrinogen and RGD containing peptides. They concluded that fibrinogen binding occurred in a two-step process where binding was initially fast and reversible (via a buffer wash) but over longer timescales was "essentially irreversible" after 2 hours.[34]

Erb *et al.* were the first group to look at the mobility of $\alpha_{IIb}\beta_3$ in an artificial lipid system. In an integrin insertion protocol based on Müller's earlier work, $\alpha_{IIb}\beta_3$ was reconstituted into DMPC/DMPG (1:1) vesicles, which were later disrupted above a quartz substrate to form an SLB. Using Fluorescence Recovery After Photobleaching (FRAP), it was concluded that the $\alpha_{IIb}\beta_3$ protein diffused at a rate of 0.70 ± 0.06 $\mu m^2/s$ at 33 °C, a value well below the diffusion co-efficient of the lipid itself (4.40 ± 0.40 $\mu m^2/s$). Of note was the fact that much of the $\alpha_{IIb}\beta_3$ protein was immobile (approximately 40 %) and so this diffusion co-efficient refers to a second round of photobleaching that discounts immobile and, therefore, bleached labelled $\alpha_{IIb}\beta_3$ molecules. As mentioned previously such protein immobility is a common problem with reconstituted systems above planar substrates. It was also found that addition of fibrinogen to the system lead to an increase in the number of immobile $\alpha_{IIb}\beta_3$ proteins (approximately 70 %) while the remaining mobile $\alpha_{IIb}\beta_3$ proteins showed a decreased diffusion co-efficient (0.58 ± 0.06 $\mu m^2/s$ at 33 °C). From this Erb concluded that the protein was non-clustered in its reconstituted state but clusters upon fibrinogen binding. Smaller ligands (an RGD containing peptide and a fibrinogen γ-chain dodecapeptide) did not alter the aggregation state of $\alpha_{IIb}\beta_3$ in the system, perhaps not surprising given the fact these molecules did not provide a bridge between adjacent integrin proteins.[30]

In an update on the earlier Erb work, Goennenwein *et al.* initially attempted to recreate these reported results. Again DMPC/DMPG was used as the target of reconstitution, mediated by triton x-100 and bio-beads SM-2. However, in this case the disruption of the proteoliposomes above a planar substrate lead to completely immobilised $\alpha_{IIb}\beta_3$, a result that contradicts Erb's findings. This problem was overcome by the formation of ultrathin cellulose films above a glass substrate to create a polymer cushion. Such a polymer cushion provided enough space between the lipid bilayer and the glass to allow for the diffusion of the bulky reconstituted protein. Here they again used FRAP to yield a diffusion co-efficient of 0.60 ± 0.2 $\mu m^2/s$ for the mobile fraction, a value in close agreement with Erb, albeit with the prior requirement of a polymer cushion. Despite the necessity for such a cushion they reported a large percentage of proteins remained immobile within the system (75 %).[31] This paper again emphasises the main drawback of membrane protein reconstitution in planar SLBs, where even the use of a polymer cushion did not fully decouple the bilayer and membrane proteins from the underlying substrate.

Purrucker *et al.* provided an alternative system that used polymer-tethered lipid membranes instead of a cellulose film to separate an $\alpha_{IIb}\beta_3$ containing bilayer from the underlying substrates. Again this insertion protocol followed Müller's work whereby integrin was first inserted into DMPC/DMPG vesicles although in this case the proteo-liposomes were disrupted above an SOPC LB transferred monolayer (with varying concentrations of lipopolymers) to form an asymmetric lipid bilayer. In this system only 20 % of the $\alpha_{IIb}\beta_3$ were mobile and the reported diffusion co-efficient was given as 0.03 $\mu m^2/s$ according to FRAP, a value well below Erb's and Goennenwein's reported values.[43] A second follow up paper by Purrucker *et al.* used a different set of polymer tethers but again reported a similarly small mobile fraction (16 – 24 %) and low diffusion co-efficient (0.08 – 0.13 $\mu m^2/s$) for membrane-reconstituted $\alpha_{IIb}\beta_3$.[44]

Feng Ye *et al.* avoided the use of vesicles and SLBs by synthesising DMPC/DMPG nanodiscs, each bearing a single lipid embedded $\alpha_{IIb}\beta_3$ protein. With access to the

intracellular domain of $\alpha_{IIb}\beta_3$ they were able to activate the protein without the use of DTT or Mn^{2+}. This was achieved via the use of the talin head domain (THD), part of the integrin-associating protein talin. They confirmed this activated state via the use of an antibody specific to the activated form of $\alpha_{IIb}\beta_3$, PAC-1. Interestingly, and in contrast to nanodisc-embedded $\alpha_{IIb}\beta_3$, detergent-solubilised $\alpha_{IIb}\beta_3$ was not readily activated by THD showing the requirement for $\alpha_{IIb}\beta_3$ to be lipid bilayer inserted. They also examined the structural status of activated and un-activated $\alpha_{IIb}\beta_3$ in their system. It was found that the addition of THD leads to an extended conformation; molecular extension of the integrin, in the absence of other proteins, ligands, or imposed forces. This was determined via cryoelectron microscopy.[45]

In a subsequent report, Streicher *et al.* were able to reconstitute $\alpha_{IIb}\beta_3$ into Giant Unilamellar Vesicles (GUVs) and monitor the spreading dynamics of the giant vesicles on a surface coated with fibrinogen, the primary ligand of $\alpha_{IIb}\beta_3$. Interestingly this is one of the few modern papers to feature a non-DMPC containing lipid composition. Instead they utilised 85 % egg PC, 10 % egg PA, and 5 % DPPE-PEG2000 to firstly create integrin-containing SUVs. They later emphasised the requirement for egg PA and DPPE-PEG2000 in the lipid mixture although it was not clarified whether this was to ensure $\alpha_{IIb}\beta_3$ reconstitution or improve the yield of GUVs. In any case this choice of lipid composition is no more biomimetically relevant than combinations of DMPC and DMPG when considering the platelet membrane. In order to validate the insertion process and confirm biological activity of the integrin RGD-containing quantum dots were used. Modelling the spreading kinetics of the GUVs on the adhesive surfaces they were able to break the process down into a 2-step process. Firstly, small adhesive patches begin to grow before fusing and to form an adhesive ring. Secondly, the ring closes with a radius decreasing linearly with time before it eventually forms an adhesive disk.[46] While $\alpha_{IIb}\beta_3$ appears to be biologically active under these conditions it is noteworthy that no cryoelecton microscopy or diffusion measurements carried out to ensure that the integrin protein was fully membrane-inserted and not just membrane-associated. This is especially relevant given the fact that $\alpha_{IIb}\beta_3$ has been highlighted to strongly adhere to the lipid bilayer in non DMPC containing compositions.[29,34]

One of the few other modern papers to feature $\alpha_{IIb}\beta_3$ liposome-reconstituted into a non-DMPC containing lipid composition is by Sloan *et al*. Here, a mixture of egg PC, bovine PS and cholesterol (60:15:25) was used for insertion. Again, biological relevance is minimal. Of note was also the use of β-OG in the $\alpha_{IIb}\beta_3$ detergent reconstitution process instead of the common use of triton x-100 in the literature. They used flow cytometry that their membrane-reconstituted integrin was capable of binding fibrinogen but did not undergo fibrinogen-mediated clustering. [47] This finding that no clustering occurred upon fibrinogen binding is in contrast to Erb's observations and Goennenwein's observations in integrin reconstituted SLBs.[30,31] As was the case with Streicher *et al.*, Sloan *et al.* did not carry out any cryoelecton microscopy or diffusion measurements to ensure that the integrin protein was fully membrane-inserted and not just membrane-associated. This means that of the two recent papers where $\alpha_{IIb}\beta_3$ has been membrane-reconstituted into DMPC-free compositions, neither has been able to provide proof of full transmembrane insertion.

Table 2: Summary of $\alpha_{IIb}\beta_3$ integrin reconstitution papers in the literature. The vast majority of papers have incorporated $\alpha_{IIb}\beta_3$ into DMPC-containing compositions using triton x-100 and bio-beads. The papers that feature diffusion measurements have all been for SLB systems and utilised FRAP.

Paper	Year	Platform	Composition	Integrin Diffusion	Notes
Parise and Philips[42]	1985	Lipid vesicles	Egg PC and Bovine PS	n/a	First reconstitution of $\alpha_{IIb}\beta_3$
Müller *et al*.[34]	1993	SLB	DMPC and DMPC/DMPG	n/a	DMPC required for proper reconstitution
Erb *et al*.[30]	1997	SLB	DMPC/DMPG	0.70 μm^2 according to FRAP	First diffusion measurements for $\alpha_{IIb}\beta_3$
Sloan *et al*.[47]	2000	Lipid vesicles	Egg PC, Bovine PS and Cholesterol	n/a	Unusual use of a non-DMPC containing

					composition
Goennenwein *et al*.[31]	2003	SLB	DMPC/DMPG	0.60 μm^2 according to FRAP	A cellulose cushion was required for $\alpha_{IIb}\beta_3$ diffusion
Purrucker *et al*.[43]	2004	SLB	Asymmetric bilayer of DMPC/DMPG and POPC	0.03 $\mu m^2/s$ according to FRAP	A polymer tether used for $\alpha_{IIb}\beta_3$ diffusion
Purrucker *et al*.[44]	2007	SLB	Asymmetric bilayer of DMPC/DMPG and POPC	0.08 – 0.13 $\mu m^2/s$ according to FRAP	A different polymer tether used for $\alpha_{IIb}\beta_3$ diffusion
Streicher *et al*.[46]	2009	Lipid vesicles	Egg PC, Egg PA and DPPE-PEG200	n/a	Unusual use of a non-DMPC containing composition
Feng Ye et al[45]	2010	Nanodiscs	DMPC/DMPG	n/a	Nanodiscs used as an alternative to vesicles/SLBs

Summarised in Table 2, a number of things are evident about the current standing of $\alpha_{IIb}\beta_3$ reconstitution in the literature. Firstly, the majority of reconstitution experiments have taken place in SLBs rather than lipid vesicles. Indeed, all $\alpha_{IIb}\beta_3$ diffusion-based experiments have taken place in SLBs. Erb was able to report laterally diffusing $\alpha_{IIb}\beta_3$ directly on a planar substrate[30] but Goennenwein[31] and Purrucker[43,44] required a polymer cushion to allow for mobile $\alpha_{IIb}\beta_3$. Of particular note is that in all cases, with or without polymer cushions, a high percentage still rendered immobile on the underlying substrate. These values ranged from 40 %[30] to 84 %[44] of the bilayer-reconstituted integrin remaining immobile. We were therefore very interested to create platforms that allowed for free diffusion of $\alpha_{IIb}\beta_3$ away from the restrictions of standard planar systems and the non-specific interactions they bring. To do so, we decided to utilise two separate systems, namely a free-standing GUV set-up, and a cavity-spanning lipid bilayer array.

Another noteworthy aspect of the literature to date is the fact that the diffusional studies have been limited to FRAP-based experiments. FRAP interrogates relatively large volumes (several μm^3) via destructive photobleaching to infer diffusion co-efficients based on the fluorescent recovery of the lipid bilayer. In the work described herein, we sought to utilise the single molecule techniques of Fluorescence Correlation Spectroscopy (FCS) and Fluorescence Lifetime Correlation Spectroscopy (FLCS) to gain insight into the diffusional characteristics of integrin-reconstituted bilayer systems. FCS/FLCS has a number of key advantages over FRAP. These methods are described in detail in the following section but of note is the fact that FCS/FLCS is non-destructive to the fluorescent molecules in the sample, can be readily used in multicolour experiments, and can be used to infer additional data about the sample such as probe concentration and kinetic data.[48] Another key advantage of FCS/FLCS over FRAP is the requirement for much lower concentrations of fluorophore in the sample. This limits any influences exogenous agents may have on the dynamics of the lipid membrane. Finally, the femotolitre volume required for FCS/FLCS is well suited to the GUV and cavity-spanning lipid bilayers we sought to create, and is in contrast to the large volume required in FRAP.[49] Of course, FCS/FLCS does have some drawbacks when compared to FRAP. For example, FRAP is more suited measuring slower moving molecules, it probes larger areas of a lipid system, is more robust when probing systems that contain a large fraction of immobile fluorophores, and is experimentally easier to carry out and interpret.[50] Nonetheless, with regards to our two designated systems of a free-standing GUV set-up and a cavity-spanning planar lipid bilayer the advantages of FCS/FLCS are clear. Therefore, this work attempts to be the first not only to characterise $\alpha_{IIb}\beta_3$ diffusion in vesicles but also to characterise $\alpha_{IIb}\beta_3$ diffusion by FCS/FLCS in any platform.

Another striking feature of the literature is the dependence on DMPC to be utilised in the lipid composition. This requirement for DMPC was first noted by Müller[34] and later re-emphasised by Erb in two separate papers[29,30] Due to this recommendation, the majority of $\alpha_{IIb}\beta_3$ reconstitutions have since taken place in DMPC-based compositions. The two exceptions to this rule are by Sloan[47] and by Streicher[46]. However, given neither of these papers address the diffusion co-efficient of $\alpha_{IIb}\beta_3$ in

their respective systems, nor do they provide cryoelectron microscopy data of $\alpha_{IIb}\beta_3$ in the vesicles there is doubt as to whether the $\alpha_{IIb}\beta_3$ has been fully inserted into the lipid bilayer. This is further highlighted by the fact that association of $\alpha_{IIb}\beta_3$ with the lipid is not proof of full reconstitution. For example, Müller stated that "Co-migration of lipid and integrin in a sucrose gradient was not a reliable measure of correct incorporation. Especially during dialysis, non-incorporated integrin formed large protein aggregates which adhered so strongly to the vesicles that they could not be separated on a sucrose gradient."[34] In our work we sought to overcome this apparent limitation by inserting $\alpha_{IIb}\beta_3$ into DMPC-free lipid compositions and strive towards a physiologically-relevant lipid mixture.

1.4. Diffusion of transmembrane proteins

One of the key goals of this thesis was to characterise the diffusion co-efficients of transmembrane proteins, with emphasis on reconstituted $\alpha_{IIb}\beta_3$ in liposomes and SLBs. We were particularly interested in determining whether conformational changes in the structure of $\alpha_{IIb}\beta_3$ and/or ligand binding would alter the diffusion of the integrin protein. To this end FCS and FLCS were major techniques utilised and these are discussed in more detail below. Before going into more detail about these experimental techniques we must first discuss diffusion and in particular transmembrane protein diffusion. Throughout this thesis much of the work focuses on obtaining the diffusion co-efficients (D, usually in $\mu m^2/s$) of molecules, that is, the distance a particle may reach due to its diffusive motion. The larger the diffusion co-efficient, the faster the particle moves. The diffusion of a molecule in solution may be described as a random walk. For example, a protein freely diffusing in water

collides with water molecules, receiving a series of small kicks in random directions. The protein then takes on a random trajectory, characterised as the mean squared displacement (MSD).[50] According to the Stokes-Einstein equation, in Brownian motion, the diffusion of spherical particles through a liquid with a low Reynolds number may be described by:

$$D = \frac{k_B T}{6\pi\eta r}$$

Where k_B is the Boltzmann constant, T is the absolute temperature, η is the dynamic viscosity, and r is the radius of the diffusing spherical particle. However much of our work does not relate to three dimensional diffusion of particles, but rather the diffusion of transmembrane protein in two dimensions within a thin lipid membrane. To explain this type of diffusion we turn to the Saffman–Delbrück model.[51] This modification to 3D diffusion describes the transmembrane protein as a cylindrical object diffusing within a thin layer of viscous fluid of defined height (the lipid membrane), and surrounded by a less viscous fluid (the bulk fluid). In said model the diffusion co-efficient is described by:

$$D = \frac{k_B T}{4\pi\mu_m h}\left(ln\left(\frac{\mu_m h}{\mu_w R}\right) - \gamma\right)$$

Where h is the thickness of the lipid bilayer, μ_m is the viscosity of the lipid bilayer, μ_w is the viscosity of the surrounding aqueous phase, R is the hydrodynamic radius of the transmembrane protein, and γ is the Euler–Mascheroni constant. The Saffman–Delbrück model is the standard model for transmembrane diffusion and widely utilised within the literature. Indeed, various papers have shown that this model of membrane protein diffusion can be used to accurately predict the diffusion of

transmembrane proteins.[41,52–54] One of the key observations that may be made about this model is the fact that predicts a weak, logarithmic dependence of the diffusion coefficient (D) with the radius (R) of the protein. In practice this means that radius of a transmembrane protein has little influence on its diffusion co-efficient. For example, increasing the protein radius from 1 to 10 nm only reduces the protein's mobility by 30 %.[55] However, despite the widespread use of the Saffman–Delbrück model, challenges do exist as to its veracity.[52] For example, Gambin *et al.* suggested that a transmembrane protein's diffusion coefficient is in fact strongly linked to its dimensions. They state, in contrast to the Saffman–Delbrück assumption that the lipid bilayer is homogenous layer of viscous fluid, that the bilayer is not a featureless continuum. Instead they emphasise the heterogeneity of the membrane, with lipid chains of varying sizes, undergoing internal degrees of freedom, and featuring packing defects. To combat this they proposed an alternative model for transmembrane protein diffusion where the diffusion coefficient is inversely proportional to the radius of the diffusing object.[55] Naji *et al.* made further advancements on this when they argued that protein-lipid interactions within the bilayer deforms the membrane leading to new hydrodynamic stresses and a suppression of mobility.[56] This was later disputed by Guigas and Weiss' calculations where their data found that while hydrophobic mismatch between transmembrane proteins and the lipid membrane did alter the membranes viscosity, it had minimal influence on protein diffusion.[57] It is therefore suggested that the Saffman–Delbrück model is applicable for particles with a radius below 10 nm, dimensions well suited to the study of transmembrane proteins.[52]

1.5. Background to key techniques

1.5.1. Fluorescence microscopy

Fluorescence is the platform for most of the methods used in this work. Therefore, to understand these techniques we must first understand fluorescence. In its simplest terms, fluorescence is the property of a molecule to molecule to absorb light at a given wavelength and, after a brief interval, emit light at a longer wavelength. The difference between the absorption and emission wavelengths is known as the Stokes shift. Photophysical properties of a fluorophore can be described by a Jablonski diagram. Starting in the ground state, the fluorophore is excited into a higher energy singlet state by absorption of light (approximately 10^{-15} seconds). The molecule then rapidly undergoes internal conversion, and vibrational and rotational relaxation (approximately 10^{-14} – 10^{-11} seconds), to an intermediate semi-stable, excited state in a process described by Kasha's rule. The molecule may return to the ground state non-radiatively, by emitting thermal energy through vibrational/rotational relaxation. Alternatively, this return to the ground state may occur radiatively via the emission of a photon under appropriate molecular conditions (approximately 10^{-9} seconds). This process is known as fluorescence. Of key importance is the fact that the emitted photon has less energy than the absorbed photon, since fluorescence occurs after the molecule has already relaxed to its lowest vibrational level within the excited state. This means that the emission occurs at longer wavelengths than the absorption, i.e. it is red-shifted (or Stokes shifted) in comparison with absorption. In an alternative relaxation pathway, the excited molecules may in some circumstances, undergo inter-system crossing

(approximately 10^{-8} – 10^{-3} seconds) to form a triplet state. From the triplet state the molecule may return to the ground state, again either radiatively, or non-radiatively. The radiative relaxation from the triplet state is known as phosphorescence (approximately 10^{-4} – 10^{-1} seconds). This process occurs on a noticeably longer time-scale than fluorescence because it originates from a spin-forbidden process.[58,59]

Fluorescence has wide ranging scientific applications. For example, the use of fluorescently-labelled proteins and peptides allows for the tracking and monitoring of biological molecules using fluorescence microscopy and confocal microscopy.[58] Furthermore, diffusion dynamics of single molecules can be examined via FCS[60], while the lifetime of a fluorescent molecule can inform us about environmental conditions via Fluorescence Lifetime Imaging Microscopy (FLIM)[61]. Additionally, the selectivity of fluorescently-labelled antibodies can be exploited for cell identification and sorting via flow cytometry.[62] These are just some of the many applications of fluorescence widely used in life sciences.

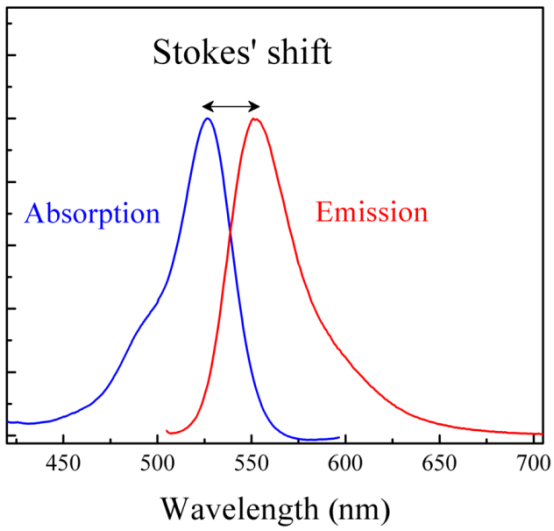

Figure 3: A Stokes shift. The Stokes shift is the difference in nm between the peak excitation and peak emission wavelengths of a fluorophore. By completely filtering out the exciting light without blocking the emitted fluorescence, it is possible to see only the objects that are fluorescent.

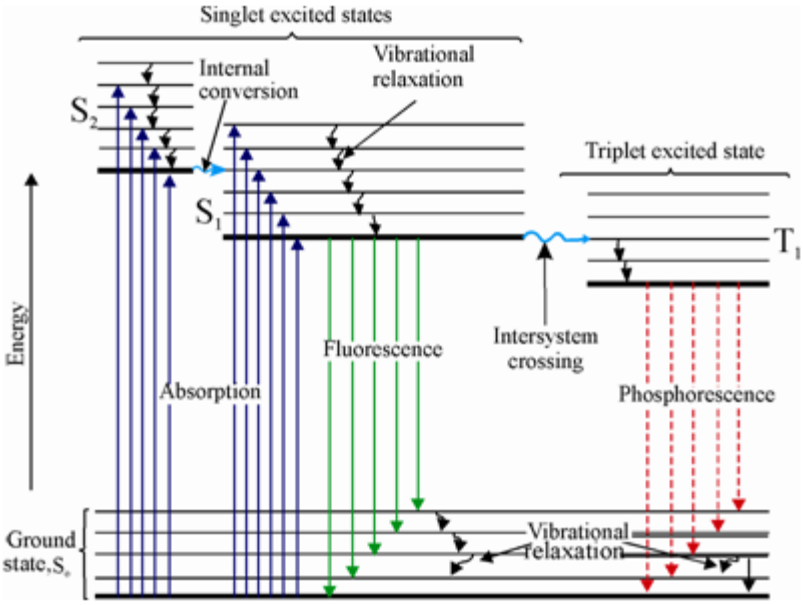

Figure 4: A Jablonski diagram. A fluorophore is excited into a higher energy singlet state. The molecule then rapidly undergoes internal conversion and vibrational relaxation, before returning to the ground state. This return to the ground state may be radiative (fluorescence), or non-radiative (thermal energy, quenching). Alternatively, the molecule may transition to an intermediate triplet state through inter-system crossing. From here it may return to the ground state radiatively (phosphorescence), or non-radiatively.

Fluorescence microscopy allows for the observation of labelled molecules within a focal volume, such as within a cell or artificial lipid bilayer. In conventional wide-field fluorescence microscopy, the entire sample is bathed in light meaning the sample's fluorescent molecules are excited in a wide focal plane. This means that large unfocused background regions are picked up by the microscope's detector. This side-effect can be overcome via confocal microscopy. Confocal microscopy is used to acquire images selecting from within a thin focal plane, while rejecting out of focus fluorescent light. This allows for high resolution images of a defined depth of field to be obtained. Confocal microscopy directs the laser beam of desired wavelength through an aperture, focusing it on a small focal volume via an objective lens in order to excite a given fluorophore. Fluorescent light from the sample as well as any other reflected light is then recollected via the objective, filtered with a mirror to exclude the original excitation wavelength and passed through a detector pinhole. This aperture only allows light from the selected focal plane through, while obstructing any out of focus light. Thus only light from a limited optical section is picked up by the detector and converted to an electrical signal to be recorded.[63] In

this thesis confocal microscopy was routinely used to image platelets, liposomes, SLBs and cytoskeletal filaments.

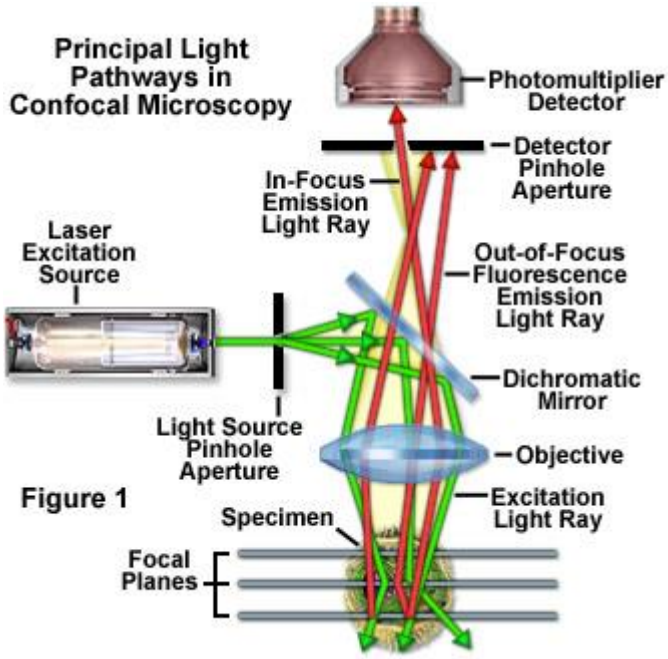

Figure 5: A typical confocal microscopy set-up. The technique uses a spatial pinhole placed at the confocal plane of the lens to eliminate out-of-focus light. This allows light from a limited optical section to be collected and thus increases spatial resolution when compared to standard fluorescence microscopes.

1.5.2. STED microscopy

Stimulated emission depletion (STED) microscopy is a form of super resolution microscopy that allows for the acquisition of fluorescence images below the diffraction limit that restricts resolution in standard confocal microscopy set-ups. First proposed in 1994[64], and later demonstrated in 2000[65], STED uses selective elimination of emission of fluorophores to minimise the focal area of illumination and thus increases the resolution of the imaging process. In a typical STED measurement, an excitation laser is used to excite a fluorophore in a sample in the same manner as confocal microscopy. The excitation pulse is immediately followed by a pulse from a red-shift depletion (STED) laser. The STED laser is shaped to a

donut profile within the focal plane which overlaps the profile of the excitation laser (Figure 6). The STED laser is of high intensity and instigates stimulated emission of the fluorophore at these overlapping peripheral regions. The result is that fluorescence from the probe is switched off at the rim of the focal spot, reducing the interrogated volume and thus enhanced resolution.[66] In practice this allows for the imaging of structures with diameters in the tens of nanometers, i.e. much smaller than achievable using standard confocal microscopy because of the diffraction limit which applies to these methods. In this thesis STED was utilised to provide super resolution images of micrometer long, nanometer wide filamentous proteins.

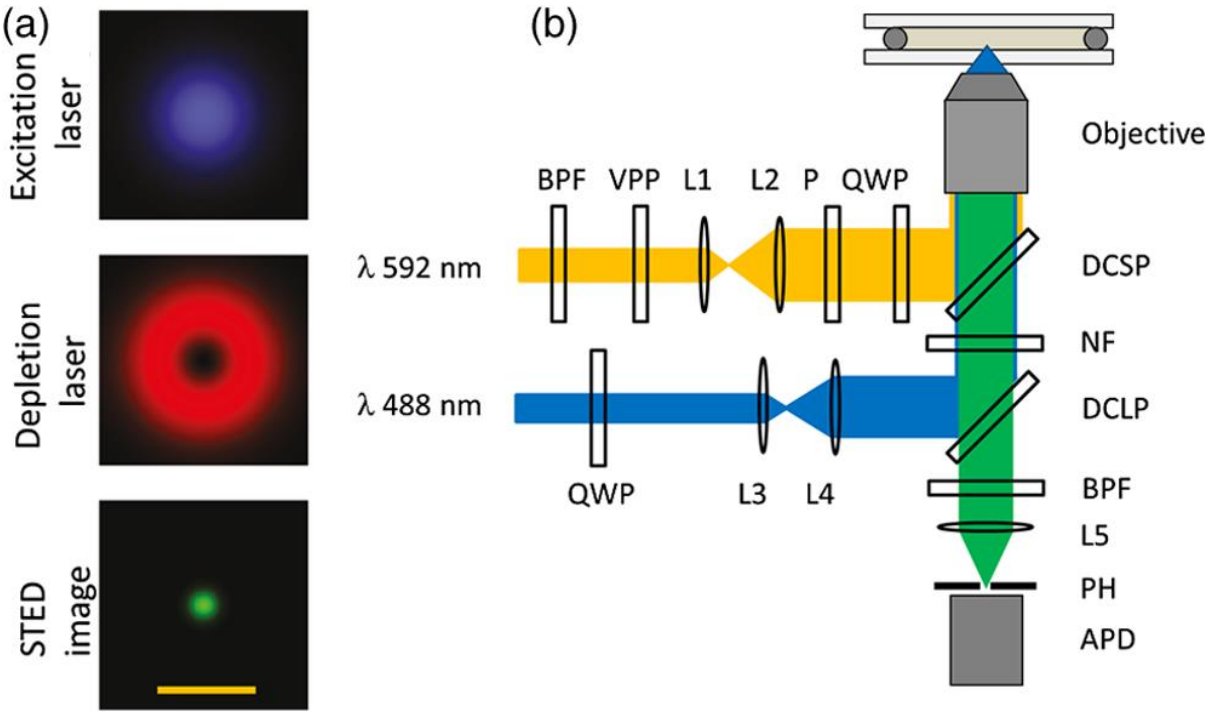

Figure 6: A) An excitation laser profile alongside the donut shaped STED laser profile. Emission from overlapping regions is switched off through stimulated emission meaning no fluorescence occurs at the periphery of the spot. Therefore, only the centre of the STED laser emits fluorescence, thus reducing the interrogated volume. B) The red shifted STED laser is pulsed immediately after the excitation laser. DCSP: dichroic mirror (short pass); VPP: vortex phase plate; BPF: bandpass filter; P: polarizer; L: lenses; QWP: quarter-wave plate; NF: notch filter; DCLP: dichroic mirror (long pass); PH: pinhole; APD: avalanche photodiode detector Image from "Review of recent developments in stimulated emission depletion microscopy: application on cell imaging".[66]

1.5.3. FCS and FLCS

Fluorescence correlation spectroscopy

Fluorescence correlation spectroscopy (FCS) and Fluorescence Lifetime Correlation Spectroscopy (FLCS) are two related techniques used to determine dynamic processes and molecular interactions through the analysis of fluorescence fluctuations in a given focal volume. Of key interest in the context of this work is the application of FCS to determine diffusion dynamics of particular molecules via these fluorescence fluctuations. To do so, an excitation laser is focused onto a sample in order to excite fluorophores. A confocal pinhole rejects light emission outside a thin focal plane and emitted photons are spectrally filtered before being detected on a suitably sensitive detector such as a SPAD, or hybrid detector (Figure 7 A). Therefore, only fluorophores within a well-defined femtoliter focal volume are registered. This process is carried over a time-period (10s of seconds to minutes) in order to form a fluctuating time-intensity trace (Figure 7 B). Using these fluorescence fluctuations, an autocorrelation curve can be calculated as follows:

$$G(\tau) = \frac{\langle \delta F(t) \delta F(t+\tau) \rangle}{\langle F \rangle^2}$$

Where F is the fluorescence intensity, t is the time and τ is the lag time. The brackets "<" and ">" indicate the time averaged over the fluorescence signal. This allows the signal at time t to be compared with the signal at time t + τ, and the similarity is averaged over all times. Over short time intervals, fluorophores in the detection volume have not moved far and thus the fluorescence signal will not have changed much. This leads to a degree of high self-similarity of the intensity trace, and a high value of the auto-correlation curve for small lag times. Over longer time intervals, fluorophores will have moved much further distances, leading to large changes in the fluorescence signal. As a result, there will be a lack of self-similarity of the

intensity trace and a low value of the auto-correlation curve for large lag times as the curve decays towards zero (Figure 7 C). Faster moving molecules will spend less time within the focal volume and thus the auto-correlation curve will decay quicker than for slow moving molecules.[60]

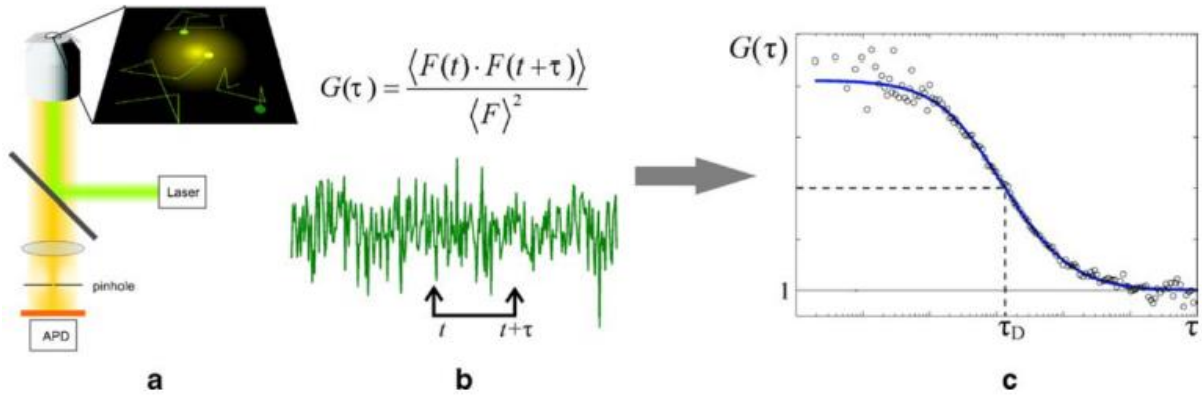

Figure 7: The basics of the FCS set-up. A) An excitation laser is focused onto a sample in order to excite fluorophores. A detector is used to register emitted photons from a small focal volume. B) Fluorescence fluctuations are measured over time and autocorrelation curve is formed. C) An autocorrelation curve. The data is fitted to suitable model (eg 2D or 3D) in order to determine the diffusion co-efficient of the fluorophore. Figure adapted from "Single molecule techniques for the study of membrane proteins".[60]

The amplitude of the autocorrelation curve is dependent on the concentration of fluorophores. At low concentrations, the relative fluctuations in the fluorescence signal are large, and thus the amplitude of the auto-correlation curve is high. Therefore, the opposite is also true and it can be said that the amplitude of the auto-correlation curve is inversely proportional to the fluorophore concentration (Figure 8). Using this knowledge, key parameters such as diffusion co-efficients and concentrations can be determined by fitting the autocorrelation data to an equation suitable for the experimental parameters.[60] For example, for a molecule freely diffusing in solution, a three-dimensional fit is best applied to the autocorrelation data, while in a planar lipid bilayer, a two-dimensional fit is best applied owing the inherent spatial restrictions of the system. Furthermore, if the fluorophore has a tendency to transition to an intermediate dark triplet-state or more than one species is present in the fluorophore population, additional parameters may be included in the fitting equation to account for this.[49] The amount of time a

fluorophore spends within the instrument's effective detection volume (V_{eff}), is dependent on how fast the molecule is diffusing. Therefore quickly diffusing molecules spend less time in the V_{eff} which results in an auto-correlation curve decaying towards zero faster than for a relatively slowly diffusing fluorophore (Figure 8).

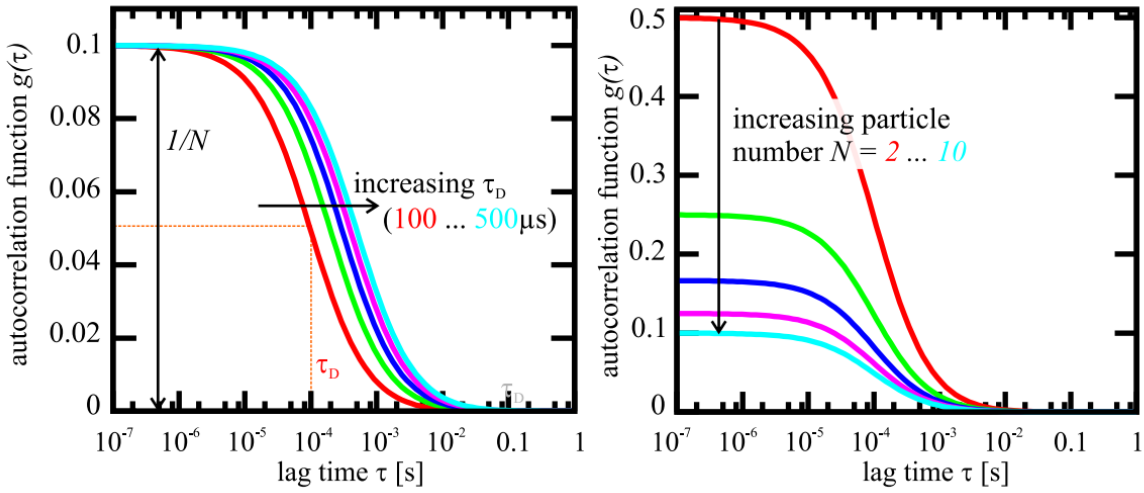

Figure 8: Left) The amount of time spent in the effective FCS volume is dependent on the fluorophore's diffusion co-efficient. Faster moving molecules will spend less time in this volume and the auto-correlation curve will decay towards zero faster. Right) The amplitude of the auto-correlation curve is inversely proportional to the fluorophore concentration. As the concentration of fluorophores increases the ACF begins to move towards zero.

Of course the amount of time a fluorophore resides in the V_{eff} is also dependent on the dimensions of said volume. The V_{eff} is not identical to the confocal volume (V_{conf}). If the volumes are approximated using a 3-dimesional Gaussian shape function, then V_{eff} is larger than V_{conf} by a factor of $2^{3/2}$. To obtain this V_{eff} value FCS setups must be regularly calibrated due to slight misalignments and changes in the optical system. To do so a number of options are available. For example, by using a freely-diffusing dye of known concentration, using a freely-diffusing dye with a known diffusion co-efficient, or via imaging fluorescent beads with a well-defined diameter. In our work a freely diffusing dye with a well-defined diffusion co-efficient was used for this calibration step. Assuming that the confocal volume can be

approximated by a three-dimensional Gaussian function, the dimensions of the confocal volume can be derived from the fit parameters using:

$$G(\tau) = \frac{1}{N}\left[1 + \frac{4D\tau}{\omega^2}\right]^{-1}\left[1 + \frac{4D\tau}{z^2}\right]^{-1/2} \quad (1)$$

Where G(τ) is the autocorrelation function of fluorescence fluctuations, N is the average number of fluorophores in the focal volume, τ is the lag-time, ω is the lateral radius of the confocal volume, z is the axial radius of the confocal volume, and D is the diffusion co-efficient. It must be remembered that the effective focal volume is an ellipsoid with two equal ω axes and z axes as shown in Figure 9.

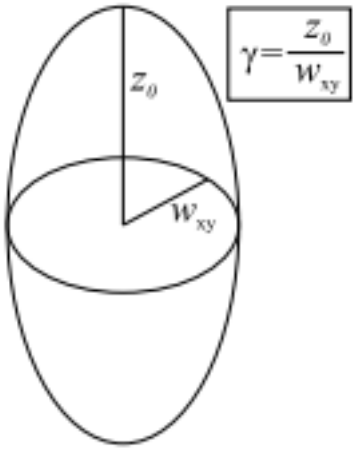

Figure 9: An approximate focal volume composed of two equal ω axes and two equal z axes. The ratio between the z and ω axes is known as the axial ratio and written as k. This value should be between 4 and 7 in a well aligned FCS set-up.

The ratio between the height and width of this ellipsoid and is known as the axial ratio (k) and can be described by:

$$k = \frac{z}{\omega} \quad (2)$$

Therefore, equation 1 can be rewritten with a slight modification to the z component:

$$G(\tau) = \frac{1}{N}\left[1 + \frac{4D\tau}{\omega^2}\right]^{-1}\left[1 + \frac{4D\tau}{k^2\omega^2}\right]^{-1/2} \quad (3)$$

Equation 3 can be further rewritten in terms of the average retention-time of the fluorophore, or diffusion time (τ_D) where:

$$\tau_D = \frac{\omega^2}{4D} \quad (4)$$

Taking this into account, equation 3 becomes:

$$G(\tau) = \frac{1}{N}\left[1 + \frac{\tau}{\tau_D}\right]^{-1}\left[1 + \frac{\tau}{k^2\tau_D}\right]^{-1/2} \quad (5)$$

Using a dye with a known diffusion co-efficient, equations 5 and 6 can be combined to experimentally determine the spatial values of the volume, ie the lateral radius of the confocal volume, the axial radius of the confocal volume, and thus the axial ratio between the two. This means that the effective volume can be determined as follows:

$$V_{eff} = (\pi)^{3/2}\,\omega^2 z = (\pi)^{3/2}\,\omega^3 k \quad (6)$$

However, if FCS is applied to a two-dimensional system, a separate 2D V_{eff} must be used. In this case the effective value is the area of intersection between the confocal volume and a planar (2D) object. In practice this occurs at the widest point of the

focal volume's ellipsoid shape. Knowing the lateral radius of the beam as determined experimentally above, the 2D V_{eff} of FCS interrogation can be determined by finding the area of a circle:

$$2D\ V_{eff} = \pi\omega^2 \qquad (7)$$

Fluorescence Lifetime Correlation Spectroscopy

While FCS has been routinely used in the literature to determine diffusion co-efficients in both 2D and 3D systems, the technique does suffer from a number of problems. For example, during conventional FCS a number of unwanted signal components, or background contributions, are incurred in the auto-correlation curve. This background noise includes Rayleigh and Raman scattered excitation light, detector thermal noise and detector afterpulsing.[67] FLCS is a modification to the standard FCS technique as described above. FLCS combines FCS with Time-Correlated Single Photon Counting (TCSPC) in order to separate the autocorrelation function of various signal components. In TCSPC, the sample is excited with a short pulse of light and the temporal delay between the excitation pulse and the arrival of a photon emitted by the sample at the detector is recorded. This procedure is repeated many times in order to obtain a statistically significant distribution of time differences. The data is captured as a histogram in which the x-axis is the time difference between the excitation pulse and the detection of the emitted photon, and the y-axis is the frequency with which each time difference is observed. Hence, this histogram describes the decay of the excited-state population following pulsed excitation of the sample, and it can be fit to an exponential decay function to obtain the luminescent lifetime of the probe. Due to the fact that the unwanted signal components (scattered light, detector afterpulsing, etc) occur on a different timescale than the lifetime of the fluorophore, this noise can be removed from the auto-correlation curve in order to improve the accuracy of the fitting model. For example, Figure 10 shows how FLCS can be applied to the removal of detector

afterpulsing, a constant offset across the experiment in order to provide more accurate diffusional data. Furthermore, this TCSPC aspect of FLCS can even be used to separate auto-correlation curves of two different fluorophores with indistinguishable emission spectra, as long as their respective fluorescent lifetimes are sufficiently different.

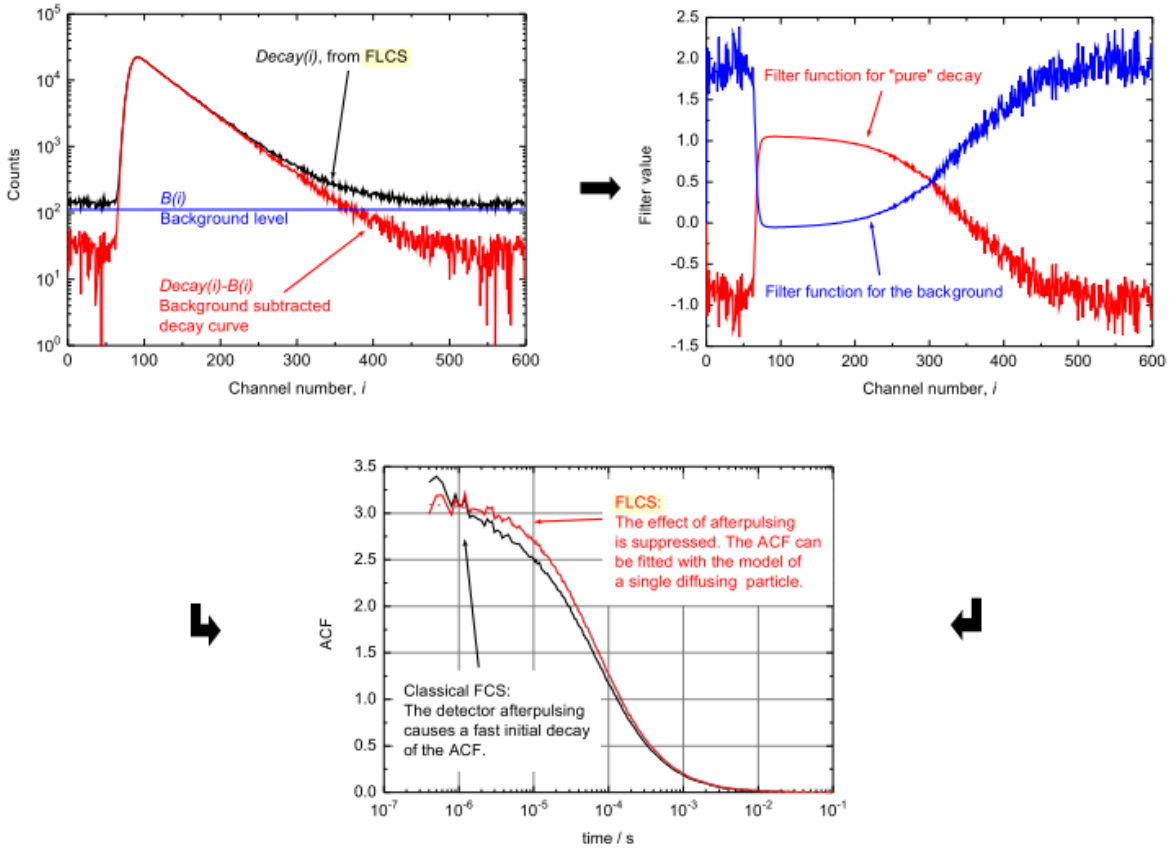

Figure 10: Left) A TCSPC histogram showing FLCS decay alongside contribution from afterpulsing. Afterpulsing is constant offset evenly distributed across the histogram and can be substracted from the initial decay. Right) Filters for the fluorescence and background decays. Weight for the fluorescence decay is high in those channels in which the vast majority of the detected photons come from the fluorophore. C) When the filters are applied to the FCS curve, the FLCS auto-correlation curve removes unwanted afterpulsing from the data. Image from Picoquant.

Within the literature, FCS and FLCS have been used for a variety of applications in a wide range of environments, for example, to study the influence of lipid composition on lipid diffusion co-efficients in liposomes[68], to examine the anomalous diffusion of proteins due to molecular crowding[69], or to determine the efficiency of cytosolic

transport within cells.[70] In this thesis FCS and FLCS were routinely used to determine both lipid and protein diffusion co-efficients in a variety of lipid compositions in both vesicle and SLBs systems.

1.5.4. Flow Cytometry

Flow cytometry is a commonly used method for identifying different cell populations based on cell size, cell granularity and protein expression. To achieve differentiation, cells are passed through the flow cytometer instrument in a stream of fluid and separated particle by particle. At an interrogation point a laser intersects with the cells. Emitted light is given off in all directions and collected by a series of detectors. Flow cytometry setups contain two important detectors known as the forward scatter (FSC) and side scatter (SSC) detector. The FSC is used to detect particle size while the SSC is used to determine particle granularity. This is a key component of a flow cytometry and it allows for the identification of cell populations by plotting one parameter against another. This can be seen in Figure 12 where granulocytes, lymphocytes, and monocytes can be differentiated on the scatter plot. As well as the FSC and SSC detectors, flow cytometry also utilises a number of fluorescence emission detectors. This means that in addition to determination of particle size and granularity, the laser can be used to excite a cell-bound fluorophore. The emitted light is then picked up the relevant detector. This means the presence or absence of a probe, such as a labelled antibody or other protein, on the cell can be ascertained. The resulting fluorescence information may then be displayed on a histogram where the horizontal axis represents the parameter's signal value in channel numbers and the vertical axis represents the number of events per channel. To quantify the histogram data a percentage gated, mean, or geo-mean value be used. Another key feature of flow cytometry is the ability to analyse selected cell populations and subpopulations. For example, using the FSC and SSC detectors the presence of a labelled antibody may be analysed for only monocytes (or any other cell population).[62] This is known as gating. This ability to analyse multiple parameters of cells is a powerful feature of flow cytometry. In this thesis the technique was applied

to both platelets and vesicles. This allowed use to determine the activation status of platelets, the conformation of $\alpha_{IIb}\beta_3$ in the platelet membrane, and the presence of reconstituted $\alpha_{IIb}\beta_3$ in lipid vesicles.

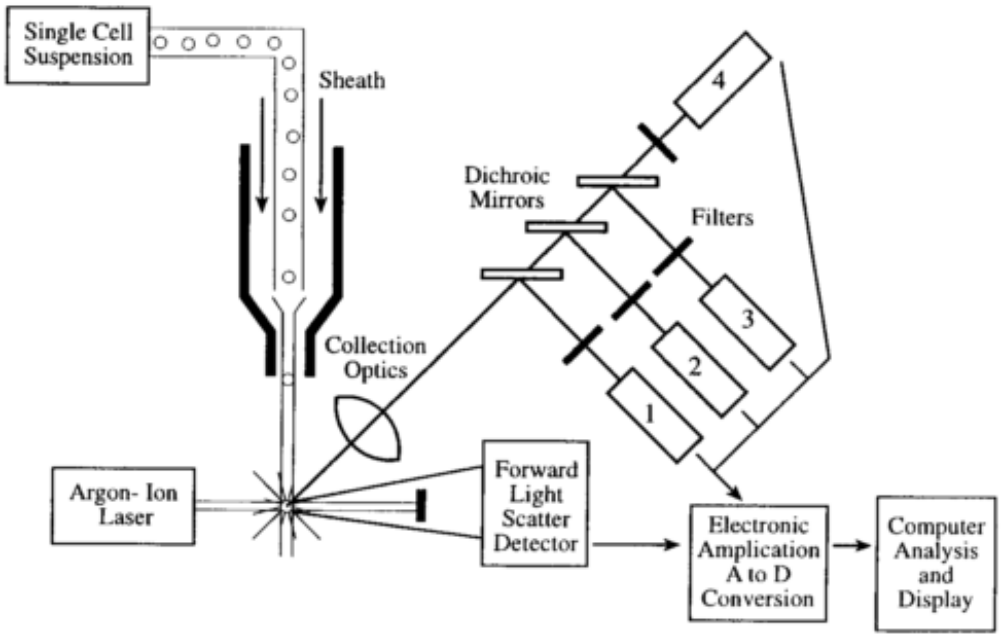

Figure 11: A schematic of a flow cytometry setup. A cell suspension is drawn into a stream and created by a surrounding sheath of isotonic fluid that creates laminar flow, allowing the cells to pass individually through an interrogation point. At the interrogation point a laser intersects the cells. Emitted light is given off in all directions. Some of this light is picked by a forward scatter detector, while some is picked up by a side scatter detector (1). Meanwhile, the system also features multiple fluorescence detectors (2 – 4), used to detect the presence of fluorescence molecules (antibodies and other proteins) and the interrogated cell's surface. The signals are amplified and converted to a digital format for analysis. Image from "Flow cytometry: principles and clinical applications in hematology".[62]

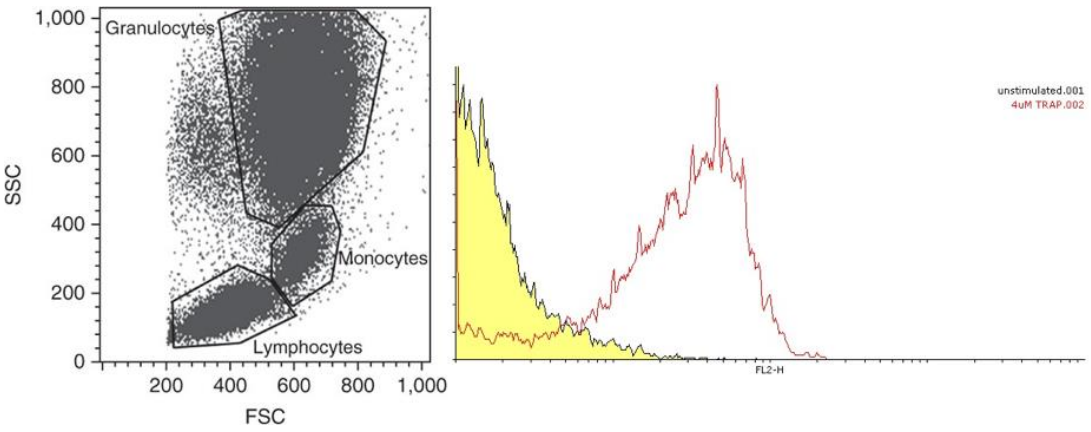

Figure 12: Left) A scatter plot of various immune cell populations from umbilical cord blood separated according to a dot plot of FSC versus SSC. Gates have been placed around these separate populations which allows these cells to be analysed separately.[71] Right) A histogram of anti-CD62P fluorescence in platelets. CD62P also known as p-selectin is an adhesion molecule exposed only in activated platelets. The yellow fill is the un-activated platelet population, while the red outline is TRAP activated platelets. The shift in fluorescence can clearly be seen.

1.5.5. Atomic Force Microscopy

Atomic Force Microscopy, or AFM, is technique that allows for the attainment of high atomic resolution topographic data. AFM can be used to analyse a wide range of samples from relatively hard glass and mica substrates to soft biological samples. AFM is a type of scanning probe microscopy that uses a tip to probe a surface rather than electrons or beam of light. Although it is an invasive method, it is not diffraction-limited and thus is capable of characterising surface roughnesses and 3D topographical data at sub-wavelength dimensions, unlike confocal microscopy. Scanning Tunnelling Microscopy (STM) was the precursor to AFM and was developed in the early 1980s. SPM allowed the high resolution imaging of surfaces but could only be applied to conductive or semi-conductive surfaces. The STM later evolved in the AFM which allowed for the probing of a much wider range of surfaces.[72] The basic set up behind AFM features a probing tip mounted on a flexible cantilever. The tip is placed in contact or close to the sample. Interactions with the surface deflect the cantilever, and this motion is monitored by a laser beam. The beam is reflected towards a split photodetector configuring an optical lever which amplifies cantilever deflections. A feedback circuit, connected to the cantilever

deflection sensor keeps tip–sample interaction at a fixed value controlling the tip–sample distance. The amount of feedback signal, measured at each scanning point of a 2D matrix, concurs to form a 3D reconstruction of the sample topography which is usually displayed as an image.[73] An example of an AFM setup is given in Figure 13.

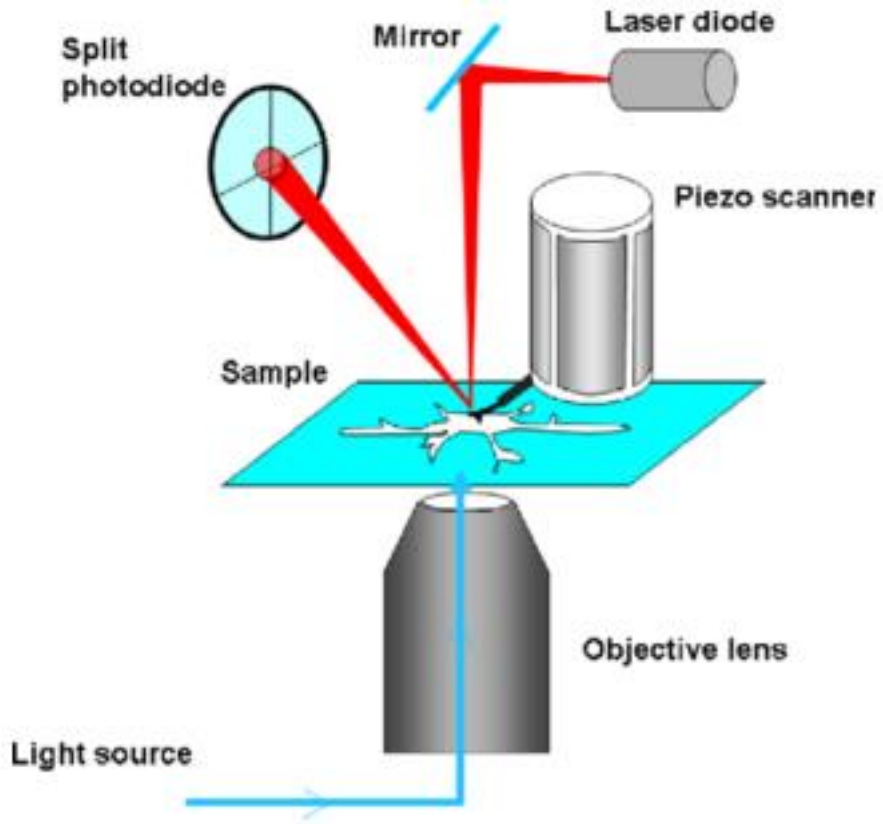

Figure 13: A typical AFM setup coupled with an inverted optical microscope. A sample is placed on the stage while a cantilever and top comes in close contact with the surface. Interaction with the surface deflects the cantilever and this motion is monitored by a laser beam. This movement can be analysed and express in topographic form.

A number of modes of operation exist for AFM. In contact mode, for example, the tip is kept in gentle contact with the sample surface. As the tip raster scans the surface, images are created by recording the piezo-vertical position required to keep the force constant.[73] In this mode, the interaction forces between the tip and the sample are mainly van der Waals repulsive forces. Another popular mode of operation is tapping mode. In this mode the cantilever is oscillated at a frequency near its resonance and the oscillation amplitude is monitored. By recording the feedback signal required to keep the amplitude constant, the topography of the

sample surface can be obtained.[73] As the tip is only intermittently in contact with the sample it overcomes problems such as friction and adhesion that are usually associated with conventional AFM imaging systems. The intermittent contact also means that tapping mode is particularly useful for soft biological samples such as supported lipid bilayers.[74] AFM has played a role in a large number of fields such as characterising materials for electronics, semi-conductors, materials and manufacturing, polymers, biology and biomaterials.[74] One of the biggest advantages of AFM in comparison to other high resolution techniques, such as SEM and TEM, is the fact the AFM allows for the imaging of biological samples in physiological like conditions. This also means that minimal sample preparation is required.[73] The technique can be used monitor mechanical properties of a sample, cell stiffness and cell viscoelasticity, adhesion forces and Young's modulus.[72] In this thesis AFM was used to obtain topographic data of PDMS surfaces at far higher resolution than was possible using optical microscopy.

1.6. Key Aims and Objectives

The key objective of this work was to provide biologically-relevant platforms to study transmembrane proteins away from the chaos and complexity of the native cell membrane. While our platforms are compatible with any number of transmembrane proteins we chose to use platelet integrin $\alpha_{IIb}\beta_3$ as the primary model protein in much of this work. As such, chapter 2 is devoted to study of the $\alpha_{IIb}\beta_3$ protein in the platelet membrane in order to better understand its physiological role in ligand binding and platelet aggregation. Emphasis was placed on inducing the activated ligand bound form of $\alpha_{IIb}\beta_3$ via the use of artificial integrin activators dithiothreitol (DTT) and Mn^{2+}, and comparing these activated states to more biologically-relevant agonist pathways. DTT and Mn^{2+} were studied as integrin activators as we later wanted to induce conformational changes in $\alpha_{IIb}\beta_3$ within our artificial lipid platforms, systems lacking the signalling machinery required for physiological agonist activation.

After characterising DTT and Mn^{2+}-mediated activation of $\alpha_{IIb}\beta_3$ in platelets, we next sought to characterise $\alpha_{IIb}\beta_3$ within liposomes in chapter 3. As such, various reconstitution protocols were explored to insert the protein into more physiologically-relevant lipid compositions than what currently exists within the literature. Next we wanted to to determine the diffusional abilities of the reconstituted protein in its un-activated, activated and ligand bound forms as well as its preference for phospholipid rich or cholesterol rich microdomains.

While liposome-based systems have their advantages over planar SLB models, we wanted to combine the best attributes of these systems in chapter 4 via the use of a novel cavity-spanning bilayer. Developed by our group over a number of years, such a system combines the stability of planar SLBs with the free-standing nature of liposomes. This was hoped to provide a planar lipid bilayer away from the non-

specific lipid-substrate interactions that plague traditional SLB platforms. Utilising the knowledge gained in our liposome work it was hope to reconstitute $\alpha_{IIb}\beta_3$ into our physiologically-relevant cavity-spanning SLB to compare and contrast the diffusional characteristics of $\alpha_{IIb}\beta_3$ in its un-activated, activated and ligand bound forms.

Finally, in preliminary work, chapter 5 focuses on increasing the complexity and physiological relevance of SLB models even further by including cytoskeletal fibres alongside the planar lipid membrane. It was hoped that such cytoskeletal structures would alter the diffusional characteristics of the SLB and that such lipid-protein interactions would more accurately mimic the intracellular-cell membrane interface found within the cell.

2. Integrin in Platelets

2.1. Introduction

Given that we wanted to later reconstitute the platelet protein $\alpha_{IIb}\beta_3$ into our various biomimetic models it made sense to first characterise the function of $\alpha_{IIb}\beta_3$ in its native environment, the platelet membrane. Therefore, this chapter seeks to examine the activation of $\alpha_{IIb}\beta_3$ using DTT and Mn^{2+} while comparing and contrasting this activation to more physiological platelet agonists. DTT and Mn^{2+} were chosen as activators due to their direct actions on integrin conformation, and thus ligand-binding ability. This is in contrast to physiological agonists which induce integrin conformational changes indirectly through complex platelet signalling pathways, pathways that will not be available in our later biomimetic models. Thus this chapter seeks to examine both DTT and Mn^{2+} as suitable $\alpha_{IIb}\beta_3$ activators for later integrin-reconstituted lipid platforms. Before looking at the structure and function of $\alpha_{IIb}\beta_3$ in more detail, we must first examine the physiological role of the platelet.

Platelets are small non-nucleated cell-fragments formed from the fragmentation of precursor megakaryocytes. There are approximately one trillion platelets in circulation at any one time in the human body. Their primary role is the maintenance of haemostasis.[75] Under normal physiological conditions, platelets remain in their resting discoid form. Understandably, this resting state of platelets must be properly maintained so as to avoid inappropriate thrombosis. Activated platelets form thrombi in response to tissue trauma and the associated exposure of the subendothelial matrix. Thrombus formation occurs in a number of stages that involve platelet adhesion, shape change, release of pro-aggregatory regulators and aggregation. To illustrate this, activated platelets can be seen in Figure 14. To initiate the thrombus formation, platelets firstly localise to the site of vascular injury before forming a platelet monolayer. Secondly, the release of platelet agonists activates and recruits additional platelets to the site. Finally, the platelet plug is stabilised in order to halt blood loss and to prevent the premature dis-aggregation of the thrombus.[76] Throughout this process, the platelet response is governed by a variety of membrane proteins that act as receptors for signalling molecules and/or as

functional adhesion molecules. These receptors are typical integral membrane proteins present within the lipid bilayer. They sense the extracellular environment and control the platelet response to stimuli, thus initiating the pro-aggregatory platelet response. The membrane receptors include the selectins, integrins, and immunoglobulin superfamily, as well as receptors specific for ADP, collagen, epinephrine and thrombin, amongst others.[77]

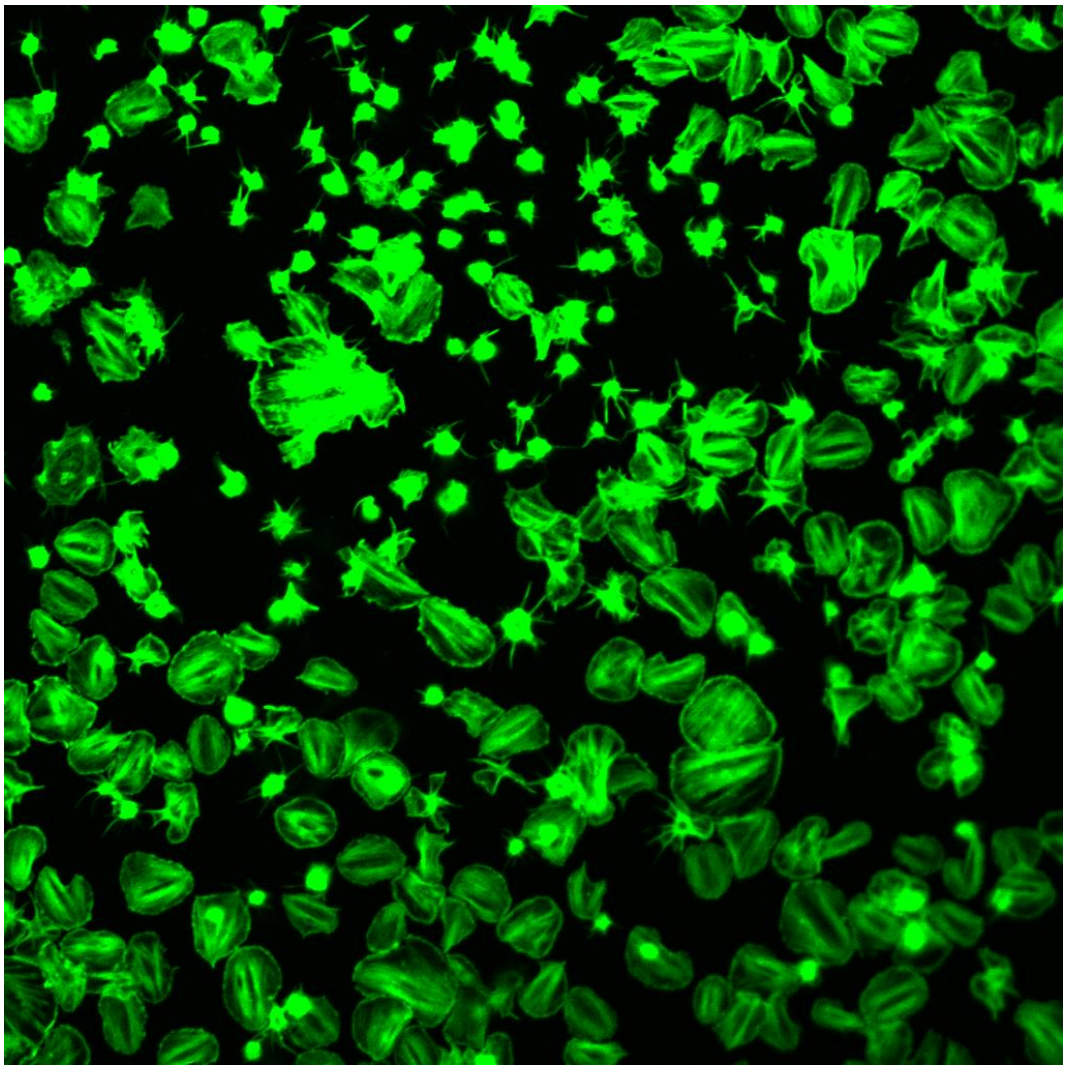

Figure 14: A confocal image of phalloidin-FITC-stained platelets activated on a fibrinogen-coated glass slide. Phalloidin is a mushroom toxin that binds to polymerised actin, one of the main components of the cell cytoskeleton, making it any excellent stain for visualising cells. Phalloidin-FITC was excited with a 488 nm argon laser line and imaged using a 63x objective.

2.1.1. Thrombus initiation

The platelet response to endothelial damage is controlled by receptors present on the platelet cell surface. GPIb-IX-V is a receptor complex, which is important in the initial stages of thrombus formation.[78] This complex primarily associates with von Willebrand factor (vWF) becomes immobilised to the subendothelial matrix following endothelial damage. vWF itself is a multimeric protein containing variable numbers of identical subunits, each over 2000 amino acids in length. The protein is produced exclusively by megakaryocytes, the precursor to platelets, and endothelial cells, and may be produced by two divergent pathways, a "regulated pathway" or a "constitutive pathway". The regulated pathway involves the storage of the protein for secretion in response to agonist stimulation in intracellular vesicles, for example, within the alpha granules of platelets. On the other-hand, in the constitutive pathway the vWF is released as soon as synthesis is complete. The key feature of the vWF is its ability to act as a ligand for a wide range of other proteins at distinct functional sites. For example, it may bind to FVIII, integrin $\alpha_{IIb}\beta_3$, collagen, and as mentioned previously, GPIb-IX-V.[79] Exposure to damaged endothelium allows vWF to act as bridge between exposed collagen and GPIb-IX-V. Of key importance is the ability for this interaction to take place under high shear stress, something which is problematic for other direct platelet-collagen receptors. This first transient interaction between the platelet and the damaged endothelium reduces platelet velocity and allows for interactions between other receptors and their ligands that can otherwise only occur at lower shear rates.[80] The next step in providing a more stable platelet-ECM interaction is mediated by the platelet receptor GP VI. GP VI is a 65 kDa platelet-specific collagen receptor that plays a significant role at lower shear stresses. It functions in conjunction with an FcR γ-chain dimer transmembrane protein which acts as the intracellular signalling subunit of the receptor.[81] Phosphorylation of this FcR γ-chain dimer, which is mediated by members of the Src family, recruits another Src family member in the form of Syk, which in turn activates an enzyme known as PLCγ2. PLCγ2 converts phosphatidylinositol 4,5-bisphosphate, a phospholipid component of the cell membrane also known as PIP_2, to inositol 1,4,5-trisphosphate (IP_3) and diacyl glycerol (DAG).[82] IP_3 is responsible for

the release of Ca^{2+} from the platelet dense tubular system, while DAG activates Protein Kinase C (PKC). Both Ca^{2+} and PKC are responsible for upcoming platelet activity including platelet aggregation and the secretion of pro-aggregatory factors.[83,84] Indeed, this intracellular signalling is important because it is required for the next integrin-mediated platelet-collagen interaction, namely by integrin $\alpha_2\beta_1$. Like other members of the integrin family, $\alpha_2\beta_1$ is restrained in its low affinity state. Intracellular signalling events promoted by GP VI-collagen interaction following platelet activation promotes conformational changes in $\alpha_2\beta_1$, thus transitioning the integrin into its high affinity state. As such, activated $\alpha_2\beta_1$ is now free to undergo its own collagen interactions further strengthening the platelet-ECM interaction.[85]

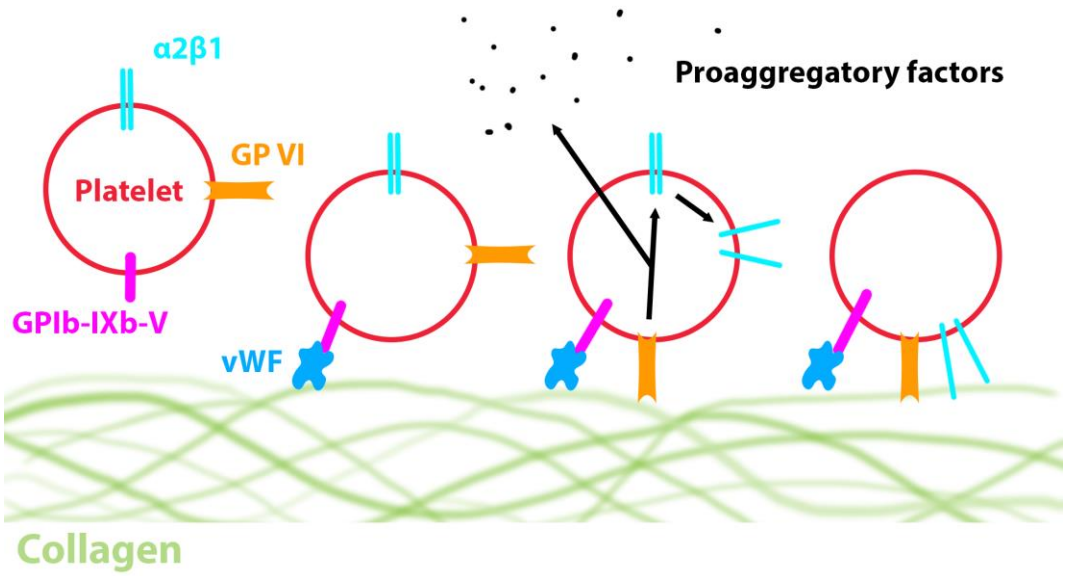

Figure 15: Initiation of thrombus formation on damaged endothelial tissue. Exposure of platelets to vWF bound to collagen leads to transient interaction via the GPIb-IX-V complex found on platelets, even under high shear stress. This interaction reduces platelet velocity sufficiently to allow for direct interaction of the platelet to the collagen via the GP VI receptor. This interaction promotes a proaggregatory platelet response via intracellular signalling. This leads to the release of agonists such as ADP and TxA_2, as well as the inside out activation of integrin $\alpha_2\beta_1$, transitioning it from a low affinity state to a receptor which readily binds to collagen, further strengthening thrombus formation.

2.1.2. Thrombus extension

Following the vWF and collagen driven initiation stage of platelet adhesion, the extension phase is distinguished by the recruitment of additional platelets to the site of vascular injury in response to various platelet agonists. These agonists may be released by the platelets themselves in response to activation and act to promote the continuation of thrombus formation. While some of the agonists are synthesised *de-novo* following platelet activation, others are stored in the cell. To store agonists, platelets make use of intracellular vesicles. Alpha granules (α-granules), for example, are vesicles that contain a wide variety of proteins including platelet factor 4, platelet derived growth factor (PDGF), beta-thromboglobulin, fibrinogen, vWF, fibronectin and P-selectin, amongst other clotting factors. Upon platelet activation these contents may be secreted by the platelet or, in the case of P-selectin, transferred to the platelet membrane for presentation. Most of these molecules are not specific to platelets (such as vWF, which is also secreted by endothelial cells), while some are already found in the plasma (such as fibrinogen), yet some are platelet specific (such as beta-thromboglobulin). A second type of intracellular vesicle found in platelets are known as dense granules (δ-granules). Dense granules also contain a wide range of components such as calcium, histamine, serotonin and nucleotides, such as adenosine diphosphate (ADP) and adenosine triphosphate (ATP).[76,77] The exact role of these secreted molecules varies but the general consequence of their secretion is clear. As a whole they function to further support the pro-aggregatory response by promoting vasoconstriction, encouraging platelet morphological changes, the recruitment of additional platelets to the site of vascular injury, increasing the adhesive properties of the platelets, as well as upholding continued agonist secretion.

In order to respond to these pro-aggregatory molecules there exists a wide range of complementary receptors on the platelet membrane. For example, ADP interacts with its receptors $P2Y_1$ and $P2Y_{12}$,[75] while thromboxane A_2 (TxA_2) is an agonist directed agonist the TxA_2 receptor (TR).[86] Thrombin is particularly interesting in that it is a serine protease with a number of roles in the pro-aggregatory response.

Converted from prothrombin by cleavage at two sites by a plasma protease known as activated factor X, the major proteolytic action of thrombin is the conversion of the blood-soluble glycoprotein fibrinogen to fibrin, an insoluble and fibrous protein that may be polymerised to form a hemostatic plug in conjunction with platelets at the site of vascular injury. It also has another key role in the pro-aggregatory response where it acts on the platelet receptors PAR-1 and PAR-4 (and also on GPIb-IX-V). Here, thrombin binds to and proteolytically cleaves the extracellular N-terminal domain of the receptor unmasking a new N-terminus with the amino acids sequence SFLLRN for PAR-1 or GYPGKF for PAR-4. This newly exposed sequence is a tethered ligand and is capable of self-activating the PAR receptor. It binds to to the second extracellular loop of the receptor to initiate intracellular signalling.[87]

Many, though not all, of the platelet agonist receptors are G-protein coupled receptors (GPCR). GPCRs are seven-transmembrane domain receptors that can bind to a cytoplasmic guanine nucleotide-binding G-protein. The G-protein segment can be thought of as the on/off switch of the receptor and is composed of an α, β, and γ subunit. Binding of an agonist to the GPCR leads to an enzymatic exchange of GTP for GDP on the α subunit and its subsequent dissociation from the $\beta\gamma$ subunits. Much of the platelet response is governed by the form of α subunit that associates with the GPCR.[88] For example ADP may act on either of its receptors $P2Y_1$ or $P2Y_{12}$. $P2Y_1$ interacts with the G_q alpha subunit and signalling via this pathway leads to phospholipase C beta (PLCβ) activation, which in turn generates IP_3 from PIP_2.[89] IP_3 is then responsible for the release of intracellular Ca^{2+} and thus Phospholipase A_2 activation (PLA_2). PLA_2 releases Arachidonic Acid (AA) from membrane phospholipids. AA is subsequently converted to thromboxane, another important platelet agonist, via the sequential actions of COX and thromboxane synthase. On the other hand, the alternative ADP receptor $P2Y_{12}$ interacts with the G_{i2} alpha subunit and thus operates via a different signalling pathway. This pathway inhibits cyclic adenosine monophosphate (cAMP) production in platelets, a messenger which would otherwise down-regulate the platelet pro-aggregatory response.[90]

One of the many effects of agonist-receptor interaction and platelet activation is seen in the morphology of the platelet. Previously discoid in shape, platelets become irregular spheres in solution, ready to spread outwards when in contact with a surface. This shape change is driven by cytoskeletal rearrangements of the actin filaments and proteins such as myosin, filamin, spectrin and ankyrin.[7,91] Again, this cytoskeletal rearrangement is driven by agonist-mediated signalling pathways. For example, myosin light chain kinase (MLCK) phosphorylates myosin in a Ca^{2+}-dependent manner.[92]

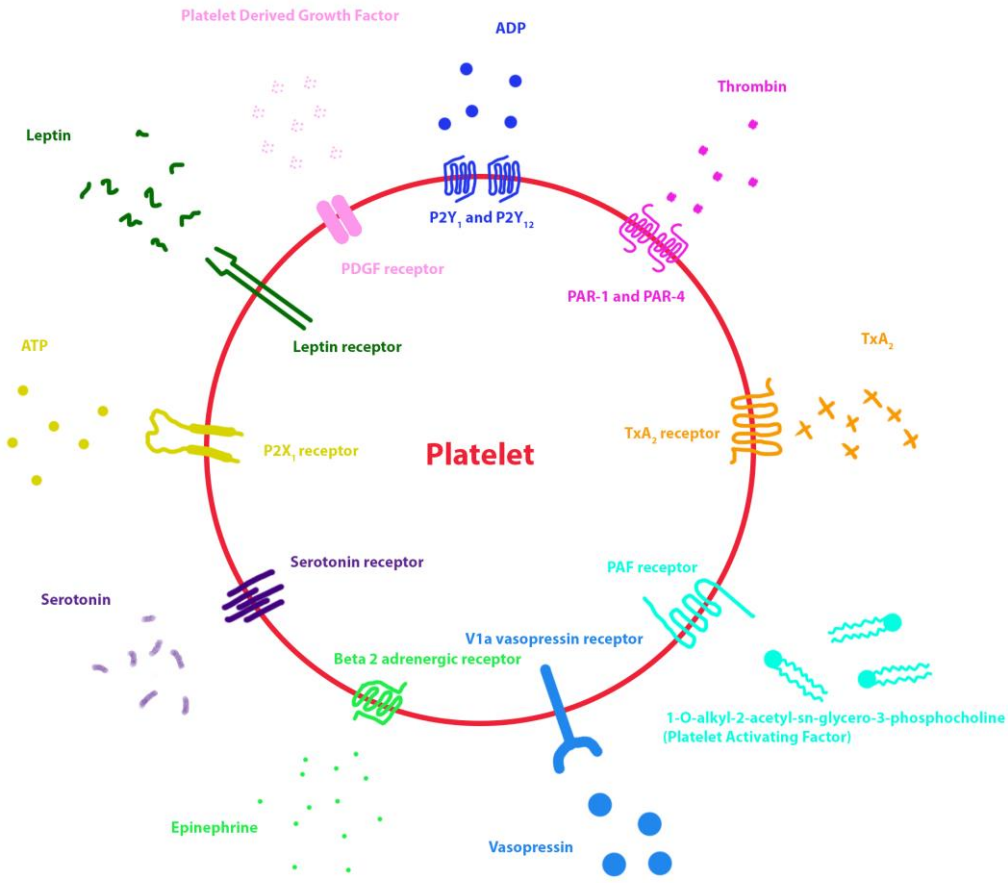

Figure 16: Platelet agonists and their respective receptors. A diagram showing just some of the important platelet agonists and their receptors that are important in the platelet activation process. These agonists promote a pro-aggregatory response that involves further agonist release in a positive feedback loop, platelet recruitment and the integrin family activation via intracellular signalling.

2.1.3. Thrombus stabilisation

Another response to agonist driven activation and maturation of the platelet response is seen in the integrin family of receptor proteins. In particular the integrin molecule $\alpha_{IIb}\beta_3$, undergoes conformational changes that alters its affinity for its primary ligand, fibrinogen. This transformation from a low-affinity state to a high-affinity state allows the formation of stable fibrinogen bridges between platelets and thus promotes plug formation. Once again intracellular signalling pathways are the key to integrin activation. For example, agonist driven mobilisation of PLCβ and PLCγ leads to a rise in intracellular Ca^{2+} levels and liberation of DAG. These converge to activate the protein CalDAG-GEFI which in turn leads to the triggering of Rap1, a precursor to integrin $\alpha_{IIb}\beta_3$ activation.[93] This activation of the $\alpha_{IIb}\beta_3$ molecule from a low-affinity state to a high-affinity state allows the integrin protein to bind to its ligands, of which fibrinogen is its primary target. This transition to a high-affinity state is mediated by conformational changes within the integrin molecule, a process known as “inside-out signalling”.

Fibrinogen binding to $\alpha_{IIb}\beta_3$ causes further conformational changes and cell signalling, this time directed from the extracellular domain of the integrin protein towards the platelet. This is known as “outside-in signalling” and this functions to perpetuate the thrombus growth. This is achieved in a number of ways. Firstly, it allows for cytoskeletal reorganisation in the form of focal adhesions. Here, an array of structural proteins assemble in an ordered fashion to provide a link between the ECM and the intracellular environment. These proteins may be adaptors with a structural function, adaptors with catalytic activity, or adaptors that fulfil scaffolding function. Via this method, a link between the ECM and the platelet intracellular machinery is formed in order to facilitate cell signalling and thus aid thrombus stabilisation.[94] Secondly, this thrombus growth is perpetuated by an increase in size of the platelet aggregates. The congregation of these platelets results in an increase in soluble platelet agonists such as ADP, released from platelet dense granules, and TXA2, synthesised in platelets in response to primary activation, which function in a

positive feedback loop to allow for development of a procoagulant surface and clot retraction that helps to narrow the gaps between platelets.[76]

2.1.4. Control of thrombus formation

Due to the fact that thrombus formation may be highly damaging if improperly initiated, the control of platelet aggregation must be highly regulated. One of the best understood mechanisms of negative control of thrombus formation involves nitric acid (NO). NO is produced by endothelial cells and diffuses across platelet membranes where it induces a rise in cytoplasmic levels of cGMP. This is achieved via the activation of guanylate cyclase which converts guanosine triphosphate (GTP) into cGMP. cGMP activates the protein kinase PKG, which in turn, reduces intracellular Ca^{2+} levels.[95,96] High levels of intracellular Ca^{2+} are normally required for platelet activation. A second mechanism of negative thrombus formation is expression of PGI_2. Similarly to NO, PGI_2 is produced by endothelial cells, but it regulates platelet responses via a seven transmembrane domain receptor, the prostacyclin (PGI_2) receptor. Occupancy of the PGI_2 receptor results in increased activity of adenyate cyclase, via the G_s cytoplasmic protein, causing a rise in platelet cytoplasmic levels of cyclic adenosine monophosphate (cAMP). cAMP functions though the activation of the protein kinase PKA, which causes a reduction in intracellular Ca^{2+} levels, similar to the actions of PKG.[97] In addition to the aforementioned mechanisms, the membrane proteins PECAM-1[82] and ESAM[98] may provide an attenuating role in thrombus formation. Finally, the previously mentioned activation of $\alpha_{IIb}\beta_3$ is not an irreversible feature. $\alpha_{IIb}\beta_3$ is capable of returning to its un-activated form which no longer has affinity for its ligands such as vWF and fibrinogen.[76]

2.1.5. Platelet Integrin $\alpha_{IIb}\beta_3$

As previously mentioned, the $\alpha_{IIb}\beta_3$ protein, also known as GPIIb/IIIa, is a key receptor molecule in maturation of thrombus formation. $\alpha_{IIb}\beta_3$ is a member of the integrin family of cell surface receptor molecules. Integrins are essential adhesion receptors found ubiquitously in metazoan cells. They function to facilitate cell migration and extracellular matrix assembly and are thus involved in a wide range of activities, including immune response, cell proliferation and apoptosis.[12] Like all 24 members of the integrin family, $\alpha_{IIb}\beta_3$ is a heterodimer of an alpha and beta subunit that spans the cytoplasmic membrane once.[13] The alpha subunit of $\alpha_{IIb}\beta_3$ is composed of a short cytoplasmic tail and transmembrane domain that crosses the cell membrane. Following this region is two calf-domains and the thigh-domain. Finally, there exists seven β-propeller repeats. The beta subunit has a longer cytoplasmic domain, a transmembrane domain that once again crosses the cell membrane once, and four cysteine-rich I-EGF (integrin epidermal growth factor-like) domains. Following this is the beginning of the PSI (plexin semaphorin integrin) domain, which features the hybrid-domain inserted into it. In turn, the β-I domain is inserted into the hybrid domain. The subunit is terminated by the PSI-domain. This region and the adjoining hybrid region fold over to expose the β-I domain.[14] (Figure 17)

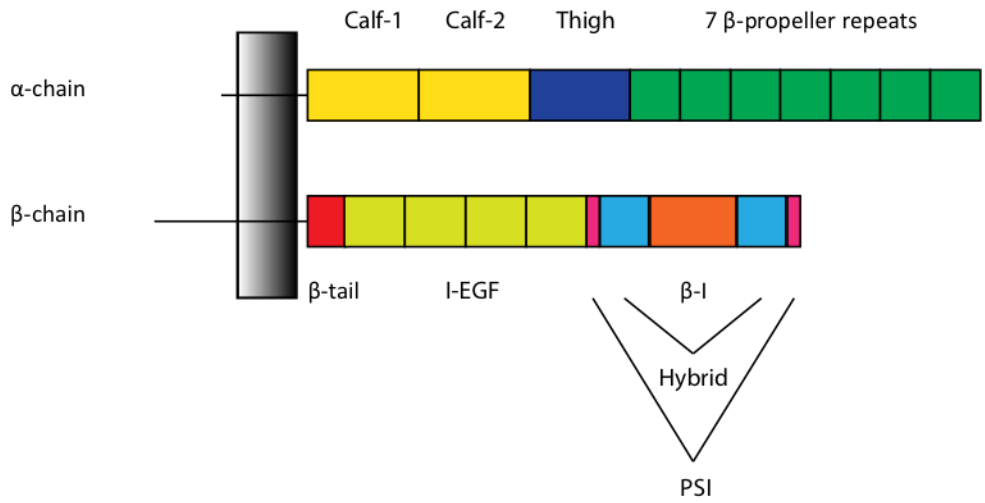

Figure 17: Schematic of the domains present in the alpha and beta chains of $\alpha_{IIb}\beta_3$. The alpha chain consists of a short cytoplasmic tail and transmembrane domain, 2 calf domains, a thigh domain, and 7 β-propeller repeats. The beta chain consists of a longer cytoplasmic tail and transmembrane domain, 4 I-EGF domains, a PSI domain, a hybrid domain, and the ligand binding domain β-I. Self-drawn figure based on "Integrins as therapeutic targets: lessons and opportunities".[14]

$\alpha_{IIb}\beta_3$ is the most abundant receptor on the platelet surface, numbering between 50,000 to 80,000 copies per platelet.[99] Its primary ligand is the soluble plasma glycoprotein fibrinogen, which is found abundantly in the plasma. Fibrinogen is a hexamer containing two sets of three different chains, namely an α, β and γ chain. $\alpha_{IIb}\beta_3$'s affinity for fibrinogen is mediated by the RGD sequence present on the α-chain of fibrinogen, as well as the AGD sequence present on the γ chain.[100,101] The symmetrical fibrinogen structure bridges platelets via their $\alpha_{IIb}\beta_3$ surface proteins, thus promoting platelet aggregation. Other cell adhesion molecules present on endothelial cells also have affinity for fibrinogen and allow localisation of a clot to the activated, or injured endothelium. While fibrinogen is $\alpha_{IIb}\beta_3$'s primary ligand, this integrin also has affinity for vWF, fibronectin, and vitronectin, amongst others.[102] As such an important facilitator in the platelet aggregation process, activation of the protein must be strictly regulated to prevent the formation of thrombi under normal physiological conditions. For example, the recognition of fibrinogen by $\alpha_{IIb}\beta_3$ is dependent on intracellular proteins that interact with the cytoplasmic domain of the integrin protein in order to initiate inside-out signalling of $\alpha_{IIb}\beta_3$. In typical thrombus

formation, initial interaction of platelets with the ECM at the site of vascular injury is mediated by glycoprotein (GP) Ib/IX/V complex and collagen receptors, GP VI and integrin $\alpha_2\beta_1$ on the platelet surface, and by vWF and fibrillar collagen at the vascular site. This initiates the release soluble agonists such as ADP, and TxA_2 as previously mentioned. Occupancy of receptors by these agonists then initiates an intracellular signalling pathway within the platelet, ultimately leading to $\alpha_{IIb}\beta_3$ activation via its cytoplasmic tail in a process known as inside-out signalling.[76] This leads to a change in conformation of the $\alpha_{IIb}\beta_3$ molecule, enabling it to bind to fibrinogen. Thus $\alpha_{IIb}\beta_3$ is said to have transitioned from a low-affinity to a high-affinity state. Upon ligand interaction an additional signal is sent inside the cell, a process known as outside-in signalling. As such $\alpha_{IIb}\beta_3$ is capable of bidirectional signalling. Outside-in signalling leads to reinforcement of the thrombus via integrin clustering and downstream activation of kinases that stabilize the integrin-mediated links between ECM proteins and actin filaments.[103] Throughout this process a variety of proteins are known to associate with the cytoplasmic tails of $\alpha_{IIb}\beta_3$ to participate in the bidirectional signalling process. These include paxillin, talin, filamin and kindilin.[94]

2.1.6. Inside out signalling

To bring about the aforementioned large scale structural changes, $\alpha_{IIb}\beta_3$ must be activated via inside-out signalling. Normally the two subunit tails of the integrin molecule keep the protein constrained in its resting state. This is maintained via a salt bridge between two conserved regions of the cytoplasmic tail, namely the HDRK sequence of the beta tail (via the aspartate [D]) and the GFFKR sequence of the alpha tail (via the arginine [R]).[94] Interruption of this clasp is required for inside-out signalling, and as the cytoplasmic tails have no known enzymatic activities, they must rely on adapter proteins to relay functionality. In this case the β_3 subunit is best recognised as the target of these adapter proteins, while the α_{IIb} subunit is more enigmatic.[14] Approximately 20 intracellular proteins are known to directly interact with integrin beta tails while a number of times this quantity are believed to

be indirectly involved. For example, the proteins paxillin, skelemin, FAK and Fyn all interact with the aforementioned HDRK motif of the β_3 subunit. While the proteins talin, filamin, Src, tensin and kindilin have affinity for the membrane-proximal NPxY motif and/or the membrane-distal NxxY motif.[94] In platelet activation, inside-out signalling owing to agonist-receptor interaction and thus intracellular signalling events, leads to separation of the lower legs of the ectodomain via the help of these adapter proteins. This separation leads to a "switchblade" like extension of the inactive bent integrin, releasing the hybrid domain from its restraining interface with the calf domains. In turn the head of the integrin may swing outwards in its high-affinity state.[13] Alternatively, the "deadbolt" model proposes that the increase in affinity for it ligand is a step that precedes the extension of the integrin molecule. In this case no change in integrin height is required for the ligand-binding and the integrin extension is in fact a post-activation event.[104] (Figure 18)

2.1.7. Outside-in signalling

Whatever the degree of integrin extension and conformational change, $\alpha_{IIb}\beta_3$ in its activated state has an increased affinity for its ligands. The β-I domain of $\alpha_{IIb}\beta_3$ contains a metal ion which interacts with the integrin's ligand. This is known as the metal ion dependant adhesion site (MIDAS). As an integrin lacking a corresponding α-I domain, the ligand binding of $\alpha_{IIb}\beta_3$ occurs between β-I domain (of the β-subunit) and the β-propeller domain (of the α-subunit). Ligand binding is believed to cause further structural modifications to the integrin mediated by movements in the α7 and α1 helices in the α-I and β-I domains. The piston like displacement of the integrin legs is thought to promote the formation of the extended $\alpha_{IIb}\beta_3$ structure and transmission of signals intracellularly.[105] This causes an indirect connection between the extracellular matrix and the platelet cytoskeletal proteins via the interaction of talin with the cytoplasmic tail of the integrin molecule. As these adhesions mature, a multitude of cytoskeletal and signalling proteins converge on clustered, ligand bound integrin molecules.[106] Proteins of these focal adhesions

include FAK, actin, paxillin, vinculin, VASP and actin, which combine to form the well organised molecular architecture of the platelet cytoskeleton.[107] (Figure 18)

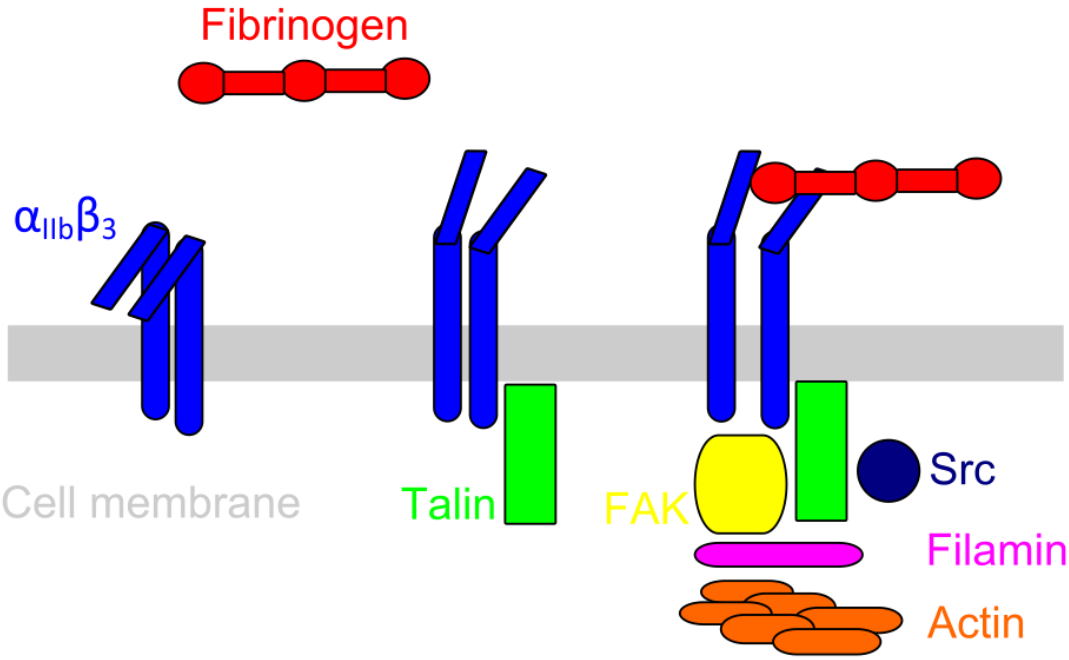

Figure 18: Activation and conformational changes of platelet integrin $\alpha_{IIb}\beta_3$. Agonist induced inside-out signalling alters $\alpha_{IIb}\beta_3$ from its low-affinity state to its high-affinity state. In this high-affinity state $\alpha_{IIb}\beta_3$ may bind to its ligand, in this case fibrinogen. Ligand binding leads to outside-in signalling. This involves integrin tail separation, signal transmission into the platelet and maturation of the platelet plug.

2.1.8. Activation of $\alpha_{IIb}\beta_3$

In order to bring about platelet or integrin activation, a variety of activators are commonly used. Thrombin, ADP, collagen, thromboxane A_2, are just some of the agonists used to bring about platelet activation, $\alpha_{IIb}\beta_3$ conformational changes and $\alpha_{IIb}\beta_3$ ligand binding.[108] In the case of these agonists, they do not directly interact with the integrin molecule but rather act on their respective receptor molecules to bring about an intracellular signalling cascade involving a rise in cytosolic calcium, activation of PKC and PI3K, as well as engagement of talin with $\alpha_{IIb}\beta_3$.[76] In addition to these physiological activators of $\alpha_{IIb}\beta_3$, a number of synthetic integrin activators are available that bring about integrin activation. In contrast to the physiological

activators mentioned, these artificial activators act directly on the integrin molecule itself rather than signalling through intracellular pathways. The reducing agent dithiothreitol (DTT) is one such artificial activator used to mimic $\alpha_{IIb}\beta_3$ conformational change. DTT functions to reduce two disulphide bonds within the integrin's cysteine-rich domain which leads to a structural and allosteric change in $\alpha_{IIb}\beta_3$. This change in conformation opens up the integrin headpiece to allow for ligand binding.[109] A second artificial integrin activator is the divalent cation Mn^{2+}. In contrast to DTT, Mn^{2+} does not bring about the same global conformational changes in the integrin molecule. Conflicting explanations exist on the exact structural changes observed in integrins when subjected to Mn^{2+}, with some reports suggesting a "switchblade" like extension of the integrin molecule[110], while others suggest that no extension of the integrin molecule occurs.[104] The differences observed with these two mimics of integrin activation once again suggest the multiple structural configurations can exist in $\alpha_{IIb}\beta_3$, but how close these are to physiological conformations is a matter for debate. In this chapter we sought to compare and contrast the use of the artificial activators DTT and Mn^{2+} with a physiologically-relevant activator in thrombin receptor activating peptide (TRAP). The purpose of this was to characterise the efficacy of DTT and Mn^{2+} as activators of $\alpha_{IIb}\beta_3$. This was examined in platelets before attention moved to the activation of $\alpha_{IIb}\beta_3$ in artificial lipid systems such as integrin-reconstituted liposomes, or integrin-reconstituted supported lipid bilayers.

2.2. Experimental

2.2.1. Washed platelet preparation

Venous whole blood was drawn from volunteers by a qualified phlebotomist with a Butterfly© 16 gauge needle. Volunteers were healthy and free from aspirin or other drugs that may knowingly affect platelet function. Ethical approval was given by the RCSI research ethics committee. To prevent coagulation, Acid-Citrate-Dextrose (ACD) (38mM citric acid anhydrous, 5 mM sodium citrate, 124mM glucose) at 15 % (v/v) was present in the syringe during withdrawal. The blood was aliquoted into 15 ml tubes and centrifuged at 150 g for 12 minutes in order to fractionate the blood. The majority of the top fraction which is known as the platelet rich plasma (PRP) is removed from the tube. The PRP is transferred to a 50 ml tube and the pH reduced to approximately 6.5 with a few drops of ACD. Prostaglandin E_1 (PGE_1) (Sigma Aldrich) was added at a final concentration of 1 µM to prevent premature platelet activation. The PRP was centrifuged at 720 g for 10 minutes to pellet the platelets. The supernatant was removed and platelets were re-suspended gently in JNL buffer (10 mM Tris, 130 mM NaCl, 9 mM $NaHCO_3$, 10 mM sodium citrate, 3 mM KCl, 0.81 mM KH_2PO_4, 0.9 mM $MgCl_26H_2O$, 6 mM glucose, pH 7.35) before bring left to rest at room temperature for 45 minutes. $CaCl_2$ was added to the platelets at a final concentration of 1.8 mM before activation studies.

2.2.2. Platelet Aggregometry

Platelet aggregometry is a technique that uses light transmission through a platelet-containing glass cuvette to determine the degree of aggregation of a platelet population. Washed platelets were placed in an aggregometry cuvette and stirred at a defined speed (1100rpm) and a controlled temperature (37^oC). Light was passed through the cell and much of the light was absorbed by the platelets before it reaches a detector. The addition of an agonist to the cuvette caused the platelets to

aggregate and fall to the bottom of the cell. This aggregation allowed for the increased transmission of light through the cell. This increase in light transmission corresponded to the degree of platelet aggregation and can be monitored over a set period of time. To perform the aggregation experiments, washed platelets were counted with a Sysmex KX-21 haematology analyser and adjusted to 3 x 10^6 platelets per µl via the addition of more JNL buffer. $CaCl_2$ was added at a final concentration of 1 mM. Platelets were added to the aggregation tubes of a PAP-8E aggregometer from BioData Corporation. At 37 °C and under constant stirring, the platelets were stimulated with varying concentrations of DTT or $MnCl_2$ (0.5 to 5 mM) (both Sigma Aldrich). Thrombin receptor activating peptide (TRAP) (Bachem) was used as a positive control throughout (4 µM). Physiologically, thrombin acts by cleaving its receptor's N-terminus revealing a tethered ligand, SFLLRN, which in turn acts as an agonist on itself. TRAP is a short peptide sequence (SFLLRN) that potently mimics this response without the additional serine protease actions of thrombin, ie the conversion of fibrinogen to fibrin. In some experiments additional fibrinogen (Calbiochem) was added at a final concentration of 1 mg/ml to aid platelet aggregation. The percentage aggregation was monitored with the in-built software of the PAP-8E aggregometer and the data was exported for analysis in GraphPad Prism (GraphPad Software Inc, CA, USA).

2.2.3. Flow cytometry

Experimentally, platelets were transferred to fluorescence-activated cell sorting (FACS) tubes and incubated at room temperature in the presence of the required antibody or protein. The final platelet concentration was always 3 x 10^5 platelets per µl as determined by a Sysmex KX-21 haematology analyser. Calcium was added at a final concentration of 1 mM to ensure that platelets were responsive. Platelets were stimulated with either DTT or $MnCl_2$ (both at 3 mM) for 30 minutes at room temperature to induce $\alpha_{IIb}\beta_3$ conformation or platelet activation. Thrombin receptor activating peptide (TRAP) at 4 µM was used as the positive control. Platelets were passed through the FACScalibur flow cytometer (Becton Dickinson, NJ, USA) and the

platelet population was identified by a dot plot of forward scatter versus side scatter. A population gate was made around this area and 10,000 acquisitions are made. Data was analysed using CellQuest Pro software from Becton Dickinson or Flowing Software from Turku Bioimaging. Data was graphed using GraphPad Prism.

$\alpha_{IIb}\beta_3$ conformational studies

For $\alpha_{IIb}\beta_3$ conformational studies, FITC labelled mouse anti-human PAC-1 antibody (BD Pharmingen) or Oregon Green® 488 conjugated fibrinogen from human plasma (OgFg) (Molecular Probes) was used. PAC-1 is an antibody specific to the activated conformation of $\alpha_{IIb}\beta_3$, while OgFg is a labelled fibrinogen which should also only bind to activated $\alpha_{IIb}\beta_3$. The final concentration of PAC-1 was 0.1 mg/ml, while the final concentration of OgFg was 0.15 mg/ml.

Alpha granules release (p-selectin expression)

As mentioned in section 2.1.2 , activated platelets mobilise alpha granules in response to pro-aggregatory signals. One of the constituents of these granules is P-selectin, also known as CD62P. P-selectin is a cell adhesion molecule that is presented on the cell membrane in activated platelets. In resting platelets, P-selectin is stored in alpha granules. Therefore, the activation state of platelets can be determined by the expression of this molecule on the platelet surface. Experimentally this expression was identified via the antibody PE mouse anti-human CD62P (BD Pharmingen). The antibody was incubated with the platelets at 0.1 mg/ml for 30 minutes at room-temperature.

2.2.4. ADP/ATP assay

As mentioned in section 2.1.2, activated platelets secrete the contents of their dense granules in response to platelet agonist stimulation. These components include histamine, serotonin, ADP and ATP. In order to investigate whether dense granule secretion has occurred, ATP release by platelets was measured. Due to the fact that ATP:ADP release occurs in the ratio of 2:3,[111] this measure can be used as a surrogate for ADP release. In order to measure ATP release in response to various agonists, platelets were incubated with DTT, $MnCl_2$ (both at 3 mM) or TRAP (at 4

μM) for a given time (5 or 30 minutes) in a 96 well plate. The final platelet concentration was always 3 x 10^6 platelets per μl as determined by a Sysmex KX-21 haematology analyser. The volume of each well was 100 μl. An ADP standard was also prepared and pipetted into the 96 well-plate. The plate was gently shaken at 37 °C during the experiment runtime. In order to detect ATP levels for each well, 10 μl of the detection reagent Chronolume (Chronolog; Labmedics Limited, UK) was dispensed in the requisite wells at the end of the experimental time and the plate was shaken for 5 seconds as per the manufacturer's instructions. Luminescence from each well was detected using a Wallac 1420 Multilabel Counter (Perkin Elmer). Data was exported to GraphPad Prism and expressed as arbitrary absorbance units (AAU).

2.3. Results

2.3.1. Platelet Aggregation

Perhaps the most straightforward method of determining the effectiveness of the artificial agonists DTT and Mn^{2+} as integrin $\alpha_{IIb}\beta_3$ activators is through the use of platelet aggregometry. Here the activators can be added to cuvettes containing platelets and the degree of aggregation can be monitored over time and compared to a positive control in the form of TRAP. Although platelet aggregation is not controlled by integrin $\alpha_{IIb}\beta_3$ activation alone, it is one of the primary players in the aggregation process.

Platelet Aggregation in Response to DTT

The first artificial activator to be examined was DTT. Washed platelets (3 x 10^6 platelets per µl) were incubated with DTT concentrations ranging from 0.5 to 5 mM, or a positive control of 4 µM TRAP and light transmission through the cell was monitored over time. Washed platelets were prepared from 9 different donors, across separate days. As expected, the well-characterised positive control TRAP lead to immediate and large degree of platelet aggregation. After reaching maximum aggregation, the percentage of aggregated platelets proceeded to slowly decrease over the course of the experiment. In contrast to this response, DTT addition resulted in a prolonged lag phase in a concentration dependent manner. Using a percentage aggregated of 1 % as the start of this aggregation process, the lag time for each concentration of DTT is given in Figure 20. At the highest DTT concentrations (5 mM) aggregation was not visible until the 4 or 5-minute mark. At the lowest concentration (0.5 mM) this lag-phase was extended to approximately 12 – 15 minutes. As well as this lag in platelet response, the rate of platelet aggregation was also much slower than the positive control. Instead of reaching a plateau within 2 minutes as with TRAP, DTT-mediated aggregation had still not reached its zenith 30 minutes into the experiment. The different dynamics of DTT versus TRAP-

mediated aggregation can be seen in Figure 19. A one-way ANOVA was performed on this data at three different timepoints. After 500 seconds, TRAP, 5 mM DTT, 4 mM DTT (all $p < 0.001$) and 3 mM ($p < 0.01$) were all found to be significantly different than the negative control. After 1000 seconds, all the activators were found to be significantly different than the negative control ($p < 0.001$, except for 0.5 mM DTT where $p < 0.05$). At 1500 seconds all activators were also found to be significantly different than the negative control, where $p < 0.001$. It is clear from this that although DTT is indeed a good platelet aggregator, consideration must be placed on the fact that the platelet response is not instantaneous.

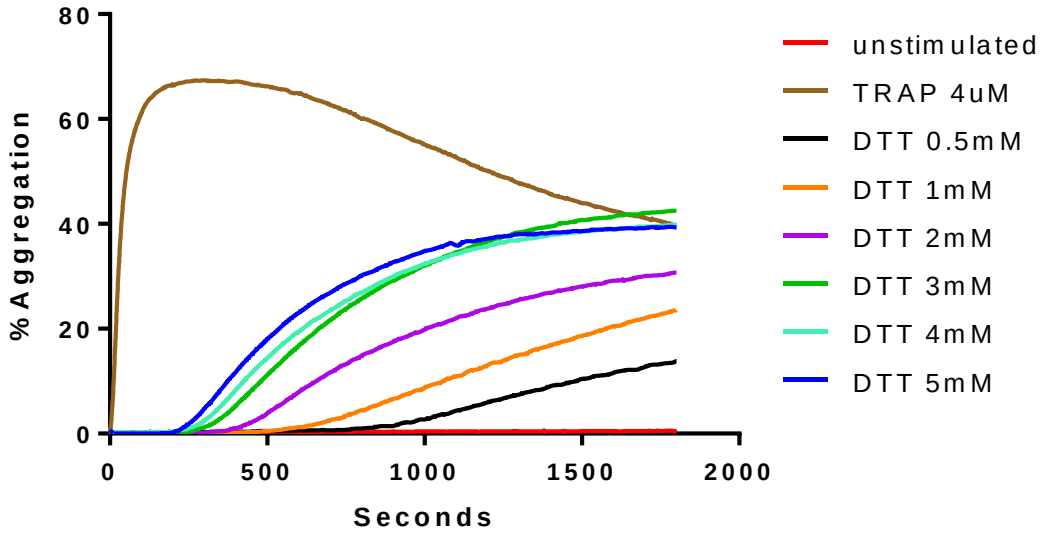

Figure 19: Aggregation of washed platelets in JNL buffer at 37°C after DTT activation (0.5 mM to 5 mM). The aggregation response was delayed when compared to activation with the positive control TRAP (brown). Additionally, the initiation of DTT-mediated aggregation was dose-dependant and even at the highest concentration used, never lead to the same degree of aggregation observed with TRAP. Unstimulated platelets did not aggregate (red). Data points were taken at 0.5 second intervals over the 30-minute duration of the experiment in a PAP-8E aggregometer and the mean value was obtained at each time-point before being plotted. (n=9, where n is the number of different donors)

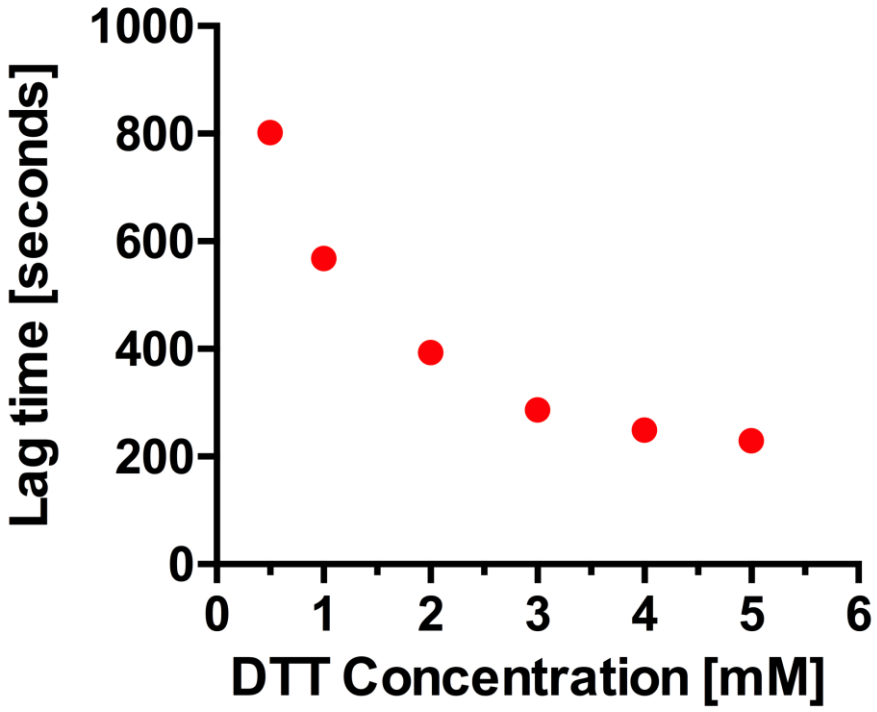

Figure 20: Lag time of DTT response. It can clearly be seen that as DTT concentration increased the lag phase was reduced, with minimal difference between 3, 4 and 5 mM concentrations of DTT. This lag phase must be taken into account when discussing the potency of DTT as an integrin activator.

Platelet Aggregation in Response to Mn^{2+}

To investigate Mn^{2+} as an integrin activator in a platelets, washed platelets (3 x 10^6 platelets per µl) were incubated with Mn^{2+} at concentrations ranging from 0.5 mM to 5 mM, as well as incubated with a positive control in TRAP (at 4 µM), and the degree of light transmission through the platelet aggregation cell was monitored over time. Washed platelets were prepared from 5 different donors on separate days. As before, the well-characterised positive control TRAP lead to immediate and extensive platelet aggregation before slowly declining over the course of the experiment. On the other hand, Mn^{2+}-mediated aggregation in washed platelets appeared to be negligible at all concentrations used. This can be seen in Figure 21. To confirm this a one, way ANOVA and post-hoc Bonferroni test was performed at

500, 1000, and 1500 seconds. Only TRAP was found to be significantly different than the negative control, where $p < 0.001$. This result was somewhat surprising given the wide use of Mn^{2+} as an integrin activator within the literature.

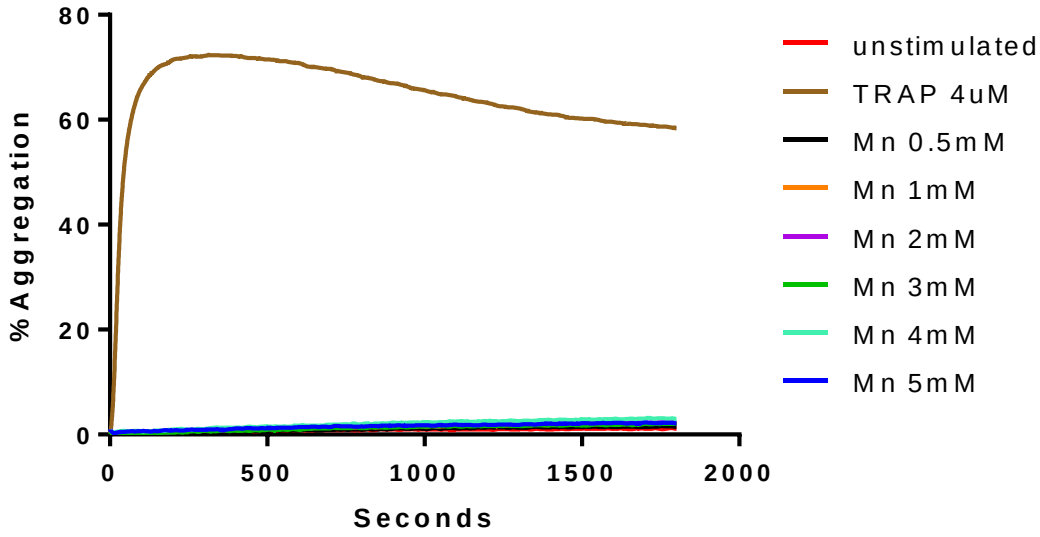

Figure 21: Aggregation of washed platelets in JNL buffer at 37°C in response to Mn^{2+} (0.5 mM to 5 mM). The aggregation of platelets in response to Mn^{2+} at all concentrations was negligible over the 30 minutes of observation. The positive control TRAP functioned as expected (brown). Unstimulated platelets did not aggregate (red). Data points were taken at 0.5 second intervals over the 30 minute duration of the experiment in a PAP-8E aggregometer and the mean value was obtained at each time point. (n=5, where n is the number of different donors)

Platelet Aggregation in Response to Mn^{2+} and Additional Fibrinogen

Due to the fact that Mn^{2+} has been widely described as an integrin activator,[13,110,112,113] it was unexpected that platelet aggregation was negligible using this agonist. In order to promote Mn^{2+}-induced aggregation it was later decided to supplement the washed platelets with fibrinogen. Fibrinogen is the primary ligand of $\alpha_{IIb}\beta_3$ and acts as bridge between platelets to aid aggregation and promote thrombus formation. Therefore, the additional of fibrinogen to our washed platelets was hoped to enable the aggregation process. It should be noted that prepared washed platelet solutions already contain a quantity of free fibrinogen, while platelets also contain fibrinogen within their alpha granules. This fibrinogen may be

released in response to to intracellular signalling events in order to promote the platelet aggregatory process.[89] As such, under these conditions, the washed platelets were simply put in solution with fibrinogen at a higher concentration then a standard washed platelet population. Experimentally the platelets were supplemented by the addition of fibrinogen at final concentration of 1 mg/ml. To this fibrinogen-augmented platelet population, Mn^{2+} was added as before at concentrations ranging from 0.5 mM to 5 mM. Once again 4 μM TRAP was used as a positive control. The experiment was carried out on washed platelets prepared from 7 different donors on separate days. Figure 22 shows the platelet aggregation profile within the aggregation cell following agonist addition.

Under these conditions TRAP was once again an excellent agonist for promoting platelet aggregation. In fact, the fibrinogen supplementation had increased the rate at which maximum aggregation was achieved, although no increase in the maximum percentage aggregated value was detected, when compared to a standard washed platelet preparation (Figure 19 and Figure 21). As before, using TRAP, the percentage of aggregated platelets began to slowly decrease over the course of the experiment after initially plateauing. Turning attention to Mn^{2+} it can clearly be seen that the cation does increase the aggregation response in fibrinogen-supplemented washed platelets. This is in contrast to results in a standard washed platelet population where no aggregation response was obvious (Figure 19 and Figure 21). However, the aggregatory response to Mn^{2+} was not as significant when compared to TRAP or DTT and did not exceed 20 % aggregation in any of the experiments. Interestingly, in contrast to DTT, no lag-phase was apparent, thus showing very different dynamics when compared with the reducing agent. A one-way ANOVA and post-hoc Bonferroni test was performed after 500, 1000, and 1500 seconds to determine how statistically significant this aggregation was. At all three time-points $p < 0.001$ for all activators, expect 0.5 mM Mn^{2+}, where $p < 0.01$ throughout.

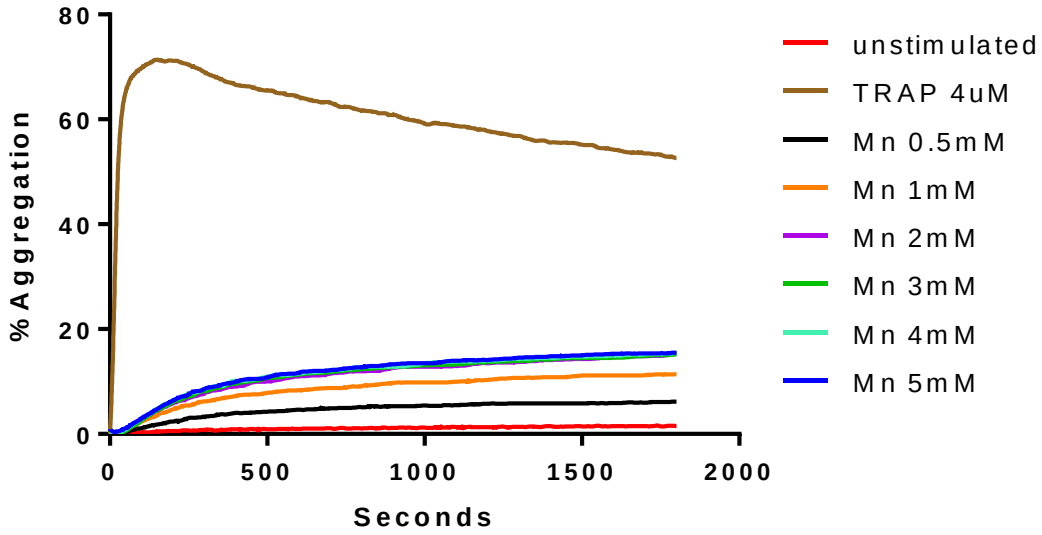

Figure 22: Aggregation of washed platelets in response to Mn^{2+} after addition of fibrinogen at 1 mg/ml. In this case the extra fibrinogen appears to facilitate the aggregation of the washed platelet preparation. TRAP results in aggregation as expected (brown). Unstimulated platelet aggregation is negligible. Data points are taken at 0.5 second intervals over the 30-minute duration of the experiment and the mean value is obtained at each time point. (n=7, where n is the number of different donors)

From our platelet aggregometry experiments it can clearly be seen that each of the agonists, TRAP, DTT and Mn^{2+}, show very different aggregation profiles. The positive control TRAP used at a half-maximal dose consistently lead to a measurable degree of aggregation within seconds and reached its maximum percentage aggregation value with 2 to 3 minutes, before a gradual decline in aggregation was seen as platelets slowly returned to solution. On the other-hand, the response to DTT was distinguished by a relatively long lag phase. This lag occurred in a concentration-dependent manner which varied from from 4 minutes (5 mM DTT) to 15 minutes (0.5 mM DTT). Despite this lag-phase the magnitude of aggregation was significant, while not as substantial as TRAP. Another noteworthy observation is the fact that the maximum percentage aggregation plateaued at approximately 40 % aggregated. For example, at 3, 4 and 5 mM DTT the same percentage aggregated value of approximately 40 % was reached. Over the time-course of the experiment no decrease in the percentage aggregation was detected, although this could be due to the length of the experiment (30 minutes). For Mn^{2+}, it was surprising to see no platelet aggregatory response in washed platelets. This was despite the fact the

Mn^{2+} has been widely used as an integrin activator.[45,46,114] In order to combat this lack of aggregation it was decided to supplement the washed platelets with extra fibrinogen. To do so fibrinogen was added at 1 mg/ml (2.9 µM) , a value which did not include any fibrinogen already present in the washed platelets, nor any fibrinogen that may or may not be released from the platelet's alpha granules during the activation response. As platelets were at a concentration of 3 x 10^6 platelets per µl and assuming between 50,000 and 80,000 $\alpha_{IIb}\beta_3$ molecules per platelet the concentration of $\alpha_{IIb}\beta_3$ in the aggregation experiments was anticipated to be between 0.249 and 0.399 µM. This meant we are working with an approximate tenfold excess of fibrinogen molecules when compared with $\alpha_{IIb}\beta_3$ molecules. It was found that only under these fibrinogen saturated conditions was Mn^{2+}-mediated aggregation observable. Using Mn^{2+} concentrations between 0.5 and 5 mM this aggregation occurs more quickly than DTT-mediated aggregation but never reaches the same degree of percentage aggregation. Fibrinogen addition without the presence of Mn^{2+} does not lead to aggregation showing the requirement for both the divalent cation and the $\alpha_{IIb}\beta_3$ ligand. The maximum percentage of platelet aggregation reached under these conditions and at varying agonist concentrations is shown in Table 3. Together, these results suggest that DTT is a much more potent activator of $\alpha_{IIb}\beta_3$ than Mn^{2+}, with the caveat that DTT activation includes a lag-phase. As previously mentioned, there is believed to be at least one intermediate partially activated state of $\alpha_{IIb}\beta_3$[115], and Mn^{2+} does not bring about the same global conformational changes with when integrin is subjected to DTT.[104,110] It is therefore interesting to speculate that Mn^{2+} stimulation results in an intermediate state $\alpha_{IIb}\beta_3$ molecule with lower affinity for its ligands, while DTT stimulation leads to an $\alpha_{IIb}\beta_3$ with high affinity for its ligands. In this case the partially-activated $\alpha_{IIb}\beta_3$ molecule may be continually moving between a ligand bound and unbound state whereby the low levels of soluble fibrinogen found in washed platelets is unable to support platelet bridging. The addition of extra fibrinogen at the concentration used in the experiments results in an approximate tenfold excess of fibrinogen in comparison to $\alpha_{IIb}\beta_3$, plus the fibrinogen already present in washed platelet preparations. This would mean that $\alpha_{IIb}\beta_3$ spends less time in its ligand unoccupied state and enough time in its ligand occupied state to facilitate some degree of platelet aggregation as

observed. Of course it these platelet aggregation experiments observe whole cell response to agonist stimulation rather than an integrin $\alpha_{IIb}\beta_3$ specific response. It must be remembered that the platelet membrane contains a variety of receptor molecules with affinity for a wide range of ligands involved in the aggregation response. For example, GPVI and integrin $\alpha_2\beta_1$ and their shared ligand; collagen[85], integrin $\alpha_V\beta_3$ and its primary ligand vitronectin[116], and the GPIb-IX-V complex and its ligand vWF[76], amongst others. Indeed integrin $\alpha_{IIb}\beta_3$ itself has specificity for a number of RGD and AGD peptide containing ligands including fibrinogen, vWF, fibronectin, and vitronectin, amongst others.[102] Furthermore, both DTT and Mn^{2+} are not specific to $\alpha_{IIb}\beta_3$ activation alone, but rather general integrin activators.[117–119] Given the fact the $\alpha_{IIb}\beta_3$, is one of five different integrins present at the platelet membrane[116], a simple whole cell platelet aggregation response to DTT and Mn^{2+} does not tell us the whole picture of how these two agonists influence integrin $\alpha_{IIb}\beta_3$'s structural response and ligand binding ability with particular emphasis on fibrinogen-binding. It was therefore decided to use flow cytometry to get more $\alpha_{IIb}\beta_3$ specific information following activation with DTT and Mn^{2+}.

Table 3: The maximum observed aggregation of washed platelets in response to DTT, Mn^{2+} and Mn^{2+} with the addition of fibrinogen at a final concentration of 1 mg/ml. While DTT alone is capable of bringing about a sizable degree of aggregation, Mn^{2+} must be co-incubated with fibrinogen for whole platelet aggregation to become observable.

Agonist Concentration	**Maximum mean aggregation in response to agonist (%)**		
mM	**DTT**	**Mn^{2+}**	**Mn^{2+} + Fg**
0	1	2	3
0.5	14***	2	7**
1	24***	3	12***
2	31***	3	16***
3	43***	3	16***
4	40***	4	16***
5	40***	3	16***

Table 4: A summary of the different responses to artificial agonists DTT and Mn^{2+} and the physiologically-relevant agonist TRAP. Both TRAP and DTT readily lead to platelet aggregation, albeit the DTT response featured a noticeable lag-phase. On the other hand, Mn^{2+} appeared to be a relatively poor agonist where fibrinogen supplementation was required to yield noticeable platelet aggregation.

Agonist	Platelet aggregation	Lag phase
TRAP	Extremely significant aggregation	No
DTT	Significant aggregation	Concentration dependent lag phase
Mn^{2+}	Negligible aggregation	n/a
Mn^{2+} and fibrinogen	Aggregation	No

2.3.2. Direct probing of $\alpha_{IIb}\beta_3$

PAC-1 binding to integrin $\alpha_{IIb}\beta_3$

The first method we used to directly probe the integrin $\alpha_{IIb}\beta_3$ conformational state was through the use of the antibody PAC-1 in a flow cytometry set-up. This antibody has specificity for the "activation-induced conformational epitope of the integrin $\alpha_{IIb}\beta_3$", according to the supplier[120], while having no affinity for the resting form of the protein. Therefore, if agonist-driven stimulation transitioned the $\alpha_{IIb}\beta_3$ protein from its low-affinity activation state to its high-affinity activation state, PAC-1 binding should be apparent. The experiment was repeated 5 times on separate donors. To gauge FITC-labelled PAC-1 binding to $\alpha_{IIb}\beta_3$, un-stimulated platelets were firstly analysed by flow cytometry for the binding of FITC–PAC-1. The platelet population was identified by forward scatter (particle size) and side scatter (particle granularity). Counts for the fluorescence data channel were piled on lowest values of the logarithmic x-axis of a histogram as the negative control. Subsequently, TRAP, DTT and Mn^{2+}-treated platelets were passed through the flow cytometer and the fluorescence data channels were plotted on the same histogram. Therefore, any PAC-1 binding is apparent as a shift in the counts to the right of the histogram. Figure 23 shows representative results for DTT (top) and Mn^{2+} (bottom) activation.

Four μM TRAP was used as the positive control and is visible in both histograms as a yellow fill. It can clearly be seen that TRAP, DTT and Mn^{2+} all lead to a shift in the counts to the right of the histogram showing that PAC-1 binding was occurring. Therefore, according to PAC-1 binding, all three agonists are capable of causing $\alpha_{IIb}\beta_3$ conformational changes and transition of the integrin protein from its low-affinity to its high-affinity state.

There are a number of ways to quantify PAC-1 binding. One such method is to use a gate on the histogram. Here, a gate was placed on the data so that 5 % of the total counts for the un-stimulated platelets were found within this gate. This way, any shift in counts to the right of the histogram results in more counts being encompassed within the gate. Figure 23 shows this gate, while Figure 24 shows the percentage gated values following agonist addition. Somewhat surprisingly, the positive control of 4 μM TRAP only lead to a small histogram shift, whereby the percentage gated value increased from 5 % to 16 ± 2 %. Using 0.5 mM and 3 mM DTT resulted in percentage gated value of 56 ± 17 % and 59 ± 8 %, respectively. Whereas, 0.5 mM and 3 mM Mn^{2+} resulted in percentage gated value of 33 ± 10 % and 35 ± 5 %, respectively. A one-way ANOVA and post-hoc Bonferroni test found all activators to lead to a significant degree of PAC-1 binding, where $p < 0.01$ for TRAP and $p < 0.001$ for DTT and Mn^{2+} at both concentrations.

An alternative method of quantifying PAC-1 binding is using the geometric mean of the counts under each condition. The geometric means of PAC-1 binding are shown in Figure 25. Using this measure, the geometric mean for unstimulated platelets was 1.55 ± 0.15. TRAP stimulation increased this value to 1.91 ± 0.28. The use of 0.5 mM DTT resulted in a geometric mean of 3.45 ± 0.97, while at 3 mM DTT the geometric mean was 3.67 ± 0.60. The use of 0.5 mM Mn^{2+} resulted in a geometric mean of 2.82 ± 0.36, while at 3 mM Mn^{2+} the geometric mean was 2.97 ± 0.41. ANOVA analysis and post-hoc Bonferroni test revealed that the agonists lead to significantly different PAC-1 binding, where $p < 0.001$ for both DTT concentrations, $p < 0.01$ for 3 mM Mn^{2+}, and $p < 0.05$ for 0.5 mM Mn^{2+}. Strangely, TRAP did not lead to significant PAC-1 binding according the geometric mean data.

All in all, these results are quite surprising. TRAP was a surprisingly poor integrin $\alpha_{IIb}\beta_3$ activator according to PAC-1 binding. On the other-hand, DTT appeared to be an excellent $\alpha_{IIb}\beta_3$ activator, while Mn^{2+} was also a good $\alpha_{IIb}\beta_3$ activator. Weak activation by TRAP can perhaps be explained by the fact that TRAP acts on the thrombin receptor rather than directly on the $\alpha_{IIb}\beta_3$ protein. This in turn leads to the activation of various intracellular pathways which include but most importantly are not limited to inside-out activation of integrin $\alpha_{IIb}\beta_3$. Thus, platelet aggregation is driven by a multitude of platelet response and not merely conformational changes in the $\alpha_{IIb}\beta_3$ protein. Taken together with our earlier platelet aggregometry experiments this may highlight the disconnect between what constitutes platelet activation (platelet aggregation) and $\alpha_{IIb}\beta_3$ activation ($\alpha_{IIb}\beta_3$ conformational changes).

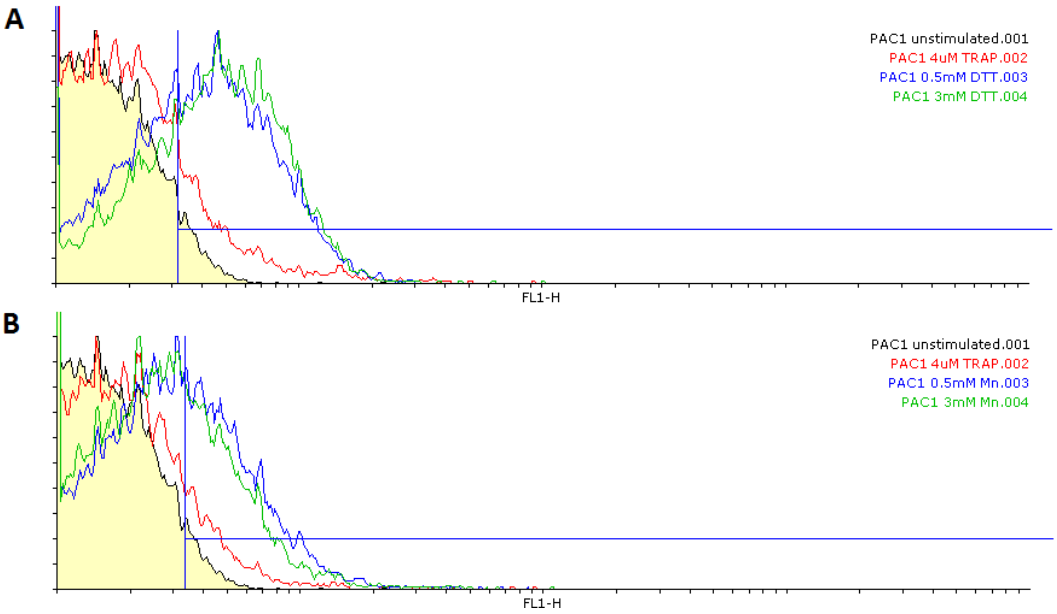

Figure 23: Representative histograms of FITC-labelled PAC-1 fluorescence after activation with TRAP, DTT and Mn^{2+}. The unstimulated gate set a 5 % meaning that 5 % of the counts for unstimulated platelets fall within this boundary. An increase in the number of counts that fall within the gate shows PAC-1 binding. A) shows PAC-1 binding in response to DTT (0.5 mM in blue, 3 mM in green) and the positive control TRAP (4 µM in red). A shift to the right is evident in all three cases when compared with the unstimulated platelets (black with yellow fill). B) shows PAC-1 binding in response to Mn^{2+} (0.5 mM in blue, 3 mM in green) and the positive control TRAP (4 µM in red). Once again a shift to the right is evident in all three cases when compared with the unstimulated platelets (black with yellow fill).

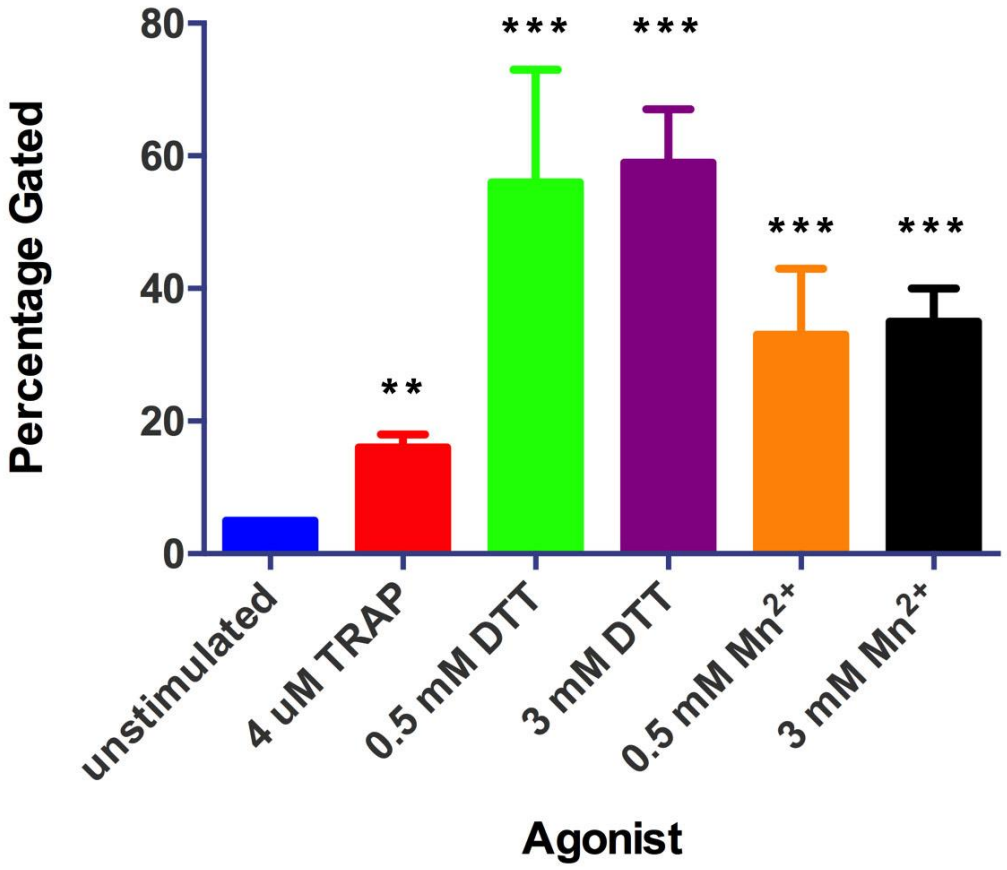

Figure 24: Both DTT and Mn^{2+}-induced integrin activation as assessed using the percentage gated of PAC-1 binding. A 5 % gated value was used for unstimulated platelets (blue). 4 µM TRAP (red) was a surprisingly weak integrin activator and only lead to a slight increase in the percentage gated value. DTT (green and purple) and Mn^{2+} (orange and black) were excellent integrin activators at 0.5 and 3 mM according to PAC-1 binding. Standard deviation was used to represent the error. (n=5, where n is the number of separate donors)

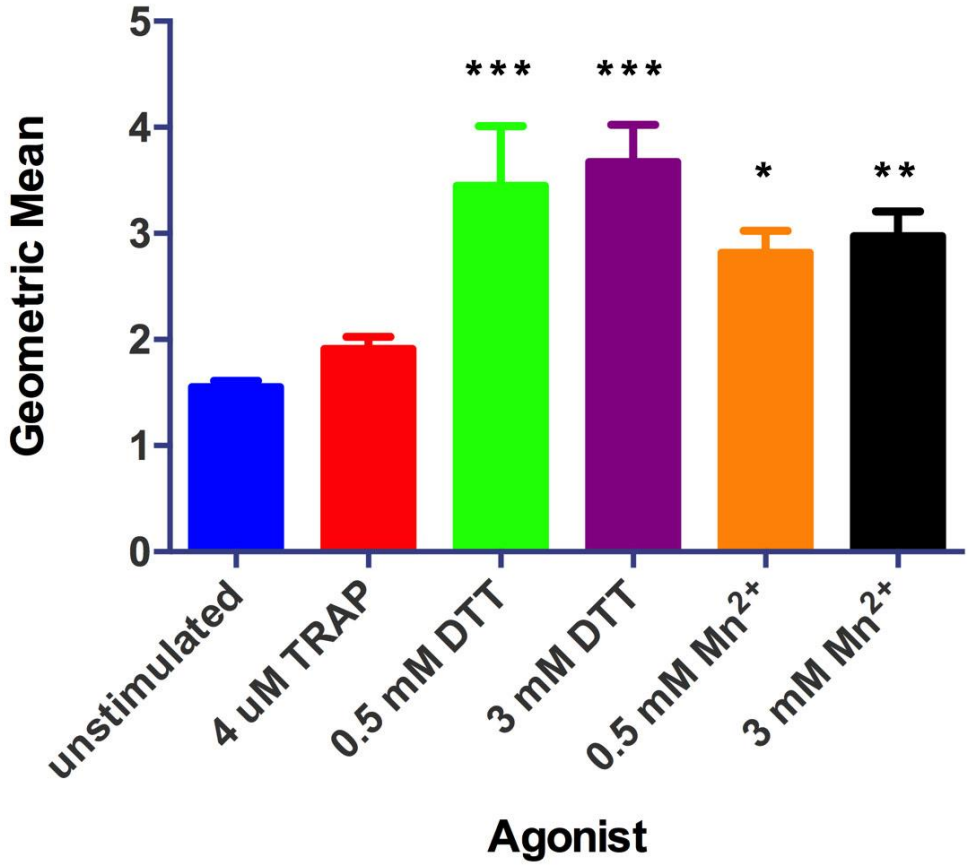

Figure 25: Both DTT and Mn^{2+}-induced integrin activation as assessed using the geometric mean of PAC-1 binding. The geometric mean of unstimulated platelets is shown in blue. 4 µM TRAP (red) was a surprisingly weak integrin activator and only lead to a slight increase in the geometric mean. DTT (green and purple) and Mn^{2+} (orange and black) were excellent integrin activators at 0.5 and 3 mM according to PAC-1 binding. Standard deviation was used to represent the error. (n=5, where n is the number of separate donors)

Fibrinogen binding to integrin

An alternative method of directly probing the activation state of integrin $\alpha_{IIb}\beta_3$ in a flow cytometry setup is via the use of a labelled fibrinogen molecule, in this case, Oregon green fibrinogen (OgFg). As only the high affinity conformation is capable of binding to fibrinogen so this experiment can be seen as proxy for the activation state of $\alpha_{IIb}\beta_3$.In this experimental setup it we sought to investigate whether fibrinogen binding could be brought about by the artificial agonists DTT and Mn^{2+}. The earlier PAC-1 binding results suggest that both agonists lead to the high-affinity activation state of integrin $\alpha_{IIb}\beta_3$. Given that this high-affinity activation state allows for ligand binding and has previously been shown to lead to platelet aggregation, it would be

expected that fibrinogen binding should occur. In order to gauge labelled fibrinogen binding to $\alpha_{IIb}\beta_3$, un-stimulated platelets were firstly passed through the flow cytometer and the population was identified by forward scatter (cell size) and side scatter (cell granularity). Counts for the fluorescence data channel were piled on lowest values of the logarithmic x-axis of a histogram as the negative control. Subsequently, TRAP, DTT and Mn^{2+}-activated platelets were passed through the flow cytometer and the fluorescence data channels were plotted on the same histogram. Therefore, any OgFg binding is apparent as a shift in the counts to the right of the histogram. The experiment was repeated using washed platelets from 5 separate donors. Figure 26 shows typical results for DTT (top) and Mn^{2+} (bottom) activation. 4 μM TRAP was used as the positive control and is visible in both cases. It is clear that TRAP leads to a massive histogram shift for OgFg binding. Interestingly, this is in contrast to the earlier PAC-1 results. DTT also brought about a histogram shift in a concentration-dependant fashion (top). Whereas, Mn^{2+} did not appear to bring about a histogram shift at either concentration (bottom). This is unusual given the fact that PAC-1 binding had earlier shown that Mn^{2+} leads to the activated high affinity form of $\alpha_{IIb}\beta_3$. In order to quantify these results two separate analysis methods were used once again applied.

Using percentage gated in the same manner as last time where a baseline gate was placed on the data so that 5 % of the total counts for the un-stimulated platelets were found within. Figure 26 shows this gate, while Figure 27 shows the percentage gated values following agonist addition. In this case, TRAP activation lead to substantial increase in the percentage gated value where 56 ± 7 % of events were found to occupy the gated region, up from the 5 % baseline in unstimulated platelets. For DTT the percentage gated value increased in a concentration-dependent manner. At 0.5 mM DTT it was found to be 14 ± 4 %, while 3 mM DTT it was found to be 86 ± 9 %. On the other-hand the percentage gated value for Mn^{2+} stimulated platelets failed to deviate from the baseline gated value at either concentration used. In this case both 0.5 and 3 mM Mn^{2+} resulted in 6 ± 1 % of events falling within the gate. ANOVA analysis and a post-hoc Bonferroni test

showed that only TRAP and DTT at 3 mM lead to significant OgFg binding, where $p < 0.001$ in both cases.

Following this analysis using a gated histogram, the geometric mean was also used to quantify OgFg binding. Using this method, un-stimulated platelets had a geometric mean of 1.80 ± 0.06 The geometric mean of TRAP stimulated platelets was 7.01 ± 0.94. For DTT stimulation, the geometric means were 2.39 ± 0.24 and 10.48 ± 2.92 at 0.5 and 3 mM, respectively. Using Mn^{2+}, the geometric means were 1.91 ± 0.27 and 1.87 ± 0.16 at 0.5 and 3 mM, respectively. ANOVA analysis and a post-hoc Bonferroni test showed that only TRAP and DTT at 3 mM lead to significant OgFg binding, where $p < 0.01$ and $p < 0.001$, respectively.

Figure 26 shows that the positive control TRAP (at 4 μM), despite earlier leading to limited PAC-1 binding, was an excellent agonist for fibrinogen binding. DTT lead to fibrinogen binding as shown in Figure 26A. Whereas, interestingly, Mn^{2+} did not appear to result in any degree of fibrinogen binding as shown in Figure 26B. This is despite the fact that PAC-1 binding had showed that $\alpha_{IIb}\beta_3$ was in its activated state and thus should be available for ligand-binding. These fibrinogen binding experiments are extremely interesting considering our earlier PAC-1 binding experiments that informed us of the activation state of integrin $\alpha_{IIb}\beta_3$. While this PAC-1 binding had shown that both DTT and Mn^{2+} transitioned the $\alpha_{IIb}\beta_3$ protein to its active ligand-available configuration, OgFg binding has shown that only DTT allowed for fibrinogen binding to the $\alpha_{IIb}\beta_3$ protein. This highlights the intricacies of $\alpha_{IIb}\beta_3$ activation and points to varying degrees of activation states which may or may not be suitable for ligand-binding. It is plausible to suggest that Mn^{2+} leads to some degree of $\alpha_{IIb}\beta_3$ conformational changes to allow for PAC-1 binding but not the extent where $\alpha_{IIb}\beta_3$ is fully available for fibrinogen binding, ie, a partially activated state. As a whole, these results suggest that both the positive control TRAP and the reducing agent DTT are good integrin $\alpha_{IIb}\beta_3$ activators in terms of fibrinogen binding. Contrary to this, Mn^{2+} stimulation does not appear to lead to fibrinogen binding.

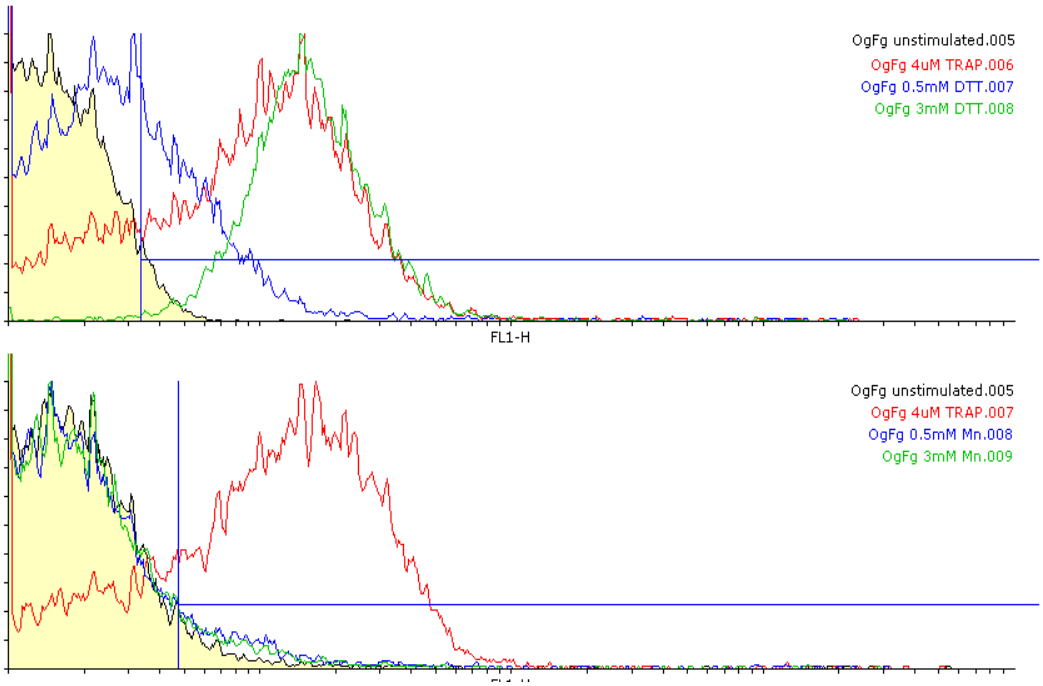

Figure 26: Representative histograms of Oregon green labelled fibrinogen (OgFg) fluorescence after activation with TRAP, DTT and Mn^{2+}. Once again the unstimulated gate set a 5 %. A) shows OgFg binding in response to DTT (0.5 mM in blue, 3 mM in green) and the positive control TRAP (4 µM in red). A shift to the right is evident in all three cases when compared with the unstimulated platelets (black with yellow fill). B) shows OgFg binding in response to Mn^{2+} (0.5 mM in blue, 3 mM in green) and the positive control TRAP (4 µM in red). In contrast to DTT, Mn^{2+} does not appear to be sufficient for observable fibrinogen binding. This is despite the previous findings Mn^{2+} stimulation leads to PAC-1 binding, indicating that $\alpha_{IIb}\beta_3$ is in its active confirmation.

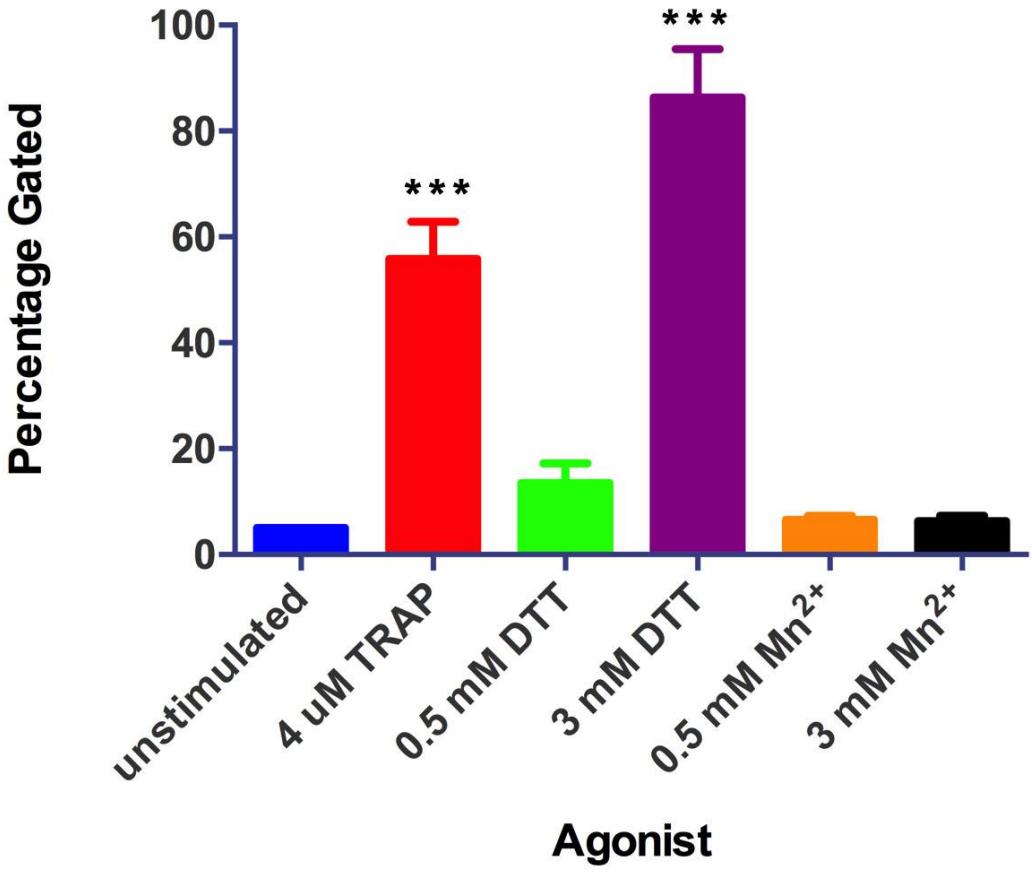

Figure 27: DTT but not Mn^{2+} induced integrin activation as assessed using the percentage gated of OgFg binding. A 5 % gated value was used for unstimulated platelets (blue). The positive control of 4 µM TRAP was also an integrin activation as determined by fibrinogen binding. DTT at 3 mM (purple) lead to integrin activation according to fibrinogen binding. Mn^{2+} (orange and black) did not lead to activation according to fibrinogen binding. Standard deviation was used to represent the error. (n=5, where n is the number of separate donors)

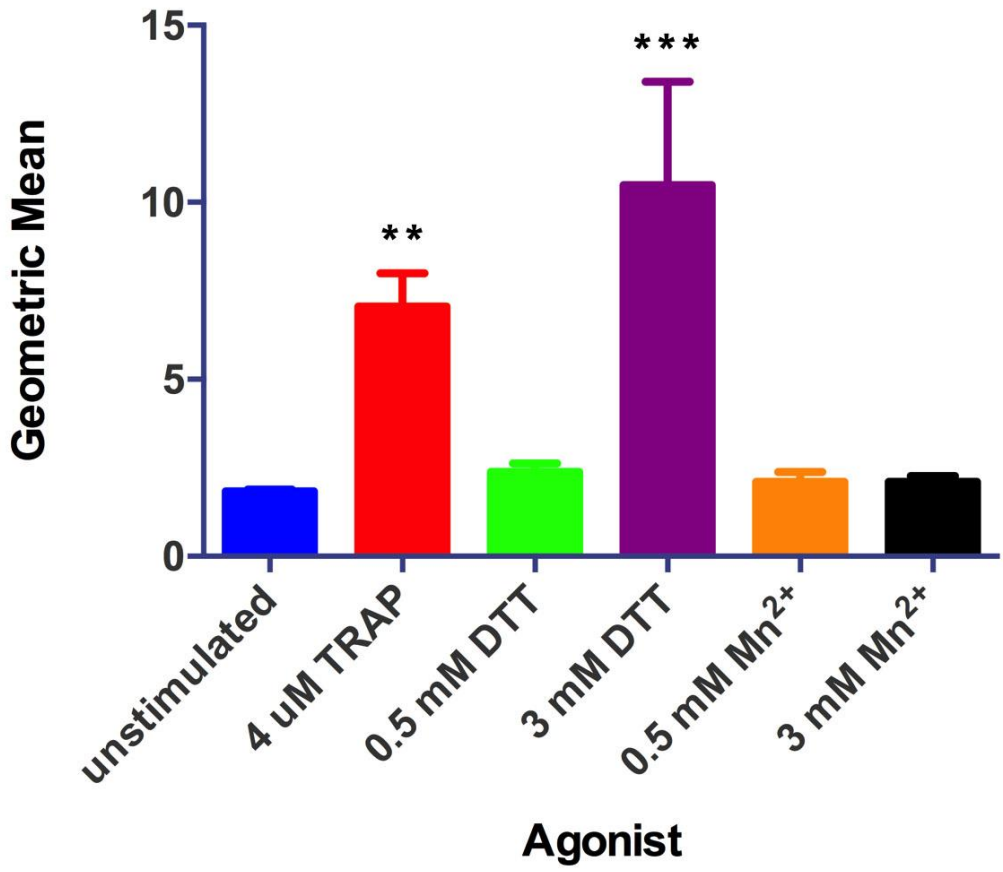

Figure 28: DTT but not Mn^{2+}-induced integrin activation as assessed using the geometric mean of OgFg binding. The geometric mean for unstimulated platelets is shown in blue. The positive control of 4 µM was an excellent integrin activator according to OgFg binding. DTT also lead to integrin activation at 3 mM (purple). Mn^{2+} did not lead to integrin activation at either concentration. Standard deviation was used to represent the error. (n=5, where n is the number of separate donors)

Taken separately these PAC-1 and fibrinogen binding results are relatively straightforward. However, taken together their contradictory nature is intriguing. TRAP leads to a small degree of conformational changes in $\alpha_{IIb}\beta_3$, yet a large degree of fibrinogen binding. DTT leads to both large scale $\alpha_{IIb}\beta_3$ structural changes and fibrinogen binding. Mn^{2+} also leads to large scale $\alpha_{IIb}\beta_3$ structural changes, yet fails to elicit fibrinogen binding.

In these flow cytometry experiments it can be said that DTT behaved as expected, based on our earlier light aggregometry experiments. DTT induced platelet activation resulted in enhanced PAC-1 binding, indicating that integrin $\alpha_{IIb}\beta_3$ had transitioned to its ligand available high affinity activated state. In addition, DTT

causes enhanced fibrinogen binding as seen in the OgFg experiments. These two results combine to agree with our earlier observation that DTT was a capable of supporting whole platelet aggregation as seen via light aggregometry. This is relatively unsurprising given the blunt nature of the reducing agent DTT as an integrin activator. Yan and Smith have reported that DTT reduces two disulfide bonds within the integrin's cysteine-rich domain and it is these reductions that are responsible for the global conformational changes in $\alpha_{IIb}\beta_3$ which make the integrin protein available for ligand binding.[109] This ability of DTT to function as general integrin was further backed up by Zhang *et al.* where the reducing agent was capable of bringing about conformational changes within integrin $\alpha_5\beta_7$, again via reduction in two disulphide bonds at the integrin knees. This disulphide bond reduction did not occur via inside-out activation or Mn^{2+} activation.[117]

TRAP was, as expected, an excellent activator of $\alpha_{IIb}\beta_3$ at least in terms of fibrinogen (OgFg) binding. This would be expected given our earlier aggregometry experiments where TRAP was an extremely potent agonist, leading to a high degree of platelet aggregation. However, the fact that PAC-1 was relatively low contrasts with this. This can be explained in a number of ways. The TRAP peptide acts on the thrombin receptor and thus signals intracellularly with all the associated responses accompanying thrombin activation. As such TRAP stimulation leads to a whole-platelet response that may include the transitioning of all five platelet present integrins[121] to their high-affinity conformation, the expression of P-selectin on the platelet surface[76], and the release of pro-aggregatory factors.[88] Thus although $\alpha_{IIb}\beta_3$ activation is a major feature of platelet activation it is not the only feature. It must also be remembered that $\alpha_{IIb}\beta_3$ is not the only receptor for fibrinogen. Indeed integrin $\alpha_V\beta_3$ is also capable of binding to fibrinogen.[122] Thus, at least some OgFg binding is possible in the absence of $\alpha_{IIb}\beta_3$ conformational changes. Of course these conclusions are based on the reliability of the PAC-1 antibody as a sign that $\alpha_{IIb}\beta_3$ is in its active conformation. As discussed below, the difference between resting and activated $\alpha_{IIb}\beta_3$ does not appear to be binary.

The final artificial integrin activator, Mn^{2+}, facilitated PAC-1 binding. This shows that structural changes in $\alpha_{IIb}\beta_3$ have occurred and according to the literature, $\alpha_{IIb}\beta_3$ should now be in its active, high-affinity ligand-binding conformation. However, contrary to this expectation, no fibrinogen (OgFg) binding occurred. This may suggest that PAC-1 binding occurs independently of the ligand-binding site for fibrinogen becoming available. For example, integrin $\alpha_{IIb}\beta_3$ is believed to have a number of intermediate activation states that may help to explain this discrepancy.

Indeed, there exists inconsistent data in the literature about the exact structural changes undergone by integrins in the presence of Mn^{2+}. Takagi *et al.* report that Mn^{2+} lead to large scale conformational changes in purified integrin $\alpha_V\beta_3$, in a "switchblade-like opening to an extended structure"[110], while Ye *et al*. report that $\alpha_{IIb}\beta_3$ in liposomes showed no change in height in the presence of Mn^{2+}, indicating that no integrin extension occured.[104] Furthermore, FRET-based measurements in live cells have also provided conflicting results. For example, Chigaev *et al.* found that $\alpha_4\beta_1$ appeared to undergo large scale structural changes due to Mn^{2+}, albeit not the same as those induced by chemokines. Meanwhile, Kim *et al.* found that $\alpha_L\beta_2$ did not appear to alter its conformation in response to Mn^{2+}.[123] Yan and Smith stated that Mn^{2+} increased purified $\alpha_{IIb}\beta_3$'s affinity for ligands without fully activating the integrin protein.[112] Kamata *et al.* reported that conformational changes in response to Mn^{2+} is an integrin isoform specific response. Here $\alpha_{IIb}\beta_3$ was highlighted as partially resistant to Mn^{2+} when compared to $\alpha_V\beta_3$. While $\alpha_V\beta_3$ showed robust ligand binding after Mn^{2+} activation, $\alpha_{IIb}\beta_3$ showed limited ligand binding, and failed to achieve full activation. Interestingly, by constructing a series of α_{IIb}/α_V domain swapped chimeras, $\alpha_{IIb}\beta_3$'s partial resistance to Mn^{2+} activation was shown to stem from its calf-2 domain, a domain which does not contain any divalent cation-binding sites. Swapping this region of $\alpha_{IIb}\beta_3$ allowed for robust ligand-binding after Mn^{2+} activation.[113] This result suggests that different integrin isoforms respond to Mn^{2+} in different manners, rather than being simply general integrin activators

As can be seen the relationship between integrins and Mn^{2+}-induced activation is complex. The complexity is summed by Ye *et al.* where it was stated that "Mn^{2+} re-

created integrin activation has multiple forms depending on the integrin isoforms and the context. It is probable that Mn^{2+}-induced integrin activation is somewhat different from the physiologic inside-out integrin signalling process. The debates about the nature of Mn^{2+}-induced integrin activation and its relevance to physiologic inside-out integrin signalling process will probably continue".[119]

Table 5: A summary of the influence of TRAP, DTT, and Mn^{2+} on PAC-1 binding and fibrinogen binding. While TRAP has been shown to be an excellent agonist in terms of platelet aggregation, PAC-1 binding appeared to show that $\alpha_{IIb}\beta_3$ conformational changes were surprisingly minimal. Despite this, labelled fibrinogen binding was readily observable. DTT was shown to result in both significant PAC-1 and fibrinogen binding. In contrast to this while Mn^{2+} resulted in significant integrin conformational changes, no labelled fibrinogen binding was detected. These results hint at a disconnect between conformational changes in the integrin protein and ligand binding.

Agonist	Integrin conformational changes (PAC-1 binding)	Ligand binding (OgFg binding)
TRAP	Yes, albeit surprisingly minimal	Significant
DTT	Extremely significant	Significant
Mn^{2+}	Significant	None

2.3.3. Whole platelet response

The previous sections have focuses on whether DTT and Mn^{2+} could support washed platelet aggregation, induce conformational changes in integrin $\alpha_{IIb}\beta_3$, and/or result in measureable binding of labelled fibrinogen. Of course the platelet reaction is not limited to these responses. *In vivo* activation includes platelet morphological changes[91], phosphorylation of intracellular proteins[124], an increase in cytosolic calcium levels[82], and granule secretion[91]. Given the general literature description of DTT and Mn^{2+} as integrin activators[119], combined with $\alpha_{IIb}\beta_3$'s bidirectional signalling ability[14], and the fact the other integrins have shown a ligand independent outside in response to these artificial modulators[117], we were keen to determine whether DTT or Mn^{2+} stimulation results in a whole-platelet response, and not just $\alpha_{IIb}\beta_3$

localised extracellular conformational changes and alterations in affinity for fibrinogen binding. For example, Zhang *et al.* used DTT to mimic activation in integrin $\alpha_4\beta_7$ and found that breakage of two disulphide bonds near the integrin knees lead lead to integrin downstream signalling independently of ligand occupancy. This was measured via the activation of FAK and paxillin, two downstream molecules of integrin outside-in signalling.[117] As such we were keen to see whether DTT or Mn^{2+} could elicit similar platelet response via $\alpha_{IIb}\beta_3$ conformational changes. To do so two different platelet assays were conducted, one based on the release of alpha granule contents, and one based on the release of dense granule contents, two events associated with the whole platelet activation response.

Alpha granule secretion

As previously mentioned, α-granules are one of the secretory granules found in the platelet cytoplasm. They contain a variety of contents including PDGF, fibrinogen, and vWF. In platelets, α–granules fuse with the plasma membrane upon activation, releasing their cargo and increasing platelet surface area. Another factor found in α–granules is the adhesion molecule P-selectin. Prior to platelet activation this protein is confined to α–granules, but following granule mobilisation P-selectin is trafficked to the platelet membrane for presentation. Therefore, display of P-selectin can be used as a measure of α–granule secretion and whole platelet activation. By using TRAP, DTT and Mn^{2+} as integrin activators it was therefore possible to gauge the whole-platelet response to these agonists via the presence or absence of is P-selectin on the platelet membrane. To determine this presence a PE-labelled CD62P antibody was used in a flow cytometry. Again, unstimulated platelets were used as the negative control where counts for the fluorescence data channel were piled on lowest values of the logarithmic x-axis of a histogram. Subsequently, TRAP, DTT and Mn^{2+}-activated platelets were passed through the flow cytometer and the fluorescence data channels were plotted on the same histogram. Therefore, any P-selectin binding could be visualised as shift in the counts to the right of the histogram. A typical histogram is shown in Figure 29. It is clear from this histogram

that only TRAP stimulation lead to anti-CD62P binding. Nonetheless, to quantify this we again used two different analysis tools in percentage gated and geometric mean in order to quantify this anti-CD62P binding. Using percentage gated in the same manner as last time where a baseline gate was placed on the data so that 5 % of the total counts for the un-stimulated platelets were found within this gate. This histogram gate is visible in Figure 29. In this case TRAP stimulation lead to a massive increase in the percentage gated value where 52 ± 17 % of events were found to occupy the gated region up from the 5 % baseline in unstimulated platelets. In the case of 3 mM DTT stimulation the percentage gated value was found to be 6 ± 1 %, while in the case of 3 mM Mn^{2+} stimulation the percentage gated value was found to be 5 ± 1 %. This data is shown in Figure 30. A one-way ANOVA analysis and post-hoc Bonferroni test was performed on this data where only TRAP stimulation was found to lead to a significant degree of P-selectin expression, where $p < 0.001$. Following this analysis using a gated histogram, the geometric mean was also used to quantify anti-CD62P binding. Using this method, un-stimulated platelets had a geometric mean of 1.69 ± 0.31. The geometric mean of TRAP stimulated platelets was found to be 5.83 ± 0.64. The geometric mean of 3 mM DTT and 3 mM Mn^{2+} stimulated platelets was found to be 1.77 ± 0.35 and 1.62 ± 0.27 respectively. This data is shown in Figure 31. Once again, a one-way ANOVA analysis and post-hoc Bonferroni test was performed on this data. In agreement with our previous analysis, only TRAP stimulation was found to lead to a significant degree of P-selectin expression, where $p < 0.01$. Therefore, according to the absence of P-selectin on the platelet surface, no alpha granule secretion has occurred due to DTT or Mn^{2+} stimulation. This suggests that the conformational changes that occur in $\alpha_{IIb}\beta_3$ due to these integrin modulators does not lead to the full range of platelet activation normally associated with physiological agonists.

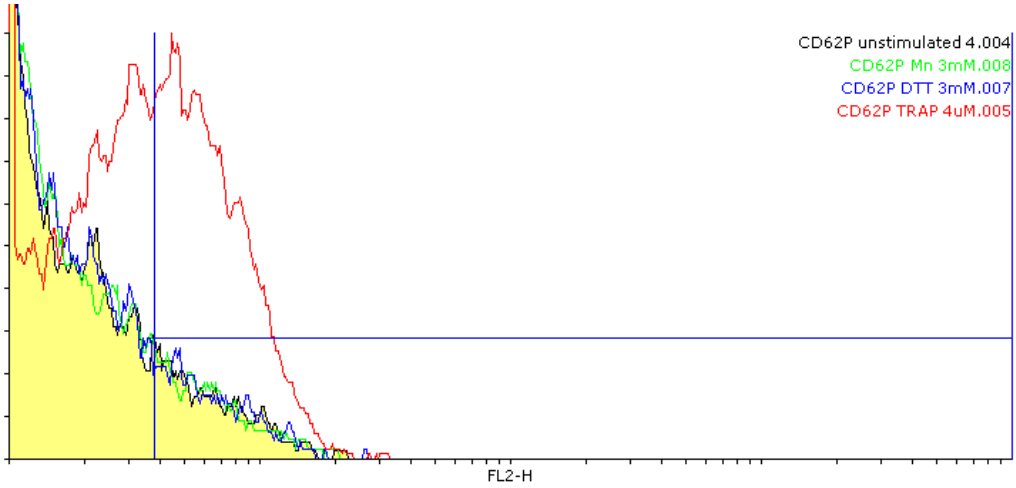

Figure 29: A representative histogram of anti-CD62P binding to p-selectin in unstimulated platelets (yellow), and following stimulation with 4 µM TRAP (red), 3 mM DTT (blue) and 3 mM Mn^{2+} (green). It can clearly be seen that TRAP stimulation is the only agonist that brings about antibody binding. This shows that alpha granules release and thus P-selectin presentation only occurs with this agonist and not DTT or Mn^{2+}.

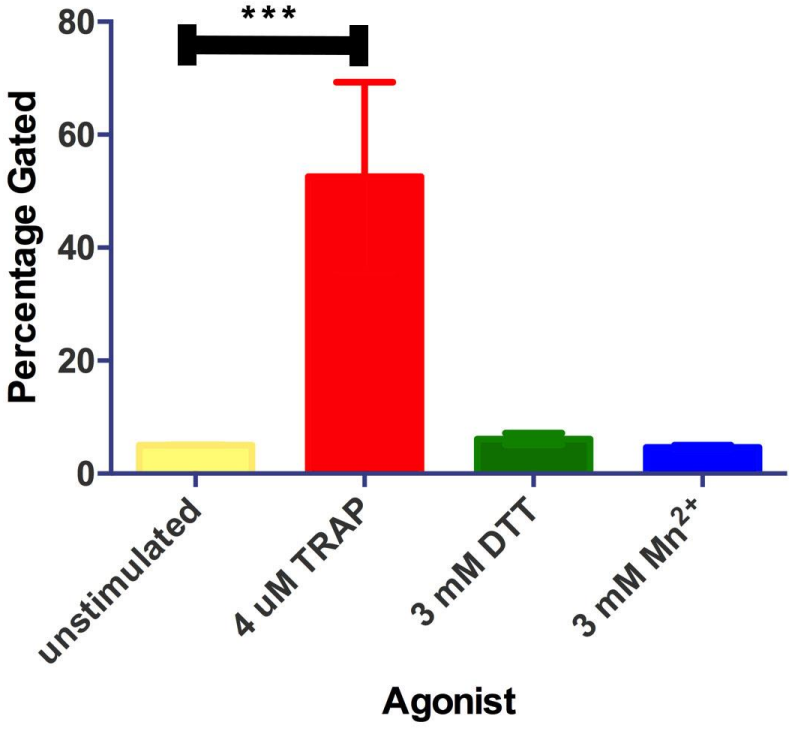

Figure 30: DTT and Mn^{2+} failed to lead to alpha granule release according to anti-CD62P binding as assessed using percentage gated. A gate was set so that 5 % of unstimulated platelet counts fall within it (yellow). TRAP at 4 µM (red) was sufficient to bring about anti-CD62P binding, meaning that P-selectin was expressed on the platelet surface. DTT at 3 mM (green) and Mn^{2+} at 3 mM (blue) did not result in P-selectin expression. Standard deviation was used to represent the error. (n=3, where n is the number of donors)

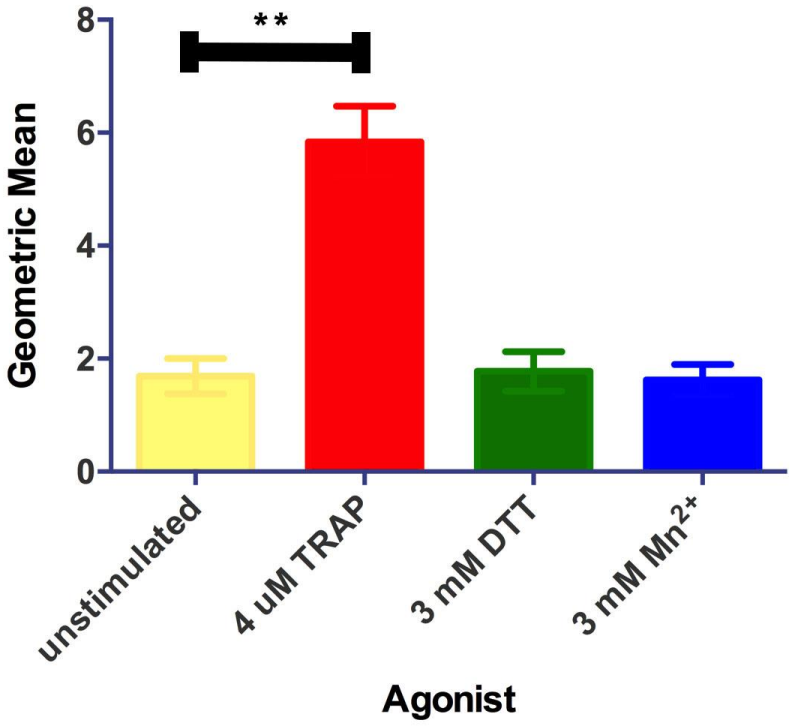

Figure 31: DTT and Mn^{2+} failed to cause alpha granule release DTT and Mn^{2+} failed to lead to alpha granule release according to anti-CD62P binding as assessed using geometric mean. The geometric mean of unstimulated platelets is shown in yellow. TRAP at 4 µM (red) was sufficient to bring about anti-CD62P binding, meaning p-selectin was expressed on the platelet surface. DTT at 3 mM (green) and Mn^{2+} at 3 mM (blue) did not result in p-selectin expression. Standard deviation was used to represent the error. (n=3, where n is the number of donors)

Dense granules secretion

The other primary secretory vesicles found in platelets are known as dense granules. Similar to alpha granules, dense granules are released by platelets during the activation process. They contain a variety of contents including histamine, serotonin, ADP and ATP.[89] In order to quantify dense granule secretion an ATP releases assay. This assay can, therefore, be used as a proxy for whole platelet response to various agonists. Normally this assay is done within 5 minutes of agonist stimulation but due to the lag-phase seen with the platelet aggregation in response to DTT, the assay was also repeated at the 30-minute time point in case dense granule secretion was dependent on this lag-phase. The experiment was carried out on 3 separate donors across different days. Figure 32 shows ADP/ATP release in AAU following stimulation

with TRAP, DTT and Mn^{2+} at these time points. It was immediately clear that 4 µM TRAP stimulation leads to a large degree of ATP release from dense granules at the 5 minute and 30 minute mark. On the other hand the use of DTT and Mn^{2+} at 3 mM failed to alter ATP from the unstimulated platelet baseline. This observation was confirmed by ANOVA anlysis and post-hoc Bonferroni test where only TRAP activation was found to lead to significant ATP release where, $p < 0.001$. This indicates that our artificial activators did not result in dense granules secretion in an outside-in signalling manner. This result is consistent with our earlier alpha granule release assay and again suggests that DTT and Mn^{2+} does not lead to the full degree of platelet activation normally associated with physiological agonists.

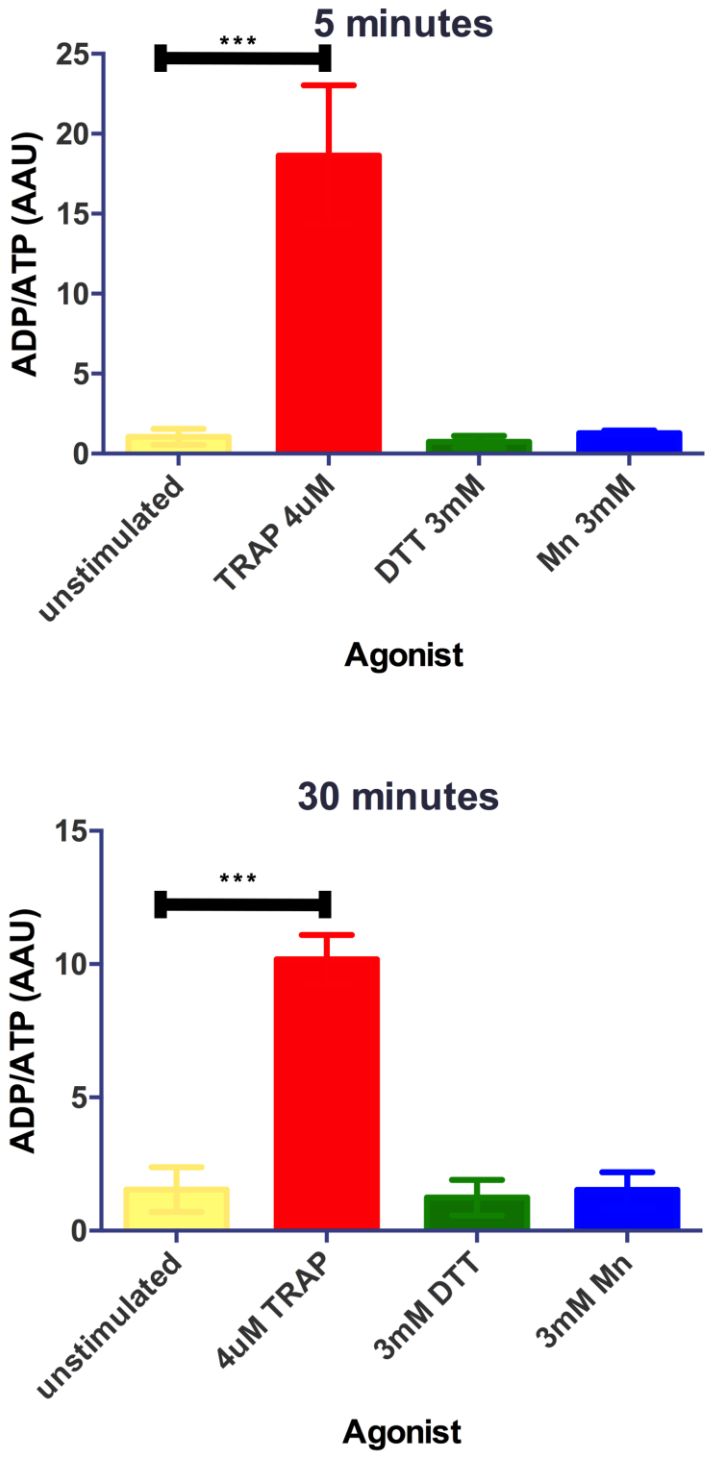

Figure 32: DTT and Mn^{2+} fail to cause dense granule release. ATP secretion after 5 minutes (top) and 30 minutes (bottom) in unstimulated platelets as well as in platelets stimulated with TRAP, DTT and Mn^{2+}. ATP release in unstimulated platelets is shown in yellow. TRAP at 4 µM (red) was sufficient to bring about ATP release. Both DTT at 3 mM (green) and Mn^{2+} at 3 mM (blue) did not lead to ATP release. This was confirmed by ANOVA analysis and a post-hoc Bonferroni test. Standard deviation was used to represent the error. (n=3, where n is the number of different donors)

As a whole these results show the complexity of the platelet response to physiological and non-physiological agonists. In the literature DTT and Mn^{2+} are widely described as integrin activators, with recognition that Mn^{2+} is a weaker integrin agonist. Our results show that while DTT and Mn^{2+} do share some similarities with TRAP-mediated activation, they do not not accurately replicate physiological activation particularly with regards to a whole platelet response. For example, DTT and Mn^{2+} failed to lead to either alpha or dense granule secretion.

Platelet aggregometry experiments show that all three agonists, TRAP, DTT and Mn^{2+} were capable of supporting platelet aggregation, with some reservations. For example, DTT appears to possess a concentration dependent lag-phase, while Mn^{2+} required additional fibrinogen to be added to washed platelets so that aggregation was readily apparent, testament to its description as a weaker integrin activator than DTT.

Moving attention to direct probing of the $\alpha_{IIb}\beta_3$ protein, all three activators lead to varying degrees of PAC-1 binding indicating that some degree of structural changes had occurred in $\alpha_{IIb}\beta_3$. As such, all three activators would be expected to lead to fibrinogen binding as measured with a labelled fibrinogen molecule in OgFg. On the contrary, only TRAP and DTT facilitated this binding. This again highlights Mn^{2+} as a weaker integrin activator.

Given that PAC-1 binding occurred in all three cases showing some degree of conformational changes in $\alpha_{IIb}\beta_3$ it could perhaps be expected that outside-in signalling would be the expected downstream result, perhaps mediated by tail separation within the integrin protein. Physiologically this outside-in signalling strengthens the platelet aggregation response. Therefore, it was hoped that these agonists could mobilise a downstream whole-cell response. To detect whether a whole cell response to DTT and Mn^{2+} was occurring, two granule release assays were used,: (1) P-selectin membrane presence indicative of alpha granule release, and (2)

ATP release assay to indicate dense granule release. In both assays the artificial agonists failed to mobilise a whole-platelet response via their influence on integrin conformation. This is in contrast to the TRAP-mediated response, a positive control, which does not act directly on the $\alpha_{IIb}\beta_3$ protein but rather via the thrombin receptor. This may indicate that DTT and Mn^{2+} activation of integrin is not sufficient to induce a full outside-in signalling response or perhaps only partial outside-in signalling occurs. For example, it is possible that prior inside-out activation is a requirement for later outside-in activation, whereby protein machinery is primed and localised at the cytoplasmic tails of $\alpha_{IIb}\beta_3$. Alternatively, the results may indicate that granule release is not an attribute of outside-in signalling but rather is confined to the earlier stages of the physiological platelet activation response. Nonetheless, the fact that DTT and Mn^{2+} are capable of bringing about some degree of positive activation response in $\alpha_{IIb}\beta_3$ brings hope to the future use of these agonists in our upcoming platelet-free, $\alpha_{IIb}\beta_3$-reconstituted systems.

3. Integrin in GUVs

3.1. Introduction

3.1.1. Liposomes

Due to the complex nature of cell membranes, it is frequently better to examine transmembrane proteins in a simplified artificial lipid model. With varying degrees of complexity, these systems seek to recreate the physiological conditions of the cell membrane. The systems may make use of a wide range of lipids (phospholipids, cholesterol, sphingomyelin, etc.) and may also include any number of membrane-incorporated proteins. A number of different systems exist to accomplish this and we can roughly divide these systems into two categories; supported lipid bilayers and liposomes. While supported lipid systems are covered in chapter 4, this chapter focuses on liposomes. Liposomes are quasi-spherical lipid vesicles composed of a lipid bilayer. Such lipid vesicles may be created in a range of sizes as well as morphologies (unilamellar or multilamellar). The nomenclature of these vesicles varies from paper to paper but generally unilamellar vesicles with a diameter of less than 50 nm are referred to as SUVs, those with a diameter of a micron or above are categorised as GUVs. Vesicles that fall between these two classifications are referred to as LUVs. Lipid vesicles have been used for a diverse range of applications including use in drug delivery[125], the study of membrane proteins in biologically-relevant conditions[126] as well as their use in lipid bilayer assembly.[127] One of the main advantages of liposomes over SLB systems is the fact they are free-standing structures meaning that they are not subjected to the same frictional and non-specific lipid-substrate interactions that occur in SLB models. To create liposomes a variety of protocols are available, each with their own advantages and disadvantages. For example, sonication is a commonly used method to create SUVs via the disruption of a multilamellar vesicle (MLV) suspension using a tip or bath sonicator.[25] Extrusion is mechanical process by which an MLV containing solution is forced through a porous membrane of a defined pore diameter in order to create unilamellar vesicles (SUVs or LUVs) of a desired size.[128] These vesicles may be

increased in size by the fusion of vesicles to form GUVs. This can be promoted by the addition of calcium.[129] Dehydration-rehydration is a simple GUV creation method that takes advantage of the fact that dried lipid bilayers may spontaneously form liposomes upon rehydration.[130] In a related technique, an electric field can be used to promote such vesicle swelling, in a process known as electroformation.[131] These procedures and various others combine to create a wide range of possible methods to create vesicles of different size distributions. (Figure 33)

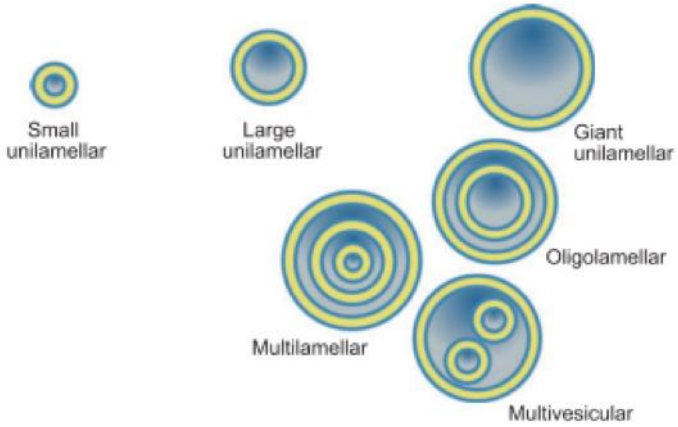

Figure 33: Vesicles can be divided into various populations based on their size and morphology. There are no strict definitions of what constitutes these descriptions and the nomenclature various from paper to paper.[125] Throughout this thesis SUVs refers to vesicles with a diameter below 50 nm, GUVs refers to vesicles with a diameter of above one micron, while LUVs refers to vesicles with a diameter between these two definitions.

3.1.2. $\alpha_{IIb}\beta_3$ reconstitution in the literature

A review of the literature shows that prior to this work, papers that use $\alpha_{IIb}\beta_3$ in artificial lipid systems share a number of common characteristics; namely the limited use of free-standing GUV systems, the use of FRAP for diffusion measurements, and the use of a limited range of lipid compositions.[29–31,34,43,44,46,47] The vast majority of papers that have reconstituted $\alpha_{IIb}\beta_3$ in artificial lipid systems have done so in planar SLB systems rather than free-standing GUV systems.[29–31,34] Indeed, prior to this work, no diffusion-based experiments had been performed in vesicle systems. Due to this limitation these pieces of literature were limited by the problems normally

associated with planar bilayers such as non-specific interaction between the lipid/protein and the underlying substrate. For example, Erb *et al.* reported that in its un-clustered form approximately 40 % of the reconstituted $\alpha_{IIb}\beta_3$ was immobilised on a glass substrate.[30] In order to eliminate these difficulties some papers have incorporated polymer cushions into their systems in order to improve $\alpha_{IIb}\beta_3$ mobility. Goennenwein *et al.* reported that $\alpha_{IIb}\beta_3$ was completely immobilised on the substrate in the absence of surface modification. The addition of a cellulose cushion to the substrate was required for protein mobility, yet up to 75 % of the $\alpha_{IIb}\beta_3$ remained immobile.[31] Purrucker *et al.* used a variety of polymers to decouple the bilayer from the substrate. Even so they stated that between 76 and 84 % of reconstituted $\alpha_{IIb}\beta_3$ remained immobile.[43,44] One of the biggest advantages to GUV systems is their free-standing nature. It was, therefore, hoped that successful reconstitution of $\alpha_{IIb}\beta_3$ into GUVs would alleviate these major drawbacks that exist in other works.

Prior to this work, all diffusion-based measurements of $\alpha_{IIb}\beta_3$ in artificial lipid systems have used FRAP as the investigative method. Here we sought to utilise the single molecule techniques, FCS and FLCS, to gain diffusion data. In contrast to FCS and FLCS, FRAP uses much larger volumes, typically several μm^3 for its measurements. An intense laser pulse photobleaches the fluorescent probe within this large volume before the recovery of fluorescence is monitored as labelled lipid molecules diffuse into the bleached area. Our use of FCS and FLCS has a number of advantages over FRAP. For example FCS/FLCS is non-destructive to the fluorescent molecules in the sample, can be readily used in multicolour experiments, and can be used to infer additional data about the sample such as probe concentration and kinetic data.[48] This data can be extremely useful in a number of ways. For example, the alpha value allows for the determination of whether a molecule undergoes Brownian diffusion or not. An alpha value of 1 represents this unhindered diffusion. A value below 1 shows anomalous hindered sub-diffusion while a value above 1 shows super-diffusion. Additionally, the fact that FCS/FLCS experiments provide a direct means of measuring probe concentration means that integrin concentration within GUVs can be measured, something not possible in FRAP. Another major

advantage of FCS/FLCS over FRAP is the requirement for much lower concentrations of fluorophore in the sample. This reduces any influences exogenous agents may have on the dynamics of the lipid membrane. Finally, the femotolitre volume required for FCS/FLCS is well suited to the curvature of GUV bilayers when compared to the large volume required in FRAP.[49] Erb, Goennenwein and Purricker all utilised FRAP to report their diffusion data.[30,31,43,44] Therefore to the best of our knowledge this is the first work to use the single molecule techniques of FCS and FLCS in $\alpha_{IIb}\beta_3$ focused experiments.

As previously mentioned, another striking feature of the literature is the use of a very limited number of lipids in artificial systems. The vast majority of papers utilise DMPC as a major component in artificial lipid systems. Beginning with Müller *et al.*, it was highlighted that $\alpha_{IIb}\beta_3$ had a tendency to strongly bind to the vesicle surface in large aggregates depending on the method of insertion and vesicle composition. Müller only reported full insertion, as determined by electron microscopy, for DMPC and DMPC:DMPG (1:1) mixtures. The use of other compositions lead to non-insertion or "partial" insertion.[34] This was later advanced upon by Erb and Engel where they stated that various combinations of POPC, POPE, POPG and POPS did not lead to good $\alpha_{IIb}\beta_3$ reconstitution. They also reiterated the need for DMPC or DMPC/DMPG in order to ensure full insertion.[29] Owing to this issue, the available literature that has presented diffusion data on $\alpha_{IIb}\beta_3$ has utilised DMPC and DMPG[30,31] or an asymmetric bilayer of DMPC/DMPG (1:1) and SOPC.[43,44] More recent pieces of literature that stray from the assertion that DMPC is an absolute requirement for full $\alpha_{IIb}\beta_3$ reconstitution, for example Sloan[47] (60 % egg PC, 15 % bovine PS, 25 % cholesterol) and Streicher[46] (85 % egg PC, 10 % egg PA, 5 % DPPE-PEG2000), perhaps somewhat tellingly did not perform any diffusion-based measurements, nor did they perform any cryoelectron experiments to verify that the integrin protein was bilayer inserted and not simply bilayer associated. Given $\alpha_{IIb}\beta_3$'s propensity to strongly associate with the membrane to give the impression of insertion, on the basis of the data they presented it is difficult to strongly state that their respective reconstitution protocols were successful. Therefore this work

sought to be first to characterise reconstituted $\alpha_{IIb}\beta_3$ diffusion in a DMPC-free system.

In contrast to this existing literature, we wanted to reconstitute $\alpha_{IIb}\beta_3$ into more physiologically-relevant lipid compositions that aimed to better mimic the platelet membrane. Then, in these GUVs, we sought to determine the diffusion co-efficient of the reconstituted protein in its un-activated, DTT activated, Mn^{2+} activated, and ligand bound forms, as well as to determine whether we could initiate activation dependant clustering of the integrin molecules. The use of free-standing vesicles was hoped, would eliminate non-specific interaction between the substrate and bilayer that hinders existing SLB work. To obtain the diffusional data, we wanted to utilise the single molecule techniques of FCS/FLCS, in contrast to the use of FRAP within the literature. Finally, in novel work, we wanted to utilise confocal microscopy to determine whether $\alpha_{IIb}\beta_3$ preferentially partitioned into the phospholipid rich disordered phase or cholesterol rich ordered phase of raft-forming GUVs.

Table 6: A summary of integrin $\alpha_{IIb}\beta_3$ diffusion in artificial lipid systems. So far diffusion measurements have only been performed in SLBs. As such, a massive percentage of the protein has been rendered immobile, even when polymer cushions were utilised. The $\alpha_{IIb}\beta_3$ that was not rendered immobile diffuses relatively slowly when compared to free-standing lipid systems such as our GUVs.

Paper	Composition	Integrin Diffusion ($\mu m^2/s$)	Percentage of immobile integrin	Notes
Erb *et al.* (1997)[30]	DMPC/DMPG	0.70	40 %	First diffusion measurements for $\alpha_{IIb}\beta_3$. Fibrinogen addition lead to decreased diffusion and increased immobility
Goennenwein *et al.* (2003)[31]	DMPC/DMPG	0.60	75 %	Contrary to Erb, $\alpha_{IIb}\beta_3$ was completely immobile on bare substrate. A cellulose cushion was required for $\alpha_{IIb}\beta_3$ diffusion
Purrucker *et al.* (2004)[43]	Asymmetric bilayer of DMPC/DMPG and POPC	0.03	80 %	A polymer tether used for $\alpha_{IIb}\beta_3$ diffusion. Very slow diffusion recorded
Purrucker *et al.* (2007)[44]	Asymmetric bilayer of DMPC/DMPG and POPC	0.08 – 0.13	76 – 84 %	A different polymer tether used for $\alpha_{IIb}\beta_3$ diffusion. Again very slow diffusion recorded

3.1.3. Proteoliposome Preparation

Throughout this thesis a number of techniques were used to create vesicles of varying sizes. SUVs were generally formed via sonication while LUVs were formed

via extrusion. Generally, these sub-micron size vesicles were not directly experimented upon but were rather used as the target during membrane protein reconstitution. In the literature a number of different reconstitution techniques exist and can be roughly divided into four different strategies; mechanical, freeze-thawing, use of organic solvents, or detergent-mediated reconstitution. In this work we primarily used detergents to reconstitute integrin in lipid vesicles. The basic premise for this is destabilisation or partial destabilisation of liposomes using a detergent, the addition of a membrane protein to this mixture and the subsequent removal of this detergent to leave behind protein-incorporated vesicles, or proteoliposomes.[37] We used two different techniques to create integrin-containing proteoliposomes. The first method was based on work by Müller *et al.*[34], and used triton x-100 to fully solubilise liposomes before $\alpha_{IIb}\beta_3$ was added and the detergent was quickly removed via the addition of detergent-absorbent beads. The second method was based on work by Moses *et al.*[27], and used β-OG (Octyl-beta-Glucoside) to partially solubilise liposomes before $\alpha_{IIb}\beta_3$ was added and the detergent was slowly removed by dialysis. Both of these techniques appeared to successfully produce proteoliposomes although the Erb method was preferred due to its speed.

In order to use confocal microscopy and FLCS measurements we required vesicles in the micrometre range so that the liposomes were easily resolved. We examined a number of ways to produce these GUVs: calcium induced fusion of smaller vesicles, dehydration and subsequent rehydration of a dried lipid film, gentle hydration of a lipid film to swell giant vesicles and finally, electroformation. Each of these techniques had their own advantages and disadvantages. For example, it was found that both calcium-induced fusion and gentle hydration regularly produced multilamellar vesicles as opposed to the unilamellar vesicles we sought to produce for microscopy experiments. The dehydration-rehydration protocol was sometimes successfully used to create GUVs but the protocol was unreliable and only produced surface tethered vesicles. In the end it was found that electroformation was the most reliable method of routinely producing GUVs. Electroformation is a technique used to produce a relatively monodisperse population of giant (20 µm plus) unilamellar vesicles. The protocol utilises an electric field to “grow” GUVs from lipid

deposited on a solid surface. This solid surface functions as the working electrode and normally takes the shape of either a platinum wire/sheet or ITO coated glass. The technique was first used by Angelova and Dimitrov in the 1980s to produce GUVs using a DC electric field.[131] This protocol was later updated to produce GUVs using an AC electric field.[132] The basic premise of this technique sees lipid in chloroform, or sometimes a mixture of chloroform and methanol, deposited on the electrode surface. A counter electrode is positioned perpendicular to the electrode and a cell is assembled around the two conductors. (Figure 34) This cell is then filled with buffer before an electric field is applied between the two electrodes. Over the course of a number of hours, the lipid begins to form GUV "nests" where hundreds of GUVs congregate. These GUVs often remain tethered to the electrode surface until removal via mechanical agitation or the use of a low frequency electric field. The exact mechanism of GUV formation is unknown, but according to Politano *et al.*, the process involves both bilayer separation and bending. To initiate bilayer separation of the deposited lipid film electrostatic and osmotic forces are believed to play a key role. This allows for the transport of water molecules between the stacks of lipid films driven by the electric field. Secondly, defects in the lipid films due to the irregular stacking of bilayers contribute to bilayer bending. These defects expose the hydrophobic interior of the bilayers to the aqueous buffer stressing the film to correct this by bulging outwards. These bulges swell further into the tethered GUVs.[133] Most electroformation protocols in the literature have been limited to GUV creation in salt-free buffers, however more recent adaptions have been made to the electroformation protocol to allow for GUV growth in a salt-containing buffer. This particular upgrade to the standard electroformation was developed by Pott, Bouvrias and Méleard and allows for the electroformation of GUVs in electrolyte-containing buffers.[134,135] While not as reliable as the standard electroformation method we found this adaption particularly useful given the fact we were dealing with membrane-reconstituted proteins throughout much of the experimentation process. By combining the aforementioned proteoliposomes reconstitution processes and the electroformation technique a protocol was developed that used the proteoliposomes solution as the lipid source for GUV growth. This allowed for the production of GUVs from a variety of lipid compositions where integrin $\alpha_{IIb}\beta_3$

was successfully reconstituted within. These $\alpha_{IIb}\beta_3$ containing GUVs were then used to explore protein and lipid diffusion, ligand binding, protein aggregation and protein partitioning.

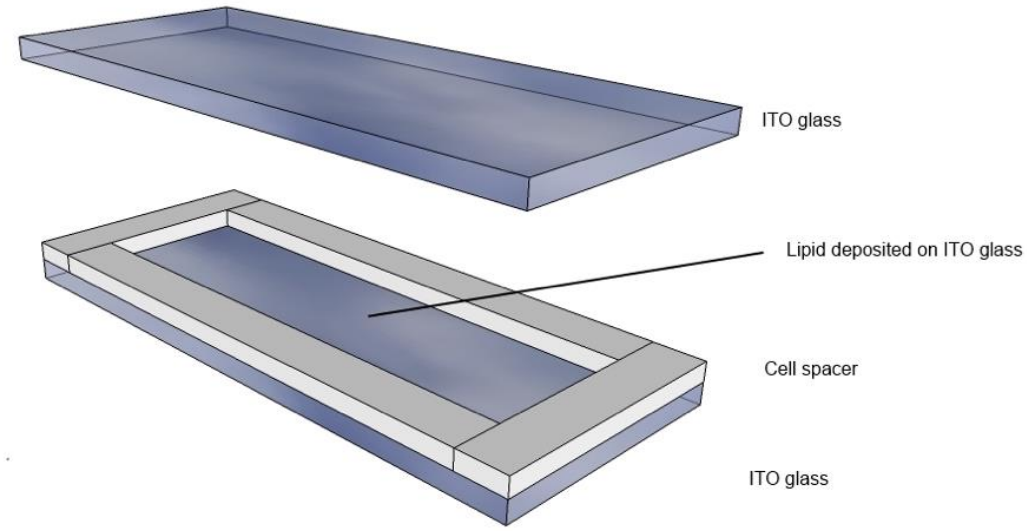

Figure 34 Assembly of the electroformation cell. Two ITO-coated slides are positioned a number of millimetres apart with the conductive side facing each-other. Dried lipid is deposited on one or both of the conductive faces. The slides are separated by a cell spacer which takes the form of a non-conductive material such as PDMS or a rubber O-ring. The cell is filled with buffer before being sealed. An electric field is then applied between the ITO glass slides for a defined period of time to allow for GUV growth.

3.2. Experimental

3.2.1. Multilamellar Vesicle (MLV) Creation

MLVs were prepared by the hydration of a lipid film. Firstly, lipid in chloroform (or in the case of DMPG, chloroform: methanol in the ratio 3:1) was evaporated in a glass vial under a steady stream of N_2. The lipid was then placed under vacuum for at least 2 hours to fully ensure solvent removal. To rehydrate the lipid film, Tris buffer (10 mM Tris, 150 mM NaCl, 1 mM $CaCl_2$, pH 7.4) or HEPES buffer (10 mM HEPES, 150 mM NaCl, 1 mM $CaCl_2$, pH 7.4) was warmed to a number of degrees above the highest phase transition temperature present in the lipid composition before being added to the vial. The lipid suspension was left to stand above the highest phase transition temperature for at least 45 minutes with occasional vortexing.

3.2.2. Small Unilamellar Vesicle (SUV) creation

In order to prepare SUVs, the sonication method was utilised. This process began with the preparation of MLVs via the hydration of a lipid film as described above. The probe of a tip sonicator (Heat Systems Ultrasonic model W350 Sonicator) was positioned into the MLV containing solution and using a predefined protocol, the solution was subjected to sonication for 20 minutes. The solution was kept in an ice bath throughout to prevent over heating of the solution which may occur to sonication. During the sonication process, pieces of the titanium probe may break off and as such, the solution was subjected to centrifugation. Centrifugation occurred at 72,000 rpm for 25 min at 15°C in a Beckman TL100 centrifuge (using a TLA100.3 rotor). This centrifugation step also removes larger vesicles that have not been successfully broken down in the sonication step.

3.2.3. Large Unilamellar Vesicle Creation

LUVs were prepared by extrusion using the Avanti mini-extruder extruder (*Avanti Polar Lipids, Alabaster, AL*). Two filter supports were pre-wetted with dH_2O and placed over the orifice of a Teflon internal membrane support. The internal membrane support was placed into the extruder outer casing with the filter supports facing upwards. A polycarbonate membrane with a pore size of 100 nm was placed on top of the filter supports. A second pair of filter supports was pre-wetted as before and placed over the orifice of the second Teflon internal membrane support. The internal membrane support was then placed face down on top of the polycarbonate membrane so that the polycarbonate membrane was separated by two filter supports on either side. A Teflon bearing is then placed into the retainer nut and the retainer nut was then tightened on the threaded end of the extruder outer casing. This was done by hand to ensure that the nut is not over-tightened. The extruder outer casing with retainer nut is placed into the supplied heating block and heated at least 5°C above the phase transition temperature of all lipids present in the lipid composition. A schematic of the extruder assembly is shown below. (Figure 35) MLVs, prepared using the film hydration method previously described, were first loaded into one of the gas-tight syringes and carefully place into one end of the mini-extruder. The second gas-tight syringe, with the plunger fully engaged, was placed into the opposing end of the mini-extruder. The lipid in buffer was then passed through the polycarbonate membrane in order to fill the other syringe. This was done a total of eleven times so that the final sample was collected from the originally empty syringe. The vesicles were then examined by DLS to evaluate the size distribution of the LUVs.

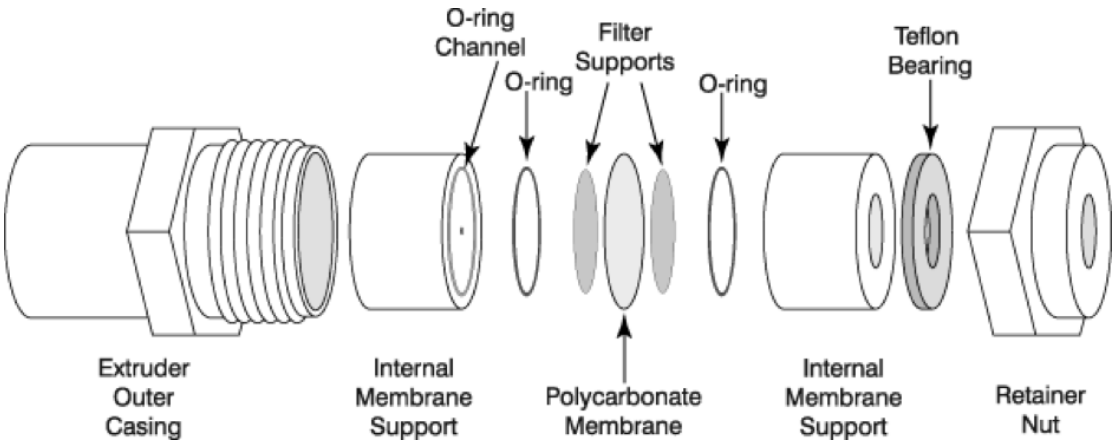

Figure 35: Assembly of the mini-extruder. The polycarbonate membrane of required pore size is place between two Teflon supports and enclosed in a metal outer casing as shown. The lipid composition of choice in Tris or HEPES buffer is passed through the polycarbonate membrane a number of times using two syringes to create vesicles of a required diameter. To confirm vesicle size, DLS was used. Figure adapted from Avanti Polar Lipids.[136]

3.2.4. Giant Unilamellar Vesicle (GUV) creation in salt free buffer

GUVs were created using the Vesicle Prep Pro (VPP) (*Nanion Technologies, Munich, Germany*) or a homemade conductive cell composed of two ITO slides separated by a PDMS spacer connected to a function generator and oscilloscope. Lipid in chloroform at 5mM was placed on the conductive sides of a pair of ITO glass slides in a number of 2 µl droplets. Depositing lipid at higher concentrations or larger droplet sizes appeared to reduce the final yield of GUVs, perhaps owing to over-stacking of lipid layers. The organic solvent was allowed to evaporate at room temperature for 45 minutes before the electroformation cell is assembled. The cell was filled with dH_2O, or 100mM sucrose in dH_2O if required for later imaging. As soon as the cell was filled with buffer the voltage was applied to prevent spontaneous swelling. This voltage was ramped up over 10 minutes from 0V to 3V and held at this amplitude for another 125 minutes before being ramped down to 0V over a 3-minute period. The frequency was held constant at 5 Hz throughout. (Figure 36) The protocol was carried out at 37 °C. This entire process was controlled by the *VesicleControl*

software supplied with the Vesicle Prep Pro (VPP), or manually when using the homemade cell.

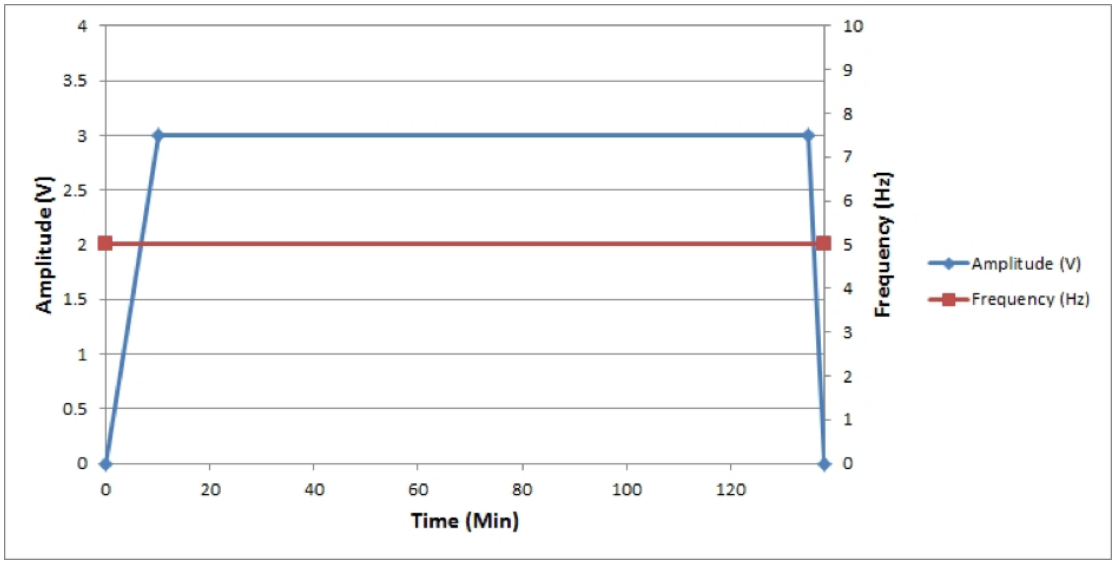

Figure 36: Amplitude and frequency profile over time of a standard electroformation protocol. The protocol runs for 128 minutes with the frequency held constant at 5 Hz throughout. The voltage varies during the experiment. The amplitude slowly ramps up to 3 V over the first 30 minutes. This ramping step is to avoid lipid shearing from the surface. This amplitude is then held constant for the next 125 minutes where the majority of the vesicle growth occurs. The final 3 minutes ramps the voltage back down to zero. If this step occurs to quickly, vesicle yield is reduced due to GUV destruction. The values and time-points used had been optimised to efficiently create GUVs from lipid deposited in chloroform.

3.2.5. GUV creation in physiological buffer

In order to perform electroformation in a high-salt buffer (greater than 10 mM total salt), the electroformation protocol was altered. After depositing the lipid mixture of interest (in a salt free buffer, with or without protein reconstitution) and partially dehydrating the composition, the cell was filled with a high-salt buffer and sealed. The voltage ramps up over 1 hour from 0 to 1.2 V, before remaining at this voltage for the next 13 hours. Importantly, these stages of the protocol took place at 500 Hz instead of between 2 and 12 Hz as normally associated with electroformation. The final stage of the protocol sees the voltage ramped down to zero over an hour. To begin with this step took place at 50 Hz as recommended in the literature[134,135], but

this step was later altered to remain at 500 Hz as better results were obtained at this frequency. (Figure 37) The protocol was carried out at room temperature.

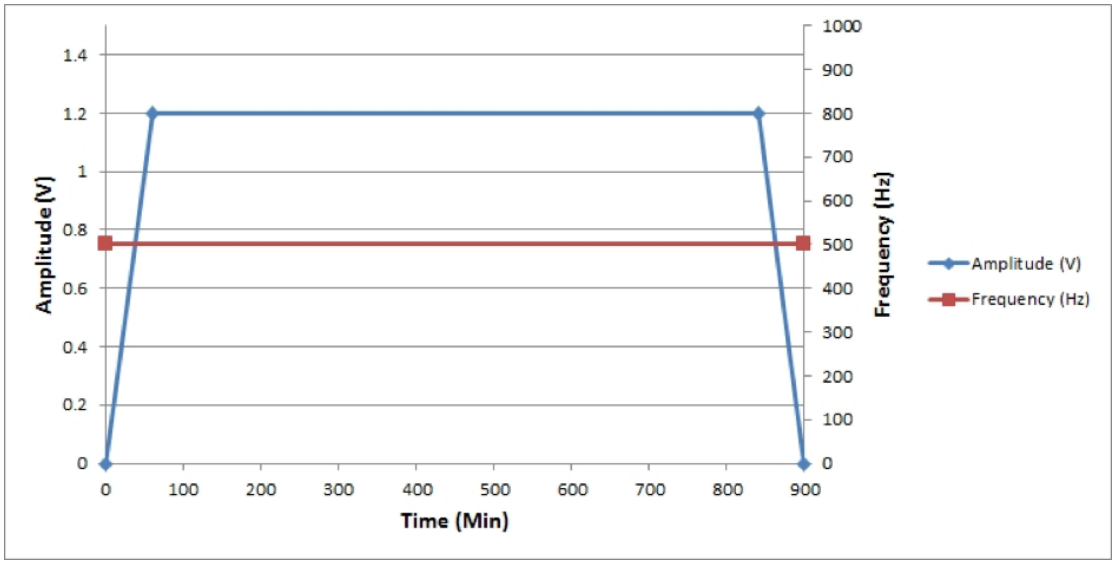

Figure 37: Amplitude and frequency profile over time of used to create protein-containing GUVs in a physiological buffer. This overnight protocol ramps the voltage to 1.2 V over the first hour where it remains constant for the next 13 hours. The last step ramps the voltage down over the final hour. The most important factor in producing GUVs in a high salt before is the use of an extremely high frequency when compared with standard electroformation protocols. 500 Hz was found to be optimal for such GUV formation.

3.2.6. Integrin reconstitution

A number of different protocols for $\alpha_{IIb}\beta_3$ reconstitution into liposomes were explored. Below are the 2 most commonly used methods for integrin reconstitution into liposomes. Both of these protocols yielded liposomes below the size associated with GUVs and therefore for microscopy work these proteoliposomes had to be converted to GUVs via electroformation.

Lentz β-OG-mediated insertion of integrin $\alpha_{IIb}\beta_3$ into liposomes

SUVs of the required composition were firstly created via sonication at a lipid concentration of 2 mg/ml in HEPES buffer. $\alpha_{IIb}\beta_3$ at 0.5 mg/ml in HEPES buffer with β-OG was added to the SUVs so that final concentration of β-OG was 20 mM. This optimal detergent concentration was determined experimentally by monitoring absorbance at 600 nm. Here, the partitioning of detergent into the bilayer of

liposomes until it saturates the liposomes causes an increase in turbidity which is reflected in the OD. As the liposomes begin to solubilise, the turbidity of the solution begins to decrease until the solution is optically transparent.[37] Due to the fact that detergent-saturated vesicles retain their structural integrity, the identification of the point where vesicles are fully saturated allows for efficient protein reconstitution without altering vesicle size. Using 20 mM β-OG, the detergent-lipid solution which was now at the onset of solubilisation was incubated at room temperature for 45 minutes to allow for the integrin-detergent micelles to fully partition into the SUV membrane. The removal of β-OG was facilitated via dialysis of the SUV-integrin-detergent mixture against a detergent free buffer of 500 times the sample buffer volume. The dialysis proceeded for 24 hours at 4 °C with one buffer exchange after 6 hours, and a second exchange after 18 hours. In order to determine whether the reconstitution was successful, reconstituted SUVs were firstly separated from free $\alpha_{IIb}\beta_3$ on a sephadex G-200 size exclusion column. The fractions were analysed for radiolabelled lipid (trace amounts of C^{14} DOPE) to determine which fractions contain the SUVs and then these lipid-containing fractions were run on a polyacrylamide gel to separate protein via its molecular weight. The gel was then stained with Coomassie brilliant blue for a number of hours to visualise any protein bands for each SUV-containing fraction.

Modified Erb Triton X-100-mediated insertion of integrin $\alpha_{IIb}\beta_3$ into liposomes

The initial protocol for the reconstitution of $\alpha_{IIb}\beta_3$ in a supported lipid bilayer was based on a method developed by Müller *et al*.[34] The desired lipids were firstly mixed and evaporated in a glass vial under a stream of nitrogen. The lipids were completely solubilised in a HEPES reconstitution buffer (10 mM HEPES, 150 mM NaCl, 1 mM $CaCl_2$, 0.1% Triton X-100 (w/v), pH 7.4) with a final detergent:lipid ratio of 2:1 (w/w). The final lipid concentration was normally 1 mM. $\alpha_{IIb}\beta_3$ in HEPES reconstitution buffer was then added to the detergent-lipid solution at the required concentration, normally 1 integrin molecule for every 8000 lipid molecules. The protein-containing solution was shaken at room temperature for 30 minutes to fully ensure that all lipid has been solubilised and that the solution was homogenous. The solution was then

incubated at 37 °C for 1 hour 30 minutes. Detergent was removed by the addition of 100 mg of biobeads per ml of solution for 3 hours 30 minutes in a slow shaken vial. The biobeads were then removed and replaced by a fresh batch of 100 mg biobeads per ml of solution for 30 minutes (slowly shaken). Flow cytometry was used to determine successful reconstitution of $\alpha_{IIb}\beta_3$ into liposomes. Proteoliposomes in the reconstitution buffer were pipetted into a FACS tube and incubated at room temperature with the anti-human CD41a antibody at a concentration of 0.1 mg/ml for 30 minutes. This antibody has affinity for both the resting and activated forms of $\alpha_{IIb}\beta_3$. The proteoliposomes were passed through the flow cytometer until 10,000 acquisitions had been acquired in a gated region that corresponds to the reconstituted vesicles. Data was analysed using CellQuest Pro software from Becton Dickinson or Flowing Software from Turku Bioimaging.

3.2.7. Proteoliposome conversion to GUVs

Instead of a lipid in chloroform solution normally used for deposition in standard electroformation protocols, proteoliposmes created from the β-OG-mediated insertion or the triton x-100-mediated insertion methods were used as the lipid source. However, due to the presence of salt in these proteoliposme containing buffers, direct electroformation was not possible. This was due to the osmotic shock that occurs when the lipid comes in contact with the electroformation buffer. Instead we required that the salt buffer be removed from the protein-containing vesicles. This was achieved through an ultracentrifugation step. Integrin-reconstituted vesicles were loaded into an ultracentrifuge tube and centrifuged at 100,000 g for 1 hour. This resulted in the pelleting of the protein-reconstituted liposomes. The supernatant was removed and the pellet was gently washed in dH_2O to eliminate any remaining salts. This pellet was then re-suspended in dH_2O at a lipid concentration of 10 mM. The re-suspended vesicles could then be stored at -20 °C for a number of weeks. When required, the solution was thawed and 2 µl droplets were placed on the conductive side of an ITO glass slide of the Vesicle Prep Pro. The slides were placed in a vacuum desiccator in the presence of a saturated sodium

chloride solution resulting in a relative air humidity of 73%. The lipid in buffer was left to partially dehydrate for between 2 and 20 hours. Once complete the electroformation cell of the VPP was assembled as before, filled 100 mM sucrose in HEPES buffer, and the electroformation protocol was started. In order to successfully create GUVs in a salt buffer the voltage was ramped up over 1 hour from 0 to 1.2 V, before being held constant at 1.2 V for 13 hours. This took place at 500 Hz in comparison to the frequency of between 2 and 12 Hz normally used for electroformation in a salt-free buffer. The voltage was then ramped down from 1.2 to 0 V over the final hour while the frequency was held constant at 500 Hz. The electroformation process was carried out at room temperature. This process was effective in yielding GUVs from a wide range of lipid compositions with $\alpha_{IIb}\beta_3$ successfully reconstituted within.

3.2.8. Integrin labelling

Integrin labelling with Atto655

In order to label $\alpha_{IIb}\beta_3$ with atto655 NHS ester, the probe (which was supplied in powder form) was re-suspended in DMF at 2 mg/ml. The integrin protein which is supplied in a Tris-based buffer (20 mM Tris, 100 mM NaCl, 1 mM CaCl2, 0.05% NaN3, 0.1% triton x-100 (w/v), 50% glycerol (v/v), pH 7.4) was dialysed into HEPES reconstitution buffer. This was necessary due to the fact that atto655 NHS ester is amine reactive. This buffer exchange was achieved via dialysis against 1000 times the original volume over a 24-hour period with buffer exchanges after 6 and 18 hours. For efficient labelling, the protein concentration should be above 1 mg/ml. The dialysis process may dilute the $\alpha_{IIb}\beta_3$ concentration and as such it may be necessary to concentrate the protein to above this threshold. Therefore, if required, $\alpha_{IIb}\beta_3$ was concentrated using centrifuge filter columns (Amicon® Ultra-4 Centrifugal Filter Units, 100 kDa cut-off). For labelling, $\alpha_{IIb}\beta_3$ was incubated with a five-fold molar excess of atto655 NHS ester for 3 hours. This occurred at room temperature under gentle stirring.

Integrin labelling with 5(6)-TAMRA SE

TAMRA labelling was achieved in a similar manner to atto655 labelling. Using $\alpha_{IIb}\beta_3$ at more than 1 mg/ml in a HEPES reconstitution buffer, 5(6)-TAMRA SE (in DMF at 2 mg/ml) at a five-fold molar excess is co-incubated for 1 hour at room temperature under gentle stirring. This was in contrast to the 3 hours used for atto655 labelling.

Separation of integrin from free dye

In order to separate labelled $\alpha_{IIb}\beta_3$ from unbound dye, size exclusion chromatography was used. Firstly, sepharose beads (Sephadex G-25) were left to swell overnight in dH_2O. These beads were then loaded onto a disposable column (20 ml Econo-Pac Chromatography Column) and the beads were allowed to pack tightly at the bottom of the column under gravity. Excess dH_2O was removed and more beads were added to the column until the packed beads filled the column entirely. Approximately 250 ml of HEPES reconstitution buffer was flushed through the column to equilibrate the beads. The labelled integrin solution was added to the top of the column where it begins to migrate through the beads. After a number of minutes two separate fluorescent bands can be resolved in the column. The first band was labelled protein as it migrates quickly through the beads. The second band was the unbound dye that moves slower through the beads. The column was flushed with detergent containing buffer throughout. The first band was collected and dialysed against HEPES reconstitution buffer for 24 hours to fully ensure all free dye had been removed.

Determination of labelling ratio

The degree of labelling (DOL) between dye and protein was obtained from the spectrum of the conjugated probe and the concentration of protein as determined by the Bradford assay or the 2-D Quant Kit assay. This is achieved after all free dye had been removed from the solution via size exclusion chromatography and dialysis. The concentration of bound dye was firstly determined by measuring the absorbance spectra of the solution in a 1 cm path length cuvette.

$$Molar\ concentration = \frac{A_{max}}{\varepsilon_{max}}$$

Where A_{max} is the absorbance of the dye at its absorption maximum (λ_{abs}) and ε_{max} is the extinction coefficient of the dye. The respective A_{max} and ε_{max} values for atto655 and TAMRA are given below. From this formula, the molar concentration of bound dye can easily be determined. Normally the concentration of protein can be determined via a similar method using absorbance at 280 nm (A_{280}), but due to the fact the detergent triton X-100 absorbs strongly in this region, an alternative method was used. For the determination of $\alpha_{IIb}\beta_3$-atto655 concentration, the 2-D Quant Kit assay method was used. For the determination of $\alpha_{IIb}\beta_3$-TAMRA concentration, the Bradford assay method was used. From these assays the molar concentration of labelled $\alpha_{IIb}\beta_3$ can be determined. As the molar concentration of dye is also known, the DOL was determined using:

$$DOL = \frac{molar\ concentration\ of\ dye}{molar\ concentration\ of\ protein}$$

3.2.9. Determination of protein concentration

Bradford Assay

To perform the Bradford assay, standard solutions were prepared by dissolving BSA in the required buffer at 2, 1, 0.5, 0.25, 0.125 and 0.0625 mg/ml, as well as a blank of buffer alone. Bradford reagents were prepared by added 20 µl of Bradford solution S to Bradford solution A to create A*. 25 µl of A* was added to each well of a 96 well plate where the experiment was to take place. 5 µl of each standard solution was added to separate wells alongside the unknown(s). The standard curve and unknowns were prepared in triplicate. The plate was incubated at room-temperature for approximately 15 minutes before absorbance was measured at 690 nm in a plate reader. Data was analysed in by plotting the standard curve and extrapolating the unknown(s).

2-D Quant Kit assay

To perform the 2-D Quant Kit assay, standard solutions were prepared using the BSA solution supplied with the kit. To the tubes 0, 5, 10, 15, 20 and 25 µl of the 2 mg/ml BSA solution were added. To another tube, 25 µl of the unknown was added. These tubes were prepared in triplicate. To each tube, 500 µl of precipitant solution was added before vortexing and incubation at room temperature for 2 minutes. 500 µl of co-precipitant solution was then added to each tube before an additional vortexing. The tubes were centrifuged at 10,000 g for 5 minutes in order to sediment the protein. The supernatant was removed without disturbing the protein pellet. 100 µl of copper solution was added to each tube and the volume was brought to 500 µl with the addition of dH_2O. The solution was briefly vortexed in order to re-suspend the protein. 1 ml of working colour reagent was added to each tube before mixing and incubation at room temperature for 20 minutes. The absorbance of each sample was read at 480 nm using dH_2O as a reference. By plotting the standard curve and extrapolating the unknown(s). It should be noted that in contrast to most protein assays, the absorbance of the assay solution decreases with increasing protein concentration.

3.2.10. Integrin detection in proteoliposomes

Flow cytometry was used to determine successful reconstitution of $\alpha_{IIb}\beta_3$ into liposomes. Proteoliposomes in the reconstitution buffer were pipetted into a FACS tube and incubated at room temperature with the anti-human CD41a antibody at a concentration of 0.1 mg/ml for 30 minutes. This antibody has affinity for both the resting and activated forms of $\alpha_{IIb}\beta_3$. The proteoliposomes were passed through the flow cytometer until 10,000 acquisitions had been acquired in a gated region that corresponds to the reconstituted vesicles. Data was analysed using CellQuest Pro software from Becton Dickinson or Flowing Software from Turku Bioimaging.

3.2.11. Confocal Microscopy of GUVs

For confocal microscopy studies, a fluorescent probe was included in lipid compositions at 0.1 % (mol/mol). Two fluorescently labelled lipids that were routinely used in these studies were DOPE-BODIPY and DOPE-atto655. Alternatively, the lipophilic tracer dyes DiL (excitation max 549 nm) or DiD (excitation max 644 nm) were used. These lipophilic tracer dyes were particularly useful to identify domain-forming GUVs due to the fact they fail to fully partition into SM and CH rich rafts. In compositions that had lower concentrations of SM and CH they appeared to partition homogenously throughout the GUV bilayers.

A number of different methods were employed for observing GUVs prepared via electroformation. GUVs may be examined within their electroformation cell by using a 10x objective with a suitable working distance (due to the thickness of the cell glass). This allows for the observation of vesicle growth, helped by the fact that the first GUVs in electroformation may be hundreds of microns in diameter. Alternatively, GUVs may be removed from their cell and pipetted onto a borosilicate glass coverslip for observation. In this case, a 63x objective was normally used. To aid GUV observation it was generally advantageous to create GUVs in a sucrose-containing buffer before transfer to a glucose-containing buffer. This meant that the inner medium of GUVs was sucrose while the exterior medium was a mixture of sucrose and glucose. This yielded two benefits. Firstly, the difference in refractive indexes between the inner and outer mediums allowed for the ready identification of GUVs under light a light microscope. Secondly, the sucrose-containing GUVs fall to the bottom of solution thus making confocal imaging easier. Care was taken to ensure the glucose and sucrose mediums were of equal osmolarity. This was important as failure to do so resulted in the rupturing of GUVs due to the osmotic gradient. If the GUVs were not created in a sucrose-containing buffer, the continual movement of vesicles made microscopy experiments difficult. The image data was analysed with LSM image browser (Carl Zeiss, Germany) or ImageJ (National Institutes of Health, USA).

3.2.12. FLCS measurements

Diffusion coefficients for labelled integrin or lipid were obtained using Fluorescence Lifetime Correlation Spectroscopy, FLCS. The autocorrelation functions obtained using FLCS are less prone to noise and distortion caused by scattered excitation light, detector thermal noise and detector afterpulsing than conventional Fluorescence Correlation Spectroscopy (FCS). FLCS measurements were performed using a MicroTime 200 confocal fluorescence lifetime microscope system. For FLCS experiments, the fluorophores were excited as described for confocal imaging and the sample fluorescence was also collected as described for confocal microscopy. The autocorrelation functions (ACF) were fit using SymphoTime software (PicoQuant GmbH, Berlin, Germany):

$$G(\tau) = 1 + \left[\frac{1}{N}\right]\left[\frac{1}{1 + (\tau/\tau_D)^{\alpha}}\right]$$

For simple single component diffusion, or in the case of the presence of a triplet state:

$$G(\tau) = 1 + [1 - T + Texp(-\tau/\tau_T)]\left[\frac{1}{N(1-T)}\right]\left[\frac{1}{1 + (\tau/\tau_D)^{\alpha}}\right]$$

where G(τ) is the autocorrelation function of fluorescence fluctuations; N is the number of fluorophores in the effective volume; T is the fraction of the molecules in the triplet state; τ_T is the relaxation time for the singlet–triplet crossing; α is the anomalous parameter; and τ_D is the diffusion time, which is related to the lateral diffusion coefficient (D) of the labelled tracer by the expression:

$$\tau_D = \frac{\omega^2}{4D}$$

In the latter equation, the radius ω is the distance at which the excitation intensity profile decreases to e^{-2} of its maximum value. This parameter was determined

experimentally, by measuring the translational diffusion of Rhodamine 6G (532 nm laser) and Atto655 (640 nm laser) in water at room temperature (approximately 21 °C).[137] These dyes, have well characterized diffusion coefficients and so were used as standards to determine the working confocal volume for FLCS measurements. Before performing FLCS measurements on the GUV membrane, confocal images were collected to identify and locate suitable vesicles for study. In order to avoid the sharp curvature of smaller GUVs or undulations in larger GUVs, only single unilamellar vesicles with diameters within the range 20 and 40 μm were selected for FLCS measurements. This selection criteria was based on that recommended by Ramadurai *et al*.[53] To precisely locate the lipid bilayer of the liposome where FLCS measurements were to be taken, fluorescence intensity measurements were performed by Z-scanning near the GUV membranes until the site of maximum intensity was located. Point FLCS measurements were then recorded at these precise positions for up to 3 minutes. Throughout the measurement, the MCS trace was monitored to ensure that the GUVs remained stationary during FLCS recording. Recordings from GUVs that exhibited drift during the measurement were eliminated from the analysis.

3.3. Results

3.3.1. Electroformation

Before we attempted to create integrin-reconstituted GUVs we first needed to establish an easy and reliable method of GUV production. A number of techniques were explored for this reason, such as dehydration-rehydration, calcium-induced swelling and electroformation. Of these techniques, electroformation was chosen as the primary method GUV production method used throughout this work owing to its reliability and its high GUV yield. In following the literature, our first attempts to produce giant vesicles via this method used relatively simple unary or binary compositions such as pure DOPC or DOPC:DOPS (9:1). These compositions were chosen to first establish a reliable protocol for GUV production. It was found that by using a microscope objective with suitably long working distance we could use confocal imaging to observe the GUV growth within the cell of the electroformation cell of the vesicle prep pro. Due to the thickness of the ITO glass used in the electroformation cell only the 10x air objective was suitable for GUV observation during this growth phase. Upon initiation of the electroformation protocol all that was visible on the ITO glass was a thick layer of fluorescently-labelled lipid that had been deposited prior to the electroformation process. After about 45 minutes of the protocol the first GUVs began to become visible. Some of these vesicles were up to 1 mm in diameter and from these “parent” vesicles many smaller GUVs (20 µm to 100 µm in diameter) began to bud. A confocal image of this is shown in Figure 38. Over the length of the electroformation process the size of the parent vesicles reduces as more and more GUVs begin to bud. By the end of the protocol many thousands of GUVs are visible, clustered together in vesicle “nests” on the glass surface. A confocal image of this is shown in Figure 39.

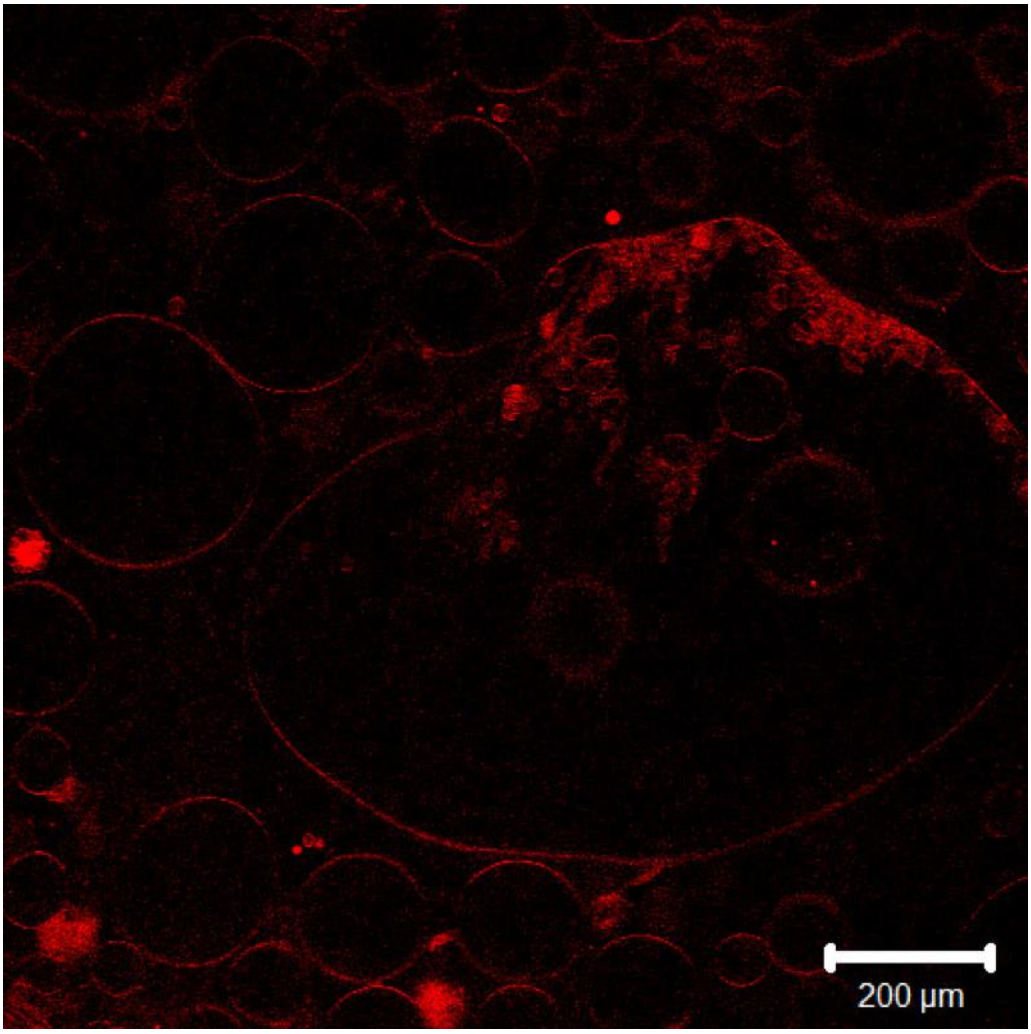

Figure 38: Confocal image of GUV growth during an electroformation protocol. After approximately 45 minutes, massive GUVs with diameter greater than 100 µm become visible. From these massive GUVs, smaller GUVs (diameter between 20 and 50 µm) begin to bud in vesicle nests. A 10x objective with a suitable working distance was used to observe GUV growth (DOPC) in the electroformation cell. DOPE-Atto655 was incorporated at 0.1 mol % and excited at 633 nm.

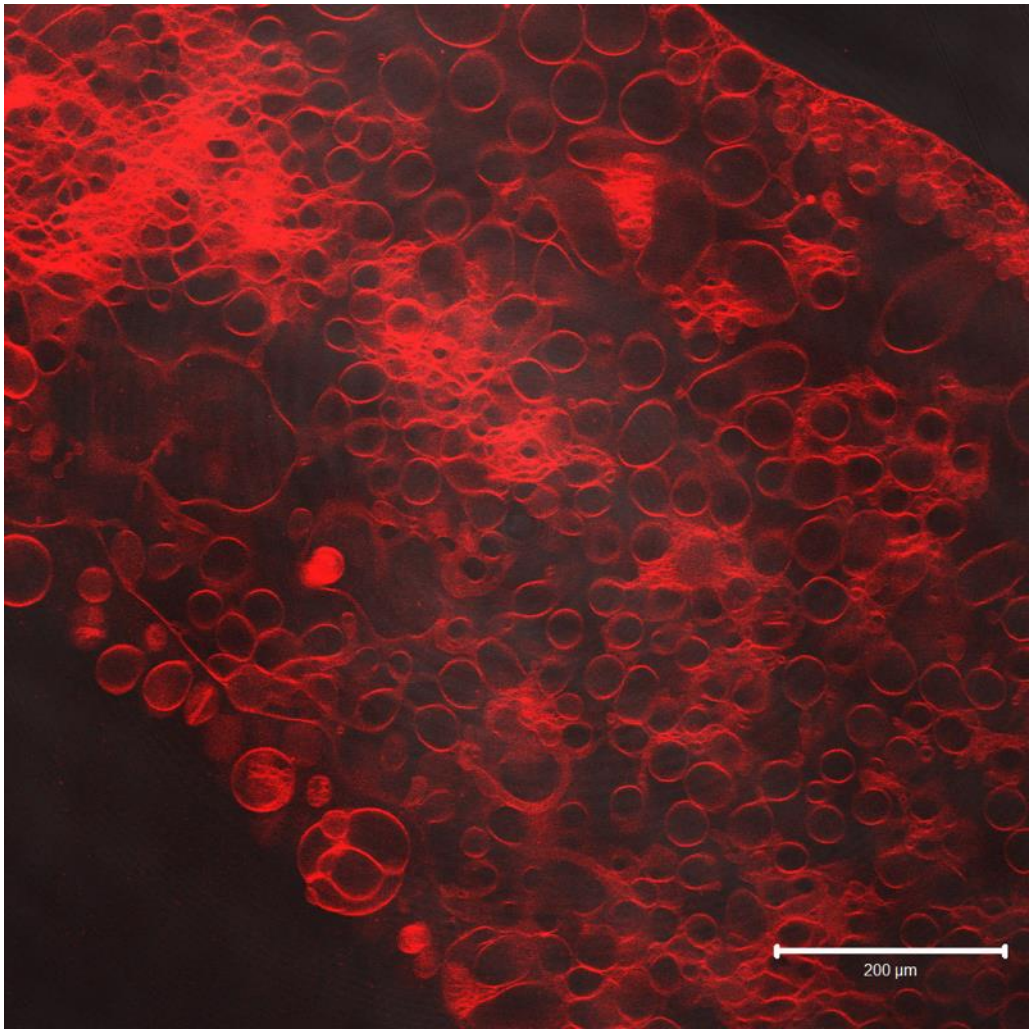

Figure 39: Confocal image of GUV growth near the end of an electroformation protocol. The massive GUVs originally observed in the electroformation protocol have been reduced in size after successive budding. These smaller GUVs have a diameter between 20 and 100 µm and occur clumped in vesicle nests. They are surface attached and require mechanical agitation or a lowering of the frequency of the electric field for removal from the surface. GUVs pictured are DOPC with 0.1 mol % DOPE-Atto655 and excited at 633 nm.

Once the electroformation process was complete these GUVs could be removed from the ITO surface by gently pipetting the solution up and down. It was noted that some of the larger GUVs visible within the electroformation cell appeared to be destroyed during the transfer process. The average diameter of the GUVs was approximately 30 µm although this value varied from batch to batch. It was also noted that GUVs created from cholesterol and sphingomyelin containing compositions appeared more polydisperese when compared to GUVs created purely from phospholipids. GUVs were stable for a number of days at 4 °C although due to

the ease of creation, new batches were generally created as required on a day-to-day basis.

As mentioned previously, initial electroformation experiments used simple phospholipid mixtures to perform the GUV growth process as these compositions were the most widely used in the literature. It was only after a routine and reliable protocol for electroformation had been established that we looked to use more complex and physiologically-relevant compositions. The most widely used of these physiologically-relevant compositions applied throughout this thesis was adopted from the Lentz group at the University of North Carolina at Chapel Hill. Titled "nature's own" this particular mixture has been regularly used by the Lentz group in their work to better model the cell membrane. Previously the Lentz group had only used nature's own in their sonicated SUV work and due to the fact that such complex compositions were not regularly used in the literature (most of the literature features quite simple unary or binary lipid composiitons,[138] although some may be ternary[139]) we first needed to establish whether the mixture was suitable for electroformation. Using the electroformation protocol we found that GUVs could be regularly formed using the nature's own composition. Examples of these electroformed GUVs are given in Figure 40 and Figure 41. As can be seen, the electroformation process allowed for the high-yield production of primarily defect-free, unilamellar giant vesicles which can be easily visualised by confocal microscopy. The conformation that nature's own could be successfully used to create GUVs was required before advancing the process to include a reconstituted membrane protein in the form of integrin $\alpha_{IIb}\beta_3$.

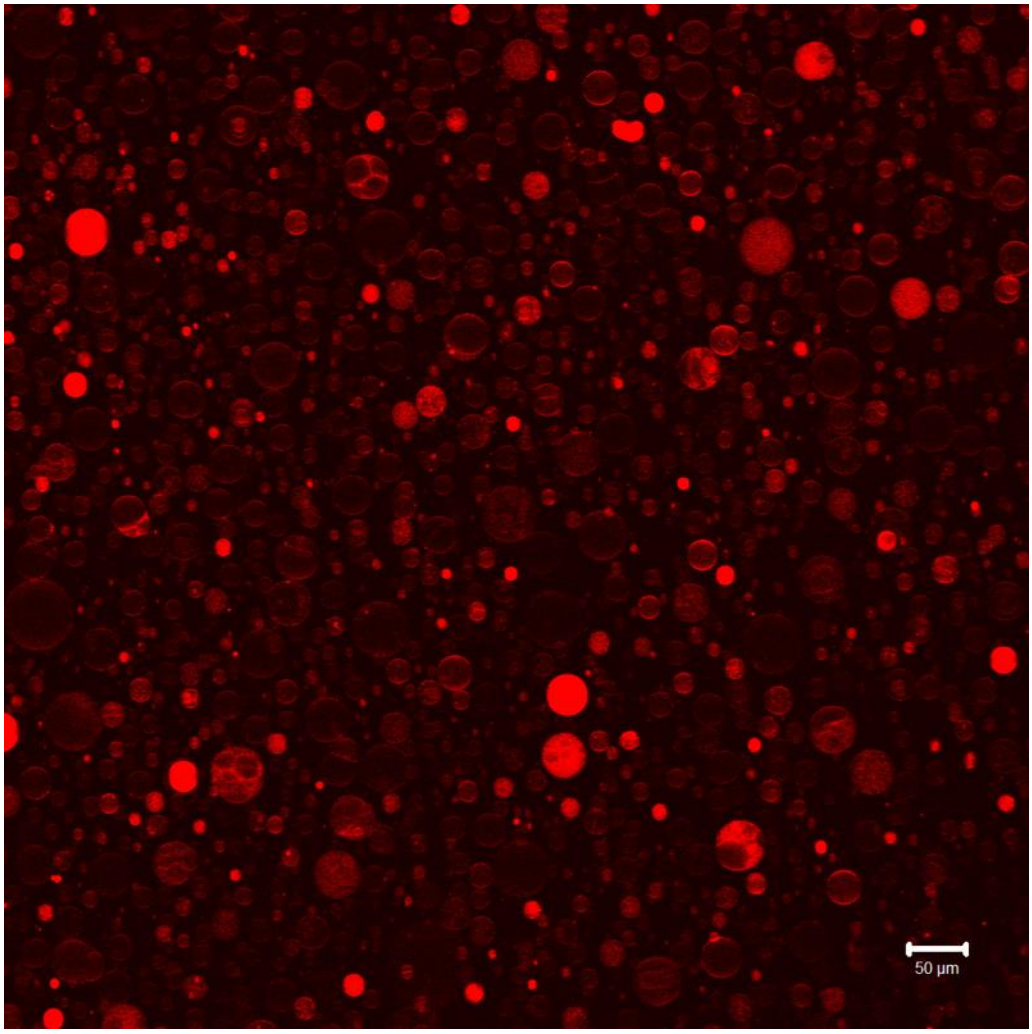

Figure 40: GUVs (32 % DOPC, 25 % DOPE, 8 % DOPS, 15 % SM, 25 % CH) following completion of the electroformation protocol and subsequent removal to a new surface. Many thousands of GUVs are created and these vesicles survive the mechanical agitation used to remove them from the electroformation cell. DOPE-atto655 was included at 0.1 mol % and excited at 633 nm.

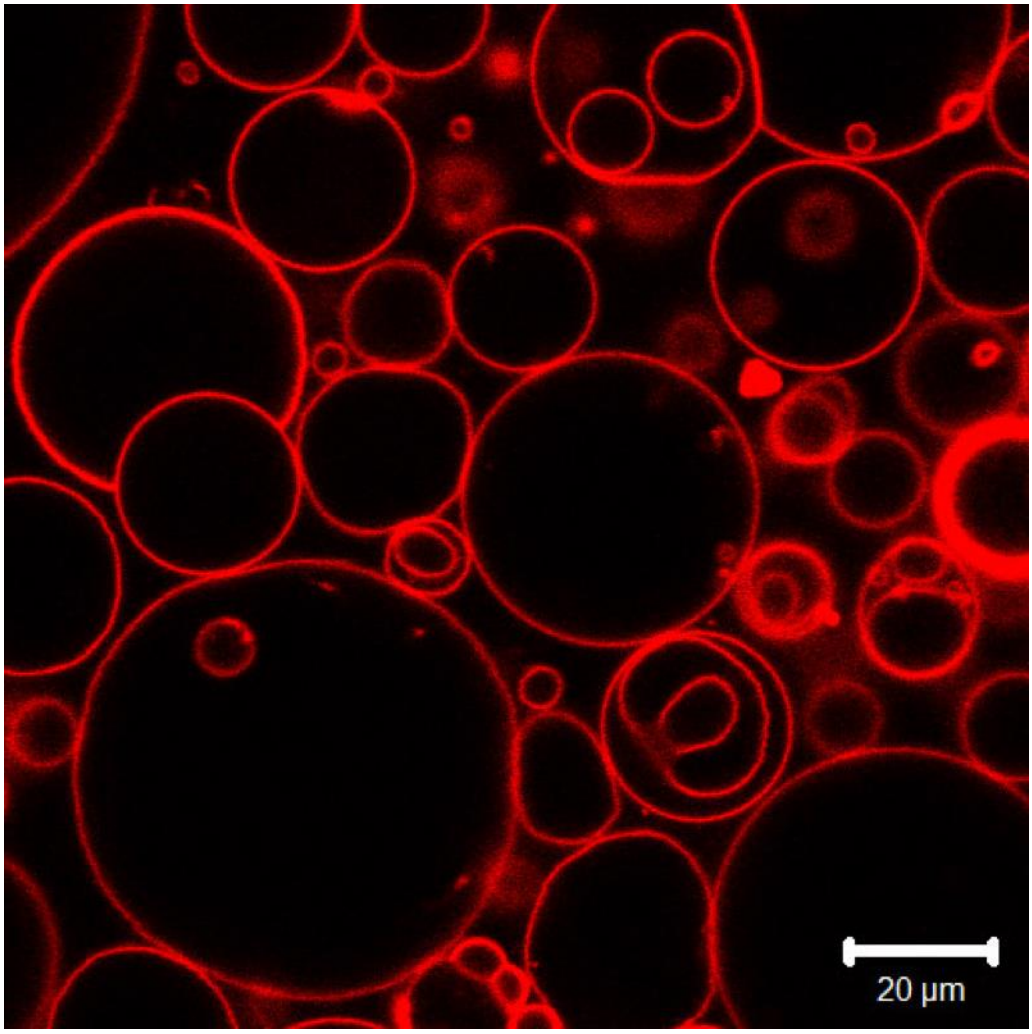

Figure 41: A close-up confocal image of GUVs (32 % DOPC, 25 % DOPE, 8 % DOPS, 15 % SM, 25 % CH) created via electroformation. The vesicles have been removed from the electroformation cell and transferred to new glass surface for imaging. The vast majority of GUVs are unilamellar. DOPE-atto655 was included at 0.1 mol % and excited at 633 nm.

3.3.2. Electroformation of raft-forming GUVs

Following on from the successful production of GUVs composed of both simple and physiologically-relevant lipid compositions, we later sought to create lipid raft-forming GUVs via electroformation. While physiologically, lipid rafts are believed to occur on the nanoscale, too small to be visible via confocal experiments, it is possible to create GUVs with microscale domains by using high concentrations of both cholesterol and sphingomyelin. We investigated a number of different cholesterol and sphingomyelin rich mixtures but one particular composition that was regularly used to form GUVs with large visible ordered and disordered phases

was the domain-forming DOPC:CH:SM (4:2:2) composition. By utilising this composition in conjunction with an appropriate lipid probe it was possible to visualise lipid rafts within GUVs via confocal microscopy.[140] For example we regularly used the lipophilic tracer dyes DiD and DiL in our lipid raft experiments. These particular dyes are known to favourably partition into the liquid disordered, phospholipid rich phase of domain-forming bilayers.[139] Figure 42 and Figure 43 show the successful production of domain-forming vesicles using the aforementioned DOPC:SM:CH (4:2:2) mixture where DiD was used as the disordered phase probe. The un-labelled regions of the GUV membranes correspond to the cholesterol and sphingomyelin-rich liquid ordered phases. As well as the aforementioned 4:2:2 ratio of DOPC:SM:CH, various other GUV compositions were explored in domain-forming experiments using different DOPC:SM:CH ratios. While many of these mixtures did produce raft-forming GUVs it was found that increasing the cholesterol concentration much above 30 % resulted in domains that were poorly defined by phase separating dyes. As well as the use of the disordered phase probes DiD and DiL we also attempted to utilise an ordered phase probe, DSPE-NBD, in order to visualise the lipid rafts directly. According to the supplier, Avanti Polar Lipids, DSPE-NBD "preferentially partitions, although not entirely, into the more ordered cholesterol and sphingolipid-enriched microdomain known as a lipid raft". However, using the raft-forming mixture DOPC:SM:CH (4:2:2) as well as other raft-forming compositions we were unable to visualise this preference for the liquid ordered phase of GUVs. However in our hands DSPE-NBD appeared to have no particular affinity for either liquid ordered and disordered phases. Thus the dye was evenly distributed throughout the GUV membrane. As such, for all our raft-forming GUV experiments we were limited to the use of liquid disordered phase probes. Nonetheless the ability to create raft-forming GUVs via electroformation was a promising basis before we attempted to reconstitute $\alpha_{IIb}\beta_3$ within such compositions.

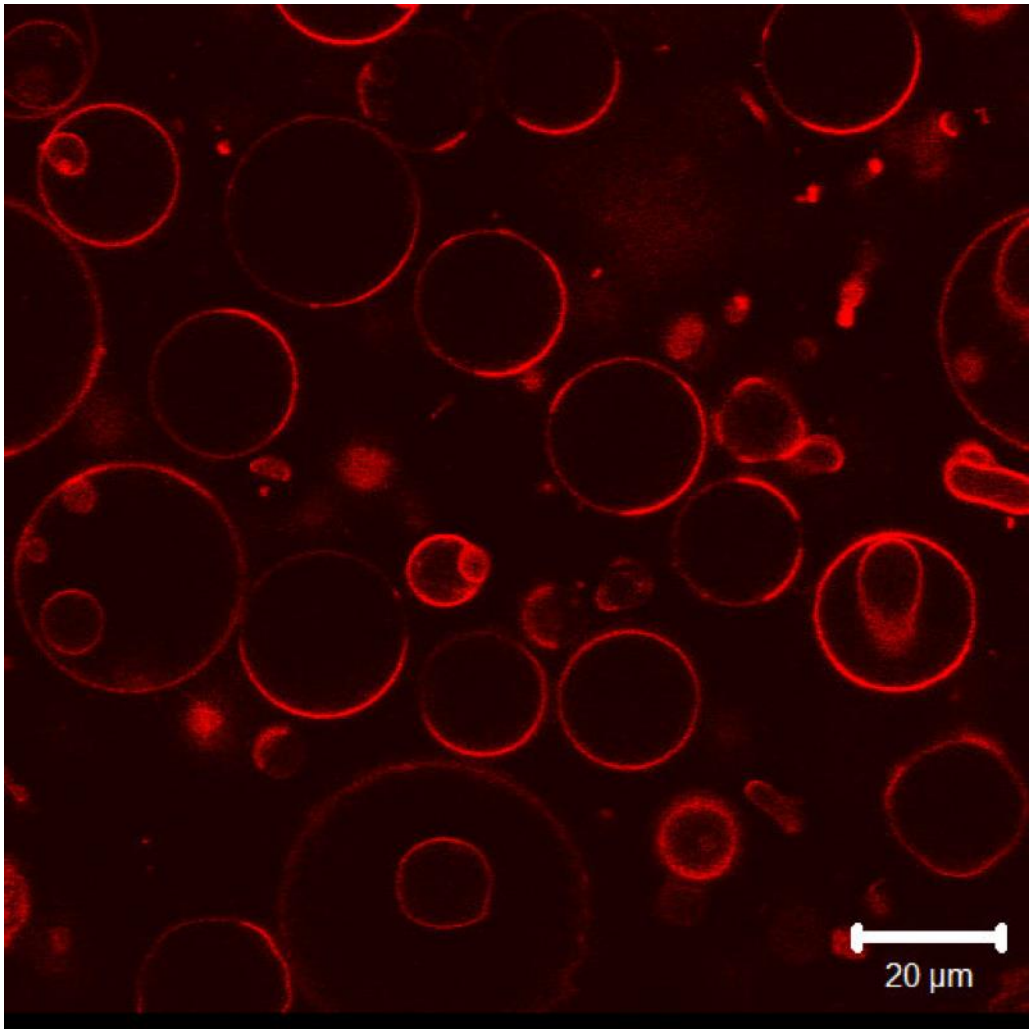

Figure 42: Confocal image of domain-forming GUVs (40 % DOPC, 40 % SM, and 20 % CH). The use of this composition leads to the formation of micron sized lipid rafts, domains rich in cholesterol and sphingomyelin. To visualise these domains, DiD is included at 0.1 mol %. DiD is a lipophilic tracer dye with affinity for the liquid disordered phase. DiD does not partition well into the cholesterol and sphingomyelin-rich liquid ordered phase. DiD was excited at 633 nm.

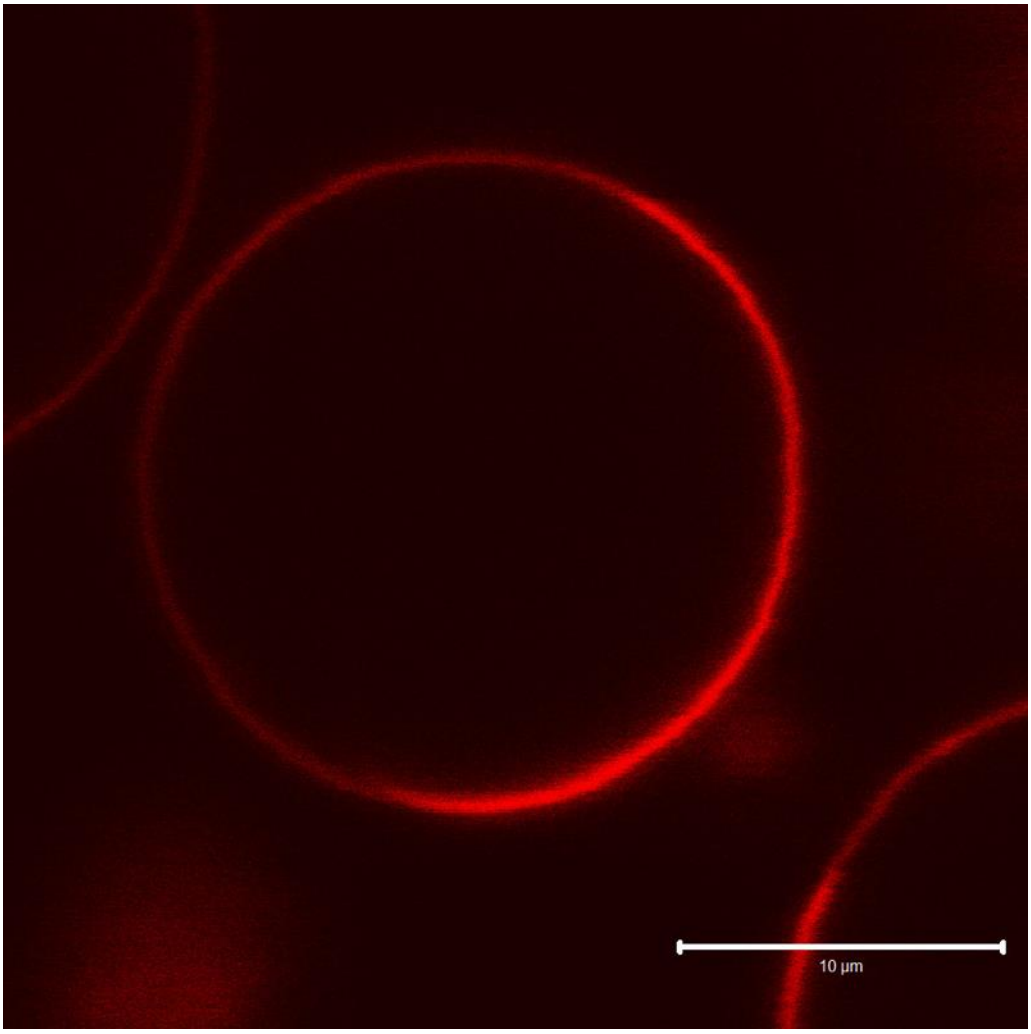

Figure 43: A close-up of confocal image of a raft-forming GUV (40 % DOPC, 40 % SM, and 20 % CH). DiD was used as a marker for the liquid disordered phase. The lipophilic tracer is clearly excluded from certain regions of the GUV. DiD was included at 0.1 mol % and excited at 633 nm.

3.3.3. Integrin Reconstitution

Due to the difficulty in reconstituting membrane proteins directly into preformed GUVs we found that the best, most reproducible approach was to firstly create smaller proteoliposomes before later "growing" these to GUVs. To create these smaller $\alpha_{IIb}\beta_3$-reconstituted proteoliposomes, two different methods were regularly utilised. The first method utilised a protocol based on Müller *et al.*[34] whereby lipid was fully solubilised by the detergent triton x-100 and the surfactant later removed by the addition of bio-beads. Alternatively a protocol based on Dennison *et al*.[27] was used whereby sonicated SUVs were brought to the onset of solubilsation with β-OG

and the surfactant removed later removed via dialysis. Because of these different protocols for integrin $\alpha_{IIb}\beta_3$ reconstitution, two different methods were used to detect the presence of $\alpha_{IIb}\beta_3$ in the liposomes.

Detection of integrin in Triton X-100 created proteo-liposomes

While the extruded vesicles used for integrin reconstitution were of uniform dimater, DLS measurements showed that the use of triton x-100 and biobeads to insert $\alpha_{IIb}\beta_3$, as per the Müller protocol, had lead to a shift in the dispersity of the resultant proteoliposomes. Proteoliposomes produced via Müller's full solubilisation method were found to have a diameter in the micrometer range. This change in vesicle size can be seen in Figure 44. Due to this increased vesicle diameter it was decided to use flow cytometry in order to detect the presence of $\alpha_{IIb}\beta_3$ in the proteoliposomes. Control liposomes were prepared via the same detergent solubilisation method but in the absence of integrin $\alpha_{IIb}\beta_3$ in order to yield protein-free liposomes of equivalent size. In order to identify integrin in the lipid membrane the anti-$\alpha_{IIb}\beta_3$ antibody CD41a was used. This antibody has general affinity for $\alpha_{IIb}\beta_3$ and will bind the protein's extracellular domain regardless of integrin activation state. To detect the presence of $\alpha_{IIb}\beta_3$ in the reconstituted proteoliposomes, flow cytometry was first performed on control liposomes using FITC labelled CD41a. To act as a negative control, $\alpha_{IIb}\beta_3$ free vesicles were passed through the flow cytometer and counts for the fluorescence data channel were piled on the lowest values of the logarithmic x-axis of the histogram. Using a gate 5 % of these counts were located within this region. Therefore, any CD41a binding leading to a shift in the histogram to the right can be quantified by the percentage gated value increasing within the region. After the control liposomes, $\alpha_{IIb}\beta_3$-reconstituted liposomes were passed through the flow cytometer and the counts were overlayed on the same histogram. A typical histogram for CD41a-FITC featuring both control and $\alpha_{IIb}\beta_3$-reconstituted liposomes is given in Figure 45. A shift in the histogram to the right can clearly be seen in the $\alpha_{IIb}\beta_3$-reconstituted liposomes due to the CD41a binding. Using this method, it was determined that the percentage gated value increased from a baseline of 5 % to 35.47 % ± 5.74 % in $\alpha_{IIb}\beta_3$-reconstituted liposomes showing the

presence of the integrin protein within the vesicle lipid membrane in proteoliposomes produced via the Müller method.

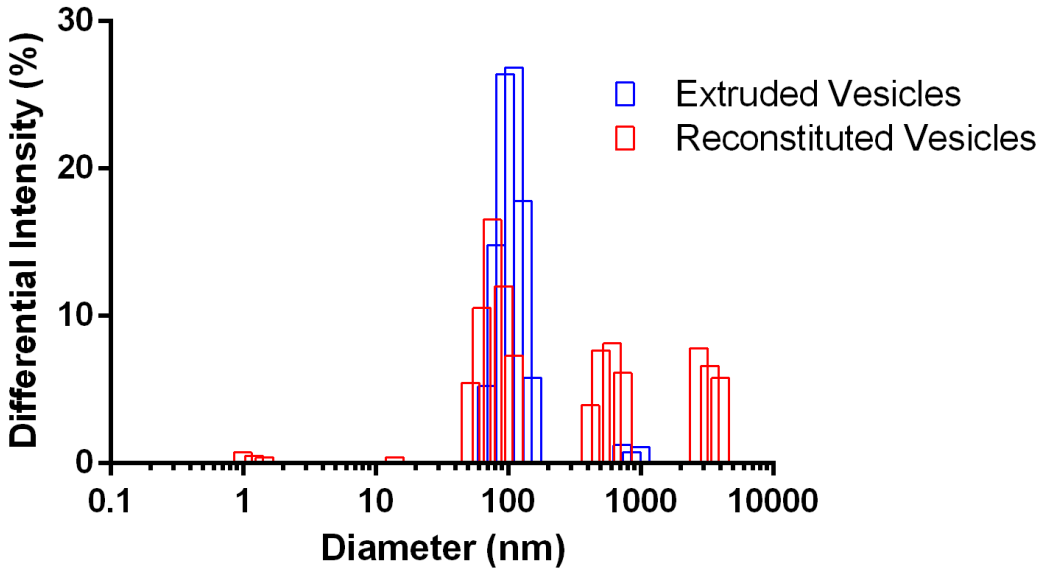

Figure 44: DLS measurements of vesicles after extrusion but before integrin insertion (blue), and after triton x-100-mediated integrin reconstitution. After extrusion vesicles were mono-disperse, around the 100 nm diameter mark. Due to detergent solubilisation and then detergent removal, reconstituted vesicles were poly-disperse with many proteoliposomes in the micrometer range.

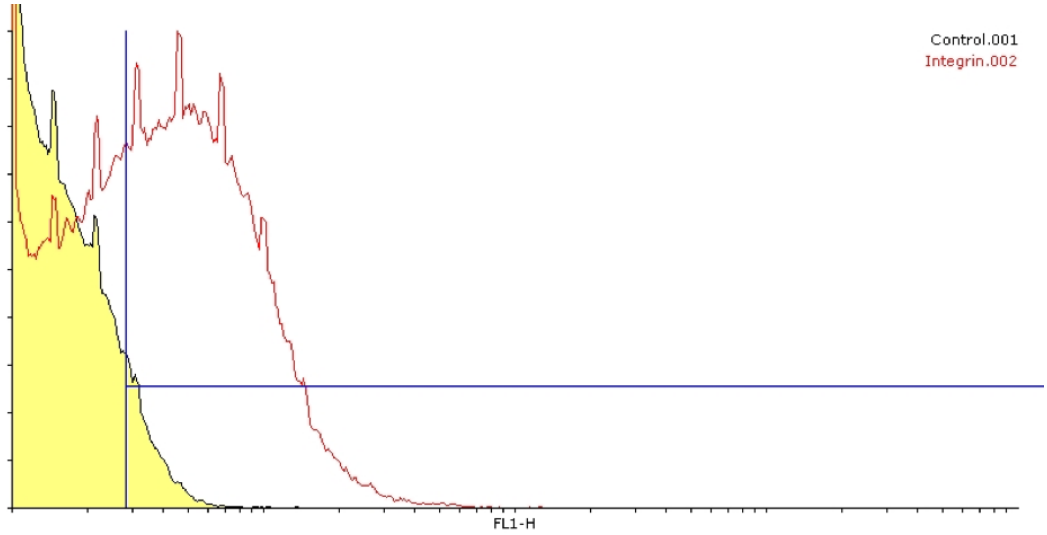

Figure 45: Representative histogram of FITC labelled CD41a binding in control liposomes (yellow fill, black outline) and reconstituted liposomes (red outline). The gate displayed is set so that 5 % of control liposome counts fall within the region. A shift in the histogram to the right can clearly be seen for $\alpha_{IIb}\beta_3$ liposomes showing the reconstitution protocol was successful.

Detection of integrin in β-OG created proteoliposomes

When compared to proteoliposomes produced via the Müller method, proteoliposomes produced via the Dennison method were relatively small. In fact, no change in vesicle diameter was detected by DLS before and after detergent treatment where the mean vesicle diameter was 31 nm ± 5 nm throughout. This was likely due to the fact that sonicated SUVs were only brought to the onset of solubilisation in this protocol, rather than being fully solubilised. Due to their SUV size it was not possible to use flow cytometry to detect the presence of $\alpha_{IIb}\beta_3$ within the vesicle membrane. Instead an alternative assay had to be used. To do so, newly reconstituted proteoliposomes that had been separated from detergent via dialysis were run on a size exclusion column to remove free integrin. The fractions were collected and analysed for lipid concentration and the presence of protein. The lipid concentration of each fraction was quantified by the presence of radiolabelled lipid. The protein (integrin $\alpha_{IIb}\beta_3$) concentration of each fraction was quantified by running each fraction on a polyacrylamide gel. Densitometry was subsequently used on each lane of the gel. Combined these two assays showed that the lipid and $\alpha_{IIb}\beta_3$ were present in the same fractions and that the concentration of each component in the fractions was roughly correlated. This is shown in Figure 46. Due to the fact that free integrin had previously been removed through a size exclusion column and only the vesicle-containing fractions collected, this co-association of lipid and protein in the same fractions showed that $\alpha_{IIb}\beta_3$ had been reconstituted in SUVs created using the Dennison protocol.

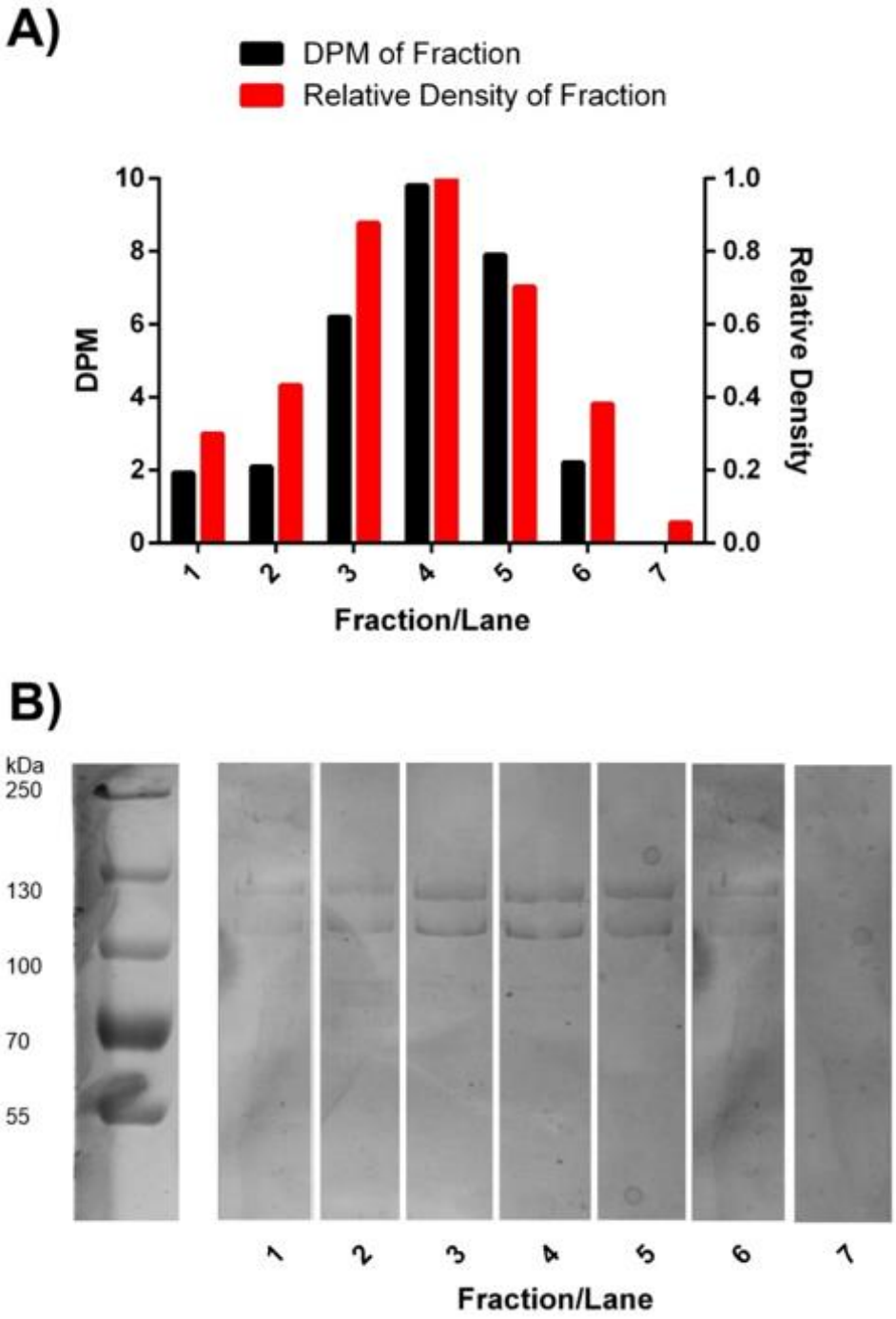

Figure 46: Lipid and protein levels in recovered fractions. A) A graph showing detected disintegrations per minute (DPM) for each fraction in black and relative density of each fraction (as determined by densitometry) in red. To determine densitometry values, each fraction was run on a polyacrylamide gel and later stained with coomasssie blue to highlight any protein present. ImageJ was used to analyse each lane and the lane with the highest density value was set to 1 (lane 4). From this value the relative density of the other lanes could be determined. It is evident that there is a correlation between the lipid concentration in each fraction (black) and the protein concentration in each fraction (red). B) A coomassie stained polyacrylamide gel from which the densitometry values were obtained. A molecular weight marker is also included (leftmost lane). $\alpha_{IIb}\beta_3$ is reduced into three subunits during the PAGE step. The alpha subunit is divided into a heavy (125 kDa, top band) and light chain (25 kDa, run off gel). The beta subunit is 105 kDa (lower band).

3.3.4. Proteoliposome to GUV conversion

Conformation of insertion in GUVs

In order to confirm the presence of $\alpha_{IIb}\beta_3$ within GUVs electroformed from smaller, $\alpha_{IIb}\beta_3$-containing proteoliposomes, confocal microscopy was used. The proteoliposomes used as the lipid source for GUV production could be produced by either the Müller or the Dennison method of reconstitution without negatively influencing the resultant GUVs. In a typical preparation, $\alpha_{IIb}\beta_3$ was fluorescently labelled with an appropriate probe such as Atto532, Atto655 or TAMRA in order to visualise integrin presence in the electroformed GUVs. Figure 47 gives a typical result of the inclusion of $\alpha_{IIb}\beta_3$ in the electroformation protocol, where the nature's own mixture was used as the lipid composition and the reconstituted $\alpha_{IIb}\beta_3$ was labelled with Atto655 . As can be seen, using $\alpha_{IIb}\beta_3$-containing proteoliposomes as the lipid source in the electroformation process was capable of producing defect free GUVs indistinguishable from protein free GUVs produced from a lipid in chloroform solution, as is normally the case in electroformation. This result shows that $\alpha_{IIb}\beta_3$-containing GUVs could be routinely created and serve as a platform for later diffusion-based measurements.

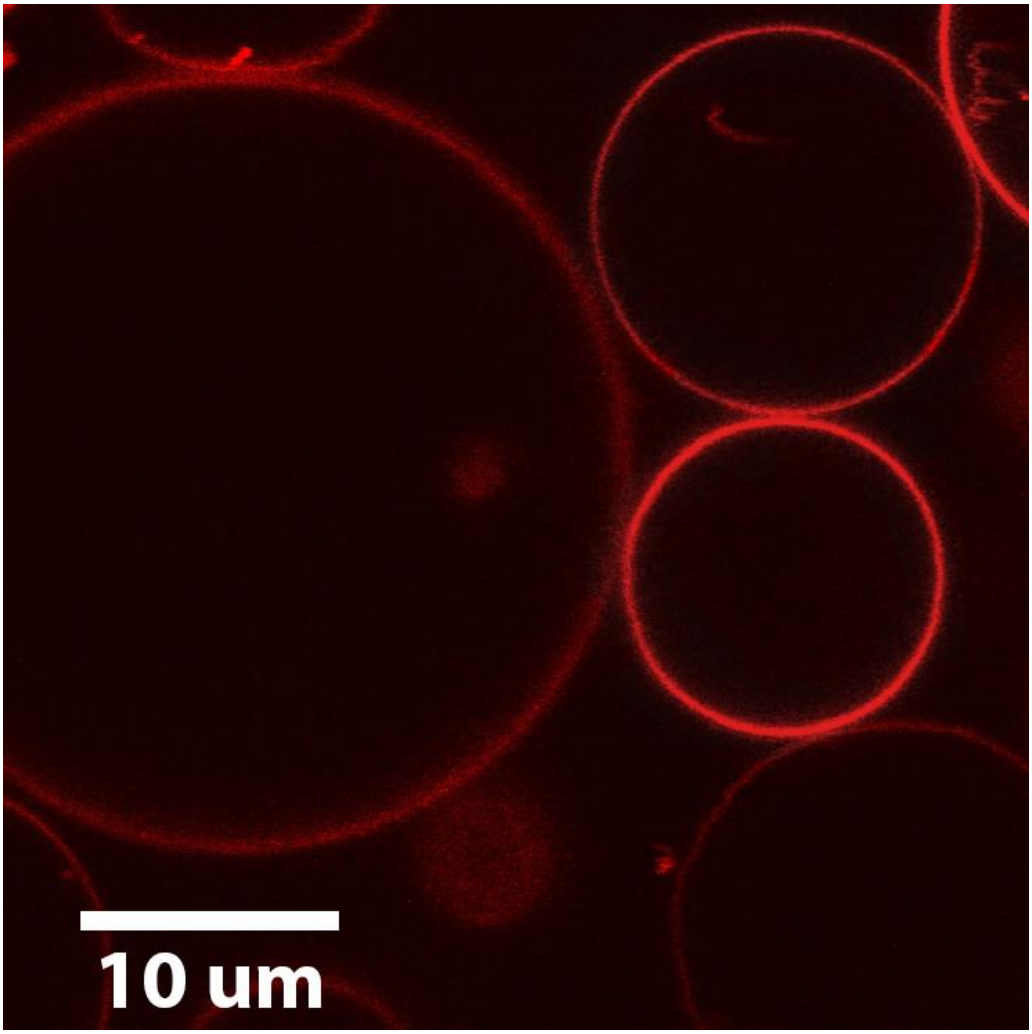

Figure 47: Atto655-labelled $\alpha_{IIb}\beta_3$-reconstituted into nature's own GUVs. The fluorescent labelling of the integrin protein allowed for the identification of it within electroformed vesicles. The inclusion of $\alpha_{IIb}\beta_3$ in the electroformation method did not appear to alter the morphology or success of the electroformation process.

Integrin concentration in GUVs

In seeking to control the loading of integrin $\alpha_{IIb}\beta_3$ into liposomes, a number of starting concentrations of labelled $\alpha_{IIb}\beta_3$ were used to firstly create integrin-containing proteoliposomes. This ranged from 1 integrin per 8000 lipid molecules, to 1 integrin molecule per 80,000 lipid molecules. Surprisingly, the starting concentration of integrin used had little effect on the final concentration of $\alpha_{IIb}\beta_3$ embedded in the GUVs. To reach this conclusion, point measurements were performed on the GUV membrane and the average number of fluorescently labelled $\alpha_{IIb}\beta_3$ molecules in the focal volume was recorded over the length of the experiment. This capability to infer the number of fluorescently labelled molecules is one of the

major advantages of FCS/FLCS when compared to FRAP. The value itself, referred to as N, remained relatively constant for the GUVs regardless of the starting concentration of labelled $\alpha_{IIb}\beta_3$ used to create $\alpha_{IIb}\beta_3$-containing proteoliposomes. This can be seen in Table 7 where the N number is given during point measurements alongside the starting lipid to $\alpha_{IIb}\beta_3$ ratio. From this data it appears that the proteo-GUVs appear to reach an integrin saturation point relatively quickly. While this concentration is low compared to native membrane concentrations, N values such as these are absolutely ideal for FCS measurements.

Table 7: $\alpha_{IIb}\beta_3$ saturation of GUVs. The use of varying starting concentrations of $\alpha_{IIb}\beta_3$appeared to have little influence on the average number of molecules in the focal volume during FLCS point measurements, indicating that nature's own GUVs are easily saturated with properly reconstituted $\alpha_{IIb}\beta_3$.

Starting lipid:protein ratio	Average number of molecules in the focal volume (N)
8,000:1	1.55 ± 0.17
20,000:1	1.67 ± 0.20
40,000:1	1.60 ± 0.22
80,000:1	1.34 ± 0.25

Integrin orientation in GUVs

In order to estimate the orientation of $\alpha_{IIb}\beta_3$ in GUVs, integrin-reconstituted nature's own GUVs were constructed as normal. GUVs were then incubated with the serine protease proteinase k for 2 hours at 37 °C. This enzyme only had access to outwardly orientated atto655-labelled $\alpha_{IIb}\beta_3$ and thus inwardly orientated atto655-labelled proteins could not be digested. Confocal images (Figure 48) were taken before and after proteinase k incubation and using a tracing tool in imageJ, the average count per pixel at the GUV membrane was determined. Before incubation the average count per pixel was found to be 46 ± 18 counts, while after incubation it was 21 ± 12

counts. (Figure 49) A two-tailed unpaired t-test was performed where the difference between the two data sets was found to be significant, where $t(14) = 2.90$, $p < 0.05$. This approximate halving of the intensity suggests that $\alpha_{IIb}\beta_3$ is orientated symmetrically within the lipid membrane. This result was somewhat predicted given the uncontrolled and seemingly random nature of $\alpha_{IIb}\beta_3$ reconstitution.

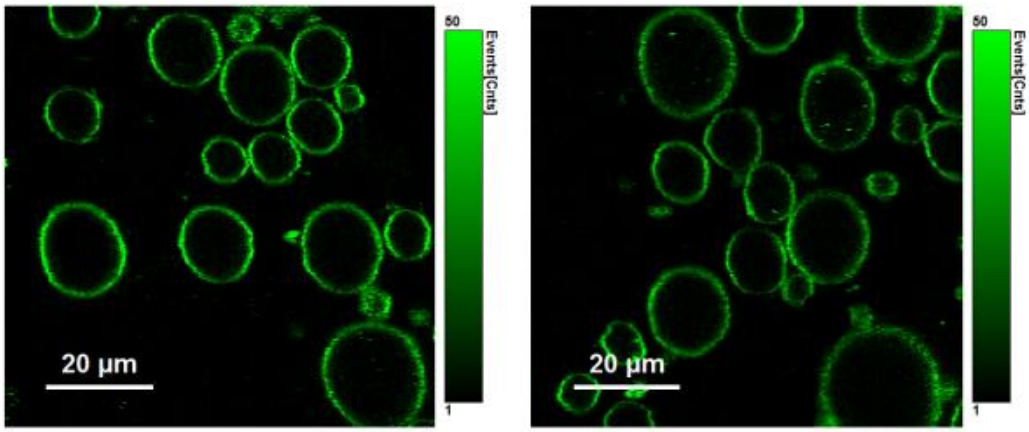

Figure 48: A representative confocal image of atto655 labelled $\alpha_{IIb}\beta_3$-reconstituted GUVs before (left) and after (right) incubation with proteinase k. A reduction in intensity at the GUV membrane is clearly visible following enzyme digestion. A line tool in imageJ was used to trace around the GUV membrane in order to find the average intensity per pixel at the lipid membrane.

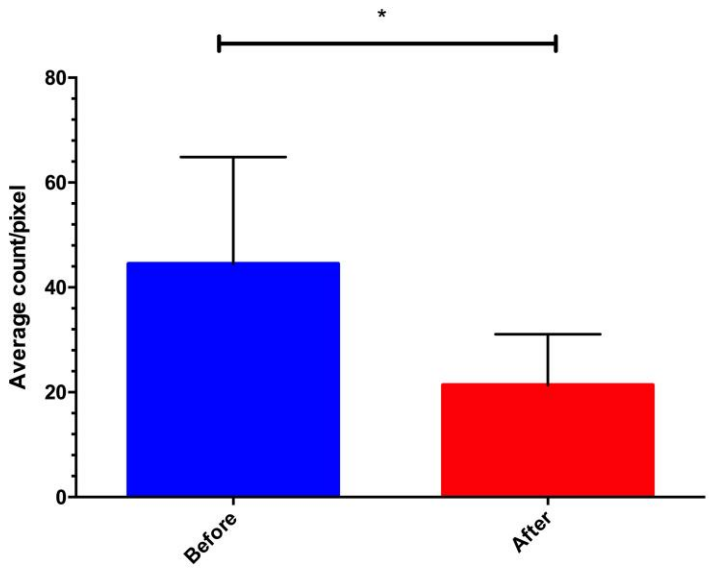

Figure 49: After the imageJ line tool was used to trace around the GUV membranes, the average counts per pixel before and after proteinase k incubation was calculated. Before incubation the average count per pixel was found to be 46 ± 18 counts, while after incubation it was 21 ± 12 counts. A two-tailed unpaired t-test was performed where the difference between the two data sets was found to be significant, where $t(14) = 2.90$, $p < 0.05$. This suggests that the enzyme digested approximately half of the labelled $\alpha_{IIb}\beta_3$ proteins, and thus half the labelled $\alpha_{IIb}\beta_3$ proteins were orientated outwardly. Therefore, it can be said that $\alpha_{IIb}\beta_3$ is orientated randomly within the GUV membrane. (n=8)

3.3.5. Diffusion in GUVs

Lipid diffusion

Following characterisation of $\alpha_{IIb}\beta_3$ within the GUV membrane where integrin presence, concentration, and orientation was examined, attention was turned to single molecule techniques in order to determine the rate of diffusion of integrin and lipid within GUVs. For these diffusion measurements, Fluorescence Lifetime Correlation Spectroscopy (FLCS) was used. Integrin-containing vesicles were created as described and located via confocal microscopy for their XY co-ordinates. A Z-scan was then performed in order to then identify the upper most pole of the GUV membrane. This was achieved by locating the position of most fluorescence intensity, which corresponded to the GUV lipid membrane that contained a percentage of labelled lipid and protein. At these positions point measurements were carried for between 60 and 180 seconds to yield an autocorrelation function

for the lipid or protein. Initial FLCS experiments simply characterised the lipid diffusion co-efficents of various lipid compositions. For example, a typical autocorrelation function and its fit to a single component, two-dimensional diffusion model for a lipid probe (DOPE-atto532) in a GUV composed of nature's own is given in Figure 50. Using this fitting model we determined that the diffusion co-efficient of DOPE-Atto532 within the nature's own bilayer was found to be 7.89 $\pm$ 0.42 $\mu m^2/s$ at room temperature, with an alpha value of 1.01 $\pm$ 0.04, i.e., the mean-squared displacements of the lipid scale as a power law of time with an exponent a of 1 indicating that the lipid is undergoing normal Brownian diffusion at the liposome interface. Alpha values of greater or less than one, indicate anomalous diffusion, which in the case of a value less than 1 is usually attributed to hindered diffusion due to barriers within the membrane.[69] This lipid diffusion value is consistent with values reported previously for GUVs as determined by FCS,[48,141] but well in excess of reported lipid diffusion values for planar SLBs.[30,31] As well as nature's own other simpler lipid compositions were characterised by FLCS. Lacking cholesterol and sphingomyelin, these mixtures such as DOPC and DOPC/DOPS at varying ratios were generally indistinguishable from one another and diffused slightly faster than the nature's own composition. Again the alpha value remained consistently at 1, as expected for the lateral diffusion of lipids in free standing GUV systems. A summary of the diffusion values for a variety of lipid compositions is given in Table 8. A one-way ANOVA to compare the means of each data set against one another, $P(4, 100) = 71.15$, $p < 0.001$. A post-hoc Bonferroni test was performed where the nature's own composition was the only composition found to show significant variation from the other compositions, $p < 0.001$. Therefore, it can be said that altering the ratios of phospholipids had a negligible influence on the rate of diffusion within the GUV membrane. Only when ordered phase lipids such as cholesterol and sphingomyelin were included, as in the case of nature's own, was membrane fluidity altered.

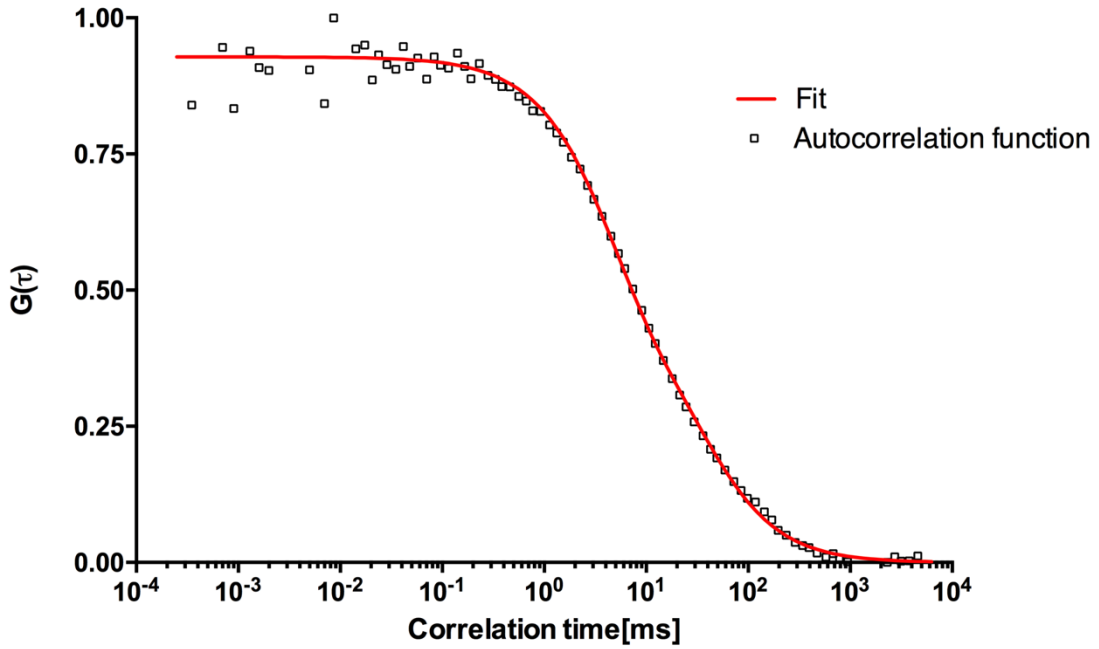

Figure 50: A typical autocorrelation function and its single component two dimensional fit for DOPE-atto532 diffusing in nature's own GUVs at room temperature. GUVs created via the electroformation protocol in a sucrose-containing buffer were pipetted into an observation buffer of 10 mM HEPES, 150 mM NaCl, 1 mM $CaCl_2$, 100 mM glucose, pH 7.4, and the GUVs were allowed to come to rest on the bottomof a glass slide over a 30-minute period. Stationary GUVs were selected before a point measurement was performed on the GUV membrane. DOPE-atto532 diffusion in nature's own GUVs was determined to be 7.89 ± 0.42 $\mu m^2/s$ at room temperature.

Table 8: The measured diffusion co-efficients for a selection of lipid compositions used in GUV experiments. Using lipid probes such as DOPE-Atto532 or DOPE-Atto655 FLCS point measurements were recorded at room temperature. At the ratios used, the inclusion of DOPE and DOPS appeared to have no influence on the diffusion of the GUV lipid bilayer. Only when cholesterol and sphingomyelin were included in the vesicle membrane such as in nature's own could a change in the diffusion co-efficient by identified. This was verified by a one-way ANOVA with Bonferroni post-hoc test ($p < 0.001$). The alpha value appeared to be unchanged by cholesterol and sphingomyelin presence and remained 1 throughout. Standard deviation was used to report the error.

Lipid Composition	Diffusion Co-efficient ($\mu m^2/s$)	Alpha Value
DOPC	9.89 ± 0.80	0.99 ± 0.02
DOPC:DOPS (9:1)	10.05 ± 0.78	1.01 ± 0.03
DOPC:DOPS (8:2)	9.65 ± 0.71	1.00 ± 0.02
DOPC:DOPE (9:1)	10.11 ± 1.02	1.00 ± 0.03
Nature's Own	7.89 ± 0.42	0.99 ± 0.02

$\alpha_{IIb}\beta_3$ diffusion

After characterisation of the diffusion co-efficients of various lipid compositions in our free-standing GUV system attention turned to the diffusion of fluorescently labelled $\alpha_{IIb}\beta_3$ in the giant vesicles. $\alpha_{IIb}\beta_3$ was membrane-inserted as described previously and the location of the integrin-reconstituted bilayer was identified by a combination of XY imaging and Z-scanning, as was the case for lipid diffusion experiments. Again point measurements were taken for between 60 and 180 seconds. A typical autocorrelation function and its fit to a single component, two-dimensional diffusion model for $\alpha_{IIb}\beta_3$–atto655 in nature's own GUVs is shown in Figure 51. The ACF fits well to a single-component model with no evidence for slower diffusing components, associated, for instance, with aggregated protein. Analysis of the ACF traces shows that $\alpha_{IIb}\beta_3$ was diffusing at a rate of 2.52 ± 0.29 $\mu m^2/s$ within nature's own GUVs. Again the alpha value showed that diffusion was Brownian. In lipid compositions lacking cholesterol and sphingomyelin, a slightly

faster $\alpha_{IIb}\beta_3$ diffusion coefficient was recorded due to the fact that these GUVs were composed of liquid disordered phase phospholipids and lacking the rigid liquid ordered sterols and sphingolipids of nature's own. A summary of diffusion coefficients for fluorescently labelled $\alpha_{IIb}\beta_3$ in various GUV compositions is given in

Table 9. A one-way ANOVA was carried out, which found that lipid composition appeared to alter the diffusion of $\alpha_{IIb}\beta_3$ within the lipid membrane, $F(3, 54) = 12.68$, $p < 0.001$. A post-hoc Bonferroni test showed that $\alpha_{IIb}\beta_3$ in DOPC:DOPS and nature's own diffused significantly slower than $\alpha_{IIb}\beta_3$ in DOPC ($p < 0.001$) and DOPC:DOPE ($p < 0.01$). To the best of our knowledge, these diffusion values are the first to be recorded for $\alpha_{IIb}\beta_3$ in a GUV system, but are in line what would be expected based on the reconstitution of other membrane proteins into GUVs.[53,142] The fact that these diffusion values are in line with other literature values suggests that the integrin protein has been properly inserted into the lipid membrane in our lipid compositions, something not investigated in other GUV-$\alpha_{IIb}\beta_3$ models.[46,47] This aspect is particularly relevant given our use of a range of lipid compositions, where other groups have asserted that that non-DMPC-containing lipid compositions do not facilitate $\alpha_{IIb}\beta_3$ insertion.[29] Therefore, not only is our work the first to confirm proper $\alpha_{IIb}\beta_3$ reconstitution into GUVs, it is also the first to confirm proper $\alpha_{IIb}\beta_3$ reconstitution into a DMPC-free system.

Another key feature of the use of a free-standing GUV system is the increased diffusion values for membrane proteins when compared to SLB systems. For example Erb and Goennenwein both reported similar $\alpha_{IIb}\beta_3$ lateral diffusion co-efficients of 0.70 and 0.60 $\mu m^2/s$, respectively[30,31], while Purricker gives a much slower diffusion co-efficient of between 0.03 and 0.13 $\mu m^2/s$.[43,44] This is in contrast to our $\alpha_{IIb}\beta_3$ diffusion values of between 2.5 and 3.4 $\mu m^2/s$, depending the lipid composition used. This mirrors the increased lipid diffusion co-efficients in GUVs, when compared to SLBs, as previously mentioned. However, and more importantly, this free standing nature of GUVs manifests itself in the unencumbered lateral mobility of membrane proteins when compared to SLBs. While existing $\alpha_{IIb}\beta_3$-reconstituted SLBs suffer from major protein immobility (Erb *et al.*; 75 %, Goennenwein *et al.*; 40 %, Purrucker *et al.*; > 75 %)[30,31,43,44], no $\alpha_{IIb}\beta_3$ immobility was apparently in our system. This can be inferred from the lack of photobleaching during point measurements at the lipid membrane. If fluorescently-labelled $\alpha_{IIb}\beta_3$ had been immobile, ie stationary, within the focal volume during point

measurements this would have obvious as a decrease in the fluorescence intensity over time, and the failure to obtain an ACF trace.

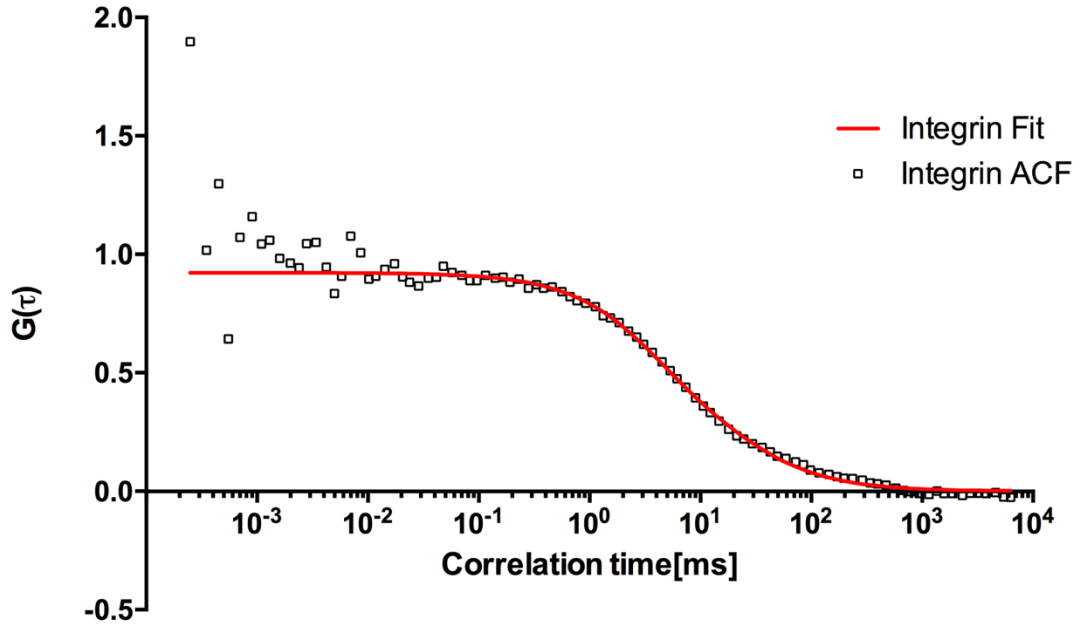

Figure 51: A typical autocorrelation function and its single component two dimensional fit for $\alpha_{IIb}\beta_3$-Atto655 diffusing in nature's own GUVs at room temperature. GUVs created via the electroformation protocol in a sucrose-containing buffer were pipetted into an observation buffer of 10 mM HEPES, 150 mM NaCl, 1 mM CaCl2, 100 mM glucose, pH 7.4, and the GUVs were allowed to come to rest on the bottom of a glass slide over a 30-minute period. Stationary GUVs were selected before a point measurement was performed on the GUV membrane. $\alpha_{IIb}\beta_3$-Atto655 diffusion in nature's own GUVs was determined to be 2.61 ± 0.35 μm²/s at room temperature.

Table 9: The measured diffusion co-efficients for a fluorescently-labelled $\alpha_{IIb}\beta_3$ in a variety of lipid compositions. Integrin in the cholesterol and sphingomyelin-containing nature's own composition diffused slower than in the other examined compositions. The alpha value, regardless of lipid composition, was 1. All point measurements took place at room temperature. Standard deviation was used to report the error.

Lipid Composition	Diffusion Co-efficient ($\mu m^2/s$)	Alpha Value
DOPC	3.40 ± 0.66	0.98 ± 0.02
DOPC:DOPS (9:1)	2.99 ± 1.04	0.99 ± 0.02
DOPC:DOPE (9:1)	3.46 ± 1.21	0.98 ± 0.03
Nature's Own	2.52 ± 0.29	1.00 ± 0.02

$\alpha_{IIb}\beta_3$ activation state

Following conformation that $\alpha_{IIb}\beta_3$ had been successfully incorporated within the GUV membrane, and the establishment of a baseline diffusion co-efficient, we next sought to infer whether the integrin protein remained in its un-activated conformation, or had transitioned to its ligand binding conformation during the membrane reconstitution process. This was important as, for example, Erb *et al.* found that $\alpha_{IIb}\beta_3$ incorporated into a planar bilayer system was capable of binding to ligands in the absence of any integrin activators.[30] In a similar experiment we decided to incubate the liposome-protein assembly with the integrin's primary ligand, fibrinogen. It was hoped that if $\alpha_{IIb}\beta_3$ was in its activated ligand binding state then formation of an integrin-fibrinogen complex could be identified via a reduction in the diffusion co-efficient or a change in the alpha value for fluorescently labelled $\alpha_{IIb}\beta_3$. To do so, reconstituted GUVs were incubated with fibrinogen at 0.1 mg/ml for 1 hour before the diffusion co-efficient was determined. However, according to our analysis, the diffusion co-efficient of $\alpha_{IIb}\beta_3$ in the nature's own composition remained constant with a value of 2.52 ± 0.29 $\mu m^2/s$. The alpha also remained constant with a value of 0.99 ± 0.02. These values, indistinguishable from those observed prior to incubation with fibrinogen, appeared to show that $\alpha_{IIb}\beta_3$ had not

bound to its ligand. Thus, we concluded that $\alpha_{IIb}\beta_3$-reconstituted in electroformed GUVs via our novel insertion method was present in it ligand unavailable un-activated conformation.

3.3.6. Diffusion of $\alpha_{IIb}\beta_3$ in GUVs after activation

DTT and Mn^{2+} activation

Knowing that $\alpha_{IIb}\beta_3$-reconstituted into nature's own GUVs appeared to remain in its un-activated state, we wanted to know whether conformational changes induced by nominally activating $\alpha_{IIb}\beta_3$ lead to a measurable change to its diffusion co-efficient as determined by FLCS. To do so the integrin activators DTT or Mn^{2+} were applied to the GUV-protein assembly. In the experimental procedure, DTT or Mn^{2+} solutions were carefully pipetted into the observation chamber containing the $\alpha_{IIb}\beta_3$-reconstituted GUVs to a final activator concentration of between 0.5 and 5 mM. The integrin and activator were incubated at room temperature for 1 hour before FLCS measurement commenced. Following incubation with 3 mM DTT, the diffusion co-efficient of liposome-bound $\alpha_{IIb}\beta_3$ was determined by FLCS to be 2.59 ± 0.24 $\mu m^2/s$, whilst for liposome-bound $\alpha_{IIb}\beta_3$ incubated with 3 mM Mn^{2+}, a diffusion co-efficient of 2.51 ± 0.19 $\mu m^2/s$ was obtained. In both cases, the alpha values were found to be approximately 1. Together these results indicate that the conformational (hydrodynamic volume) changes induced in $\alpha_{IIb}\beta_3$ by DTT or Mn^{2+} are not alone sufficient to induce a measurable change in the integrin diffusion coefficient. Furthermore, the ACFs fit well to a single component model with no evidence for slower diffusing components in the ACF which might suggest integrin clustering. These results were repeated with a range of activator concentrations with no change in the reported diffusion co-efficient.

DTT and Mn^{2+} activation in the presence of fibrinogen

Following on from the activation of membrane-reconstituted $\alpha_{IIb}\beta_3$ in the absence of a ligand, we later sought to repeat this activation in the presence of $\alpha_{IIb}\beta_3$'s primary ligand, fibrinogen. While we had established that conformational changes alone were not capable of bringing about a change in integrin diffusion it was hoped that DTT or Mn^{2+}-mediated fibrinogen binding would be sufficient to lead to a change in $\alpha_{IIb}\beta_3$'s diffusion co-efficient. Using 3 mM DTT or 3 mM Mn^{2+} in conjunction with fibrinogen at a concentration of 0.1 mg/ml it was found that the diffusion co-efficient of $\alpha_{IIb}\beta_3$-Atto655 was altered in nature's own GUVs. The co-addition of DTT and fibrinogen reduced the diffusion coefficient to 1.56 ± 0.26 $\mu m^2/s$. Similarly, co-addition of Mn^{2+} and fibrinogen to $\alpha_{IIb}\beta_3$-reconstituted into liposome resulted in a diffusion co-efficient of 1.49 ± 0.41 $\mu m^2/s$.

A one-way ANOVA was was performed on $\alpha_{IIb}\beta_3$ diffusion in nature's own under the previous conditions (before activation, before activation in the presence of fibrinogen, after DTT and Mn^{2+} activation, DTT and Mn^{2+} activation in the presence of fibrinogen) where significance was found within the data ($F(5, 134) = 100.10$, $p < 0.001$). A post-hoc Bonferroni test between all the variables revealed that this significance was only found when fibrinogen was added to DTT and Mn^{2+} activated integrin, where $p < 0.001$. These results suggest that the DTT or manganese activated integrin binds fibrinogen and the resulting complex diffuses more slowly. An example of an ACF trace and its fit to a single component, two dimensional diffusion model before and after fibrinogen binding it given in Figure 52.

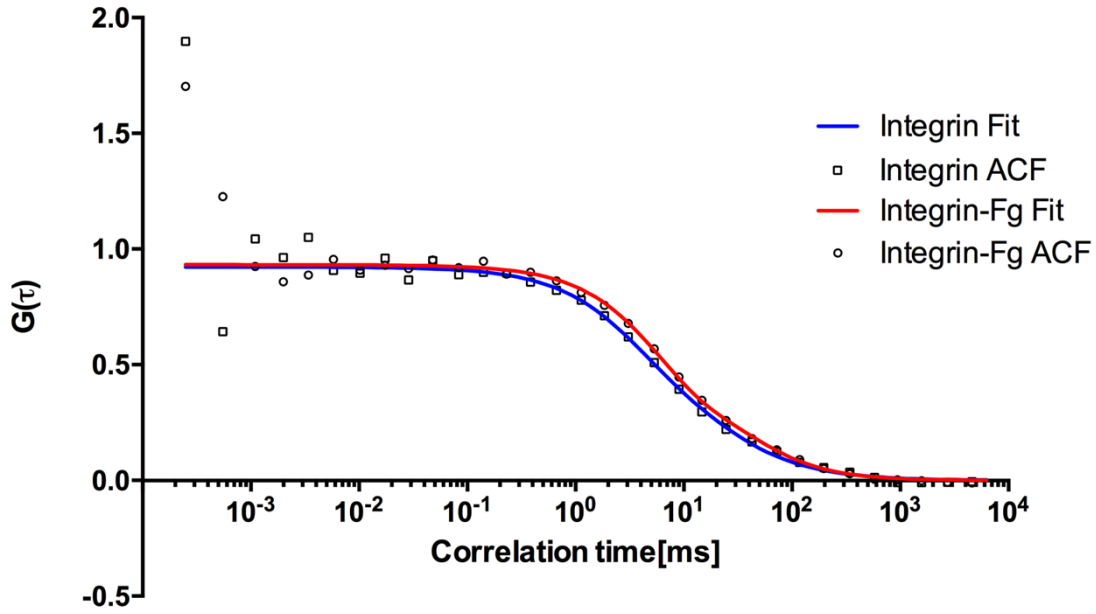

Figure 52: Representative single component fits (solid lines) to ACFs collected from resting $\alpha_{IIb}\beta_3$-atto655 (blue) and activated, fibrinogen bound $\alpha_{IIb}\beta_3$-Atto655 (red) in nature's own GUVs at room temperature. The $\alpha_{IIb}\beta_3$-reconstituted GUVs were created in a sucrose-containing buffer before being pipetted into an observation buffer of 10 mM HEPES, 150 mM NaCl, 1 mM CaCl2, 100 mM glucose at pH 7.4. The GUVs were allowed to come to rest on a glass slide over a 30-minute period prior to measurement. Stationary GUVs were selected before a point measurement was performed on the GUV membrane. $\alpha_{IIb}\beta_3$-Atto655 diffusion in nature's own GUVs before the addition of activators or fibrinogen was determined to be 2.52 ± 0.29 μm²/s at room temperature. Following integrin activation and addition of fibrinogen, this diffusion co-efficient reduced to 1.56 ± 0.26 μm²/s with DTT and 1.49 ± 0.41 μm²/s with Mn^{2+}.

In order to interrogate the change in integrin diffusion we turned to the Saffman–Delbrück model of protein diffusion. The Saffman–Delbrück model[51], is one of the most widely used models used to describe the 2-dimensional diffusion of protein bound to a membrane. According to this the model, the diffusion co-efficient of a membrane protein integrated into a lipid membrane exhibits logarithmic dependence on the reciprocal of the hydrodynamic radius R, of the protein as expressed by[53]:

$$D = \frac{k_B T}{4\pi\mu_m h}\left(ln\left(\frac{\mu_m h}{\mu_w R}\right) - 0.5772\right)$$

where D is the lateral diffusion co-efficient of the protein, k_B is Boltzmann constant, T is the absolute temperature, h is the thickness of the lipid bilayer, μ_m is the viscosity of the lipid bilayer and μ_w is the viscosity of the surrounding aqueous phase. Although there have been challenges to the broad veracity of the SD model[55], there are numerous convincing studies which demonstrate its applicability across membrane proteins with hydrodynamic radii up to approximately 10 nm.[52,53] The integrin within both resting and activated conformational ranges have hydrodynamic radii below this value.[143] According to the SD model, the only parameter of the protein exerting an influence on its diffusion coefficient is its hydrodynamic radius and this value weakly affects the diffusion co-efficient. For example, increasing the protein radius from 1 nm to 10 nm only changes the mobility by 30 %.[55] Here, upon fibrinogen binding, the diffusion coefficient of $\alpha_{IIb}\beta_3$ decreases by approximately 40 % when compared with unbound, resting $\alpha_{IIb}\beta_3$. This suggests, relying on the Saffman–Delbrück model as a first approximation, a 20-fold increase in the radius of the diffusing protein following ligand binding. Such an increase is too large to be accounted for by the formation of 1:1 or even 1:2 fibrinogen–$\alpha_{IIb}\beta_3$complexes. Rather, it strongly suggests that significant aggregation of the integrin is occurring on fibrinogen binding following $\alpha_{IIb}\beta_3$ activation by either DTT or Mn^{2+}. In turn, fibrinogen binding and aggregation only occur after treatment of the integrin with the activator.

Another factor that could be examined and used to explain the diffusional characteristic of our $\alpha_{IIb}\beta_3$ protein was the alpha value from our two-dimensional fits. In our initial set-ups where integrin was in its un-activated or activated but un-liganded states, analysis of the ACFs had shown that Brownian diffusion was occurring, ie the alpha value remained at 1. We found that when the integrin protein was activated with DTT or Mn^{2+} and incubated in the presence of fibrinogen at 0.1 mg/ml a reduction in the alpha value was witnessed alongside the aforementioned reduction in the diffusion co-efficient. These values were 0.87 ± 0.03 and 0.88 ± 0.03 for DTT (and fibrinogen) and Mn^{2+} (and fibrinogen), respectively. This reduction in the alpha value suggests that the diffusion of labelled $\alpha_{IIb}\beta_3$ is hindered under the ligand-binding conditions and can therefore the diffusion can now be described as

anomalous. This same phenomena of anomalous protein diffusion has previously been described in cells due to molecular crowding for example.[69] A summary of the diffusion co-efficients and their associated alpha values can be seen in Table 10.

Table 10: Lipid and integrin $\alpha_{IIb}\beta_3$ diffusion in nature's own GUVs. The table shows the diffusion coefficient before activation in the presence and absence of fibrinogen, and after activation in the presence and absence of fibrinogen. Activation or ligand addition alone was not sufficient to bring about a measurable change in $\alpha_{IIb}\beta_3$ diffusion. The combination of activation and ligand addition was sufficient to bring about a reduction in diffusion of $\alpha_{IIb}\beta_3$ attributed to integrin aggregation. This was confirmed by a one-way ANOVA and post-hoc Bonferroni test where $p < 0.001$. Furthermore, the combination of activation and ligand addition led to anomalous diffusion of $\alpha_{IIb}\beta_3$ as indicated by the alpha values. Error was reported used standard deviation.

Condition	Diffusion co-efficient ($\mu m^2/s$)	Alpha value
Lipid (DOPE-Atto532)	7.89 ± 0.42	1.01 ± 0.04
$\alpha_{IIb}\beta_3$	2.52 ± 0.29	0.99 ± 0.03
$\alpha_{IIb}\beta_3$ + fibrinogen	2.61 ± 0.35	0.99 ± 0.02
$\alpha_{IIb}\beta_3$ + DTT	2.59 ± 0.24	1.02 ± 0.03
$\alpha_{IIb}\beta_3$ + Mn^{2+}	2.51 ± 0.19	1.02 ± 0.04
$\alpha_{IIb}\beta_3$ + DTT + fibrinogen	1.56 ± 0.26	0.87 ± 0.03
$\alpha_{IIb}\beta_3$ + Mn^{2+} + fibrinogen	1.49 ± 0.41	0.88 ± 0.03

In combination, this large reduction in the lateral diffusion co-efficient and fall in the recorded alpha values all pointed toward the formation of large protein aggregates within the GUV bilayer when $\alpha_{IIb}\beta_3$ becomes ligand bound. Further exploration of this phenomenon was possible via examination of the MCS trace over time. The MCS trace displays fluorescence fluctuations over time during the point measurements and can be used to visualise the movement of fluorescently-labelled integrin

molecules passing through the focal volume over the timescale of the FLCS experiment. An example of the MCS traces before and after assembly incubation with activator and fibrinogen is given Figure 53. Un-activated atto655 labelled $\alpha_{IIb}\beta_3$ diffuses through the focal volume regularly with evenly distributed fluorescence bursts during point measurement. (blue) Addition of DTT or Mn^{2+} did not alter the pattern of the MCS trace, nor did fibrinogen alone. However, the addition of fibrinogen to either DTT or Mn^{2+} treated $\alpha_{IIb}\beta_3$ dramatically altered the MCS trace during point measurements. The regular, high frequency of bursts in fluorescence intensity was replaced with less frequent, clustered bursts in the MCS trace (red). This indicates that groups of the labelled proteins are diffusing together through the confocal volume. It is important to note that the sum of fluorescent intensity before and after activation and on fibrinogen addition does not change, so although the integrin proteins diffuse through the focal volume in clusters, the total integrin number remains unchanged.

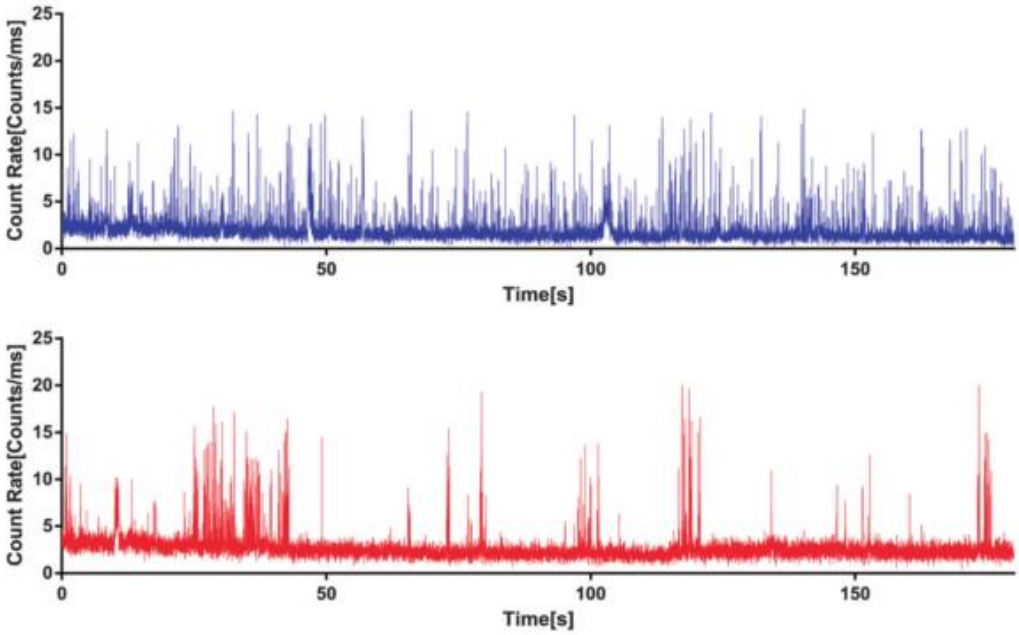

Figure 53: Fluctuating photon-counting time traces, binned at 1 ms resolution, from single point measurements in the plane of the liposome membrane. The upper trace (blue) shows diffusion of un-activated Atto 655 labelled-$\alpha_{IIb}\beta_3$ in nature's own GUVs while the lower trace (red) shows diffusion of DTT activated Atto 655 labelled- $\alpha_{IIb}\beta_3$ in nature's own GUVs following the addition of fibrinogen. The un-activated form of $\alpha_{IIb}\beta_3$ passes through the focal volume with a regular fairly homogeneous frequency. Whereas, fibrinogen bound $\alpha_{IIb}\beta_3$ passes through the focal volume in heterogeneous, irregular bursts, each burst appears to contain clusters of fluorophores migrating together through the focal volume.

3.3.7. Integrin in Raft-Forming GUVs

We had earlier established that it was possible to create raft-forming GUVs via electroformation through the use of lipid compositions with high concentrations of cholesterol and sphingomyelin. These raft-forming GUVs were visualised using lipid probes with affinity for the cholesterol poor liquid disordered phase. Combining this raft-forming composition (50 % DOPC, 25 % CH and 25 % SM (mol/mol)) with our integrin reconstitution method we sought to understand whether $\alpha_{IIb}\beta_3$ favourably associated with the liquid ordered or liquid disordered phase of these GUVs. In the literature this technique has previously been used to investigate the preferential partitioning of other membrane proteins into lipid domains. For example, syntaxin, synaptobrevin and bacteriorhodopsin have been shown to associate with the liquid disordered phase,[36,144] while the GPI-anchored human prion protein, involved in Creutzfeld–Jakob disease associates with the liquid ordered phase.[145] Whereas $\alpha_{IIb}\beta_3$ has been shown in platelets to exhibit low affinity for detergent resistant (cholesterol rich domains),[124] other integrins have been shown in both artificial membrane models and in cells, to exhibit variable affinity for cholesterol rich domains depending on their activation and ligand binding status.[146,147] To data no such investigation has taken place for integrin $\alpha_{IIb}\beta_3$ in artificial lipid systems. Using dual colour confocal microscopy we created raft-forming GUVs with $\alpha_{IIb}\beta_3$ reconstituted within. Figure 54 shows one such dual colour experiment where the lipid has been labelled with the disordered phase probe DiD (left), while the integrin $\alpha_{IIb}\beta_3$ has been labelled with TAMRA (right). As can clearly be seen both probes co-localise. This indicates that $\alpha_{IIb}\beta_3$ has affinity for the phospholipid rich and cholesterol poor liquid disorder phase of raft-forming GUVs.

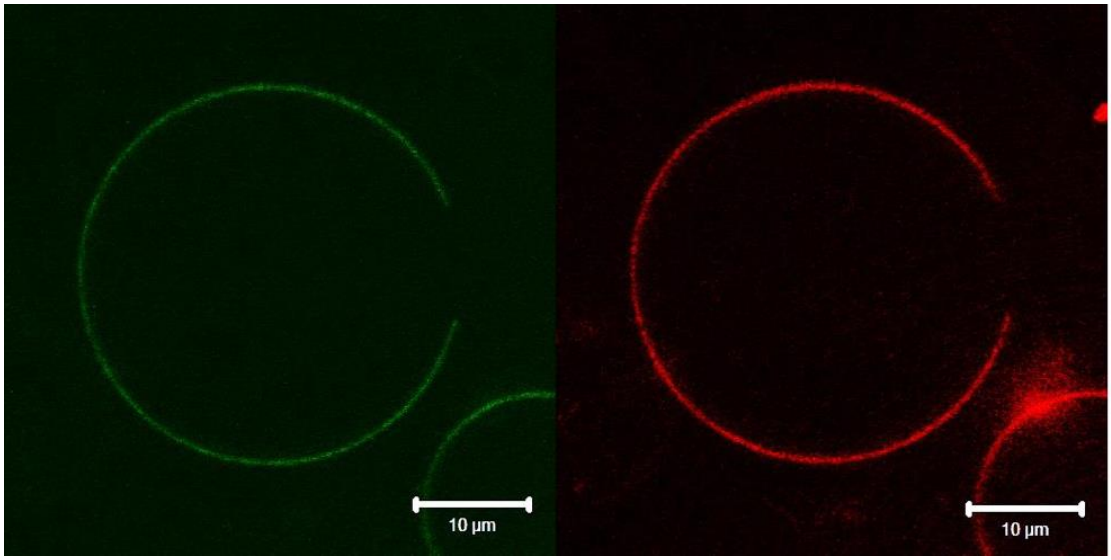

Figure 54: (Left) The liquid disordered probe DiD partitioning into the DOPC rich phase of raft-forming GUVs composed of 50 % DOPC, 25 % CH and 25 % SM. (Right) TAMRA labelled $\alpha_{IIb}\beta_3$ co-localises into the same regions as DiD showing that $\alpha_{IIb}\beta_3$ also has affinity for the liquid disordered phase in raft-forming GUVs.

This observation in raft-forming GUVs is consistent with previous reports on $\alpha_{IIb}\beta_3$ in platelets[124] and with a recent report by Siegel *et al.* on polymer-tethered lipid bilayers of ternary lipid mixtures where they observed that the integrins; $\alpha_V\beta_3$ and $\alpha_5\beta_1$, also sequestered into L_d (cholesterol poor) domains.[146] However, interestingly, this paper also found that exposing these integrins to their native ligands; vitronectin and fibronectin respectively, led to integrin sequestering to liquid ordered (L_o) phase domains or loss of specific sequestering respectively for each integrin. Therefore, we were interested to see if molecular activation and fibrinogen binding of $\alpha_{IIb}\beta_3$ induced similar changes in its domain preference. In an analogous experiment to the FLCS experiment described previously, the integrin activators DTT and Mn^{2+} (0.5 mM to 5 mM) were incubated with $\alpha_{IIb}\beta_3$–reconstituted into raft-forming GUVs in the absence of fibrinogen. Confocal fluorescence microscopy showed this did not alter the partitioning of $\alpha_{IIb}\beta_3$ in the liposomes where the integrin remained sequestered in the L_d regions along with DiD. Furthermore, the addition of integrin activators DTT and Mn^{2+} to $\alpha_{IIb}\beta_3$ in the presence of fibrinogen (0.1 mg/ml) similarly failed to alter its preference for the L_d phase. Therefore, in contrast to Siegel *et alia.* observation of integrins $\alpha_V\beta_3$ and $\alpha_5\beta_1$, $\alpha_{IIb}\beta_3$ does not change its affinity for the L_d phase following either activation or ligand binding in a model membrane.

4. Integrin in SLBs

4.1. Introduction

4.1.1. SLBs

Due to the complexity of the cell membrane an important research objective has been to model this lipid interface *in vitro* to enable study of the unit functions of the membrane and its constituents in a simpler, more controllable system. One of the first attempts to create fluidic planar lipid bilayer systems were black lipid membranes (BLMs). Developed in the 1960s, BLMs consist of phospholipid molecules painted across a small orifice between two solution-filled chambers, rather than above a solid supported substrate used in SLBs.[148] It was not until the 1980s that model systems began to resemble the supported lipid bilayers we recognise today. In one of the earliest papers, simply entitled "Supported Phospholipid Bilayers", Tamm and McConnell were able to form a laterally diffusing lipid bilayer on glass, quartz, and silicon surfaces using a variety of lipids.[149] Supported Lipid Bilayers, or SLBs, are now a commonly used means of mimicking the cell membrane. SLBs can be deposited on a range of different substrates including glass[150], mica[151], silicon wafer[152] and PDMS[153], amongst others. The biggest advantage of SLBs over vesicles systems is their mechanical stability. This allows for a wide range of experimental techniques to be utilised on the bilayer, such as Fluorescence Correlation Spectroscopy[153], Fluorescence Recovery After Photobleaching[30], Atomic Force Microscopy[127], Surface Plasmon Resonance[154] and Ellipsometry[155]. These techniques range from difficult to impossible in freestanding vesicle systems.

SLBs can be formed via a number of methods, perhaps the simplest of which is the spontaneous disruption of SUVs or LUVs onto the substrate surface. Such a protocol involved the creation of vesicles via extrusion or sonication as normal and the later introduction of these vesicles to the surface of a substrate. Vesicles are left in contact with the substrate from minutes to hours where they spontaneously disrupt

to form lipid bilayers. The bilayer itself is not in direct contact with the underlying substrate, but rather separated by an approximate 1 to 2 nm water layer which allows for the diffusion of lipid within the bilayer.[152] Another method of SLB formation utilises the transfer of amphiphilic monolayer films from a water-air interface to a solid substrate. This method is known as the Langmuir-Blodgett (LB) method and can be used to create monolayers, bilayers or even multilayers of lipid (or other amphiphilic molecules).[156] Alternatively, the LB method can be used in conjunction with the vesicle disruption method to form lipid bilayers whereby the first monolayer is formed via the LB transfer of a lipid monolayer and the bilayer is completed via the disruption of SUVs/LUVs to form an SLB.[157]

SLBs have been formed from a wide range of lipid compositions and have been used to for a number of *in vitro* applications. For example, Montero *et al.* used SLBs to study drug interactions with lipid bilayers[158], Richter *et al*. used SLBs to insert membrane proteins within[159], while Mingeot-Leclercq *et al.* describe a method to study lipid raft formation in an SLB.[160] This diverse range of applications for SLBs has in turn lead to the need for a wide range of modifications from standard SLB formation on planar substrates. One of the driving forces behind this diversification is the need for more sophisticated biomimetic models of lipid and protein diffusion, which eliminate the restrictions of non-specific substrate interactions. One such modification is the use of polymer cushions. Polymer cushions provide a soft and deformable layer that separates the lipid bilayer from the underlying substrate. The role of the cushion is to allow for diffusion of the bilayer without non-specific interaction from the planar surface. This can be particularly important in studying membrane proteins as large intracellular (or extracellular) domains of these proteins will interact with the underlying substratein turn leading to protein immobilisation or even protein denaturation. To date polymer cushions have been produced from a number of materials including, but not limited to, polyethyleneglycol[161], cellulose[31] and polydopamine.[162]

Polymer-tethered bilayers have a similar aim to decouple the lipid bilayer from the substrate. They utilise linear polymers to link yet separate the bilayer from the

surface. Wagner *et al.* used polyethyleneglycol as a covalent linker between silane and lipid that allowed for the diffusion of both the lipid bilayer and the diffusion of membrane-reconstituted Annexin V and cytochrome b_5, proteins which were found to be immobile in the absence of the polymer linker.[163] Purrucker *et al.* developed a range of well-defined lipopolymers with a proximal silane coupling group and a distal lipid anchor. The intermediate hydrophilic polymer tether length could be controlled allowing for determination of the distance between the substrate and the bilayer. Using this system they were able to create protein-reconstituted tethered bilayers whereby the membrane proteins (integrin $\alpha_{IIb}\beta_3$) were freely diffusing.[43,44]

Supported vesicular systems bridge the gap between SLBs and vesicle systems. For example, Yoshina-Ishii and Boxer created a system in which a lipid bilayer is firstly created using vesicle disruption. This bilayer contained a short oligonucleotides sequence. Subsequently fresh vesicles displaying the antisense oligonucleotide were flushed over the bilayer. This lead to specific tethering of the intact vesicles to the supported bilayer.[164] Similarly Svedhem *et al.* used cDNA-immobilised on gold to spatially direct DNA labelled vesicles to specific locations on the substrate. The now immobilised vesicles remained intact on the gold surface and available for experimentation.[165]

Another way in which planar lipid bilayers are dissociated from non-specific interactions with the underlying surface is the use of porous substrates where surfaces can be patterned with nano- or micro-cavities and a lipid bilayer can be formed across the cavity-containing surface whereby some regions of the lipid bilayer or in contact with the planar substrate but other regions span the cavities. For example, Romer *et al.* developed a system whereby a lipid bilayer was suspended across a porous alumina substrate allowing decoupling of the lipid membrane from the otherwise planar surface. They utilised this system for electrochemical impedance measurements where they were able to insert membrane proteins into the pore-spanning bilayer.[166] Kumar *et al.* explored methods to create nanopore-spanning lipid bilayers using vesicle disruption. They found that to successfully span bilayers across their nanopore system a number of

criteria had to be met including a minimum liposome to pore diameter ratio, high-curvature pore edges, and a sufficiently strong liposome-substrate adhesion energy.[167] Urban *et al.* presented a method whereby they produced a membrane on nanopore chip containing tens of thousands of nanocavities. The membrane was reconstituted with membrane proteins and was stable across their silicon dioxide substrate. Using this system they studied transport events across the lipid bilayer.[168]

Our novel cavity-spanning bilayer system has a number of advantages of existing systems. For example, many porous systems are limited by their nanoscale size.[167,169] Our PDMS cavities range in size from hundreds of nanometres to 8 μm in diameter. This pore size opens up the system to a new range of experiments such as diffusion measurements via FCS and FLCS, something impossible in nanoscale cavities. Furthermore, our cavities are buffer-filled. This is in contrast to the use of un-filled pores within the literature, which means the spanning lipid bilayer (and any incorporated membrane proteins) are interfaced by an air-filled pocket.[170–172] Our use of buffer-filled cavities therefore has more biologically relevance, particularly in relation to the diffusion of spanning molecules. Both the substrate construction and the bilayer construction are also advantageous. For example, while other other pore-containing systems utilise more complex and labour intensive preparations[173], our PDMS cavities are easily produced in bulk. Likewise, while some techniques utilise high shear stresses and harsh pHs to form spanning bilayers,[174] our method of bilayer construction is well suited to membrane protein inclusion. Our novel system to decouple the bilayer from the underlying substrate has been developed within the group over a number of years. Mallon *et al.* describes the initial steps in the construction of our system whereby polystyrene nanospheres were dropcast onto a glass slide before PDMS was cured above to form a closely packed array of voids imprinted on the PDMS surface.[175] Using this substrate as a base, we were successfully able to expand on this knowledge to produced suspended lipid bilayers with and without the inclusion of various membrane proteins.

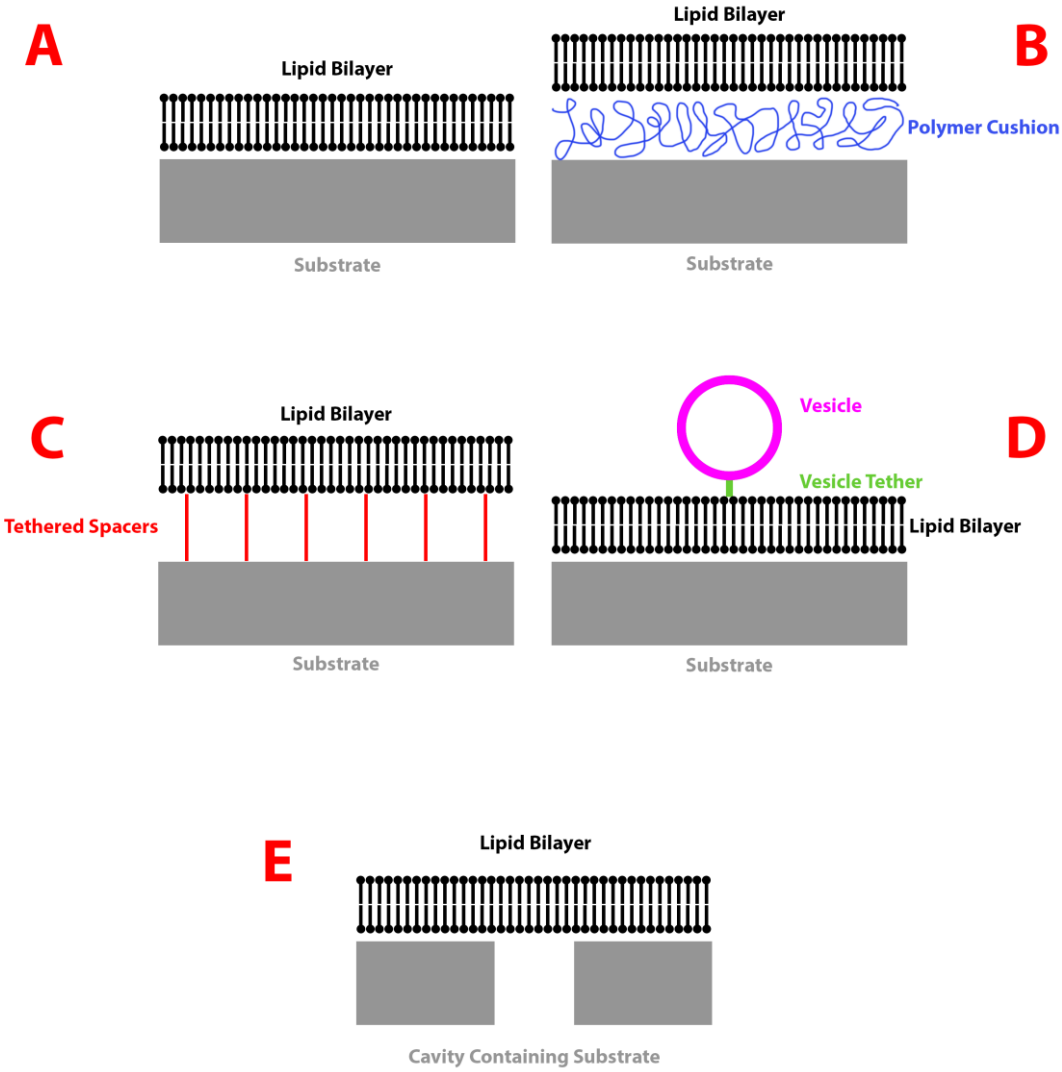

Figure 55: Different types of SLB systems within the literature. A) shows a basic SLB where a lipid bilayer is formed above a planar substrate. The substrate may be made from glass, mica, quartz, amongst others, while the bilayer may be formed via vesicle disruption, LB, LS, or a combination of the above. While easy to form, these simple systems often suffer from non-specific interactions between the substrate and the lipid membrane. This is particularly relevant when bulky membrane proteins are also included. B) One of the most common means of de-coupling the lipid bilayer from the substrate is via the use of polymer cushions. This has been widely used to allow for membrane protein mobility. C) With a similar aim, tethered polymer spacers have also been used to allow for protein mobility be increasing the distance between the substrate and the lipid membrane. D) Bridging the gap between vesicular set-ups and planar bilayers, tethered vesicles grants increased stability to liposome systems. E) The use of porous substrates is another method by which the lipid bilayer may be decoupled from the substrate. These pores have been formed in a variety of ways and across a variety of diameters to allow for the free diffusion of the lipid membrane as well as any reconstituted proteins.

4.1.2. Protein incorporation into our set-up

The ultimate goal of our cavity-containing system was to incorporate integrin $\alpha_{IIb}\beta_3$ into the spanning lipid bilayer. Similar goals have previously been achieved in a number of different ways. For example, glycophorin A is capable of self-incorporation into lipid bilayers[176], and this may be exploited to insert said protein into preformed SLBs *in situ*.[153] In a modification to this method, protein incorporation into preformed SLBs may also be promoted by the use of membrane weakening detergents. For example, using specific concentrations of the detergent β-OG, Hussain *et al.* were able to allow for the partitioning of integrins $\alpha_V\beta_3$ and $\alpha_5\beta_1$ into a bilayer without the destruction of the SLB.[35] On the other hand, the incorporation of membrane proteins into planar bilayers may also be achieved via an intermediate proteoliposomes formation step. In this protocol, membrane proteins are reconstituted into lipid vesicles, before these lipid-protein assemblies are disrupted on a substrate in order to form an SLB.[163] Indeed it is via this scheme that the majority of integrin $\alpha_{IIb}\beta_3$-reconstituted bilayers have been formed.[29–31,34,43,44,46,154]

Given that we had successfully reconstituted integrin $\alpha_{IIb}\beta_3$ into vesicles (Chapter 3), it would appear natural that this method would be ideal for the formation of a cavity spanning, integrin-containing, supported lipid bilayer system. While this $\alpha_{IIb}\beta_3$ reconstitution was eventually achieved, the process was more challenging than first thought and so in the meantime and alternative membrane protein was sought as a proof of concept for our novel cavity-spanning bilayer system. For this role annexin V, also known as annexin A5, was selected. Annexin V was chosen for a number of reasons. For example, it is well characterised in the literature, it is widely commercial available, and the reconstitution process is relatively straightforward. The protein itself is a member of the conserved Annexin multigene protein family. Annexins are characterised by their ability to interact with biological membranes in a calcium dependent manner.[177] They are believed to play a role in exocytosis, endocytosis, cell signalling and may also act as ion channels,[178] at least *in vitro*.[179] Like other members of the protein family, Annexin V features a core domain made

up of four similar repeats, each approximately 70 amino acids long. This core region controls annexin V's ability to bind membranes that contain negatively charged phospholipids in a calcium dependant manner.[180] Interestingly, annexin V is also capable of functioning as a transmembrane protein. At mildly acidic pH, annexin V transitions from its soluble form (in the absence of calcium) or membrane associated form (in the presence of calcium) to its transmembrane form where it functions as an ion channel.[177] It was this characteristic of annexin V to become membrane inserted at mildly acidic pHs that could be exploited in our cavity-spanning system. This insertion process contrasts with protocols required for integrin $\alpha_{iib}\beta_3$ insertion, where the use of detergents was necessary for reconstitution. Owing to this relatively straightforward method of reconstitution, Annexin V was an ideal candidate to evaluate protein diffusion within a cavity-spanning lipid bilayer.

4.2. Experimental

4.2.1. Lipid bilayer formation on a planar substrate

In order to form an SLB via vesicle disruption it was firstly necessary to prepare extruded LUVS. To do so, the desired lipid composition in chloroform was evaporated under a steady stream of nitrogen in a glass vial. A fluorescent lipid probe was usually included for imaging or single molecule techniques. For FRAP experiments the labelled lipid made up 0.1 % of the lipid molecules (molar percentage), while for point measurement experiments such as FLCS the labelled lipid made up 0.001 % of the total lipid molecules (molar percentage). The lipid was then placed under vacuum for at least 2 hours to fully ensure solvent removal. To rehydrate the lipid film, the buffer of choice (Tris, HEPES, or PBS) was added to the glass vial and mixed so that the rehydrated lipid was at a concentration between 1 and 2 mM. The lipid suspension was left to stand above the highest phase transition temperature for at least 45 minutes with occasional vortexing. The lipid solution was extruded through an Avanti mini-extruder extruder (Avanti Polar Lipids, Alabaster, AL) that was assembled as before. Once the lipid solution was extruded 11 times the LUVs could be stored for up to 5 days at 4 °C. The bilayer could be formed on a number of substrates such as glass, mica, or PDMS. In all cases the substrate was firstly placed in Harrick PDC-002 plasma cleaner at 1000 mT for 5 minutes. The substrate was then assembled as part of a temperature control cell (Focht Chamber System 2) or “home-made” PDMS cell. The LUVs were diluted to a concentration of approximately 0.3 mM and then injected into the now assembled flow cell. The LUVs were left in contact with the substrate for at least 30 minutes to allow for the spontaneous rupture of the vesicles and thus the formation of a lipid bilayer. In order to remove any remaining un-disrupted LUVs or other lipid fragments the flow cell was then flushed with buffer leaving behind only the SLB. In order to confirm the

formation of the SLB the substrate surface was examined via confocal microscopy for fluorescently labelled lipid.

4.2.2. PDMS fabrication

In order to construct PDMS cavities, mica was freshly cleaved to provide an ultraflat surface for later polystyrene sphere deposition. This mica was then carefully glued to a glass slide to provide a platform for PDMS pouring. It was important to minimise the thickness of the glued mica sheet as the working distance of the microscope objective needed to be greater than this thickness for later confocal and FCS experiments. If required, the mica, glued to the glass slide, was carefully cleaved with sticky tape to further reduce its thickness. Once the mica thickness was judged to be sufficiently thin, polystyrene spheres at 0.1 % w/v were pipetted onto the mica surface. Our group has used a variety of polystyrene spheres with diameters ranging from hundreds of 100 nm to 10 µm in various experiments. However, for simplicity this thesis only focuses on PDMS cavities constructed from polystyrene spheres with a diameter of 2.88 µm. The volume of the 2.88 µm polystyrene sphere solution, now at 0.1 % w/v, varied in accordance with the size of the mica sheet, but approximately 150 µl of the sphere solution was used per 1cm^2 mica sheet. The solution was subsequently allowed to evaporate over a 24-hour period in order to yield a mica surface with immobilised polystyrene spheres left behind. In order to prepare the PDMS solution, 10 parts PDMS elastomer to 1 part PDMS curing agent were mixed (w/w). Approximately 3 g of final solution was required per PDMS cavity array. The PDMS was thoroughly mixed and then placed in a vacuum desiccator for 30 minutes to ensure that all air bubbles were removed. Meanwhile, an aluminium foil “boat” was folded around the mica-glass slide platform. The now bubble free PDMS solution was then carefully poured into this foil. The array was then placed on hotplate which had been preheated to 150 °C and cured over a 15-minute period. Once complete the PDMS arrays were removed and left to cool before the aluminium foil was peeled from the substrate. Using a scalpel, the PDMS was then cut from the glass-mica platform to yield an imprinted PDMS array. The PDMS was

then immersed in a THF solution for 10 – 15 minutes in order to dissolve any remaining polystyrene spheres. During this time the THF was stirred and the PDMS pieces were occasionally removed from the solution to detach any remaining mica. Once the time had elapsed the THF was poured off and the PDMS was left in the fume hood overnight. During the THF treatment the PDMS swelled and warped but returned to its original dimensions a number of hours later. These cavity arrays could be kept in a dust free environment for an indefinite period of time. A diagram of these PDMS fabrication process is shown below in Figure 56.

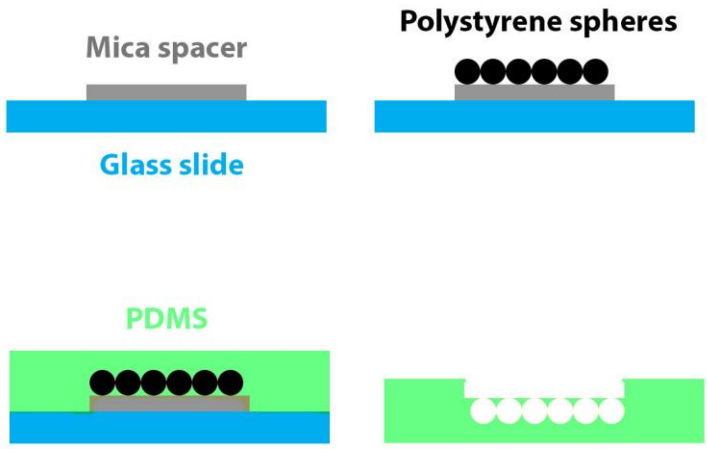

Figure 56: Construction of PDMS cavity arrays. Construction began with the gluing of a mica spacer to a glass slide. This acts as the platform for deposition of the polystyrene spheres. It was important to minimise the thickness of the glued mica sheet as this sheet defined the distance between the cavities and the opposing cover slip that would later be glued to complete the cell. If the distance was too great, then the objective would not have a sufficient enough working distance to image the cavity-spanning bilayer. Next, polystyrene spheres were deposited on the mica and allowed to air dry overnight. This diameter of these spheres controlled the size of the cavities. PDMS was then poured atop the spheres and allowed to cure at 150 °C. The cured array was then pealed from the support and placed in THF to dissolved any remaining polystyrene, leaving behind the finish PDMS cavity array.

4.2.3. Cavity spanning

Due to the hydrophobic nature of PDMS, buffer filling of the cavities for lipid bilayer spanning required that the substrate be rendered hydrophilic. This was achieved via air-plasma treatment of the PDMS array. To do so, the PDMS was placed in a Harrick

PDC-002 plasma cleaner at 1000 mT for 5 minutes. Immediately following plasma treatment, the PDMS was sonicated for 1 hour in the buffer of choice. This combination of plasma treatment and sonication was essential for the majority of cavities to be buffer filled.

In order to then create a cavity-spanning lipid bilayer across the buffer-filled cavities, a number of different techniques were explored. The first of these was the direct disruption of extruded LUVs atop the PDMS surface. It was hoped that the buffer filling of the cavities would allow for the formation of a continuous bilayer. This was later changed to the disruption of electroformed GUVs via the incubation of these giant vesicles in contact with the PDMS surface and in the presence of a buffer containing 30 mM $CaCl_2$. Finally, and most successfully, a 2-step protocol that combined both Langmuir Blodgett (LB) and vesicle disruption was utilised to create a continuous bilayer.

This 2-step protocol was based on the work by Klab *et al*.[157] Firstly, a monolayer of the desired lipid composition was formed onto the air-water interface of a NIMA 120m Langmuir trough by spreading 150 µL of a chloroform solution of the appropriate lipids at 50 mg/mL. For single molecule measurements, DOPE-Atto532, DOPE-Atto655 or another appropriate probe was included at a concentration of approximately 0.001 mol %. The chloroform was allowed to evaporate for at least 30 minutes, after which the lipids where compressed at a barrier speed of 30 cm/min to a surface pressure of 32-36 mN/m. (Figure 58) Surface pressure was measured using a paper Wilhemy plate. Holding the surface pressure constant, the substrate was rapidly lowered into the dipping well at a dipper speed of 67 mm/min and slowly withdrawn at a dipper speed of 5 mm/min to allow the transfer of a monolayer onto the surface. Once the monolayer was formed, two holes where punched at the extremities of the PDMS and at this stage the substrate was glued to a cover glass slide using epoxy glue to obtain the flow chamber. Teflon tubing was attached to the two holes to allow the circulation of solution into the flow chamber.

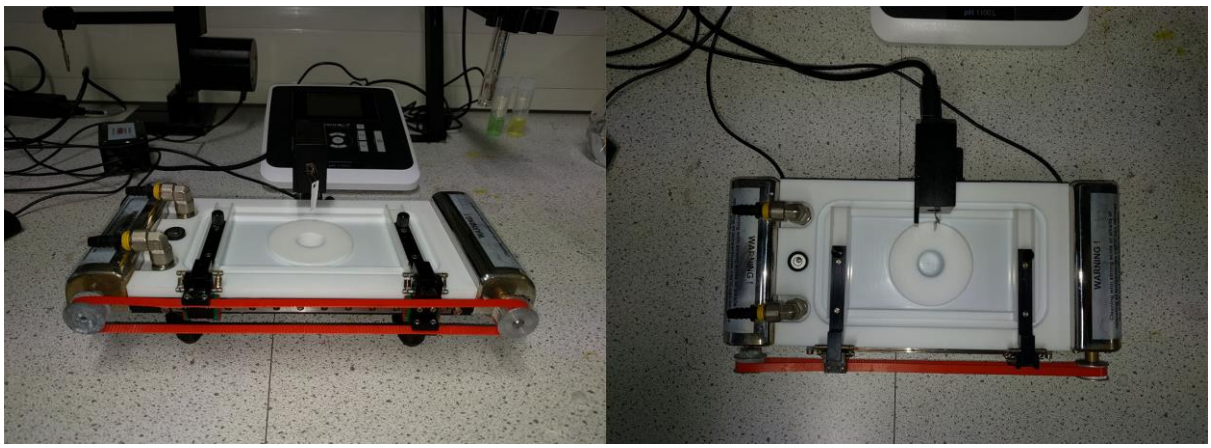

Figure 57: A NIMA 120m Langmuir trough. The trough was filled with buffer and the lipids of choice were deposited at the air-water interface. After evaporation of the solvent, the lipid was compressed to 32-36 mN/m. A buffer-filled cavity-containing PDMS array was dipped into the trough in order to transfer the lipid monolayer to the substrate. Two holes where punched at the extremities of the PDMS and at this stage the substrate was glued to a cover glass slide using epoxy glue to obtain the flow chamber. Teflon tubing was then attached to the PDMS array to allow for buffer circulation.

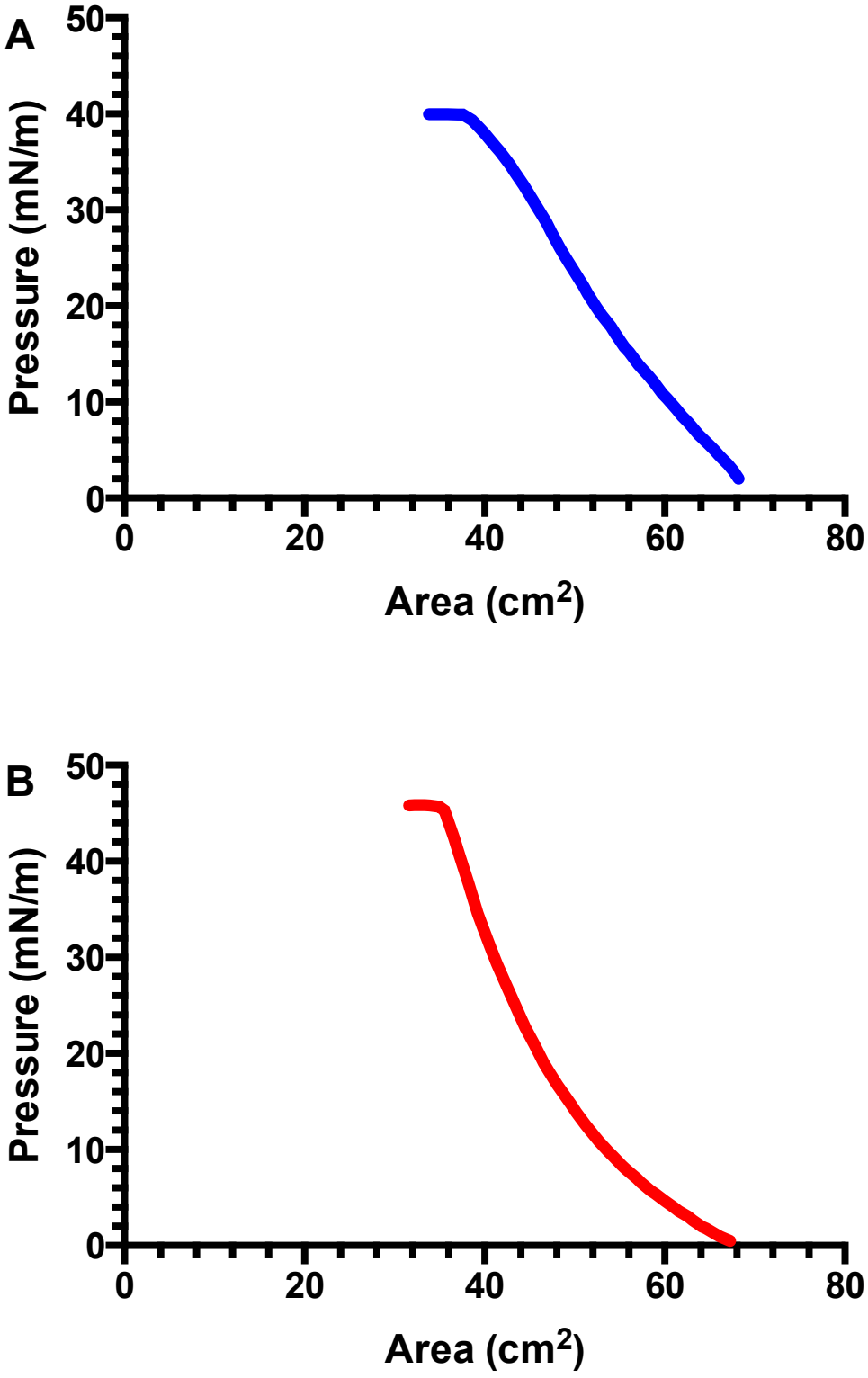

Figure 58: Examples of typical LB isotherms before PDMS dipping and lipid transfer. A) shows an isotherm of a pure DOPC while B) shows an isotherm of the nature's own mixture. The lipids were compressed at a barrier speed of 30 cm/min to a surface pressure of 32-36 mN/m for the lipid monolayer transfer process.

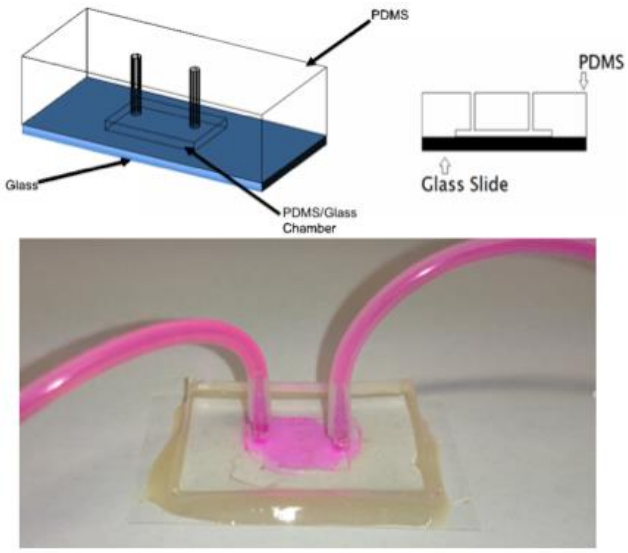

Figure 59: Completion of the PDMS cell. After production of the PDMS array, sonication was used to fill the cavities with buffer. LB was then used to transfer a lipid monolayer to span the buffer-filled cavities. Teflon tubing was then attached to the the array to provide a flow-cell set-up. Here, the cell has been flushed with dye so that the flow chamber can be better visualised.

To complete the bilayer, the vesicle disruption method was utilised. Extruded LUVs of the desired composition were created via extrusion as normal using the required buffer. The LUVs were then diluted to a concentration of 0.3 mM before being injected into the cell via the Teflon tubings. The LUVs were incubated at room temperature for 30 minutes to allow for the vesicles to distrust above the LB transferred monolayer. After the elapsed time un-disrupted LUVs and excess lipid were flushed from the cell with additional buffer. This protocol yields a lipid bilayer that spans the PDMS cavities.

4.2.4. Microscopy of cavities

Due to the refractive index difference between the PDMS (n ≈ 1.45) and the buffer (n ≈ 1.33), as well as the way in which incident laser light scatters at the site of cavities, reflectance images could be used to identify cavities. In fact, filled and un-filled cavities could readily be differentiated due to the degree of scattering where buffer-filled cavities were more intense than un-filled cavities in reflectance images. Cavities were imaged using a MicroTime 200 fluorescence lifetime microscope

system (PicoQuant GmbH, Berlin, Germany). For imaging of reflectance an OD3 filter was used to attenuate the signal obtained by the detectors 1000 fold.

4.2.5. Fluorescent imaging of the bilayer

Enabled by the inclusion of a fluorescently lipid probe, confocal microscopy was used to observe the lipid bilayer. This also allowed for confirmation that the lipid bilayer spanned the cavities of the PDMS arrays. Confocal images were taken using the same MicroTime 200 fluorescence lifetime microscope system. Fluorophores were excited with 532 nm PicoTA or 640 nm light from a LDH-P-C-640B diode laser. The laser was directed toward a z532/635rpc dichroic mirror and focused on a water immersion objective (NA 1.2 UPlanSApo 60 x 1.2 water/ CC1.48, Olympus). The sample fluorescence was collected through the same objective and filtered by the aforementioned dichroic mirror, as well as by an HQ550lp AHF/Chroma filter (Olching, Germany) for the 532 nm laser, or a BLP01-635R-25 Semrock filter (New York, USA) for the 640 nm laser. Finally, the sample fluorescence was passed through a 50 mm pinhole onto a MPD SPAD detector.

4.2.6. Single molecule experiments

Diffusion coefficients for labelled integrin or lipid were obtained using Fluorescence Lifetime Correlation Spectroscopy, FLCS. The autocorrelation functions obtained using FLCS are less prone to noise and distortion caused by scattered excitation light, detector thermal noise and detector afterpulsing than conventional FCS.[67] FLCS measurements were performed using a MicroTime 200 confocal fluorescence lifetime microscope system. For FLCS experiments, the fluorophores were excited as before and the sample fluorescence was also collected as described for confocal microscopy. The autocorrelation functions (ACF) were fit using SymphoTime software (PicoQuant GmbH, Berlin, Germany):

$$G(\tau) = 1 + \left[\frac{1}{N}\right]\left[\frac{1}{1 + (\tau/\tau_D)^{\alpha}}\right]$$

For simple single component diffusion, or in the case of the presence of a triplet state:

$$G(\tau) = 1 + [1 - T + Texp(-\tau/\tau_T)]\left[\frac{1}{N(1-T)}\right]\left[\frac{1}{1 + (^{\tau}/_{\tau_D})^{\alpha}}\right]$$

where G(τ) is the autocorrelation function of fluorescence fluctuations; N is the number of fluorophores in the effective volume; T is the fraction of the molecules in the triplet state; τ_T is the relaxation time for the singlet–triplet crossing; α is the anomalous parameter; and τ_D is the diffusion time, which is related to the lateral diffusion coefficient of the labelled tracer by the expression:

$$\tau_D = \frac{\omega^2}{4D}$$

In the latter equation, the radius ω_0 is the distance at which the excitation intensity profile decreases to e^{-2} of its maximum value. This parameter was determined experimentally, by measuring the translational diffusion of Rhodamine 6G (532 nm laser) and Atto655 (640 nm laser) in water at room temperature (approximately 21 °C).[137] These dyes, have well characterized diffusion coefficients and so were used as standards to determine the working confocal volume for FLCS measurements. Before performing point measurements on bilayers the surface was imaged in the XY direction for both fluorescence and reflectance in order to better target MCS or FLCS measurements (ie to differentiate between planar and cavity regions of PDMS). This allowed for selection of the XY coordinates for upcoming measurements. On the other-hand, the Z-position was firstly roughly tuned using the built in CCD camera of the microscope. This allowed us to identify the approximate Z-position of planar substrates. To fine-tune this position to the lipid bilayer, a Z-scan was then quickly performed to locate the point of highest fluorescence intensity due to the presence of fluorescently-labelled lipid within the bilayer. Due to drift within the system the Z-position was recalibrated between each point measurement.

4.2.7. Atomic Force Microscopy

For AFM characterisation of the PDMS cavity arrays a Digital Instruments Bioscope II AFM system was utilised. For imaging, contact mode was used under dry conditions. To begin imaging a commercial Si_3N_4 cantilever tip with spring constants between 0.04 and 0.08 N/m was inserted into the tip holder, placed into the prongs of the Bioscope II head, and the head was then positioned onto the EasyAlign base. The laser beam was positioned on the back of the cantilever where a sum signal of approximately 5 V was obtained. The exact value of this is dependent on the reflective properties of the material and the geometry of the probe. The position of the laser spot in the photodetector was adjusted using the adjustment knobs on the Bioscope II head where the red dot was centred in the BioScope head filter screen. The vertical position was set to -2 V and the horizontal position to 0 V. The PDMS cavity sample was placed on the Bioscope stage and clamped in place. The Bioscope head was then moved to the Bioscope stage above the sample. The cantilever was then lowered toward the sample until the tip was almost in contact with the PDMS. Before engagement the scan properties were set to their default values (Deflection gain of 0 V, integral gain of 0.5 V, proportional gain of 1, scan angle of 0 degrees, scan rate of 1 Hz). Following that the tip was slow engaged to the sample. Channel 1 was used to monitor height while channel 2 was used to monitor deflection error. The scanning parameters of the experiment were optimised if necessary with particular attention placed on integral and proportional gain. Once imaging was complete the AFM tip was withdrawn and the images saved for analysis.

4.2.8. Annexin V reconstitution

For annexin V experiments, bilayers composed of 80% DOPC and 20% DOPS (molar percentages) were created via a combination of LB and vesicle deposition as used by Klab *et al*.[157] Unlike integrin insertion in the literature, annexin V has been

membrane-reconstituted without the need for detergent-mediated insertion. The protocol we used was based on the technique used by Diaz *et al.*,[181] with some modifications. Atto 547N-labelled annexin V (Enzo Life Sciences, Exeter, UK) in an insertion buffer of 10 mM sodium acetate, 100 mM NaCl, 1 mM CaCl2, pH 5.5 was injected into the flow cell and incubated at room temperature for 1 hour. At this pH and under these conditions the annexin V protein should insert itself into the bilayer. To remove any unincorporated protein, the cell was extensively flushed with a buffer of 10 mM sodium acetate, 100 mM NaCl, 5 mM EDTA, pH 5.5. Finally, the cell was injected with a working buffer of 10 mM sodium acetate, 100 mM NaCl, pH 5.5 before FLCS measurements began.

4.2.9. First integrin reconstitution method

The initial protocol for the reconstitution of $\alpha_{IIb}\beta_3$ in a supported lipid bilayer was based on Müller *et al.*[34] Desired lipids were mixed and evaporated in a glass vial under a stream of nitrogen. The lipid, was completely solubilised in a HEPES reconstitution buffer (10 mM HEPES, 150 mM NaCl, 1 mM $CaCl_2$, 0.1% Triton X-100 (w/v), pH 7.4) with a final detergent:lipid ratio of 2:1 (w/w). The final lipid concentration was normally 1 mM. $\alpha_{IIb}\beta_3$ (Enzyme Research Laboratories, Swansea, UK) in HEPES reconstitution buffer was then added to the detergent-lipid solution at the required concentration, normally 1 integrin molecule for every 8000 lipid molecules. The protein-containing solution was shaken at room temperature for 30 minutes to fully ensure that all lipid has been solubilised and that the solution was homogeneous. The solution was then incubated at 37 °C for 1 hour 30 minutes. Detergent was removed by the addition of 100 mg of bio-beads per ml of solution for 3 hours 30 minutes in a slow shaken vial. The biobeads were then removed and replaced by a fresh batch of 100 mg biobeads per ml of solution for 30 minutes (slowly shaken). In order to separate non-incorporated protein from the proteo-liposomes ultracentrifugation across a four-step sucrose gradient was used. From bottom to top of the ultracentrifuge tube 0.8 ml of 2 M, 1.2 M, 0.8 M and 0.4 M sucrose was used. The proteoliposome solution was then stacked on top of the 0.4

mM solution and the tube was carefully loaded into the ultracentrifuge and centrifuged for 20 hours at 275,000 g. Following the centrifugation step the protein-reconstituted vesicles could be visualised as a thin white layer within the tube. (Figure 60) The layer was carefully pipetted out of the tube and dialysed against a HEPES buffer (10 mM HEPES, 150 mM NaCl, 1 mM $CaCl_2$, pH 7.4) to remove any remaining sucrose. The proteoliposomes were stored at 4 °C for up to a week. When an integrin-reconstituted bilayer was required the solution was added above the substrate, usually in a flow cell, and left to disrupt over a 30 minutes period as was the case with protein free vesicles. After flushing the cell with buffer the bilayer could be probed as required.

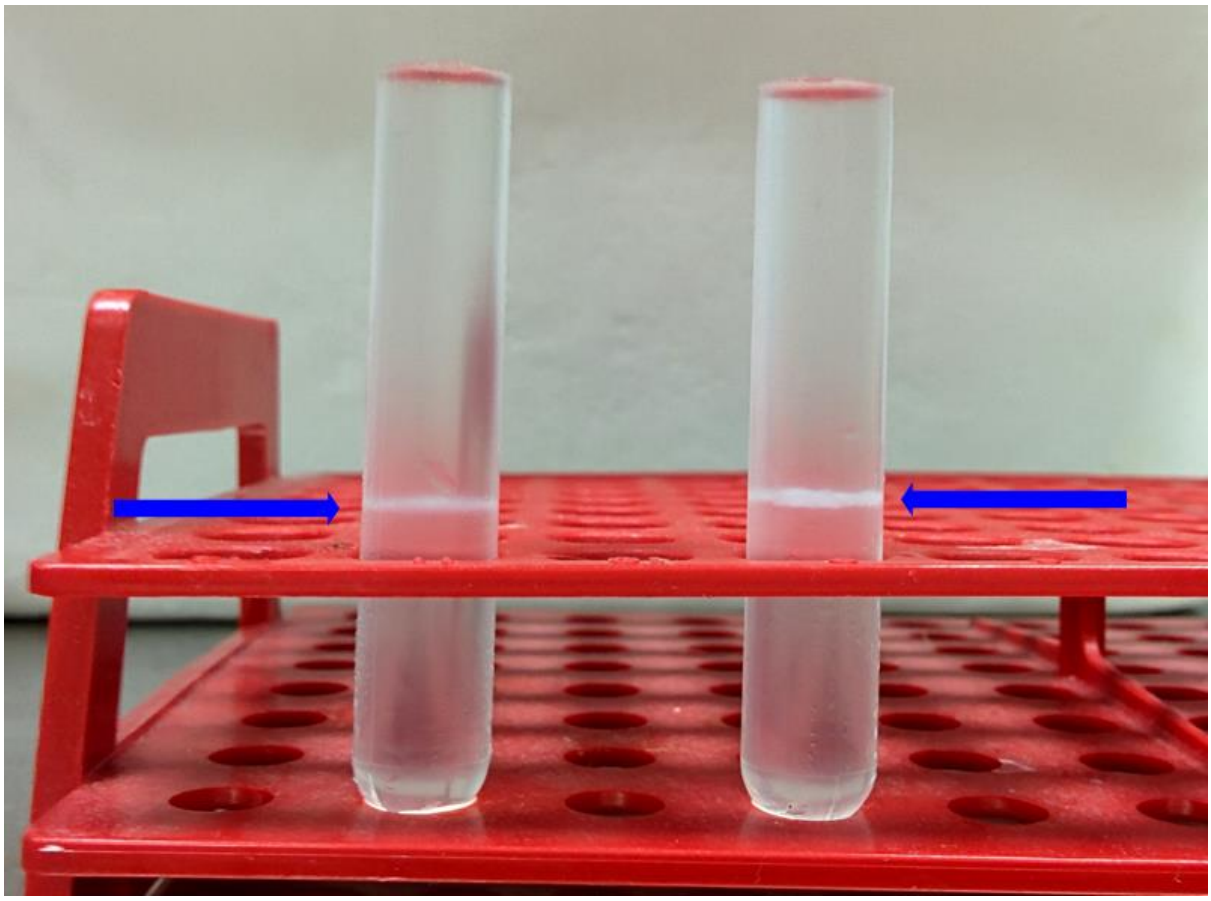

Figure 60: Proteoliposomes separated from un-incorporated protein via sucrose gradient ultracentrifugation. The proteoliposomes were easily visible as thin white layer within the sucrose solution as shown by the blue arrows.

4.2.10. Alternative integrin reconstitution method

A novel integrin insertion method was later developed to insert $\alpha_{IIb}\beta_3$ into non-DMPC-containing lipid compositions. The protocol began with the creation of integrin-reconstituted proteoliposomes as per the Müller method. Following detergent removal via bio-beads the vesicles were loaded into an ultracentrifuge tube and centrifuged at 100,000 g for 1 hour. This resulted in the pelleting of the protein-reconstituted liposomes. The supernatant was removed and the pellet was gently washed in dH_2O to eliminate any remaining salts. This pellet was then re-suspended in dH_2O at a lipid concentration of 10 mM. The re-suspended vesicles could then be stored at -20 °C for a number of weeks. When required, the solution was thawed and 2 µl droplets were placed on the conductive side of an ITO glass slide of the Vesicle Prep Pro (VPP). The slides were placed in a vacuum desiccator in the presence of a saturated sodium chloride solution resulting in a relative air humidity of 73%. The lipid in buffer was left to partially dehydrate for between 2 and 20 hours. Once complete the electroformation cell of the VPP was assembled as before, filled 100 mM sucrose in HEPES buffer, and the electroformation protocol was started. In order to successfully create GUVs in a salt buffer the voltage was ramped up over 1 hour from 0 to 1.2 V, before being held constant at 1.2 V for 13 hours. This took place at 500 Hz in comparison to the frequency of between 2 and 12 Hz normally used for electroformation in a salt free buffer. The voltage was then ramped down from 1.2 to 0 V over the final hour while the the frequency was held constant at 500 Hz. The electroformation process was carried out at room temperature. This process yield GUVs from a wide range of lipid compositions reconstituted with $\alpha_{IIb}\beta_3$. These GUVs did not readily disrupt above planar substrates or lipid monolayers in contrast to smaller SUVs or LUVs. Therefore, to initiate vesicle rupture the GUVs had to be incubated in the presence of calcium. To do so, GUVs mixed with an equal volume of glucose-containing buffer (eg for GUVs in a buffer containing 10 mM HEPES, 150 mM NaCl, 1 mM $CaCl_2$, pH 7.4, 100 mM sucrose the solution was mixed with 10 mM HEPES, 150 mM NaCl, 1 mM $CaCl_2$, pH

7.4, 100 mM glucose). $CaCl_2$ was then added to the buffer so that the final concentration was 30 mM. The solution was then injected into the desired flow cell, normally a PDMS cavity array, and the sucrose-containing GUVs were allowed to fall to the bottom of the cell. The cell was left at room temperature for 1 hour, which allowed for the GUVs to rupture above the substrate. When using PDMS arrays this disruption process took place an already created LB monolayer although the same process could also be done above a solid planar substrate.

4.2.11. Determination of integrin orientation

In order to determine the orientation of the reconstituted $\alpha_{IIb}\beta_3$ within the bilayer a protein-cleaving enzyme was used. Proteinase K is a serine protease that predominantly cleaves peptide bonds adjacent to the carboxyl group of aliphatic and aromatic amino acids with blocked alpha amino groups. Due to the fact that the labelling ratio of $\alpha_{IIb}\beta_3$ was 1:1 and this labelling took place in the integrin headpiece only properly orientated integrin proteins were physically available to larger molecules that were flushed across the bilayer. With a molecular weight of 28 kDa proteinase K only had access to the regions of the integrin protein facing away from the underlying substrate. Although both downwards and upward facing $\alpha_{IIb}\beta_3$ proteins were likely to be partially digested by the enzyme, only properly orientated integrins were likely to lose their fluorescently-labelled portion. Proteinase K was injected into the cell containing the already formed integrin reconstitution bilayer at a concentration of 0.01 mg/ml and incubated at room temperature for 2 hours. Once the digestion was complete the cell was then flushed with buffer to remove digested protein fragments. The bilayer was imaged for fluorescence before and after the digestion process and the mean fluorescence per pixel was compared. Any reduction in fluorescence would be due to cleavage of properly inserted integrin and this could be used to determine the percentage of $\alpha_{IIb}\beta_3$ proteins that were properly or improperly orientated.

4.3. Results

4.3.1. Creating a supported lipid bilayer on glass

Before work began on our novel microcavity arrays, we first looked at forming SLBs on planar substrates. Using the vesicle disruption method, it was possible to routinely create a homogenous and laterally diffusing lipid bilayer on plasma-cleaned glass. Initial experiments used DOPC as the primary lipid component with fluorescently labelled DOPE used as the probe at a concentration of approximately 0.001 % (mol/mol). (Figure 61) Later experiments expanded on this composition to also include various combinations of DOPE, DOPS, DMPC, DMPG, cholesterol, and sphingomyelin, amongst others. We were particularly interested to use the Lentz Group's nature's own composition in our experiments. While we had previously created GUVs using this mixture, it had not been previously utilised to create SLBs. As with simple lipid compositions, it was also possible to create nature's own SLBs on plasma-cleaned glass. (Figure 62)

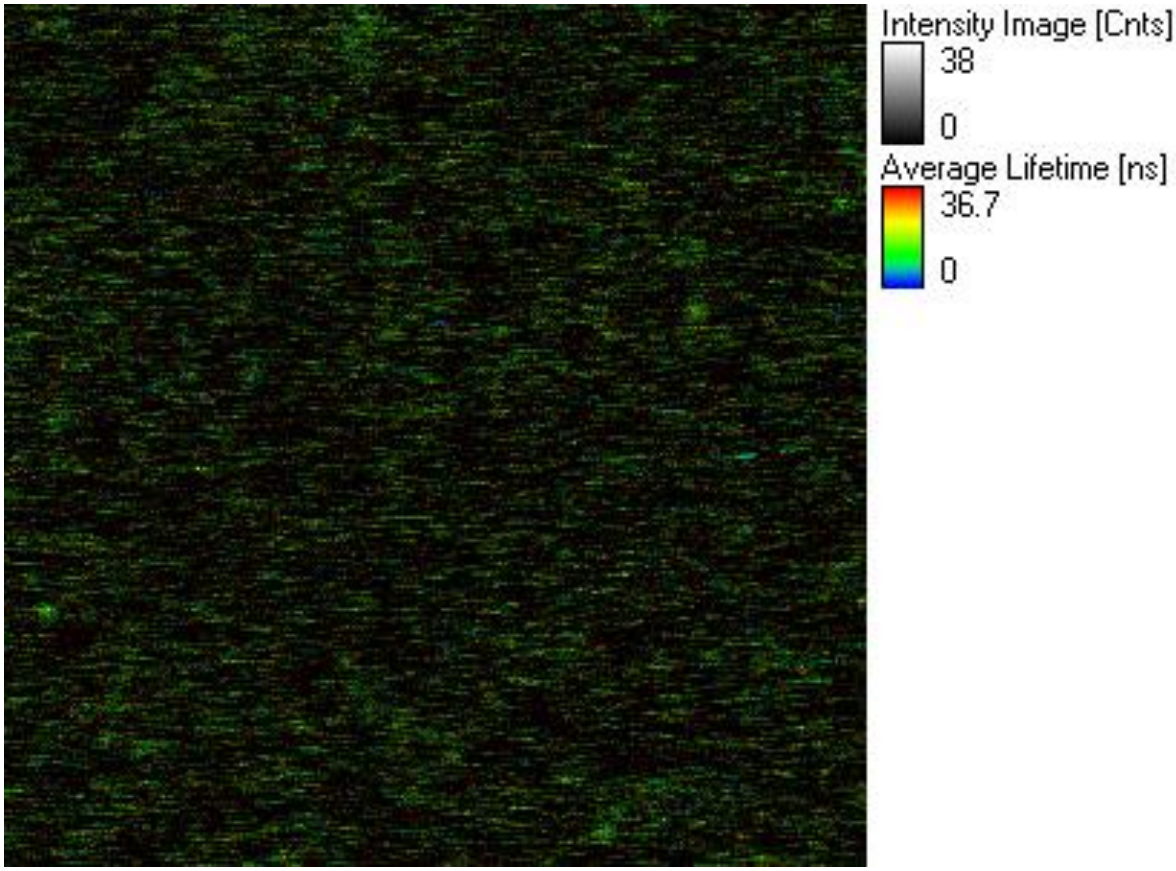

Figure 61: A DOPC bilayer created above a plasma-cleaned planar glass substrate. 0.001 % of the lipid was made up of DOPE-Atto655 which allowed for fluorescence microscopy to be used to image the lipid bilayer. The completed bilayer was continuous and defect free. FCS and FCLS measurements could be subsequently carried out on the SLB.

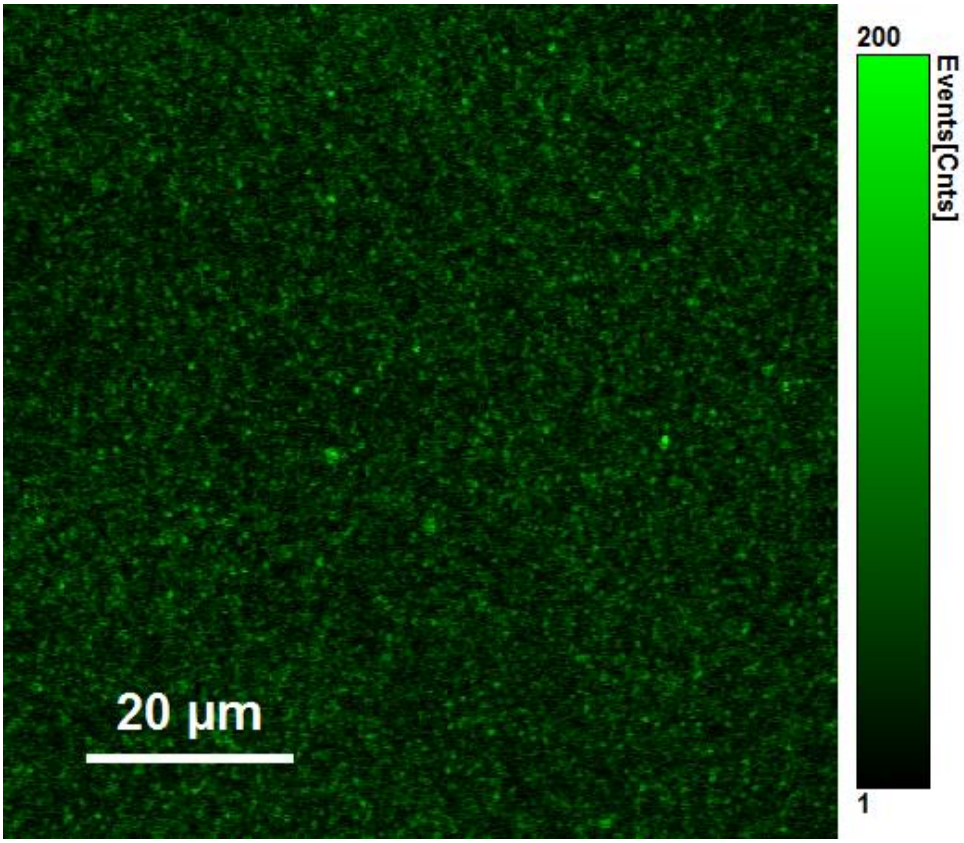

Figure 62: A nature's own bilayer created above a plasma-cleaned planar glass substrate. 0.001 % of the total lipid was made up of DOPE-Atto655 which allowed for fluorescence microscopy to be used to image the lipid bilayer. As was the case for less complex lipid compositions, the completed nature's own bilayer was continuous and defect free. FCS and FCLS measurements could be subsequently carried out on the SLB.

In order to demonstrate the temperature dependence of lipid diffusion, DOPC SLBs were created in a temperature controlled flow cell and FLCS measurements were performed at 21, 25, 30 and 37 °C. As expected, increasing temperature leads to an increase in the lateral diffusion co-efficient of the lipid bilayer. As can be seen in Figure 63, increasing temperature leads to a shift in the ACF curve to the left indicting the fluorescently-labelled probe spends less time in the confocal volume and thus was diffusing faster than the same probe at lower temperatures. The diffusion co-efficient of a DOPC SLB on plasma-cleaned glass was found to be 3.72 ± 0.52 $\mu m^2/s$ at 21 °C. Increasing the temperature to 25 °C resulted in a diffusion co-efficient of 6.07 ± 0.55 $\mu m^2/s$, while at 30 °C the diffusion co-efficient was found to be 8.25 ± 0.77 $\mu m^2/s$. Finally, at 37 °C, the diffusion co-efficient of a DOPC bilayer was found to be 14.25 ± 1.43 $\mu m^2/s$. These diffusion co-efficient are shown in Figure 64. In all cases the alpha value was determined to be approximately 1, indicating

Brownian diffusion. Only when the underlying glass substrate was not plasma-cleaned was the alpha value found to indicate hindered diffusion (0.6 – 0.9).

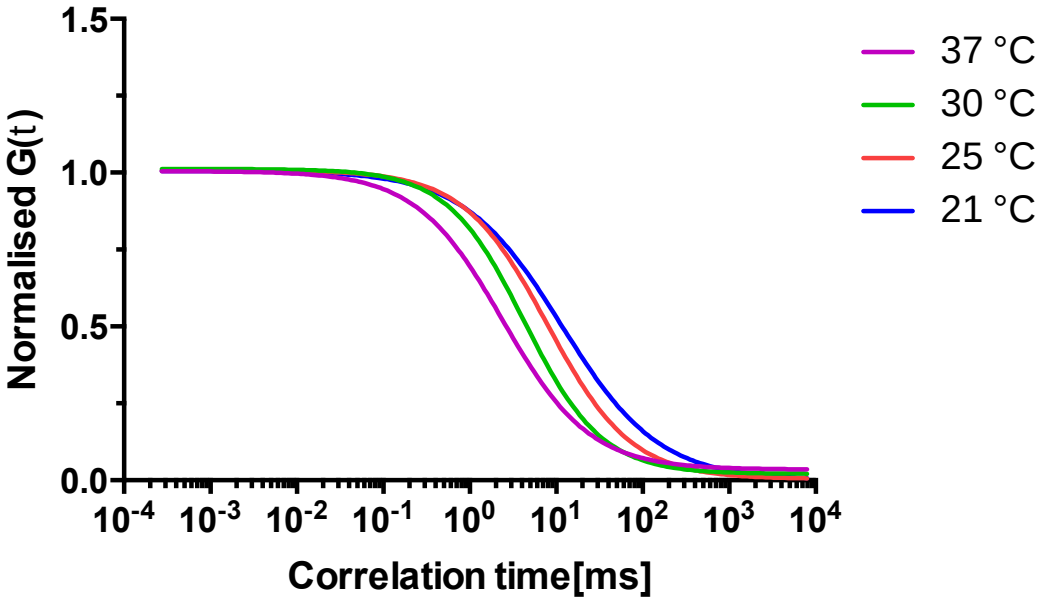

Figure 63: Two-dimensional fits to the ACF trace of DOPE-Atto655 in a DOPC bilayer on plasma-cleaned glass at 21, 25, 30 and 37 °C. As expected, increasing temperature leads to an increase in the lateral diffusion coefficient of SLBs. This can be seen where the fluorescent molecules spend less time within the focal volume and the ACF decays towards zero faster.

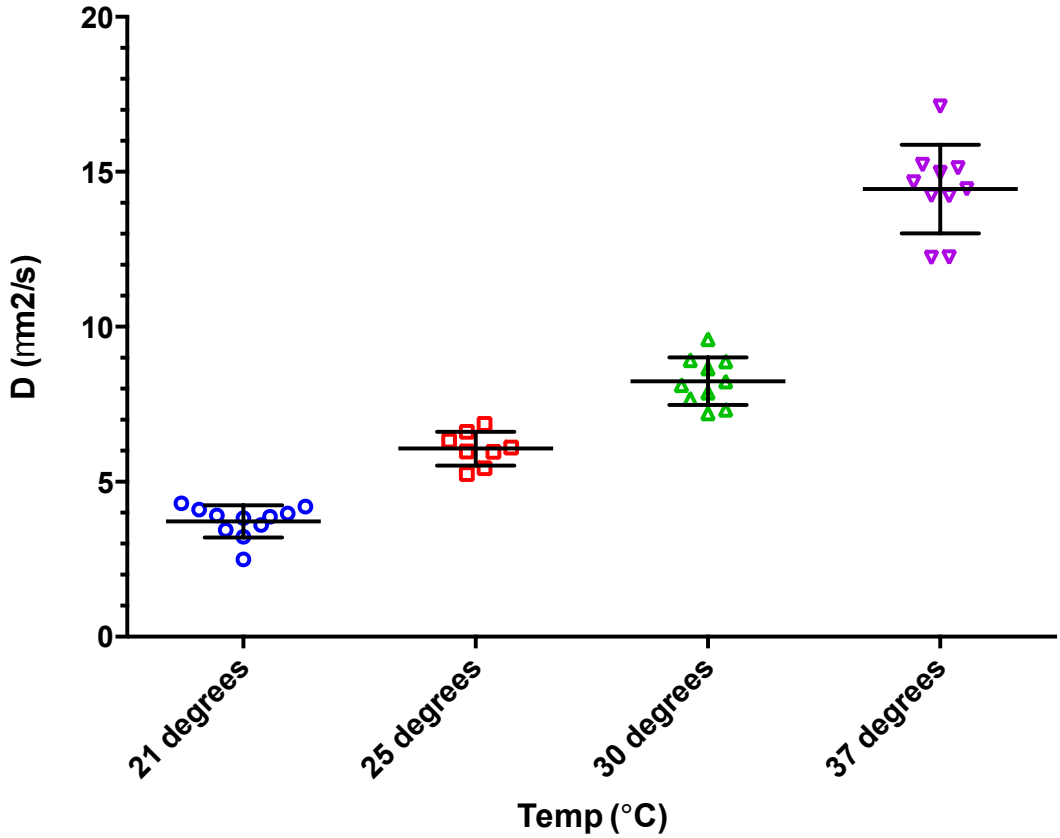

Figure 64: Diffusion of DOPE-Atto655 in a DOPC SLB on plasma-cleaned glass. Increasing temperature resulted in an increase in the determined diffusion co-efficient. Each point is a 60 – 180 seconds FLCS measurement of the lipid bilayer fitted to a two-dimensional model. Standard deviation was used to report the error.

As well as temperature, another major influence on the lateral diffusion co-efficient of an SLB is the lipid composition. A wide variety of lipid compositions were used in SLB experiments but for comparison the diffusion co-efficient of a DOPC bilayer is contrasted with a nature's own lipid bilayer below. Nature's own contains both cholesterol and sphingomyelin leading to a more ordered and rigid lipid bilayer when compared with a pure DOPC bilayer. Thus, the diffusion co-efficient of nature's own SLBs would be expected to be lower than DOPC at the same temperature. The diffusion co-efficient of a nature's own SLB on plasma-cleaned glass was found to be 2.58 ± 0.65 $\mu m^2/s$ at 21 °C. Increasing the temperature to 25 °C resulted in a diffusion co-efficient of 3.81 ± 0.54 $\mu m^2/s$, while at 30 °C the diffusion co-efficient was found to be 6.65 ± 0.73 $\mu m^2/s$. Finally, at 37 °C, the diffusion co-efficient of a nature's own bilayer was found to be 12.43 ± 0.90 $\mu m^2/s$.

As with the DOPC SLB, the alpha value was consistently found to be 1 as long as the plasma cleaning process was properly carried out on the underlying glass substrate. Thus, the diffusion of the nature's own bilayer can also be described as Brownian. Nature's own diffusion co-efficients are shown in Figure 65, while a comparison of the diffusion co-efficients of DOPC versus nature's own SLBs at various temperatures are shown in Table 11.

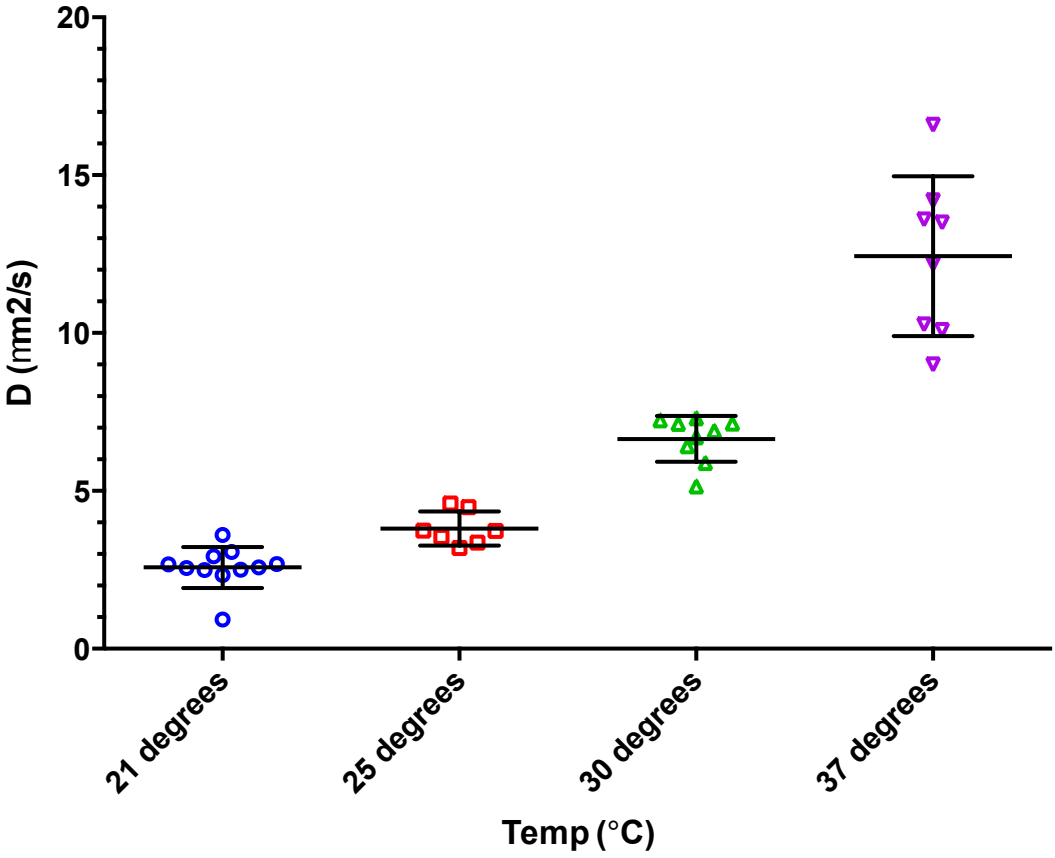

Figure 65: Diffusion of DOPE-Atto655 in a nature's own SLB on plasma-cleaned glass. Increasing temperature resulted in an increase in the determined diffusion co-efficient. Due to the inclusion of ordered phase lipids, nature's own was slightly less mobile than a DOPC bilayer. Each point is a 60 – 180 seconds FLCS measurement of the lipid bilayer fitted to a two-dimensional model. Standard deviation was used to report the error.

Table 11: The lateral diffusion co-efficient of DOPE-Atto655 in DOPC versus nature's own bilayers on plasma-cleaned glass at 21, 25, 30 and 37 °C. Increasing the experimental temperature lead to an increase in the diffusion co-efficient of the lipid bilayer. The nature's own lipid composition was slightly less mobile than a pure DOPC bilayer due to the inclusion of cholesterol and sphingomyelin. Standard deviation was used to report the error.

Temperature (°C)	DOPC SLB diffusion co-efficient ($\mu m^2/s$)	Nature's own SLB diffusion co-efficient ($\mu m^2/s$)
21	3.72 ± 0.52	2.58 ± 0.65
25	6.07 ± 0.55	3.81 ± 0.54
30	8.25 ± 0.77	6.65 ± 0.73
37	14.25 ± 1.43	12.43 ± 0.90

4.3.2. Integrin $\alpha_{IIb}\beta_3$ in a DMPC-supported lipid bilayer

Before moving onto our novel microcavity arrays, we first attempted to construct $\alpha_{IIb}\beta_3$-reconstituted bilayers on planar glass substrates. This protocol was based on Müller *et alia.* work and therefore used DMPC:DMPG (1:1) as the lipid composition. This was in contrast to our ultimate goal of a reconstituting $\alpha_{IIb}\beta_3$ into a physiologically-relevant composition, but nonetheless served as a useful starting point. The $\alpha_{IIb}\beta_3$ proteoliposomes were formed as per the Müller method and then disrupted above plasma-cleaned glass to yield a DMPC:DMPG SLB. Using DOPE-Atto532 as a lipid probe at 0.001 % (mol/mol) it was possible to visualise the bilayer as shown in Figure 66. Within this bilayer, Atto655-labelled $\alpha_{IIb}\beta_3$ can be seen in Figure 67. Due to the high phase transition temperature of DMPC and DMPG, all point measurement experiments were carried out at 25 °C. It was found that the lipid bilayer (DOPE-Atto532) diffused at 4.2 ± 0.51 $\mu m^2/s$, in line with the values

reported by Erb and Goennenwein for their DMPC/DMPG bilayers.[30,31] However, the reconstituted $\alpha_{IIb}\beta_3$ was found to be immobile on planar glass surface where photobleaching of the Atto655-labelled integrin was observed. This photo-bleaching is demonstrated in the MCS trace shown in figure Figure 68. This result is in contrast with observations by Erb where reconstituted integrin was found to laterally diffuse on a planar quartz substrate[30] but in agreement with Goennenwein where integrin was found to be immobile above planar glass and quartz substrates. Only when Goennenwein utilised a cellulose cushion was integrin found to laterally diffuse. Indeed, even when using this cellulose cushion 75 % of integrin proteins remained immobile.[31] This difficulty with not specific interaction between membrane proteins and the underlying substrate is the key problem that we hoped to target in the development of our upcoming microcavity arrays.

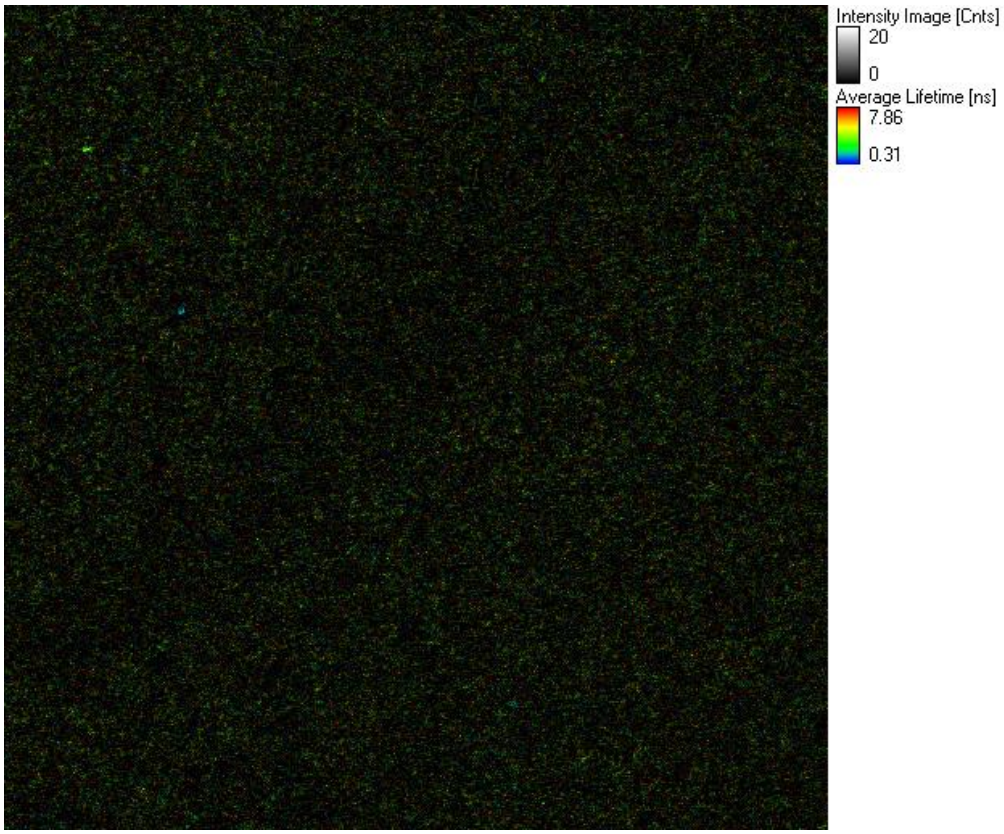

Figure 66: A fluorescence image of an DOPE-Atto532 in an integrin-reconstituted DMPC/DMPG lipid bilayer. The bilayer appeared defect free and was identical to a DMPC/DMPG SLB created in the absence of $\alpha_{IIb}\beta_3$. Due to the high phase transition temperature of DMPC and DMPG (approximately 21° C) the experiment was carried out at 25° C.

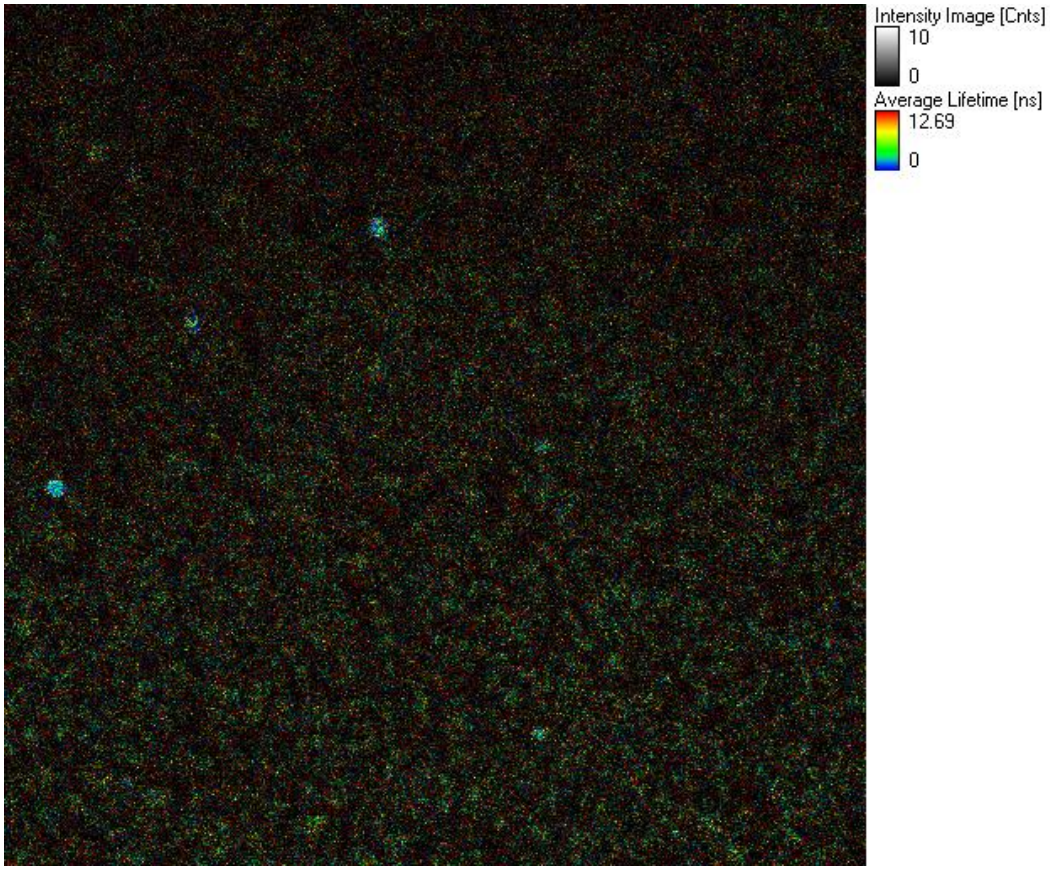

Figure 67: $\alpha_{IIb}\beta_3$-Atto655 in DMPC/DMPG SLB created on glass via the disruption of integrin-reconstituted vesicles. Integrin was found well distributed throughout the SLB. However, point measurements found that the labelled integrin was immobile on the glass substrate as indicated by photobleaching of the lipid probe.

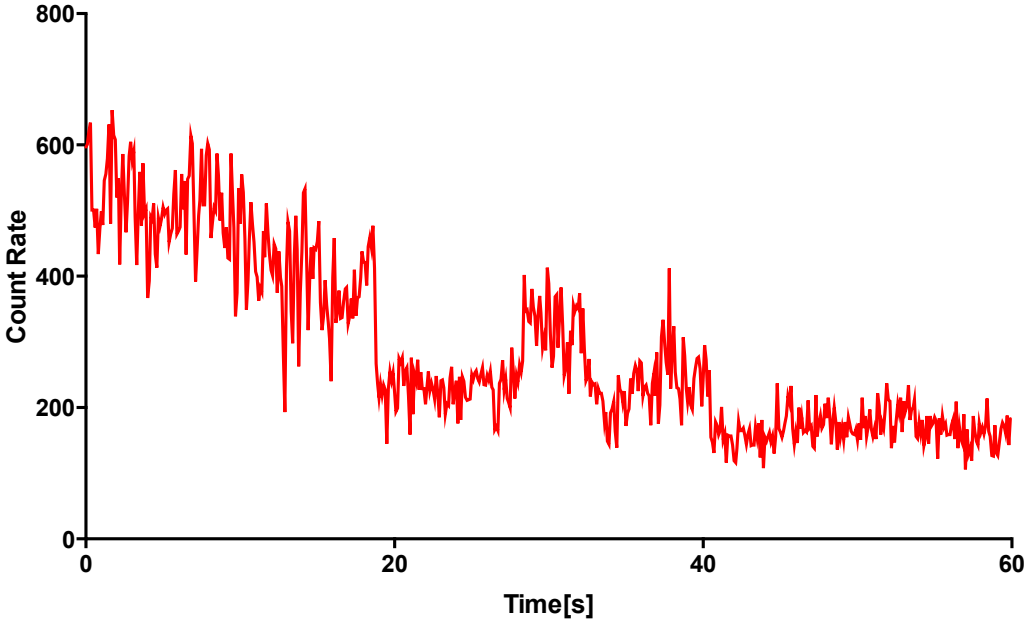

Figure 68: MCS trace of atto655 labelled $\alpha_{IIb}\beta_3$ in a DMPC/DMPG (1:1) lipid bilayer above planar glass. Photobleaching was clearly visible over time indicating that the reconstituted integrin was immobilised on the glass surface. This photobleaching of a reconstituted transmembrane protein is a key drawback of membrane-reconstituted SLB system. It was hoped that our PDMS arrays would eliminate this protein immobilisation.

4.3.3. Lipid-spanning of cavities

After construction of our PDMS microcavities (section 4.2.2) we next sought to creating a spanning lipid bilayer across the array. Due to the spherical porous nature of the cavities within the PDMS support as well as the significant refractive index mismatch between PDMS (n ≈ 1.45) and the buffer (n ≈ 1.33) it was possible to visualise the location of the cavities using reflectance imaging. The laser light scatters strongly within the buffer-filled cavities with the effect that filled cavities appear much brighter than the un-filled cavities or the surrounding planar regions of the PDMS support. A close-up image of the cavities suggests that that the aperture of the cavities is about 2 μm across when constructed from polystyrene spheres with a diameter of 2.88 μm. (Figure 69)

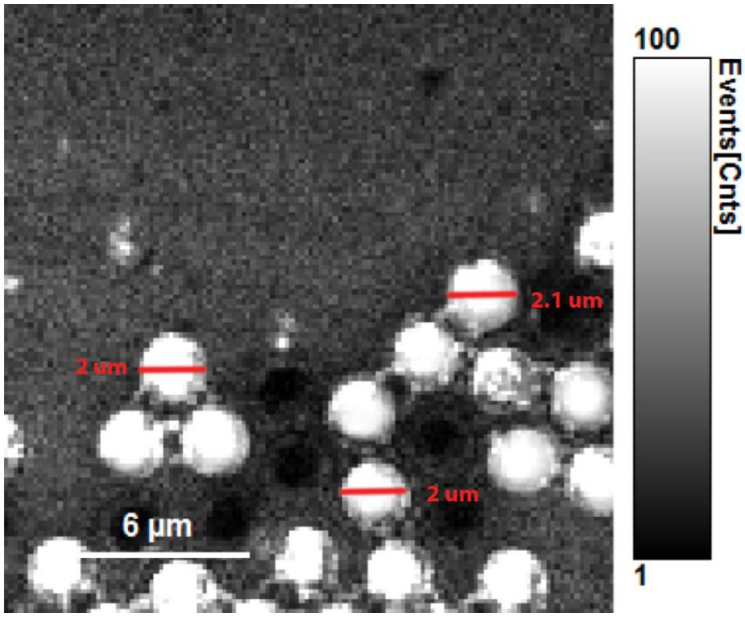

Figure 69: Close up reflectance imaging of the PDMS cavity array following sonication. Due to the scattering of the laser light buffer-filled cavities appear much brighter than the surrounding PDMS substrate. Measuring the diameter of the cavities using ImageJ suggest that the aperture of the cavities was approximately 2 µm when constructed from 2.88 µm polystyrene spheres.

Unlike experiments that featured completely planar substrates, a continuous bilayer could not be formed across the PDMS cavity arrays using the standard vesicle disruption method that utilise, for example, sonicated SUVs or extruded LUVs. This is because the diameter of the cavity aperture exceeds the diameter of the SUVs or LUVs, and so the vesicles enter the cavities rather than span them. To combat this, it was instead hoped to form a continuous lipid bilayer across the cavities via the disruption of electroformed GUVs. Unlike smaller vesicles, GUVs do not readily rupture on planar substrates. In order to promote disruption GUVs were incubated in the presence of $CaCl_2$ at 30 mM. This is because calcium increases the rate of vesicle fusion and has been shown to promote the tendency of vesicles to form SLBs.[182] Figure 70 and Figure 71 shows attempts to span cavities using disruption of GUVs via the addition of $CaCl_2$. As can be seen from the reflectance and fluorescence imaging, the lipid bilayer failed to span the cavities of the PDMS platform. Instead characteristic "halos" were observed around non-spanned cavities, while the cavities themselves were devoid of fluorescence. Backing up this imaging data, point measurements above the cavities showed no fluorescence intensity. This was in contrast to MCS point measurements on planar PDMS regions where fluorescence

intensity fluctuations over time showed the presence of a freely diffusing lipid bilayer.

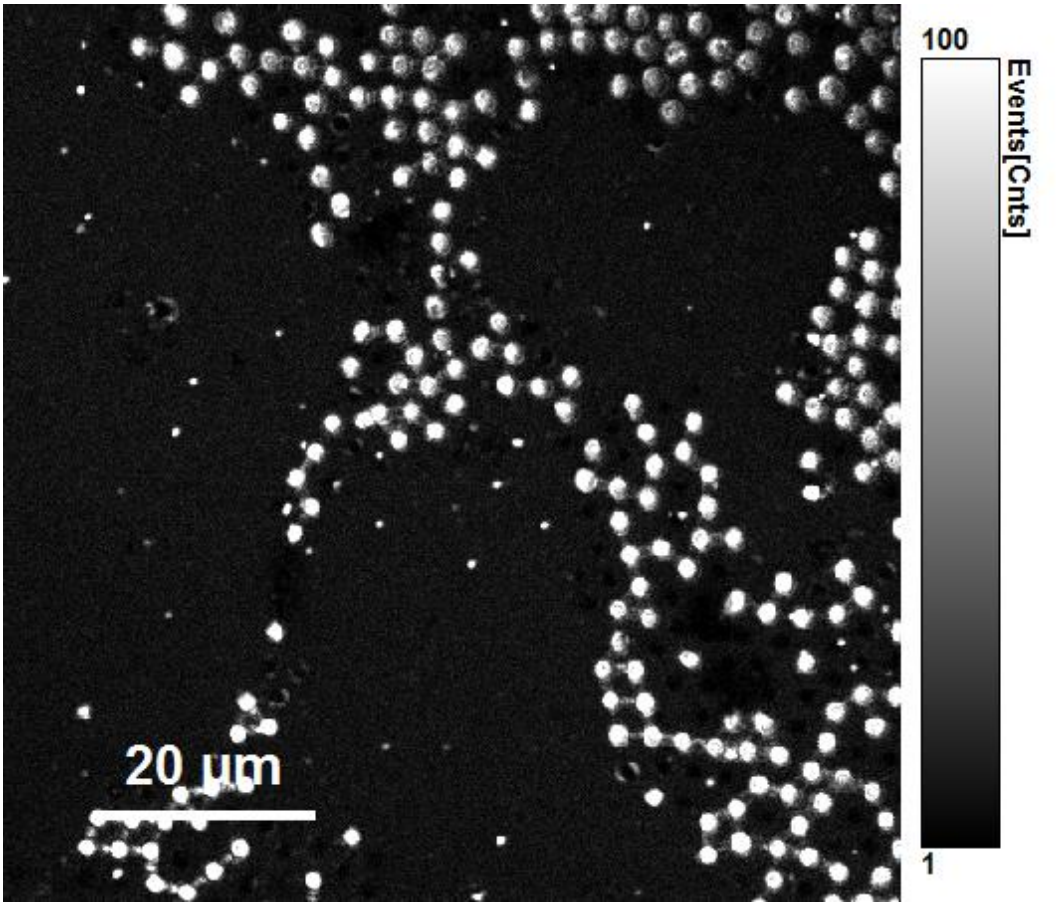

Figure 70: A reflectance image of a PDMS cavity array created with 2.88 µm polystyrene spheres. Filled cavities are visible as bright white circles. In order to attempt to form a lipid bilayer above this PDMS array we used GUVs as the lipid source. The GUVs were disrupted via the use of calcium, with the hope the the ruptured vesicles would span the buffer-filled cavities.

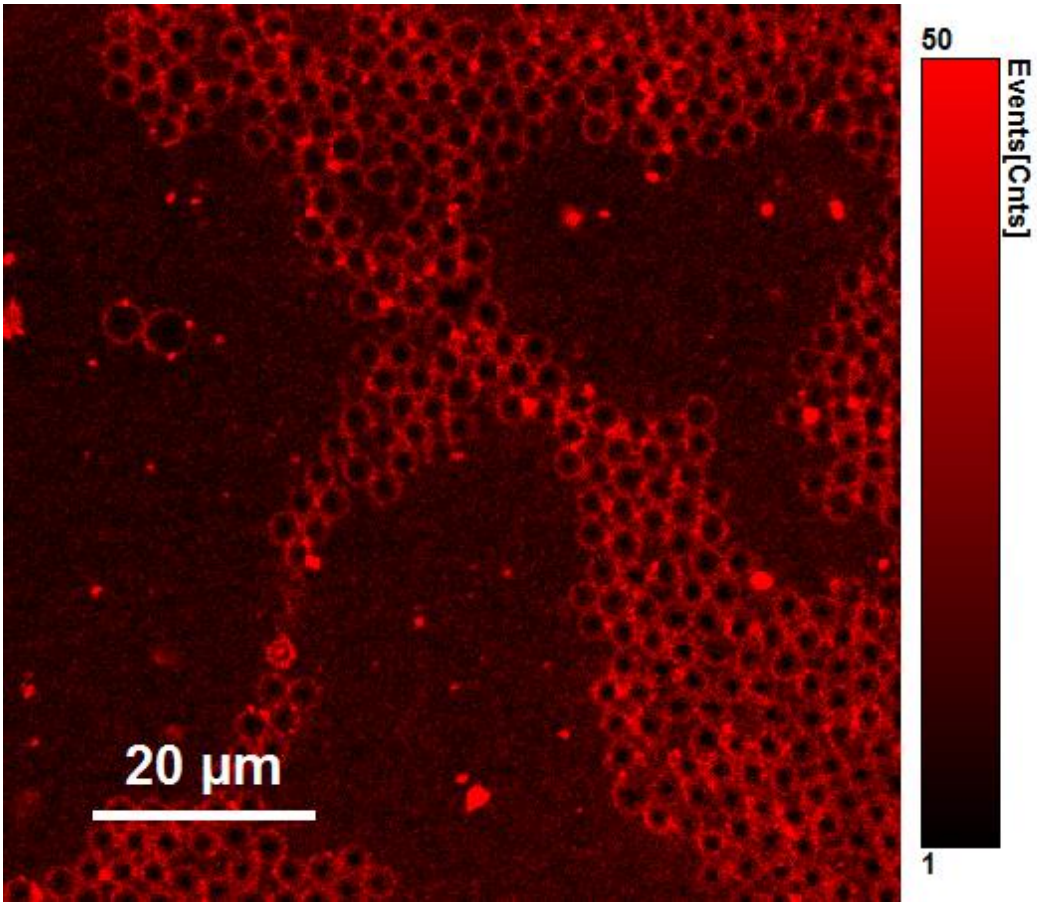

Figure 71: A fluorescent image of the DOPC lipid bilayer formed via the disruption of GUVs. DOPE-Atto655 was included as a lipid probe for imaging. While the SLB formed on planar regions of the PDMS, no bilayer was present above cavities. Instead a characteristic fluorescent "halo" was visible around non-spanning pores where the labelled lipids were found at high concentrations.

In order to circumvent the lack of cavity-spanning, an alternative method of bilayer formation was investigated. The chosen protocol was a combination of LB and vesicle disruption whereby the first monolayer was deposited by the LB and the bilayer was completed by the disruption of extruded LUVs Figure 72 shows the lipid bilayer across the same PDMS array, this time created via the two-step LB and vesicle disruption. In contrast to Figure 71, the lipid bilayer appeared continuous across the buffer-filled cavities. However, un-filled cavities did not appear to be traversed. To further investigate the continuity of the bilayer MCS point measurements were taken above buffer-filled cavities, above un-filled cavities, as well as on planar PDMS regions. In agreement with the imaging results, buffer-filled cavities and planar PDMS regions displayed fluorescence intensity fluctuations over time, indicating the presence of a freely diffusing lipid bilayer. MCS measurements

above un-filled cavities did not show any fluorescence intensity fluctuations indicating no bilayer was present. As such it was confirmed that buffer filling of our cavity system was a requirement for full lipid spanning.

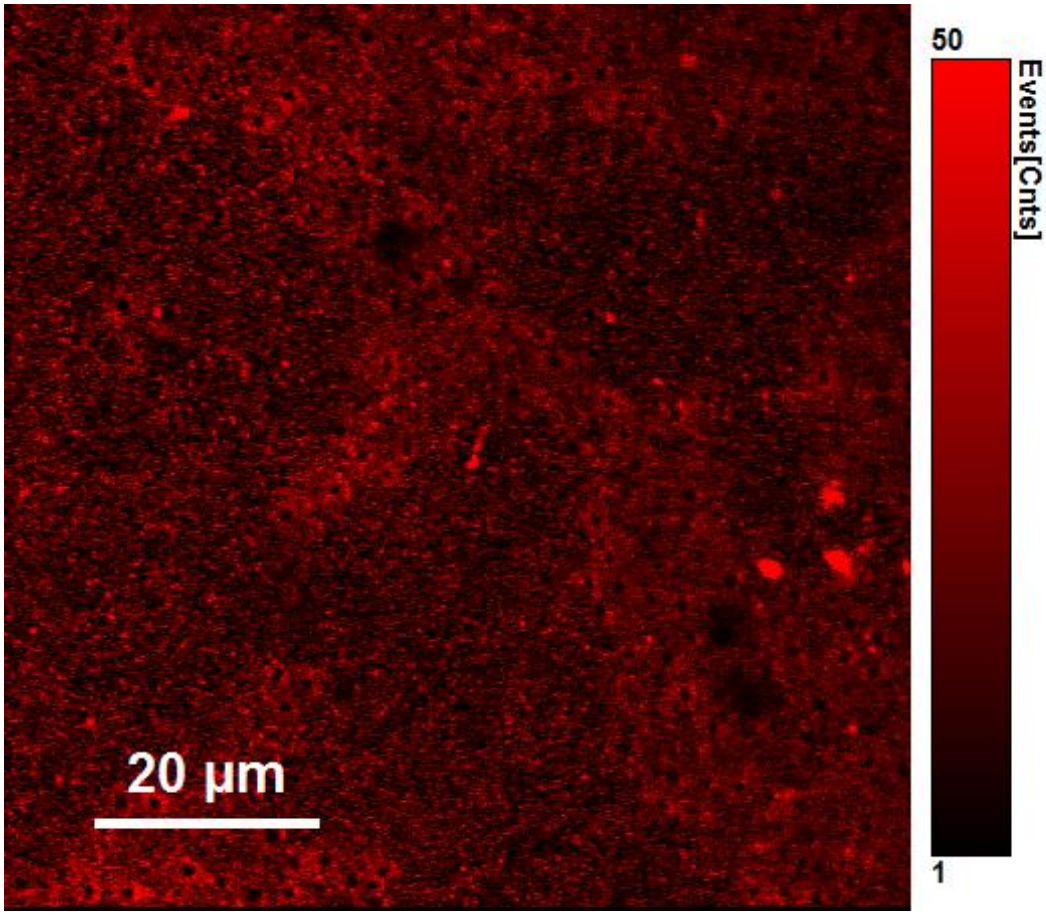

Figure 72: A fluorescent image of the DOPC lipid bilayer that was spanned across the PDMS cavity array. DOPE-Atto655 was included at 0.001 % for imaging and point measurements. Surface coverage of the bilayer is excellent and the bilayer trans-versed the buffer-filled cavities. Only un-filled cavities prevented bilayer coverage.

Following the establishment of a protocol that allowed for the formation of a cavity-spanning lipid bilayer, we were interested to know how the lipid diffusion coefficient of planar regions compared with the diffusion co-efficient above cavities. An example of the ACF traces and accompanying fits for FLCS measurements above planar regions and above cavities is shown in Figure 73. It is immediately evident that the lipid bilayer was diffusing faster above cavities (blue) when compared to above planar PDMS regions (red). Using a DOPC lipid bilayer it was found that the lipid probe DOPE-Atto655 diffused at 3.97 ± 0.36 $\mu m^2/s$ above planar PDMS regions.

The alpha value was found to be 1. These values are indistinguishable from diffusion measurements above plasma-cleaned glass for an identical lipid composition (3.72 ± 0.52 μm^2/s, alpha = 1). When diffusion measurements were performed above 2.88 μm cavities it was found that the lateral diffusion co-efficient of a DOPC bilayer was 11.06 ± 0.52 μm^2/s. Again the alpha value was determined to be 1. Importantly, these diffusion values above microcavities are approximately three-fold higher than diffusion values above planar substrates and are in line with our free-standing GUV values as described in chapter 3. This high lipid mobility shows that the bilayer has been decoupled from underlying substrate. This decoupling of the lipid bilayer from our PDMS arrays is the key feature of our platform. We hoped that this decoupling of the bilayer could be exploited in upcoming protein reconstitution experiments to allow for full protein mobility without the need for polymer cushions or other surface modifications.

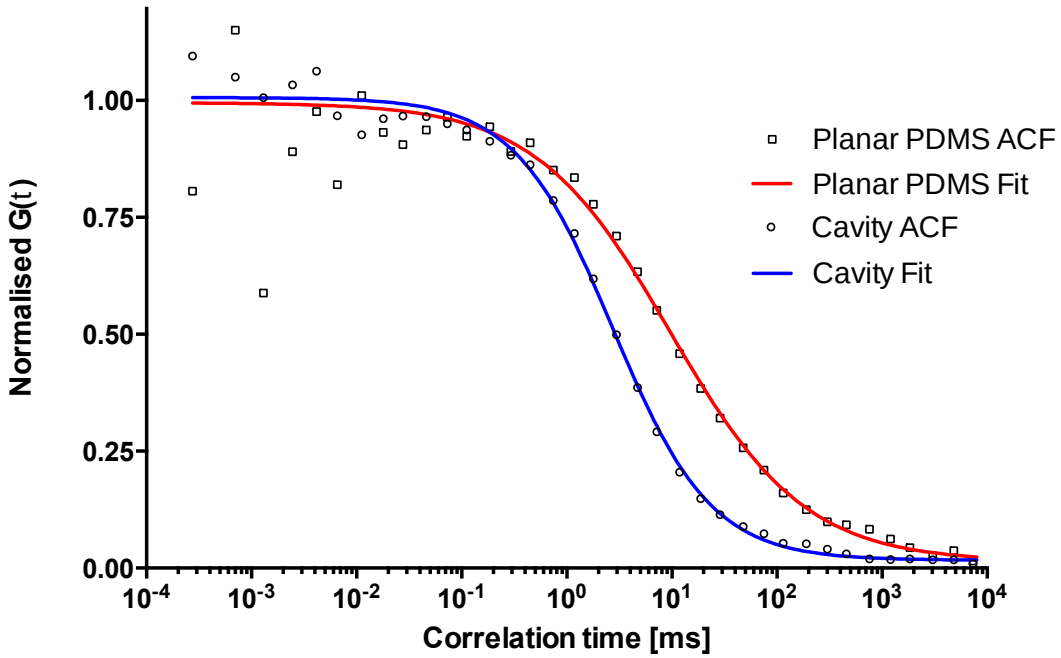

Figure 73: Representative ACFs of DOPE-Atto655 in a DOPC bilayer diffusing on planar PDMS (red) and above cavities (blue). It is apparent that lipid above cavities is much more mobile than lipid above a planar substrate. This is because the lipid bilayer has been decoupled from the PDMS and free-standing. As such these diffusion values above cavities are line line with GUV diffusion values.

In order to investigate the importance of positioning for point measurements, additional FLCS experiments took place whereby the cavities were approximately divided into different regions and point measurements undertaken. Figure 74 shows the areas in which cavities were divided. To perform these point measurements, close-up, high resolution images were taken of individual cavities in order to accurately position point measurements. While at the centre of the cavities the lateral diffusion co-efficient was in agreement with our previous value for 2.88 μm cavities, the diffusion co-efficient at "off-centre" regions was found to fall to 9.88 ± 1.12 μm^2. When point measurements were performed at "edge" regions where the cavities and planar regions converged the diffusion co-efficient was found to be 7.45 ± 2.12 $\mu m^2/s$, although the data here appears bimodal, where some values reflect planar lipid regions and other values reflect free-standing lipid regions. This data is summarised in Figure 75. Using the centre position as the control, a one one-way ANOVA was performed to compare diffusion between here and the off centre and edge data. This data showed statistical significance, where $F(2, 28) = 18.03$, $p < 0.001$. A post-hoc Bonferroni test showed that this significance lay between the centre control and the edge regions. There was no significant difference between the centre control and off centre regions. Despite this statistical analysis we believed that failure to properly place point measurements at the centre of the cavities meant that a second component from the slower diffusing planar PDMS regions was present in the ACF trace and thus the apparent diffusion co-efficient was slower than the actual diffusion co-efficient of the lipid bilayer above cavities. This result was perhaps surprising given the dimensions of the cavity apertures according to reflectance imaging. With an elongated focal volume with a diameter of between 600 – 700 nm, slight deviations from the centre of the cavity would not be expected to influence the measured diffusion co-efficient as the entire focal volume should be within the 2.88 μm cavities.

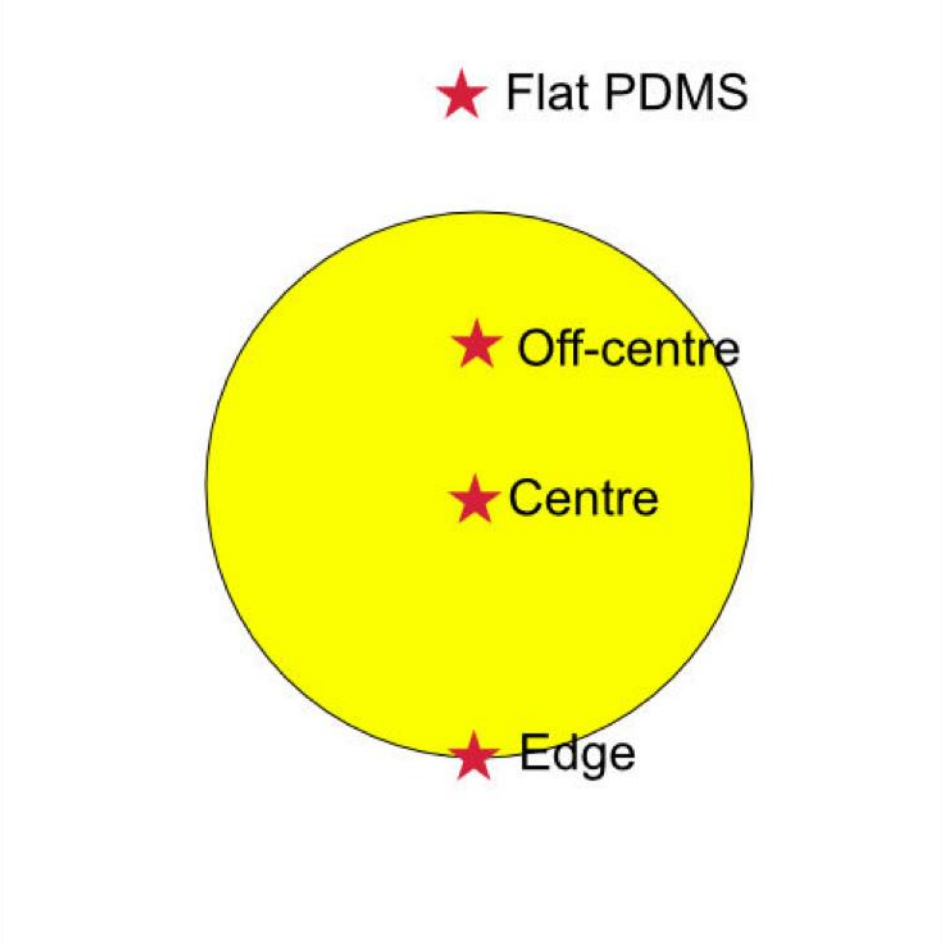

Figure 74: To examine the influence of point measurement positioning within the cavities and experiment was designed whereby the cavities were roughly divided up into different regions, namely "centre", "off-centre" and "edge". High resolution images were taken of cavities that appeared to be approximately 2 μm in diameter and point measurements were taken at the aforementioned regions.

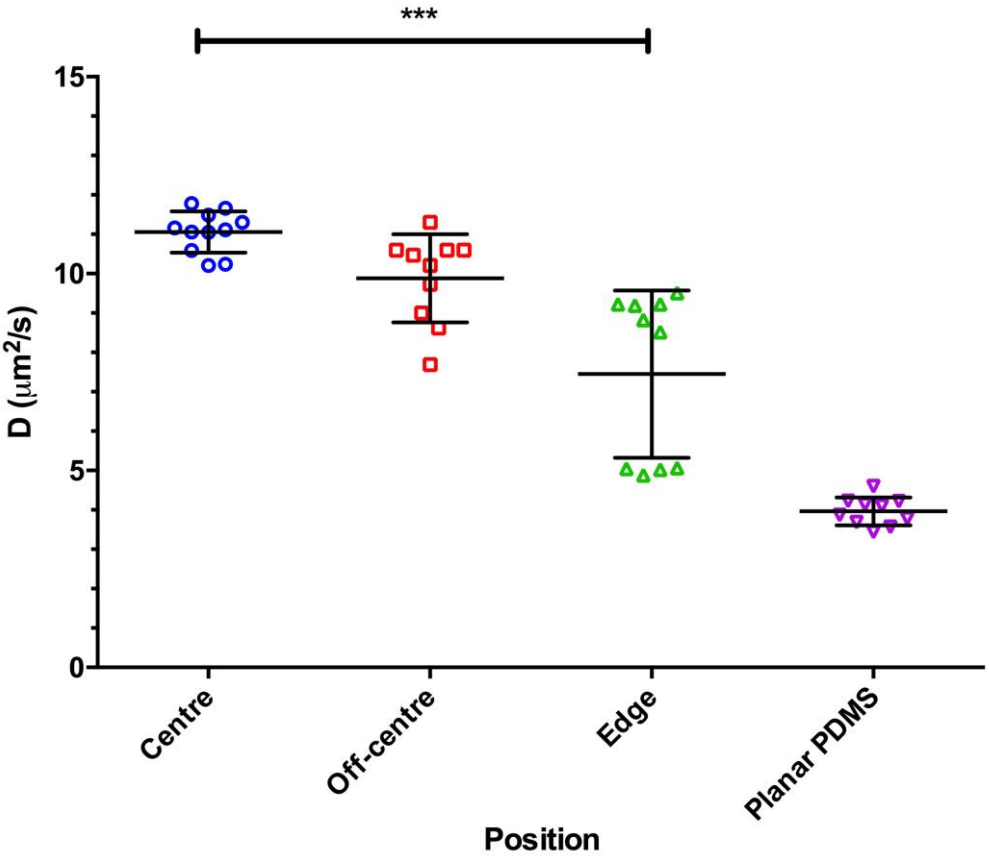

Figure 75: Diffusion of a DOPE-Atto65 in a DOPC bilayer by position. Each point represents a 60 second measurement of the lipid bilayer at a particular location. Slight deviations from the centre of the cavities lead to a noticeable drop in the apparent diffusion co-efficient measured via FLCS. While large deviations from the centre of the cavities would be expected to alter the diffusion co-efficient, the ease at which this occurred was surprising given the width of the confocal volume at its widest point and the apparent dimensions of the cavities. Error was reported using standard deviation.

Table 12: Summary of diffusion co-efficients obtained by positon. Slight deviations from the centre of cavities lead to a considerable fall in the apparent diffusion co-efficient owing to influence from the slower moving lipid above planar PDMS regions. This sudden fall off in diffusion co-efficients was unexpected in the "off-centre" regions given the apparent dimensions of the cavities and the focal volume of the point measurements. Error was reported used standard deviation.

Position	Lateral Diffusion Co-efficient ($\mu m^2/s$)
Centre	11.06 ± 0.52
Off-centre	9.88 ± 1.12
Edge	7.45 ± 2.12
Planar PDMS	3.97 ± 0.36

4.3.4. Further characterisation of the PDMS arrays

The apparent reduction in lipid diffusion co-efficients when performing point measurements slightly off centre was surprising given the apparent dimensions of the microcavities as observed via reflectance imaging (diameter of approximately 2 μm) and the area interrogated by point measurements (diameter of approximately 600 nm).In order to investigate this result further it was decided to further characterise the PDMS surface further using AFM. Due to the fact that AFM is not diffraction limited the technique allows for much higher resolution imaging of the cavity dimensions when compared to reflectance imaging previously used. Figure 76 shows AFM images of the PDMS cavity array made with 2.88 μm polystyrene spheres. In contrast to the reflectance images which suggest a cavity diameter of approximately 2 μm (Figure 69), AFM imaging shows that the cavities are in fact closer to 1 μm in diameter. Therefore, it appears that reflectance imaging overestimates the size of the cavities, perhaps due the scattering of laser light within the cavities and below the cavity aperture. This examination of the PDMS surface and cavity size explains why slight deviations from the centre of the cavities lead to a reduction in the observed diffusion co-efficient during point measurements as the focal volume overlapped with the planar PDMS regions. As such it was noted that correct positioning of point measurements was a key requirement in obtaining accurate data.

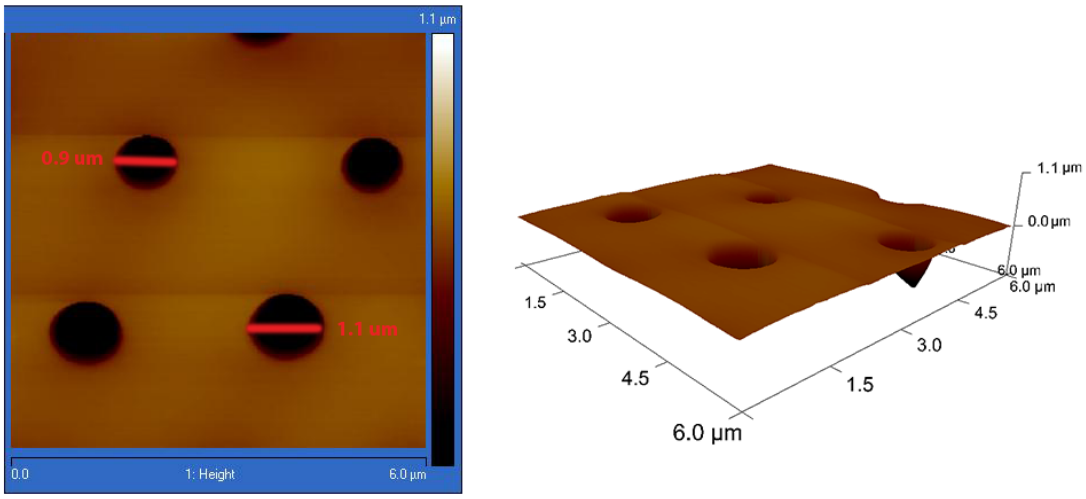

Figure 76: AFM of PDMS cavity arrays constructed from 2.88 µm polystyrene spheres. According to AFM the aperture of the cavities was about 1 µm. This was in contrast to the apparent size of the aperture obtained via reflectance imaging which was approximately 2 µm across. This difference in the apparent size as obtained via reflectance imaging and the actual size as obtained via AFM explained why lipid diffusion co-efficients were reduced when point measurements were performed slightly off-centre.

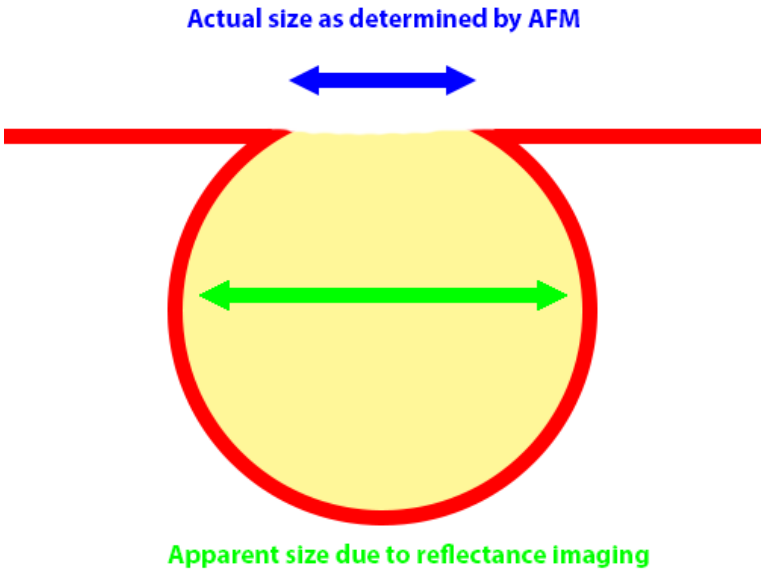

Figure 77: Cavity diameter aperture as determined via AFM versus apparent diameter determined via reflectance imaging. AFM was used to shows the actual aperture of the cavities created with 2.88 µm polystyrene spheres. AFM measurements show that reflectance imaging had been overestimating the size of the cavities due to light scattering within the buffer-filled cavities.

4.3.5. Insertion of Annexin V into cavity supported lipid bilayers

After a reliable protocol was developed to construct continuous lipid bilayers across PDMS cavity arrays it was hoped to expand the complexity of our platform by inserting membrane proteins in the system. The first model protein to be successfully inserted into the platform was Annexin V. In comparison to other larger and more complex membrane residing proteins, Annexin V could be readily and easily inserted into a preformed cavity-spanning lipid bilayer. This protein insertion process (section 4.2.8) could be achieved without the need for detergent-mediated reconstitution, making it a straightforward process. For all Annexin V experiments the lipid bilayer was formed as normal using a combination of LB and extruded vesicle disruption, although the composition was always a mixture of DOPC (80 %) and DOPS (20 %). Figure 78 shows buffer-filled cavities of a PDMS array in which the lipid bilayer was formed across. Figure 79 is the accompanying fluorescence image of Atto547N labelled Annexin V inserted within the DOPC/DOPS bilayer. Following imaging of the cavity array, and in order to assess whether the Annexin V was mobile within the bilayer, we then performed FLCS measurements on the system. Firstly it was determined that above cavities, the lipid probe DOPE-Atto655 in the DOPC/DOPS (8:2) bilayer had a lateral diffusion co-efficient of 10.91 $\pm$ 0.72 $\mu m^2/s$, a value indistinguishable from a pure DOPC bilayer. In comparison, it was determined that Annexin V-Atto547N had a lateral diffusion co-efficient of 7.10 $\pm$ 0.80 $\mu m^2/s$ in the DOPC/DOPS (8:2) bilayer. The alpha value was 1. Switching attention to the planar regions of the PDMS array, the DOPE-Atto655 lipid probe was found to diffuse at 3.96 $\pm$ 0.77 $\mu m^2/s$ in the DOPC/DOPS bilayer, again a value indistinguishable from a pure DOPC bilayer. The alpha value was 1. Although the bilayer was freely diffusing in these planar regions, point measurements of annexin V-Atto547N showed that the fluorescently probe was quickly photo-bleached. This photobleaching of the probe was due to the immobility of the protein planar PDMS regions owing to its bulky nature. An example of this photobleaching is given in the MCS trace shown in **Figure 81**. While of course this protein immobility is not ideal in

any protein-reconstituted system, this contrast with the readily mobile cavity data shows the power of our cavity-spanning bilayer system.

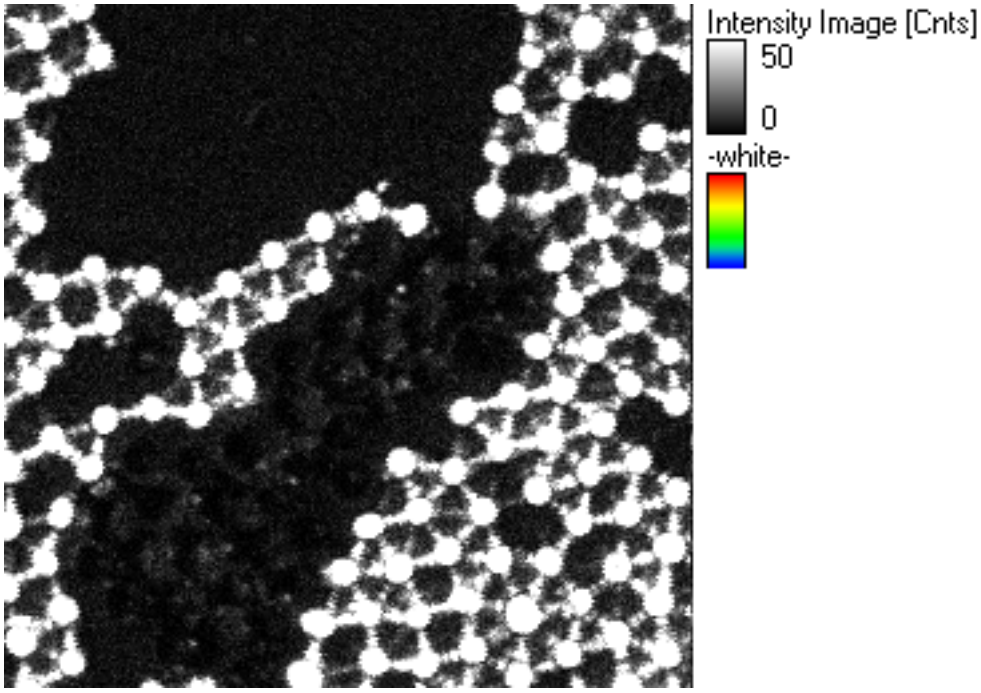

Figure 78: PDMS cavities created using 2.88 µm polystyrene spheres. Buffer-filled cavities were clearly visible on the PDMS surface. A lipid bilayer was transferred to this array using LB and vesicle rupture before annexin V was reconstituted within.

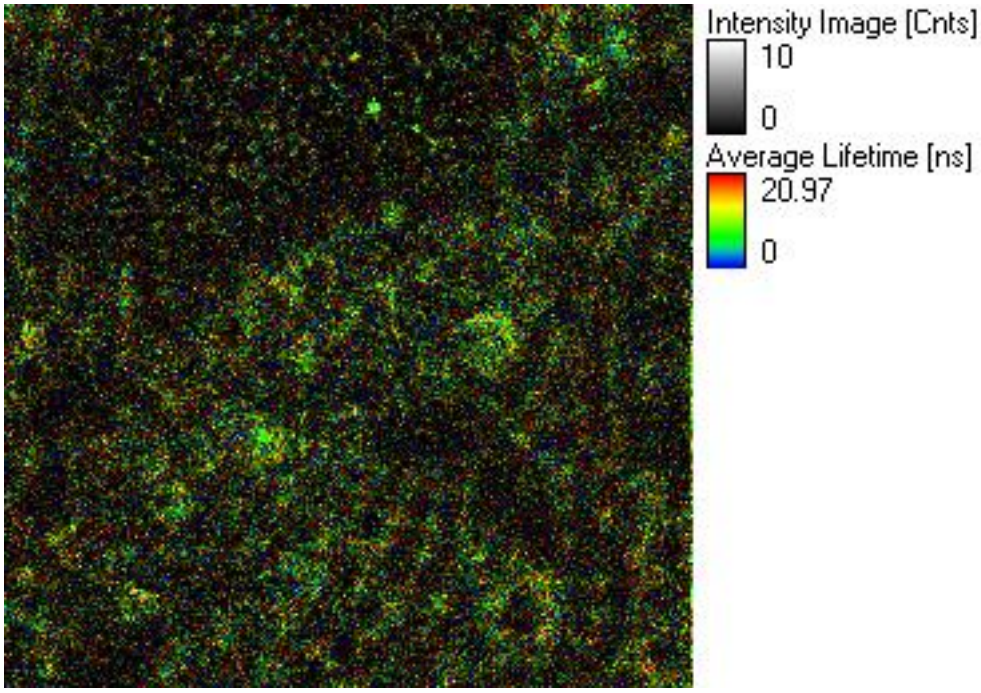

Figure 79: Atto547N-labelled annexin V in a DOPC:DOPS (8:2) lipid bilayer formed above the PDMS cavities shown in the previous figure. Annexin V appeared to aggregate at the locations of un-filled cavities but was also present above buffer-filled cavities on in planar PDMS regions. It was these locations that were probed with point measurements.

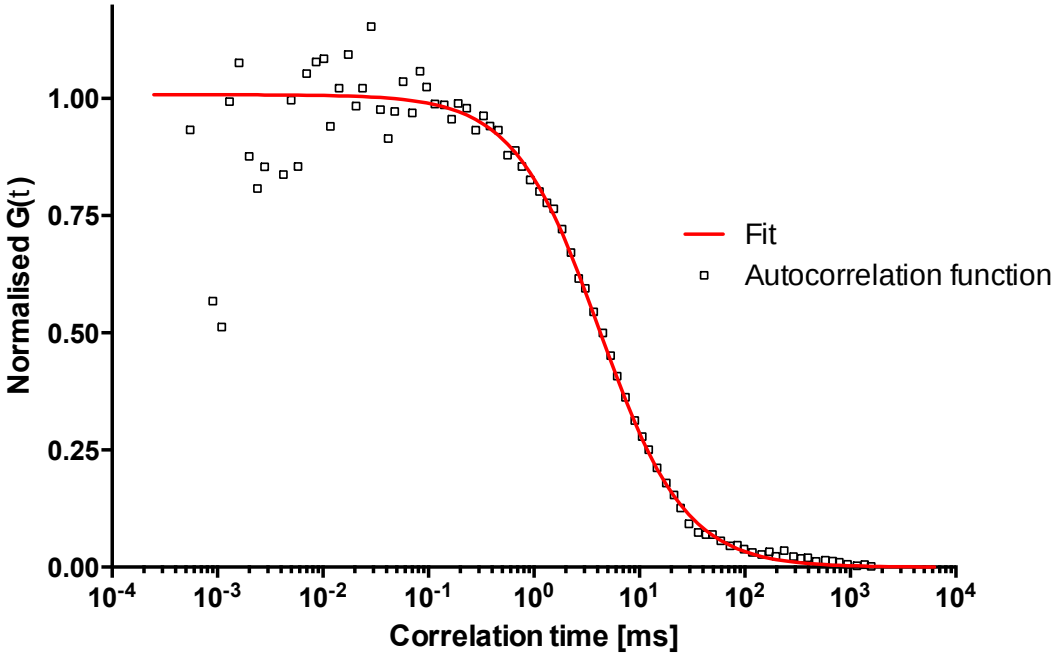

Figure 80: An example of an ACF trace and it accompanying fit for annexin V-Atto547N above cavities when reconstituted into a DOPC/DOPS (8:2) lipid bilayer. A single component fit was used to determine that the protein had a diffusion co-efficient of $7.10 \pm 0.80\ \mu m^2/s$ following reconstitution, a value substantially smaller than the lipid diffusion co-efficient at the same location.

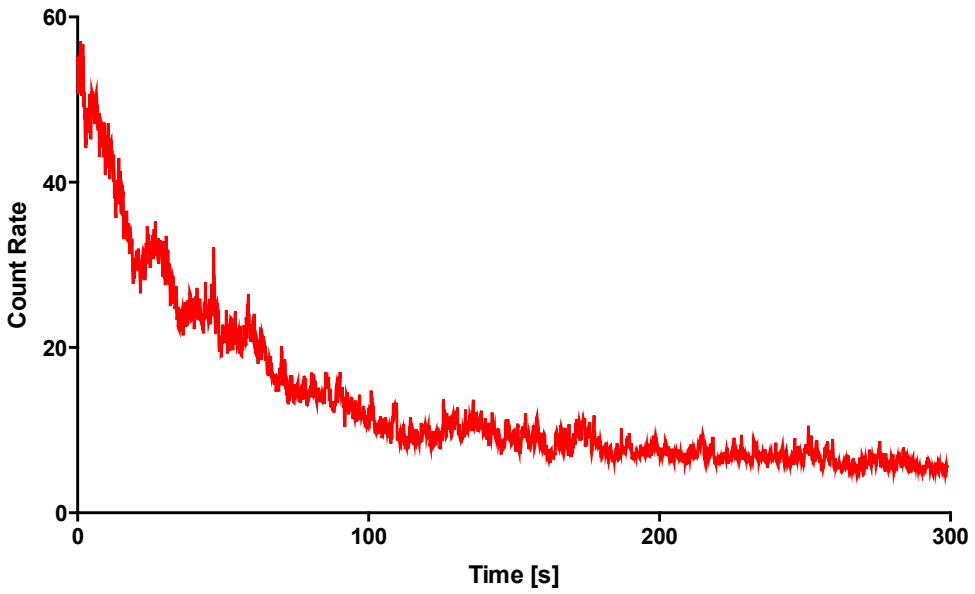

Figure 81: An MCS trace of annexin V-Atto547N on planar PDMS regions when reconstituted into a DOPC/DOPS (8:2) lipid bilayer. While annexin V-Atto547N was mobile above cavities, it was completely immobile on planar regions of the substrate leading to bleaching of the probe during point measurements. This contrasting mobility shows the power of our PDMS cavity arrays.

Table 13: Summary of diffusion co-efficients of components in a DOPC/DOPS (8:2) lipid bilayer reconstituted with annexin V. The protein was highly mobile above cavities although the diffusion co-efficient was below that found for lipid at the same location. On the other and, while the lipid was mobile on planar PDMS regions, annexin V was immobile at these locations where photo-bleaching was evident. Standard deviation was used to report the error.

Component	Lateral Diffusion Co-efficient ($\mu m^2/s$)	Alpha Value
DOPC/DOPS bilayer above cavities	10.91 ± 0.72	0.98 ± 0.01
Annexin V above cavities	7.10 ± 0.80	0.97 ± 0.02
DOPC/DOPS bilayer on planar PDMS	3.96 ± 0.77	0.98 ± 0.03
Annexin V on planar PDMS	bleaching	n/a

To the best of our knowledge this is the first time that an annexin protein has been reconstituted into a cavity-spanning system such as this one. Previously a number of groups have, however, used polymer cushions to decouple annexin V from the

underlying substrate. For example, Diaz *et al.* found that in the absence of PEG cushion annexin V diffused at 0.3 ± 0.1 $\mu m^2/s$. Using varying concentrations of PEG in a single cushioned set-up they were able to obtain a diffusion co-efficient of between 1 and 2 $\mu m^2/s$, while the use of a doubled cushioned set-up allowed for a diffusion co-efficient of between 0.4 and 3.5 $\mu m^2/s$. Of particular note was the percentage of mobile annexin V throughout their experiments where only between 20 and 36 % of the protein was mobile in their PEG-containing systems.[181] While we experienced this lack of annexin mobility on planar regions of PDMS, the freely diffusing environment present above buffer-filled cavities meant that no photobleaching was detectable in our cavity arrays. This shows the case for cavity supported bilayer systems as valuable tools for the biophysical study of membrane proteins.

4.3.6. Insertion of integrin $\alpha_{IIb}\beta_3$ into cavity supported lipid bilayers

Using the protocol developed by Müller *et al.*, we had earlier successfully inserted $\alpha_{IIb}\beta_3$ into a DMPC/DMPG bilayer on glass (section 4.3.2). In order to expand on this work we wanted to insert $\alpha_{IIb}\beta_3$ into a more physiologically-relevant compositions within our microcavity PDMS arrays. While previously we had observed that $\alpha_{IIb}\beta_3$ was immobile on planar glass, we hoped that these arrays we allow for full membrane protein mobility as had been shown in annexin V experiments (section 4.3.5). Beginning with a pure DOPC system the Müller reconstitution protocol (with a different lipid composition) was used to create integrin-reconstituted vesicles. This protocol had been used in chapter 3 to produce proteoliposomes that were used to construct GUVs. However, here these proteoliposomes were disrupted above an already created lipid monolayer that had been transferred via LB. As such the bilayer creation process was similar to our previous 2-step cavity-spanning bilayer protocol, albeit utilising integrin-reconstituted vesicles rather than protein-free LUVs. Initial fluorescent imaging of the $\alpha_{IIb}\beta_3$-containing bilayer was promising. Figure 83 shows

Atto655 labelled $\alpha_{IIb}\beta_3$ within a DOPC bilayer that was spanned across cavities made using 2.88 μm polystyrene beads. (Figure 82) As can be seen the labelled $\alpha_{IIb}\beta_3$ protein is well distributed throughout the lipid bilayer and appears to be membrane inserted. Figure 84 shows an ACF trace and it's fit of $\alpha_{IIb}\beta_3$-Atto655 in DOPC bilayer above cavities. While at first this protein mobility appeared to show that $\alpha_{IIb}\beta_3$ had been successfully reconstituted within the bilayer, analysis of the ACF traces showed that $\alpha_{IIb}\beta_3$-Atto655 was diffusing much faster than would be expected for our system. While DOPC had already been characterised to having a lateral diffusion co-efficient of 11.06 $\pm$ 0.52 $\mu m^2/s$ above cavities, values for integrin showed that the protein was diffusing at between 16 and 30 $\mu m^2/s$. Likewise in planar regions where DOPC was known to diffuse at 3.97 $\pm$ 0.36 $\mu m^2/s$, $\alpha_{IIb}\beta_3$-Atto655 was found it diffuse much faster than the lipid with a diffusion co-efficient in excess of 8 $\mu m^2/s$. In further contrast to this value, $\alpha_{IIb}\beta_3$ in DMPC above glass was previously found to be immobile. These diffusion values for the $\alpha_{IIb}\beta_3$ protein which were consistently well above the reported lipid values suggested that the protein was not fully reconstituted into the lipid bilayer. Instead, it was believed, that the labelled $\alpha_{IIb}\beta_3$ was loosely attached to the bilayer and was membrane-associated rather than membrane-inserted.

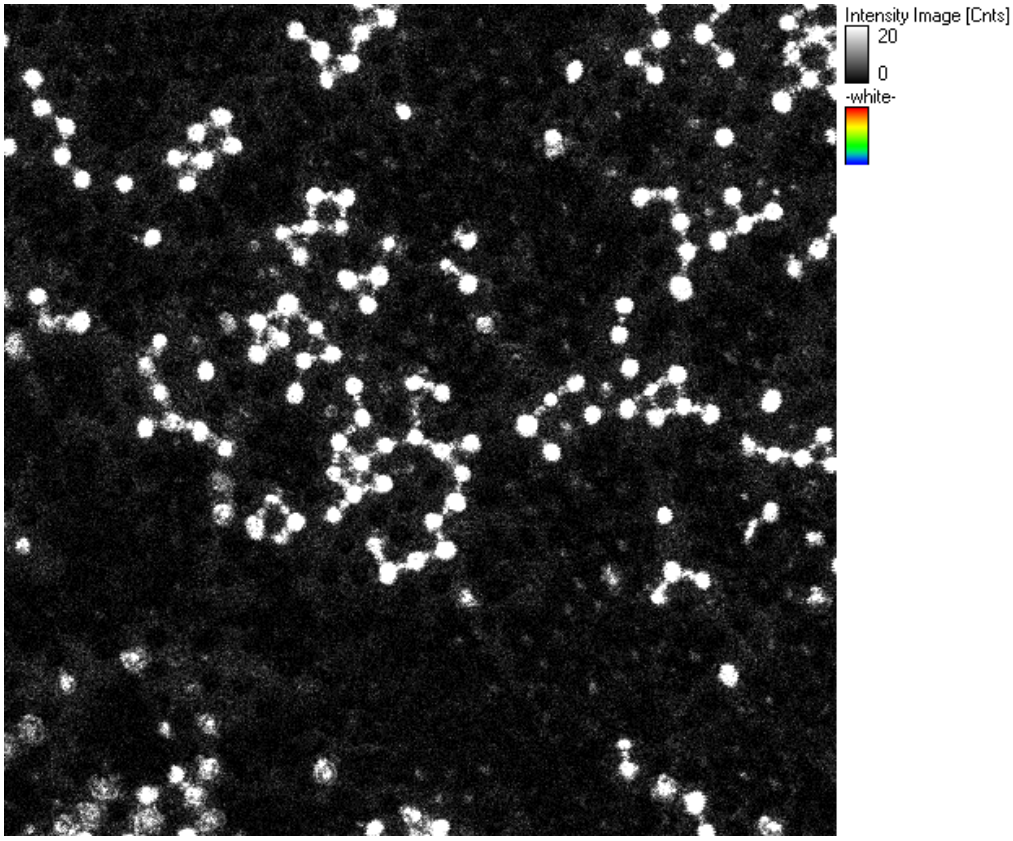

Figure 82: Reflectance image of PDMS array used for lipid-spanning and integrin reconstitution experiment. Buffer-filled cavities were visible in white due to the scattering of light within the cavities. Un-filled cavities and planar regions did not scatter light and there was no refractive index mismatch, and as such, these regions were black.

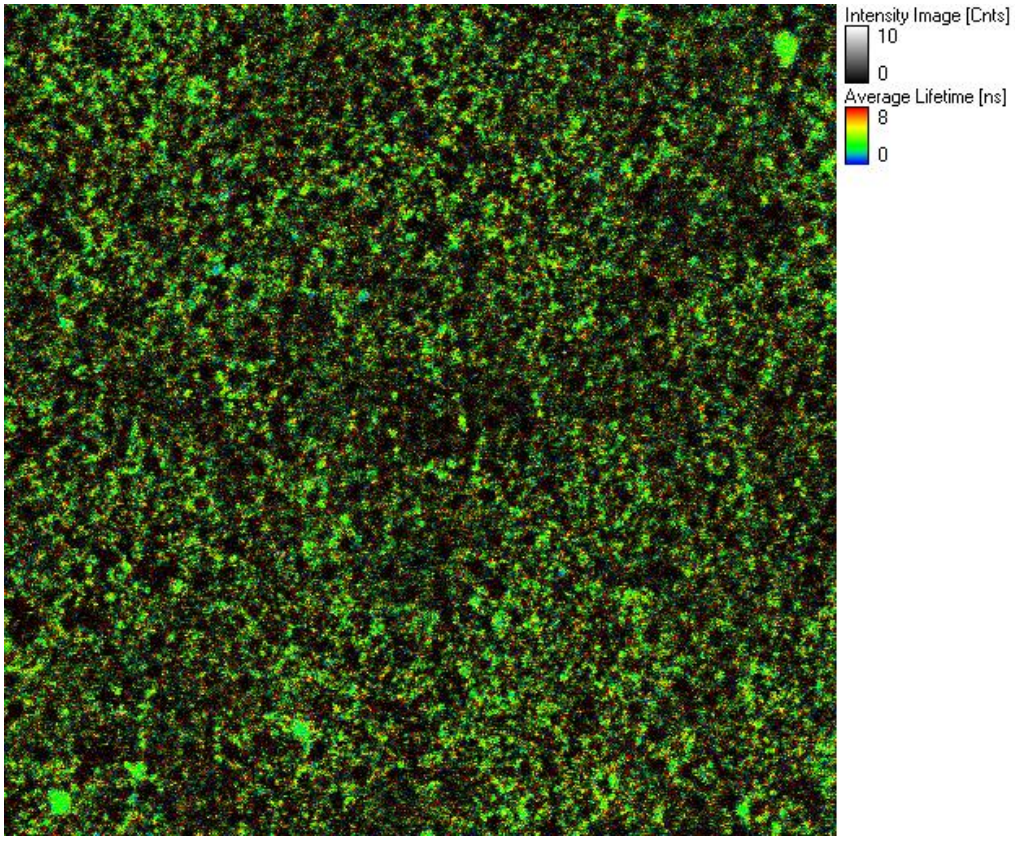

Figure 83: Fluorescence image of atto655-labelled $\alpha_{IIb}\beta_3$ reconstituted into a cavity-spanning DOPC bilayer. $\alpha_{IIb}\beta_3$ was well distributed throughout the bilayer and present above the buffer-filled cavities. Fluorescent "halos" were evident around un-filled cavities where no lipid bilayer spanned the cavities.

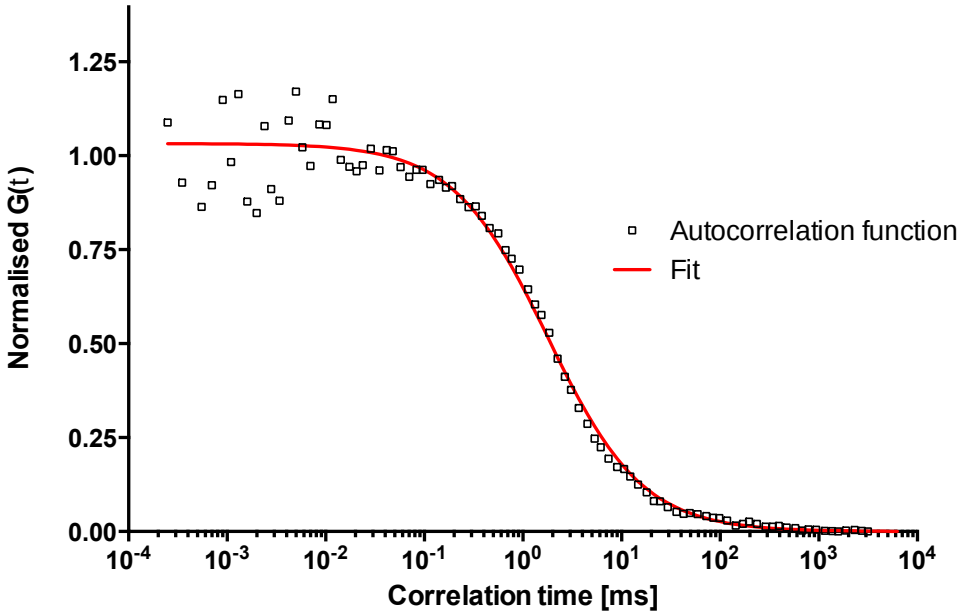

Figure 84: A representative ACF of integrin super-diffusion above buffer-filled cavities. Atto655 labelled $\alpha_{IIb}\beta_3$ was found to diffuse at between 16 and 30 $\mu m^2/s$, values way above the lipid diffusion co-efficient at the same location. This data suggests that the integrin protein was not fully inserted into the lipid bilayer.

Table 14: Summary of diffusion co-efficients in a DOPC lipid bilayer reconstituted with $\alpha_{IIb}\beta_3$ using the Müller *et al.* method. The reconstituted $\alpha_{IIb}\beta_3$ protein was found to have a diffusion co-efficient well in excess of the surrounding lipid phase indicating that protein was not properly inserted into the bilayer in our SLB system. This is in contrast to our GUV results were $\alpha_{IIb}\beta_3$ was found to diffuse much slower than the lipid membrane. Standard deviation was used to report the error.

Component	Lateral Diffusion Co-efficient ($\mu m^2/s$)
DOPC above cavities	11.06 ± 0.52
$\alpha_{IIb}\beta_3$ above cavities	16 – 30
DOPC on planar PDMS	3.97 ± 0.36
$\alpha_{IIb}\beta_3$ on planar PDMS	> 8

This rate of integrin diffusion was perhaps in agreement with observations by a number of other groups which stated that DMPC-based lipid compositions were a requirement for proper $\alpha_{IIb}\beta_3$ insertion into the membrane. For example, Müller reported "partial" insertion of $\alpha_{IIb}\beta_3$ into POPC/POPS vesicles and stated that co-location of lipid and integrin was not a reliable measure of correct incorporation, but instead a sign that $\alpha_{IIb}\beta_3$ had a tendency to strongly adhere to the lipid, an association that could not be removed by sucrose gradient centrifugation.[34] Later, Erb *et al.* stated that integrin reconstitution was performed using lipid/lipid mixtures of "POPC, POPC/POPS (molar ratio 75:25), POPC/POPG (molar ratio 50:50), PC/PE (molar ratio 70:30), which did in neither case result in a good integrin reconstitution" while DMPC and an equimolar mixture of DMPG/DMPC did result in good integrin reconstitution.[29] In agreement with this, the vast majority of paper that feature $\alpha_{IIb}\beta_3$ reconstitution utilise a DMPC-based mixture.[29–31,34,43–45] Many of these also perform diffusion-based measurements on the reconstituted $\alpha_{IIb}\beta_3$. Perhaps somewhat tellingly, of the limited number of papers on $\alpha_{IIb}\beta_3$ reconstitution into non-DMPC-based mixtures,[42,46,47] none perform diffusion-based measurements. Given the apparent difficulties with proper $\alpha_{IIb}\beta_3$ reconstitution in non-DMPC-containing compositions it is therefore unclear whether the integrin protein is membrane-inserted or merely membrane-associated in these cases.

However, this requirement for DMPC-based compositions is in contrast to our earlier GUV results where reconstituted $\alpha_{IIb}\beta_3$ was found to diffuse well below the lipid diffusion co-efficient in a range of DMPC-free compositions (3.3.5). While the reconstitution process in our GUV-based experiments shares a lot of similarities with the reconstitution process in our cavity-spanning experiments, the two protocols diverge after the formation of proteoliposomes precursors. In SLB-based experiments these proteoliposomes were directly disrupted above LB monolayer to form bilayers (section 4.2.9), while in GUV-based experiments these proteoliposomes were converted to giant vesicles (section 3.2.7). This conversion process involved the ultracentrifugation of the proteoliposomes to a lipid-protein pellet, and later electroformation of this pellet to form GUVs. We speculated that this two step ultracentrifugation and electroformation step somehow facilitated correct $\alpha_{IIb}\beta_3$ insertion. We therefore proposed a new method of bilayer formation (section 4.2.10) that used these $\alpha_{IIb}\beta_3$-reconstituted GUVs to complete the bilayer after LB monolayer transfer, rather than the use of smaller proteoliposomes. A schematic for the new insertion method is shown in Figure 85.

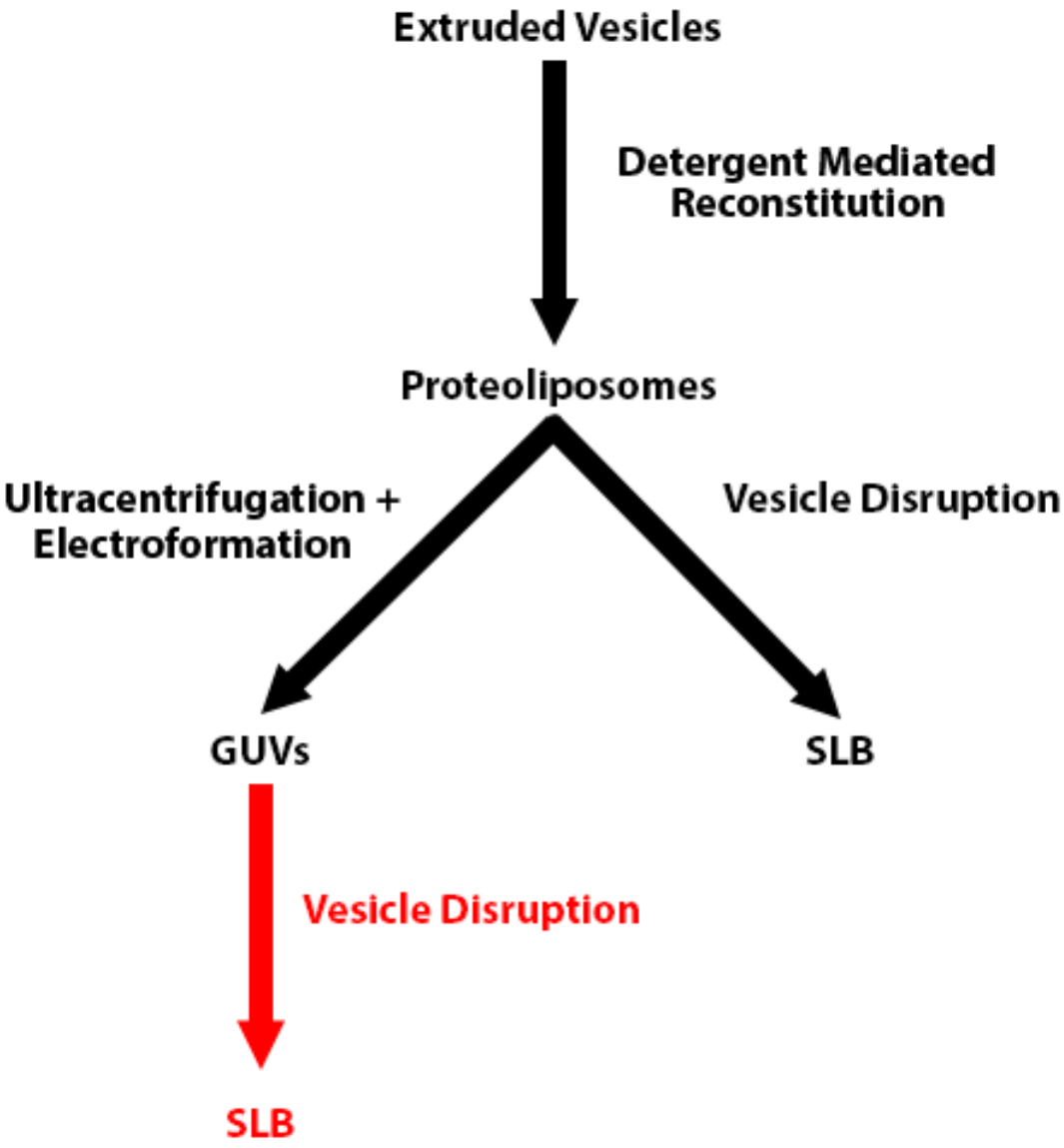

Figure 85: A schematic of the insertion protocol for GUVs and SLBs as well as the proposed new method of integrin reconstitution into an SLB (red). In all cases the initial protocol is the same whereby the protein is inserted into vesicles via the use of detergents to create proteoliposomes. These vesicles can then be used as the lipid course for electroformation (left), or as the lipid source for bilayer formation (right). Given the fact that direct disruption of the proteoliposomes to create an SLB did not result in integrin incorporation it was proposed that the successfully reconstituted GUVs be used as the lipid source for SLBs instead.

4.3.7. Alternative insertion method

As described above, we had proposed a new method of $\alpha_{IIb}\beta_3$ insertion into our PDMS cavity arrays based on the success we had achieved in our GUV-based experiments (Chapter 3). As before, a cavity-spanning lipid monolayer was transferred to the PDMS array using LB. Parallel to this, $\alpha_{IIb}\beta_3$-containing integrin-containing GUVs were also constructed from proteoliposomes precursors, as described in section 4.2.10. The GUVs were then flushed across the monolayer-containing PDMS array in a buffer containing 30 mM $CaCl_2$ in order to promote disruption of the giant vesicles. GUVs were incubated for 1 hour to allow for bilayer formation which yielded a continuous lipid bilayer with a well-distributed protein presence. In order to determine whether the protein was membrane inserted point measurements were required. Probing the cavities with FLCS measurements for $\alpha_{IIb}\beta_3$-Atto655 showed that $\alpha_{IIb}\beta_3$ was indeed mobile within the bilayer as expected (Figure 86). Fitting these traces yielded a diffusion co-efficient of 3.20 ± 0.33 $\mu m^2/s$ for $\alpha_{IIb}\beta_3$-Atto655 in a DOPC bilayer above cavities. This figure is well below the values for $\alpha_{IIb}\beta_3$ diffusion in an bilayer created from direct disruption of proteoliposomes. There $\alpha_{IIb}\beta_3$ diffusion co-efficients were well in excess of the surrounding lipid values (4.3.6). Here, above cavities, the alpha value was found to be 1, showing the diffusion of $\alpha_{IIb}\beta_3$ was unhindered. FLCS measurements were also performed for $\alpha_{IIb}\beta_3$-Atto655 above planar PDMS regions. In contrast to the high diffusion co-efficients in SLBs created via direct proteoliposomes disruption, $\alpha_{IIb}\beta_3$ was found to be immobile on planar PDMS regions. This can be seen in MCS measurements where $\alpha_{IIb}\beta_3$-Atto655 photo-bleaching was immediately evident (Figure 87). This result is in line with what would be expected of a large, membrane traversing, reconstituted protein. Therefore this result appears to confirm the insertion status of $\alpha_{IIb}\beta_3$ in an SLB model system via GUV disruption. This immobilisation of the integrin protein is also in agreement with our earlier annexin V work where the annexin protein was highly mobile above buffer-filled cavities, yet immobile above planar PDMS regions (4.3.5). Again this contrast between locations highlights the power of our PDMS cavity-spanning bilayer system, when compared to standard SLB set-ups.

Table 15: Summary of diffusion co-efficients in a DOPC lipid bilayer reconstituted with $\alpha_{IIb}\beta_3$ using the GUV intermediate method. In contrast to the high diffusion values witnessed using the original integrin insertion method, this new reconstitution method delivered $\alpha_{IIb}\beta_3$ diffusion co-efficient well below the lipid diffusion co-efficient above cavities. On planar regions the integrin protein was immobile where bleaching was evident. Standard deviation was used to report the error.

Component	Lateral Diffusion Co-efficient ($\mu m^2/s$)	Alpha Value
DOPC above cavities	11.06 ± 0.52	1.01 ± 0.02
$\alpha_{IIb}\beta_3$ above cavities	3.20 ± 0.33	0.99 ± 0.02
DOPC on planar PDMS	3.97 ± 0.36	0.98 ± 0.02
$\alpha_{IIb}\beta_3$ on planar PDMS	immobile	n/a

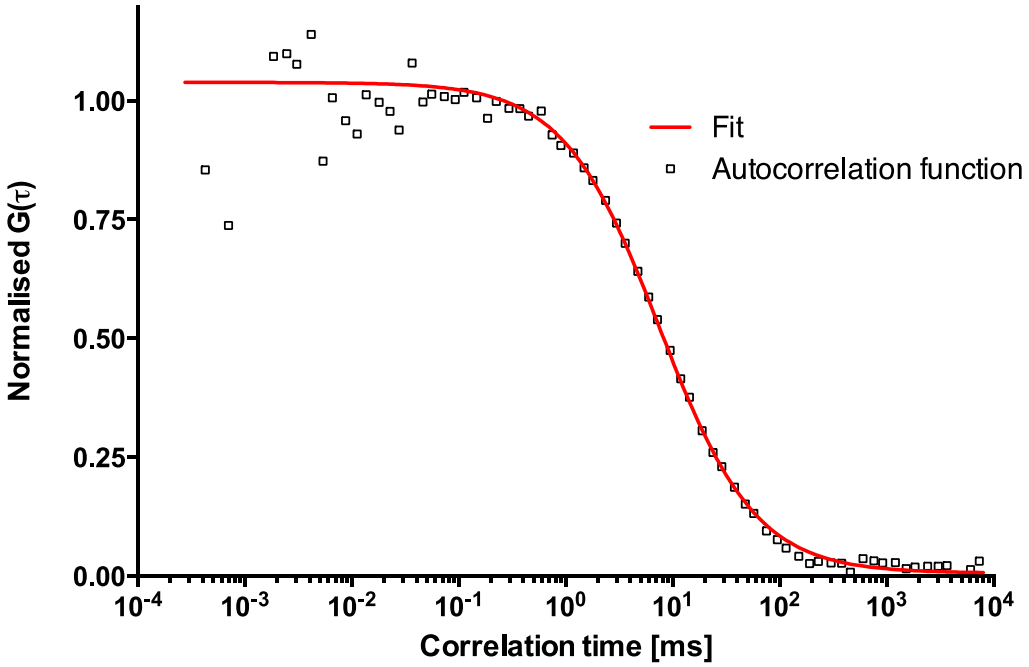

Figure 86: Representative ACF for atto655 labelled $\alpha_{IIb}\beta_3$ inserted into a cavity-spanning lipid bilayer using integrin-containing GUVs as an intermediate. In contrast to the extremely high diffusion co-efficients witnessed using the original integrin reconstitution method, using GUVs as an intermediate resulted in a diffusion co-efficient of 3.20 ± 0.33 $\mu m^2/s$ above cavities. This value is well below the diffusion co-efficient of the surrounding lipid bilayer.

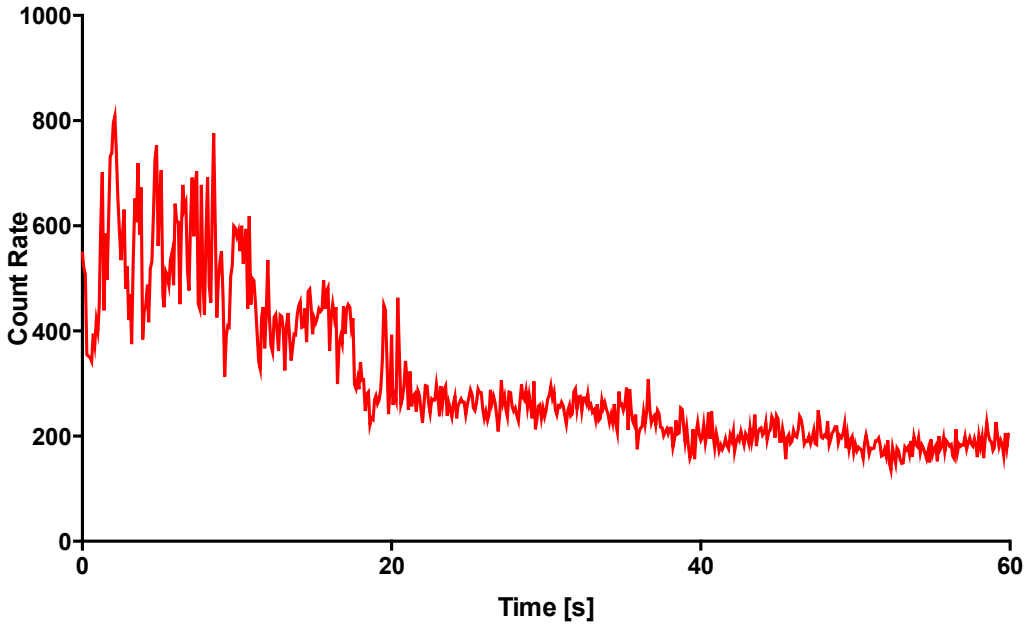

Figure 87: A representative MCS trace of atto655 labelled $\alpha_{IIb}\beta_3$ on planar PDMS. Photobleaching of the probe is clearly evident over time showing that the labelled integrin is immobile above the substrate. This is in contrast to the original integrin reconstitution method where $\alpha_{IIb}\beta_3$ diffused faster than the lipid bilayer at the same position due to loose association with SLB. Such protein immobility on planar regions appears to confirm that the use of GUVs as an intermediate lead to the proper reconstitution of the integrin protein.

Having successfully inserted $\alpha_{IIb}\beta_3$ into a non-DMPC-containing composition in the form of DOPC it was decided to expand the scope of the experiments by using a more complex and biomimetic lipid composition. Having previously successfully inserted $\alpha_{IIb}\beta_3$ into GUVs composed of the nature's own composition it was seen as the natural progression to use nature's own in our PDMS cavity arrays. The use of a biometic composition in combination with $\alpha_{IIb}\beta_3$ reconstitution emphasises the power of the PDMS cavity arrays in developing a powerful cell membrane mimic. As before, integrin-containing GUVs were formed from detergent-reconstituted proteoliposomes and disrupted to complete a lipid bilayer. The surface was then imaged and later probed via point measurements in order to determine diffusion co-efficients. FLCS showed that $\alpha_{IIb}\beta_3$-Atto655 diffused at 2.80 ± 0.59 $\mu m^2/s$ above cavities, with an alpha value of 1. This integrin diffusion co-efficient was slightly below the value for a pure DOPC bilayer. This was to be expected given the presence of liquid ordered phase lipids in cholesterol and sphingomyelin within the nature's

own composition. For example, previously the nature's own bilayer itself was shown to diffuse slightly slower than a pure DOPC bilayer on planar glass across a range of temperatures (Figure 64 and Figure 65). Positioning point measurements above planar PDMS regions, again it was found that the labelled integrin protein was readily photobleached. This shows that $\alpha_{IIb}\beta_3$ was immobile above planar PDMS regardless of lipid composition. This was to be expected given the bulky nature of bilayer-spanning lipid membrane proteins, such as integrin $\alpha_{IIb}\beta_3$, above a planar substrate, and mirrors our earlier results for annexin V, where it too was immobile above PDMS. Once again this contrast between the high mobility of proteins above buffer-filled cavities and the immobility of proteins above planar regions shows the power of our novel PDMS array set-up.

Table 16: A summary of diffusion co-efficients in a Nature's own lipid bilayer reconstituted with $\alpha_{IIb}\beta_3$ using the GUV intermediate method. As with a pure DOPC bilayer the $\alpha_{IIb}\beta_3$ diffused much slower than the lipid value above cavities. Likewise the $\alpha_{IIb}\beta_3$ was immobile above planar PDMS. Of particular note is that the integrin protein diffused slower in this composition than in a pure DOPC bilayer. Standard deviation was used to report the error.

Component	Lateral Diffusion Co-efficient ($\mu m^2/s$)	Alpha Value
Nature's own above cavities	9.12 ± 0.67	0.99 ± 0.02
$\alpha_{IIb}\beta_3$ above cavities	2.80 ± 0.59	0.97 ± 0.02
Nature's own on planar PDMS	2.98 ± 0.32	1.00 ± 0.03
$\alpha_{IIb}\beta_3$ on planar PDMS	immobile	n/a

4.3.8. Integrin orientation in the bilayer

In order to determine the orientation of $\alpha_{IIb}\beta_3$ in the lipid bilayer proteinase K was flushed into the PDMS cell at 0.01 mg/ml and incubated at room temperature for 2 hours. During this time the enzyme could digest any exposed regions of the integrin protein it had access to. Given that $\alpha_{IIb}\beta_3$ was only labelled once per protein and this

was located on the extracellular head region, the probe could only be removed from integrin molecules that were “correctly” orientated with their extracellular domain pointed away from the PDMS substrate surface. Previously, a similar set-up had shown that, in GUVs, the ratio between outwards and inwardly orientated $\alpha_{IIb}\beta_3$ was 1:1, meaning the insertion process was completely random. We were keen to see whether this ratio was maintained during the SLB formation step, or whether the process changed the orientation of the integrin proteins. Experimentally, the nature’s own bilayer was imaged for $\alpha_{IIb}\beta_3$-Atto655 fluorescence and the mean pixel intensity was determined for the 80 x 80 μm image. Across 5 different locations the mean pixel intensity of the integrin-reconstituted bilayer was 56.25 $\pm$ 9.99 counts per pixel. Following proteinase K incubation and subsequent removal via a buffer flush the mean pixel intensity had been reduced to 23.50 $\pm$ 4.24 counts per pixel based on the imaging of 5 new locations. (Figure 89) A two-tailed unpaired t-test was performed where the difference between the two data sets was found to be significant, $t(14) = 8.53$, $p < 0.001$. As the average average count per pixel fell to approximately 40 % of its original value. This suggets that approximately 60 % of the integrin proteins were available for digestion at their fluorescently labelled terminus. As such, it can be said that the SLB system slightly favoured “correctly” orientated $\alpha_{IIb}\beta_3$, ie integrin molecules with their extracellular domain pointing away from the PDMS substrate.

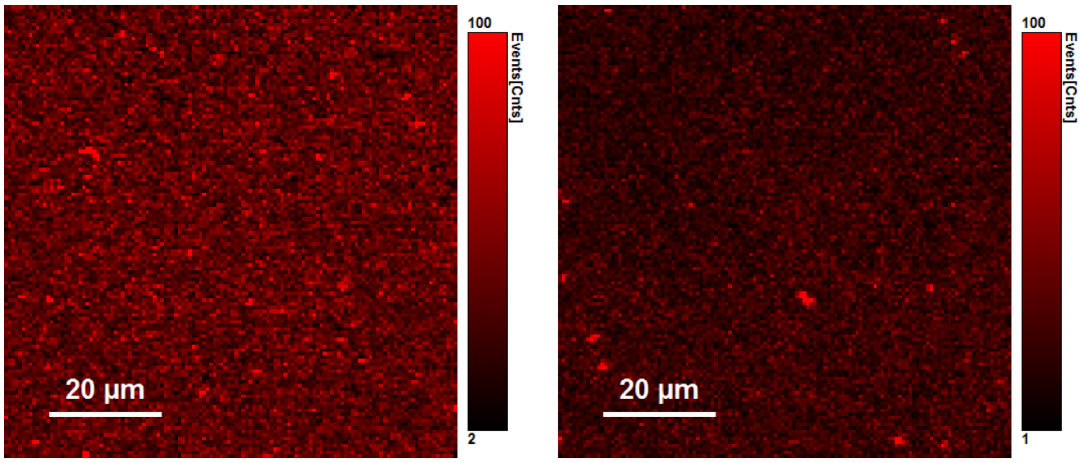

Figure 88: Atto655 labelled $\alpha_{IIb}\beta_3$ in a nature's own bilayer before (left) and after (right) proteinase K addition. Following 2 hours of proteinase K incubation, the cell was flushed with buffer to leave behind a bilayer where many of the extracellular integrin domains have been digested by the enzyme. Only labelled integrin molecules with their headpiece orientated towards the PDMS remained. (n=8)

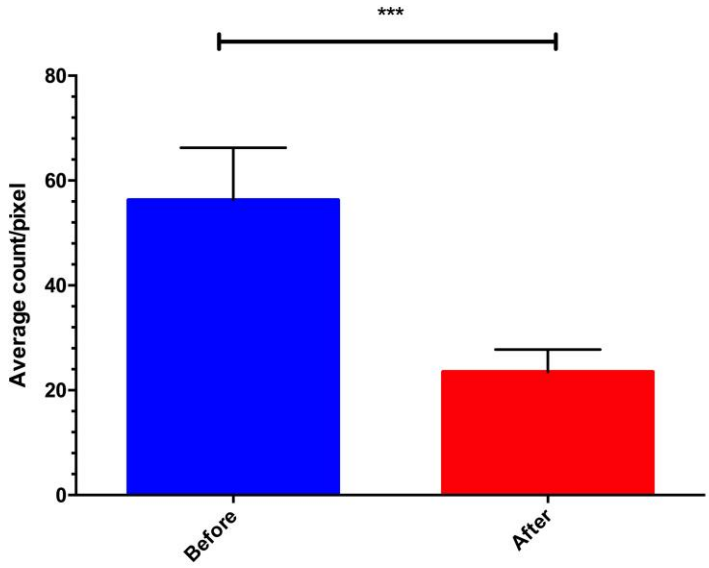

Figure 89: Average count per pixel before (left) and after (right) proteinase K incubation. Following incubation and buffer flushing the average count per pixel was fell to approximately 40 % of its original value, indicating that the system slightly favoured "correctly" orientated integrin, with their extracellular domain pointed outwards. A two-tailed unpaired t-test was performed where the difference between the two data sets was found to be significant, $t(14) = 8.53$, $p < 0.001$.

4.3.9. Addition of integrin ligands

In complimentary experiments to the addition of integrin ligands to GUVs, we examined how integrin activation and ligand-binding influenced $\alpha_{IIb}\beta_3$ behaviour within the cavity-spanning bilayer. As with the GUV experiments, DTT and Mn^{2+} were used as integrin activators. DTT or Mn^{2+} in buffer were injected into the PDMS cell at concentrations ranging from 500 nM to 5 mM and the cell was incubated at room temperature for 1 hour. Point measurements were then performed at the bilayer above cavities and the ACFs compared to an un-activated control. Where no integrin activators were present, the lateral diffusion co-efficient of $\alpha_{IIb}\beta_3$-Atto655 was found to be 2.80 ± 0.59 $\mu m^2/s$. Upon addition of 5 mM DTT and 5 mM Mn^{2+}, the lateral diffusion co-efficient of $\alpha_{IIb}\beta_3$-Atto655 was found to be 2.76 ± 0.44 $\mu m^2/s$ and 2.95 ± 0.46 $\mu m^2/s$ respectively. A one-way ANOVA with post-hoc Bonferroni test between the three data sets showed no statistically significant difference between the activation states of the integrin protein, where $F(2, 98) = 3.07$, $p > 0.05$. Therefore, consistent with the results observed for GUVs, (section 3.3.6) structural changes induced by integrin activators alone were not sufficient to alter the mobility of $\alpha_{IIb}\beta_3$ above cavities where the diffusion co-efficient remained unchanged. (Table 17)

Table 17: The influence of integrin activators alone on the diffusion co-efficient of $\alpha_{IIb}\beta_3$ above cavities in a nature's own bilayer. No change in the mobility of the integrin protein was recorded as confirmed via ANOVA analysis. This was to be expected given our results in GUVs. Standard deviation was used to display the error.

Activator	Lateral Diffusion Co-efficient ($\mu m^2/s$)	Alpha value
No activator	2.80 ± 0.59	1.00 ± 0.01
5 mM DTT	2.76 ± 0.44	0.99 ± 0.02
5 mM Mn^{2+}	2.95 ± 0.46	0.98 ± 0.02

The unchanged lateral diffusion co-efficient for activated $\alpha_{IIb}\beta_3$ was expected given our results when working with $\alpha_{IIb}\beta_3$ in GUVs, where conformational changes alone that were brought about by DTT and Mn^{2+} were not sufficient to bring about a

measurable change in the lateral mobility of of $\alpha_{IIb}\beta_3$. On the other-hand, the co-inclusion of fibrinogen with activated $\alpha_{IIb}\beta_3$ did bring about a change in the lateral mobility of $\alpha_{IIb}\beta_3$ in our integrin-reconstituted GUV system. Thus, it would be expected that the application of fibrinogen would also reduce the mobility of pre-activated $\alpha_{IIb}\beta_3$ in our cavity supported bilayer system. To explore this integrin-containing bilayer was formed above a PDMS array as before and the cell was flushed with DTT or Mn^{2+} (500 nM to 5 mM) as well as fibrinogen (at 0.1 mg/ml) and the system was left to equilibrate for 1 hour at room temperature. Following the incubation period, the integrin-containing bilayer was probed with point measurements above the location of the cavities. Surprisingly, fitting of the ACF traces did not show any change in the lateral diffusion co-efficient of $\alpha_{IIb}\beta_3$-atto655 where the protein did not appear to alter its rate of diffusion, remaining near the 2.80 $\mu m^2/s$ value recorded with the un-activated, unliganded form of $\alpha_{IIb}\beta_3$. (Table 18) A one-way ANOVA with post-hoc Bonferroni test confirmed this to be non-significant, where $F(2, 114)$, $p > 0.05$. The alpha value also remained at 1, consistent with unhindered diffusion.

This was in contrast to our GUV system where fibrinogen binding resulted in anomalous sub-diffusion represented by a reduction in the recorded alpha value. Another characteristic of integrin-fibrinogen binding in our GUV system was the movement of large integrin clusters through the focal volume in large fluorescent bursts as visible in the MCS trace. Therefore, the MCS trace was examined for similar traits in our cavity supported lipid bilayer system. Figure 90 shows a representative MCS trace before and after DTT-mediated activation of $\alpha_{IIb}\beta_3$ in the presence of fibrinogen. In contrast to our GUV-based results (Figure 53) but in agreement with the unchanged diffusion and alpha values in our cavity supported lipid bilayer system, the MCS trace appeared unaffected when its characteristics were compared before and after integrin activation in the presence of fibrinogen. As displayed in the MCS trace, the atto655-labelled $\alpha_{IIb}\beta_3$ proteins transitioned through the focal volume at regular intervals throughout the length of the point measurement under all conditions. No major changed in the number of fluorescent molecules present in

the focal volume during measurements was obvious (N). Taken together these three unchanged variables (diffusion co-efficient, alpha value, and MCS trace) suggest that the integrin $\alpha_{IIb}\beta_3$ proteins present above cavities were not fibrinogen bound and/or aggregated above cavities, in contrast to the free standing GUV system (section 3.3.6).

Table 18: The influence of integrin activators in the presence of the integrin ligand fibrinogen. No change in the mobility of the integrin protein was detected. This was shown via one-way ANOVA analysis. This was unexpected given our results in GUVs where the use of an integrin activator in the presence of fibrinogen lead to measureable reduction in the mobility of $\alpha_{IIb}\beta_3$. Standard deviation was used to display the error.

Activator	Lateral Diffusion Co-efficient ($\mu m^2/s$)	Alpha value	N value
No activator	2.80 ± 0.59	1.00 ± 0.01	1.58 ± 0.41
5 mM DTT + fibrinogen	2.85 ± 0.71	1.01 ± 0.03	1.77 ± 0.56
5 mM Mn^{2+}+ fibrinogen	2.69 ± 0.33	0.99 ± 0.02	1.49 ± 0.62

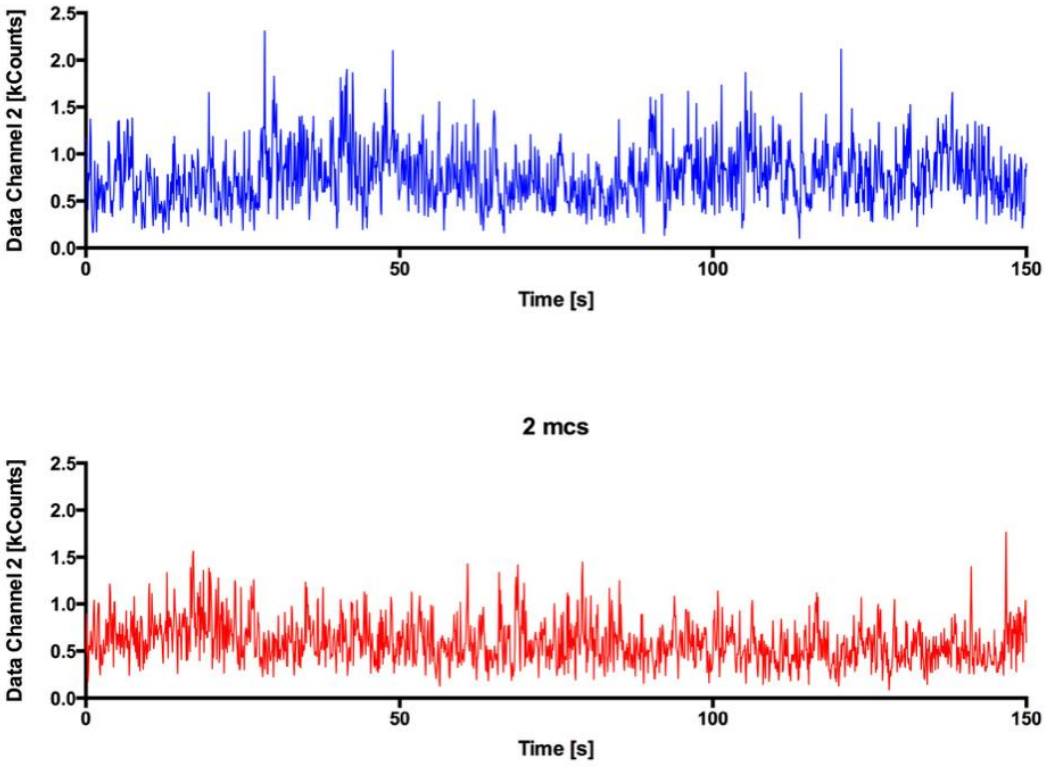

Figure 90: MCS trace before (blue) and after (red) ligand addition. No major changes in the characteristics of the time-trace were evident. This is in contrast to the findings in our GUV studies before and after fibrinogen addition where large fluorescently labelled aggregates were found to diffuse through the focal volume.

The absence of fibrinogen binding to DTT and Mn^{2+} activated $\alpha_{IIb}\beta_3$ above buffer-filled cavities was surprising given the earlier GUV-based results. This suggests that here the $\alpha_{IIb}\beta_3$ proteins had an altered affinity for their ligands when compared to GUV-reconstituted $\alpha_{IIb}\beta_3$. Therefore, in order to gain more insight, confocal microscopy was also carried out on the system. Interestingly, it was noted that after the addition of fibrinogen to DTT or Mn^{2+} activated $\alpha_{IIb}\beta_3$, integrin aggregation began to become evident on planar PDMS regions over time. Also of note was the fact that neither the use of activators nor fibrinogen caused integrin aggregation over the time course of an experiment (up to 8 hours). Figure 91 shows the PDMS array over which a nature's own SLB was formed, as well as the spanning nature's own SLB. Before the addition of activators or ligands the atto655-labelled $\alpha_{IIb}\beta_3$ was homogenously distributed within the bilayer. Figure 92 shows atto655-labelled $\alpha_{IIb}\beta_3$ after DTT-mediated activation and incubation with fibrinogen, as well as the labelled fibrinogen itself. After addition of DTT and incubation with fibrinogen, large integrin

clusters became visible. Importantly these aggregates were co-localised with fluorescently-labelled fibrinogen clusters. This shows that the large scale integrin aggregation was mediated by fibrinogen. Importantly, this aggregation was only witnessed when both an activator (DTT or Mn^{2+}) and fibrinogen were co-incubated together above the $\alpha_{IIb}\beta_3$-reconstituted bilayer. The ability of an activator and fibrinogen to bring about integrin clustering was surprising given that earlier experiments had shown that $\alpha_{IIb}\beta_3$ was immobile on planar PDMS regions. This was shown in MCS traces where fluorescently labelled integrin readily photobleached during point measurements. The reason for this ability of $\alpha_{IIb}\beta_3$ to form aggregates is therefore unclear but we speculate that the slow moving (below the limits of FLCS) integrin protein at the planar PDMS surface is preferentially aggregating and binding to fibrinogen. Such slow diffusing labelled $\alpha_{IIb}\beta_3$ would be susceptible to photobleaching due to the length of time they remain in the focal volume during point measurement, and therefore give the impression of complete immobility. Therefore, it is only over the length scales of these confocal images that the mobility of $\alpha_{IIb}\beta_3$ becomes apparent. Another aspect of the results that is not immediately obvious is why the ability of $\alpha_{IIb}\beta_3$ to bind fibrinogen and aggregate in GUVs and on planar regions of PDMS is not replicated above buffer-filled cavities. Again we can only speculate why this is the case. For example, perhaps the $\alpha_{IIb}\beta_3$ located on planar PDMS regions has more affinity for its ligand, fibrinogen. This could be due its slower diffusive properties when compared with the highly mobile $\alpha_{IIb}\beta_3$ found above cavities. Or perhaps it can be speculated that the planar substrate has a direct influence on the structure and conformation of the integrin $\alpha_{IIb}\beta_3$ protein increasing its affinity for fibrinogen binding.

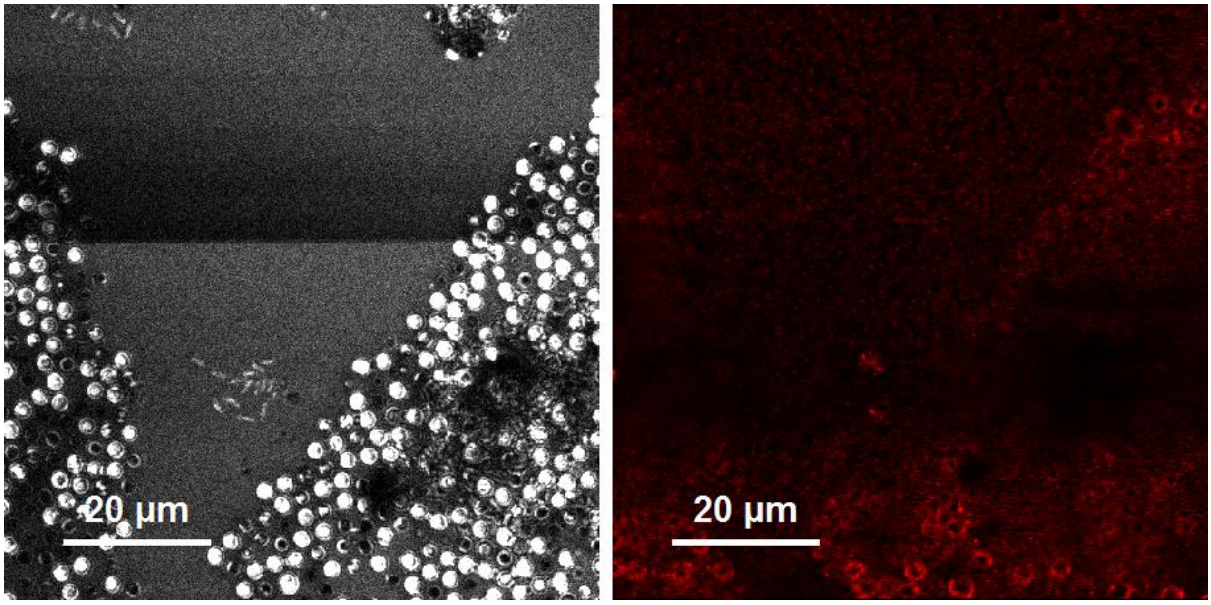

Figure 91: Left) Reflectance image of a PDMS cavity array. The majority of cavities are buffer-filled and appear as a bright white circle due to light scatter. Right) An integrin-containing nature's own lipid bilayer was constructed across the the PDMS array. $\alpha_{IIb}\beta_3$ was labelled with atto655 to allow for imaging of the bilayer. The reconstituted integrin protein was well-distributed throughout the bilayer with no defects visible. Un-filled on non spanned cavities were highlighted by a fluorescent halo.

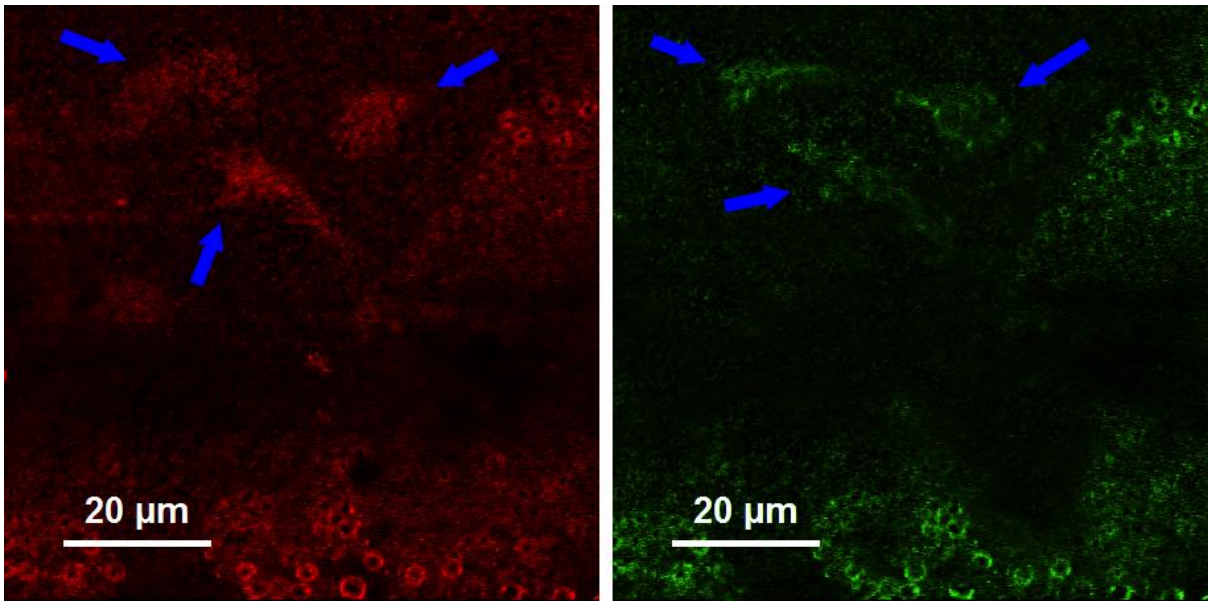

Figure 92: Left) Atto655-labelled $\alpha_{IIb}\beta_3$ after DTT activation and fibrinogen incubation. Activation and ligand addition lead to large integrin aggregates to form on planar regions of the PDMS. Right) The use of atto655-labelled fibrinogen showed that fibrinogen appeared to cluster in the same location as integrin aggregates. This shows that fibrinogen was mediating the aggregation process.

Overall the creation and use of our PDMS cavity supported lipid bilayer system has provided a novel method of decoupling both the lipid bilayer, and more importantly, membrane-reconstituted proteins from the underlying substrate. Importantly, our PDMS cavity arrays are cost effective, simple to fabricate, and easy to produce on a large scale. The use of such arrays also avoids the use of extensive surface[31] or lipid modifications[183] used be other groups.

The substrates themselves were stable for an indefinite period of time and the cavity-spanning bilayers were capable of producing reliable diffusion data for up to 5 days after spanning. The PDMS arrays were also extremely well suited to single particle measurements such FCS and FLCS-based experiments owing to the large cavity diameter. Many existing cavity systems utilise nanometer scale pores where such diffusional measurements would not be possible.[167,169] The use of such single molecule techniques to obtain diffusion data is also relatively unique within the existing SLB models. For, example the majority of the literature has utilised FRAP to obtain diffusional characteristics of fluorescently labelled molecules within planar systems and these have been characterised by large scale protein immobility even where polymers cushions or tethers have been included.[29–31,34,43,44,163,181,183–186]

As such FCS and FLCS measurements of membrane proteins have generally been the preserve of free-standing GUV-based systems. Here we have been able to provide GUV-comparable diffusion co-efficients in conjunction with 100 % protein mobility[36,41,142,144], with the spatial stability of an SLB system. This meant that point measurements could easily be carried out at carefully defined locations. In comparison, point measurements in GUVs may be particularly difficult and time consuming due to the mobility of the vesicles within the buffer, where even slight fluctuations of GUV membranes within the focal volume may render FCS data useless.

Another major advantage of our PDMS arrays is the fact that the set-up is chip-based, with an inlet and outlet available for buffer flow. Therefore, different proteins, drugs, buffers, etc. can be brought in contact with the bilayer for a defined

period of time before being flushed from the cell. For example, this was exploited during the annexin V insertion protocol (section 4.2.8) whereby the protein was membrane-reconstituted using a calcium-containing insertion buffer before being flushed with an EDTA-containing buffer to remove non-incorporated protein.

Another feature of our cavity arrays is the fact that the buffer-filled cavities provide access to both side of the lipid bilayer and this both the intracellular and extracellular domains of any membrane-reconstituted proteins. It is hoped to take advantage of this feature in future experiments. For example, through the controlled release of integrin interacting cytoplasmic proteins such as talin to the tails of membrane-reconstituted $\alpha_{IIb}\beta_3$, in conjunction with extracellular ligands such as fibrinogen, fibronectin, vitronectin, etc. It is also clear from the fibrinogen binding studies that the cavity top surface is not innocent in these studies, this may be an exploitable feature depending on the process under study but for integrins, reducing the relative amount of area of top surface may be a useful way to reduce its influence.

5. Cytoskeletal Mimics

5.1. Introduction

Much of this thesis has been devoted to modelling the complexity of the cell membrane in a physiological manner. Starting with $\alpha_{IIb}\beta_3$ in the platelet membrane (chapter 2), we transferred this knowledge to liposome-based mimics of the cell membrane (chapter 3). There we expanded upon the existing literature in the search for physiologically-relevant lipid compositions in our GUV model, and studied the functional ability of $\alpha_{IIb}\beta_3$ within this system. This knowledge was later transferred to our novel PDMS arrays (chapter 4) where we were able to convert our physiologically-relevant, $\alpha_{IIb}\beta_3$-containing GUVs to a $\alpha_{IIb}\beta_3$-reconstituted planar bilayer that spanned the buffer-filled microcavities. This planar system combined the main advantages of vesicle-based systems (free-standing, no lipid-substrate or protein-substrate interaction) with the main advantages of planar SLBs (increased stability, flow-cell setup) to create a biologically-relevant mimic of the cell membrane. Here, in the quest to increase the physiological relevance even further, we explored the inclusion of cytoskeletal structures in SLB models. Such cytoskeletal structures have an important role in the localisation and clustering of transmembrane proteins, the formation and deformation of lipid domains as well as the rate of protein diffusion. As these subjects were of particular interest to us in previous chapters the inclusion of such cytoskeletal proteins within an artificial lipid platform was the natural progression. For example, it was hoped that the use of cytoskeletal fibres below and in contact with a spanning lipid bilayer would provide a physiologically-relevant environment for lipid and transmembrane protein diffusion and interaction and thus alter the diffusion of the bilayer to more accurately mimic the cell membrane. This use of a cytoskeletal cushion is in contrast to existing work within the literature where lipid bilayers tend to be in contact with buffers (eg GUVs or PEG cushions) or solid substrates (eg SLB above glass or mica).

5.1.1. The cytoskeleton

The cytoskeleton is an interconnected network of filamentous polymers and regulatory proteins that underlies the cell membrane. It is a dynamic and adaptive structure whose constituents are in constant flux. It carries out three main functions, namely spatial organisation of the cell contents, connects the cell (physically and biochemically) to the external environment, and generates co-ordinated forces that enable the cell to move and change shape.[187] This involves the interactions of hundreds of associated proteins – molecular motors, crosslinkers, capping proteins and nucleation promoting factors.[188] The cytoskeleton can be approximately divided into three different categories, namely microfilimants, microtubules, and intermediate filaments.

Microfilaments, made from actin polymers, are the thinnest filaments of the cytoskeleton with a diameter of approximately 7 to 10 nm.[189] Actin is the most abundant protein in the majority of eukaryotic cells. It exists as a globular 42 kDa monomer known as G-actin but has the ability to transition to a filamentous form known as F-actin induced by nucleotide hydrolysis, ions, and a large number of actin-binding proteins in a reversible manner.[190] F-actin forms long linear structures of varying architecture and these different architectures support varying roles within the cell. For example, bundled networks support filopodial protrusions that are involved in cell-cell communication, while branched networks support the leading edge of motile cells and generates the forces involved in morphological changes. One of filamentous actin's key functions is to act as an intracellular train track for the movement of myosin, and thus enable muscle contraction.[187] The formation of F-actin begins with the nucleation step where actin dimers and trimers are first formed. They elongate rapidly as a function of monomer availability. Polymerisation of actin monomers at the filament end followed by hydrolysis of ATP bound to the actin subunits inside the filaments as well as phosphate dissociation. Additionally, actin monomers bind divalent cations like calcium and magnesium which influence polymerisation dynamics.[191]

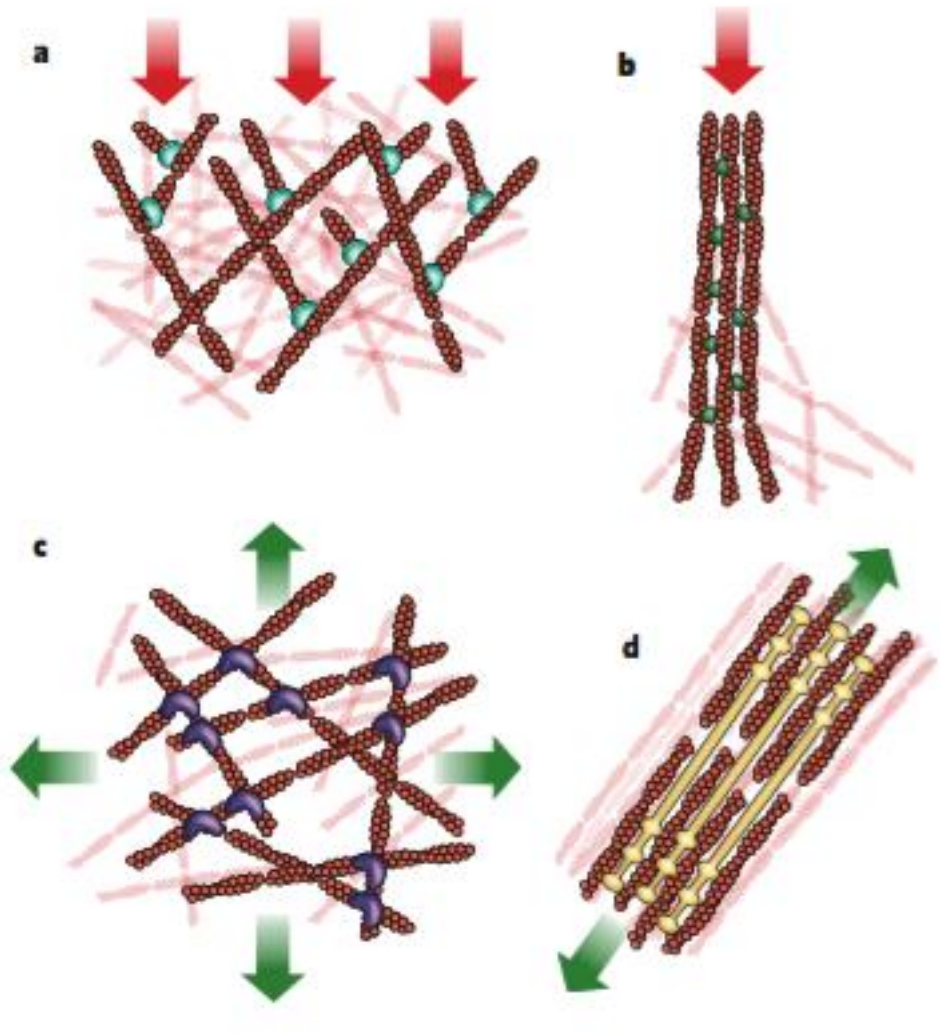

Figure 93: Actin networks may take different architectures, which in turn lends different functions. Red arrows show compression, while green arrows show tension. A) Branched actin networks push against the cell membrane and external barriers as they generate protrusons. B) Filopodia also generate protrusive forces as they extend from the cell. C) Cortical networks such as those involving filamin crosslinking carry tension loads in multiple directions. D) Stress fibres form bundled actin filaments and generate tension against cell adhesions to the extracellular matrix. Diagram from "Cell Mechanics and the Cytoskeleton". [187]

The second category of cytoskeletal proteins; microtubules, are formed from tubulin proteins. They form hollow cylinders with a much larger diameter than actin filaments at approximately 23 nm. They are polymers of alpha and beta tubulin that combine to form stiff, relatively long networks. Microtubules are capable of rapidly disassembling and it is this dynamic instability that allows for quick cytoskeletal

reorganisation and their ability to quickly search the cellular space. They play a role in intracellular transport such as the movement of vesicles and mitochondria.[187]

The third category of cytoskeletal proteins are intermediate filaments. They have diameters of approximately 10 nm. Intermediate filaments are found widely distributed throughout the intracellular space. This complex network ranges from the plasma membrane through to the nucleus, and includes association with both microfilaments and microtubules. Unlike microfilaments and microtubules, intermediate filaments are not directly involved in cell movement but appear to play a purely structural role organising the 3 dimensional cell structure as well as anchoring cell organelles. This fibre category includes a wide range of proteins (over 50) and includes keratins, lamins and nerofilament proteins.[192]

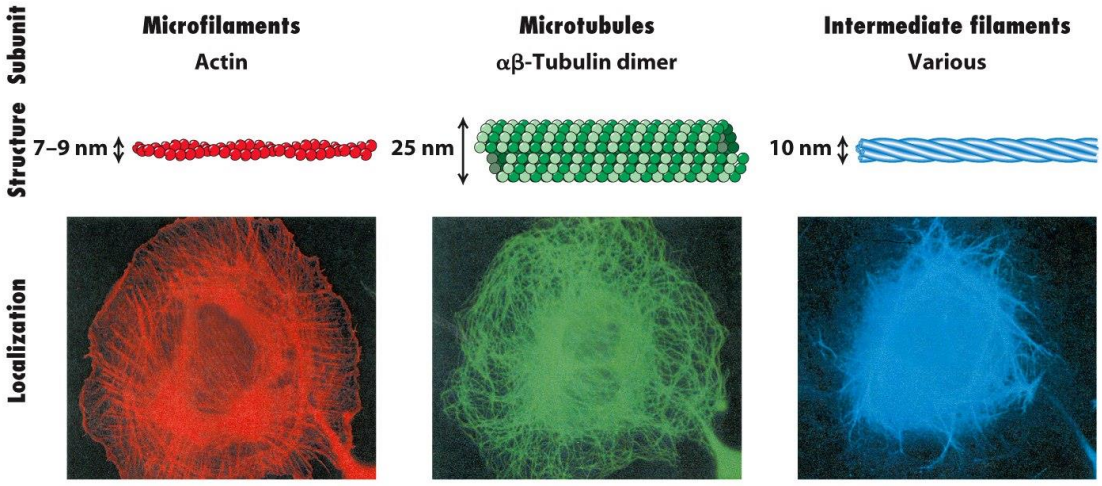

Figure 17-2
Molecular Cell Biology, Sixth Edition
© 2008 W. H. Freeman and Company

Figure 94: Microfilaments, microtubules and intermediate filaments within the cell. The cytoskeleton is a complex matrix of structures that combine to play a role in spatial organisation, while allowing changes in cell morphological in response to the external environment. This figure shows the approximate scale of microfilaments, microtubules and intermediate filaments, as well their position within the cell. Image from "Molecular Cell Biology".[193]

5.1.2. Cytoskeletal interactions with lipids and proteins

The cytoskeletal proteins provide a regulatory and functional role via their interaction with both lipids and other proteins. For example, there exists evidence for the role of actin in the formation and turnover of ordered lipid rafts, highly ordered cholesterol and sphingolipid rich nanodomains (previously discussed in section 1.1).[194] *In vivo* experiments have shown that the formation of ordered domains can be controlled by actin polymerization. Inhibiting the polymerization process decreased the fraction of ordered domains in the cell membrane, while stabilizing actin filaments had the opposite effect. Therefore, it appears that lipid rafts form when actin filaments attach to the plasma membrane.[195,196] In addition the reverse may also be true, wherein depletion of cholesterol from the cell membrane seems to result in actin disassembly.[197] Therefore, the cytoskeletal-lipid raft relationship appears to be both complex and reciprocal in nature.

The cytoskeleton is also recognised as the intracellular scaffold upon where extracellular ligand recognition and signal transduction takes place. Focal adhesions occur at sites where the cell membrane interacts with the ECM. Here, mechanical force and regulatory signals are transmitted between the actin cytoskeleton and the ECM via large macromolecular assemblies. More precisely, focal adhesions are the sub-cellular structures that mediate the regulatory effects (i.e., signalling events) of a cell in response to ECM adhesion. Focal adhesions serve as the mechanical linkages to the ECM, and as a biochemical signalling hub to concentrate and direct numerous signalling proteins often at sites of integrin binding and clustering. The assembly of focal adhesions is regulated by the GTP-binding protein Rho. Rho stimulates contractility which, in cells that are tightly adherent to the substrate, generates isometric tension. In turn, this leads to the bundling of actin filaments and the aggregation of integrins in the plane of the lipid membrane. The aggregation of integrins activates the focal adhesion kinase and leads to the assembly of a

multicomponent signaling complex including talin, filamin, tensin and vinculin.[198] The exact structure of these focal adhesions varies from cell to cell, as well as by location within the membrane but they can be roughly grouped into a number of categories. For example, focal complexes are small adhesions associated with spreading and migrating cells and usually concentrated within membrane protrusions. Over time they may mature into larger and more elongated structures. Larger adhesions are normally found in resting cells or within areas of low motility and act as attachment points between the cell membrane and actin stress fibres. Fibrillar adhesions are a type of focal adhesion where extracellular fibronectin fibrils are arranged in a parallel orientation with actin stress fibres. Fibrillar adhesions also lack proteins such as vinculin and paxillin, which are normally present in standard focal adhesions. Finally, podosomes are ring like assembles of matrix adhesion components surrounding an F-actin core and are involved in cell motility.[199]

The complex interaction between the cell cytoskeleton, the lipid bilayer, and membrane proteins is perhaps summed up best by Head *et al.* where they stated that "The combination of lateral membrane movement and transmembrane interaction among integrins, membrane bilayer lipids, and membrane proteins within membrane lipid rafts, along with interaction of the actin/myosin cytoskeleton and cytoskeletal tethering partners, can contribute to cellular migration, mechano-transduction, cell growth, endothelial and epithelial barrier formation, and immune cell activation—physiologically important responses and ones that can be altered in disease settings".[200]

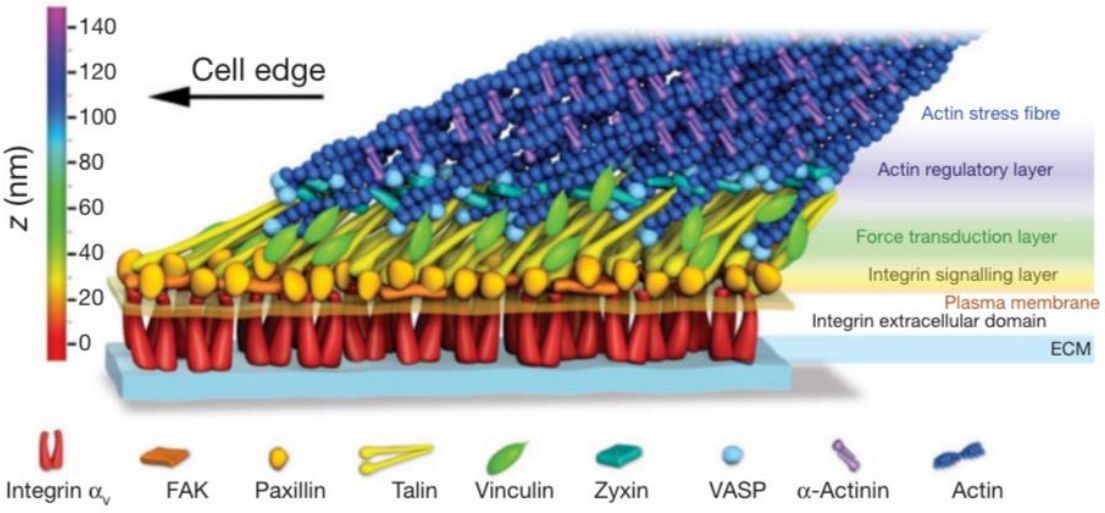

Figure 95: The nanoscale architecture of focal adhesions. The integrin proteins span the cell's lipid membrane to provide a link between the ECM and the cell. This is mediated by a variety of intracellular proteins including focal adhesion kinase and paxillin in an integrin signalling layer, talin and vinculin in an intermediate force transduction layer, and an uppermost actin-regulatory layer containing zyxin, vasodilator-stimulated phosphoprotein and a-actinin. Image from "Nanoscale architecture of integrin-based cell adhesions".[107]

5.1.3. Actin in platelets

Due to the morphological changes that platelets undergo during activation, as well as the importance of integrin $\alpha_{IIb}\beta_3$ in the aggregation process, the role of actin is particularly relevant in platelets. In fact, actin makes up approximately 20 % of the total protein found in platelets. In the resting platelet state 40 – 50 % of the actin is unpolymerised, much of it sequestered in protein complexes. The resting platelet cytoskeleton contains around 2000 F-actin filaments of approximately 1 μm in length which are crosslinked by actin-binding proteins (ABP) and which bind to spectrin rich lamina. As the platelet becomes activated, the cell fragment undergoes morphological changes and this is driven by an increase in the fraction of polymeric actin as the platelet filopodia extend.[201] For example, within 20 seconds of thrombin stimulation the percentage of polymerized actin has been shown to increase from 40 – 50 % to 70 %.[202]

In their resting form, discoid platelets are thought to contain a trilaminar membrane shield made up of an outer membrane, a spectrin and ABP-rich inner membrane, and a cage of closely aligned actin filaments that connect to the central core via radiating spokes. Along these spokes the pro-polymerization protein VASP is found, while ABP, tropomyosin, and spectrin stabilise the filaments. Once activated many existing filaments are disassembled while new fibres form. The once discoid platelet begins to initially round as the connections between the core actin filaments and the membrane skeleton appear to be dissociated. Following this, the membrane skeleton is dismantled, and the core filaments contract in a myosin-mediated process into a microfilamentous shell, known as the contractile ring. This cytoskeletal reorganisation results in the platelet becoming less rigid as deformation allows the filopodial and lamellipodial protrusions to occur. New actin monomers become available as previously sequestered actin is released. This allows actin growth to be facilitated. Finally, receptors such as $\alpha_{IIb}\beta_3$, GP1b/IX and GPVI interact with their respective ligands as the adhesions mature and higher ordered actin-based stress fibres begin to form.[202] For example, Bennett *et al.* found a direct role for actin polymerization in $\alpha_{IIb}\beta_3$ activation. They found that inhibition of actin polymerisation within platelets mimicked the effects of platelet agonists and promoted fibrinogen binding to $\alpha_{IIb}\beta_3$. The reverse was also true where stabilizing actin filaments prevented agonist induced $\alpha_{IIb}\beta_3$ binding to fibrinogen. To explain this, they proposed that actin constrains $\alpha_{IIb}\beta_3$ in a low affinity state and that agonist-stimulation increases the concentration of cytosolic calcium in the platelet which in turn initiates actin filament turnover that leads to relief of cytoskeletal constraints on $\alpha_{IIb}\beta_3$, allowing it to assume the high affinity conformation required for ligand binding.[203]

Integrin clustering within the platelet membrane is believed to instigate the formation of focal adhesions. Some focal adhesion proteins are known to be particularly important with regards to both integrin activation and actin interactions. For example, talin is a well recognized activator of integrin both *in vivo*[204] and *in vitro*[45]. It is also an F-actin binding protein where it is involved in initiation of matrix adhesion formation and the linkage of integrin receptors to the actin cytoskeleton. It

is vitally important in the first steps of focal complex formation and also the turnover of adhesions owing to its degradation. Talin can also bind to and activate vinculin which subsequently promotes and stabilises talin-mediated integrin clustering by providing additional F-actin crosslinks to the nascent focal complex. Furthermore, filamins are large (280 kDa) proteins with the ability to bind to both integrins and actin. Tensin is a 220 kDa protein which binds to F-actin via 3 actin binding domains. It is also capable of binding to β_3, β_5, β_7, and more weakly, β_1-containing integrins. Finally, α-actinins are F-actin crosslinkers that also possesses affinity for the cytoplasmic β-tails of some integrins. It also has a considerable number of additional binding partners such as the aforementioned vinculin.[199] As can be seen there exists a complex and multicomponent relationship between integrins, actins, and actin binding proteins during the $\alpha_{IIb}\beta_3$ activation process.

5.1.4. Cytoskeletal mimics in artificial lipid systems

In spite of the prevalence of fibrillar protein structures with cells, their interaction with the lipid membrane and associated proteins, and the wide range of model membrane systems reported, there is a limited body of work that combines these artificial model lipid systems with cytoskeletal structures. Instead most SLB and liposome models focus on the lipid itself or reconstituted membrane proteins. Yet model systems can extract useful insights into the influence of fibrullar protein structures on lipid dynamics, domain formation and on diffusion and clustering of reconstituted protein away from the complexity of the cell.

In one example, *Yi et al.* attempted to mimic the cell cytoskeleton and lipid diffusion in contact with the cytoskeleton by creating nanofiber networks made from polycaprolactam which had been modified by coating it with silica in order for it to be highly hydrophilic. POPC lipid vesicles were then disrupted above the mesh and FRAP was used to characterise the bilayer fluidity in contact with the fibres. Above an aperture-spanning nanofiber network, the diffusion co-efficient was determined

to be 0.98 ± 0.15 $\mu m^2/s$. In contrast to this, the diffusion co-efficient over a glass substrate was determined to be 0.40 ± 0.09 $\mu m^2/s$.[205] This shows how the diffusion co-efficient of lipid can be impacted by the construction of a substrate designed to mimic the cell cytoskeletal.

In a paper titled "Minimal F-actin cytoskeletal system for planar supported phospholipid bilayers", Barfoot *et al.* showed that is was possible to construct actin tethered lipid bilayers. While they did not study the actin's influence on lipid diffusion, crucially they were able to show the ability to construct F-actin-spanning SLBs.[189] Sterling *et al.* were able to construct an actin-spanning DMPC SLB although they utilised the globular form of actin (G-actin) immobilised on a glass surface as a protein cushion, rather than the polymerised F-actin form. Nonetheless, they were able to compare this lipid diffusion versus a glass substrate control across a range of temperatures from 20 to 44 °C. Above glass the diffusion co-efficient ranged from approximately 0.6 $\mu m^2/s$ to 3 $\mu m^2/s$. In contrast, above G-actin this diffusion co-efficient ranged from approximately 0.4 $\mu m^2/s$ to 2 $\mu m^2/s$. Thus, although the lipid bilayer was still mobile above G-actin, the lateral diffusion co-efficient was notably reduced when compared to the glass substrate control. Also of interest was the increase in the phase transition temperature from 24.3 °C in the glass supported bilayer to to 32.7 °C for the actin supported bilayer.[206] Our goal in this final experimental chapter was similar to this set-up with the key difference being the use of the filamentous form of actin, to mirror the cytoskeletal lipid membrane scaffolding of the cell, rather than the use of the globular form of actin.

In a reversal of the above examples, some groups have added actin above SLBs rather than creating actin-spanning bilayers. For example, Heath *et al.* utilised a lipid bilayer to promote the self assembly of actin filaments. They found that when G-actin was added to a buffer solution above a lipid bilayer containing a positively-charged lipid; DOTAP, the globular actin began to adsorb at the SLB. At 15 % DOTAP, filamentous actin began to become obvious above the bilayer as the nucleation concentration threshold had been reached. In the case of fluid-phase lipid bilayers,

the actin adsorbed to form a uniform two-dimensional layer with complete surface coverage, whereas gel-phase bilayers induced a network of randomly oriented actin filaments, of lower coverage.[207]

Honigmann *et al.* showed that membrane bound actin networks had an important influence on lipid phase separation. Here, actin was added above an ordered/disordered domain-forming ternary mixture of DOPC, DPPC and cholesterol and attached to the bilayer via a biotin-streptavidin linkage. It was found that actin prevented macroscopic liquid-ordered and liquid-disordered domain formation in this domain-forming membrane. Instead the disordered phase lipids appeared to associate with the actin filaments themselves. FCS measurements showed that the diffusion of the lipid bilayer was hindered under these conditions.[208]

Thus, although there exists some SLB models that have incorporated cytoskeletal structures within, no literature exists where lipid diffusion has been examined as part of SLB above the filamentous form of actin as exists within the living cell. There are also no model studies investigating the influence of actin network on integrin diffusion and aggregation.

This purpose of this chapter was to take the first steps toward building static actin structural analogues into the membrane model. Herein we describe preliminary efforts to assemble actin and related fibrous proteins above or below the membrane in a supported lipid bilayer system, with the long term objective of translating these structures to our PDMS cavity arrays. It is eventually hoped that we can build these arrays in which actin is assembled across the cavity apertures in order to examine the impact of these proteins and other fibrillar structures on integrin (and other membrane protein) diffusion.

Actin

Here, we attempted to firstly create F-actin-spanning lipid bilayers, comparing assembly of bovine cardiac, rabbit skeletal, and human platelet actin to study lipid

diffusion in contact with each fibre. Although actin is often thought of as single protein, in mammals it actually consists of 6 different isoforms, each encoded by a different gene. The isoforms are remarkably similar to one another, with only slight variations in amino acid sequence.[209] *In vivo* these different isoforms lend themselves to different actin binding proteins. Of the three different commercially available actins used, the primary difference is the isoform composition. Bovine cardiac actin is 84 % alpha cardiac and 16 % alpha skeletal actin. Rabbit skeletal actin is 99 % alpha skeletal. Human platelet actin is 85 % beta actin and 15 % gamma actin isoforms. Actins have a diameter of approximately between 7 and 10 nm and an isoelectric point of approximately 4.8.[210] *In vitro* they form fibres up to 10 μm long.

Ryadnov group fibres

As a comparison to actin, we also utilised fibre-forming peptide sequences that were designed and constructed by the Ryadnov group at the National Physical Laboratory in London. Dr Radnov's group specialise in *de novo* biomolecular design and engineering functional nanostructured materials.[211] In this case Dr Ryadnov provided us with three different self-assembling peptide-based nanofibres known as cyan(+)4, cyan(+)6 and SR_EDS_02.[211] The objective of comparing these with the actin fibres was that they are synthesized, so that their fibres are of consistent and of controlled length and diameter. According to data supplied by Dr Ryadnov's group, cyan(+)4 fibres are composed of polymerised polypeptides, 28 amino acids in length with a molecular weight of 3069. The polymerised fibres are between 90 and 500 nm in length, with a thickness of 5 – 25 nm. Cyan(+)6 fibres are composed of polymerised polypeptides, 42 amino acids in length with a molecular weight of 4573. They form fibres with a length between 70 and 90 nm and a thickness between 4 and 6 nm. Finally, SR_EDS_02 polypeptides are 42 amino acids in length, with a molecular weight of 4713. Polymerised, the fibres are on the micrometre scale with an approximate width of 300 nm. The isoelectric points of these fibres ranges from 7.1 to 9.5, much higher than the isoelectric point of actin. The SEM images, supplied by Dr Ryadnov's group, of the formed fibres are given in Figure 96. The lengths and widths of the fibres were obtained from multiple SEM experiments and measured

using Image J. Further detail on the structure of the polypeptides is given in Table 19. Using these *de novo* nanofibers, alongside *in vitro* formed actin filaments, we sought to compare and contrast the influence of fibre dimension on the fluidity of an interfaced, supported lipid membrane.

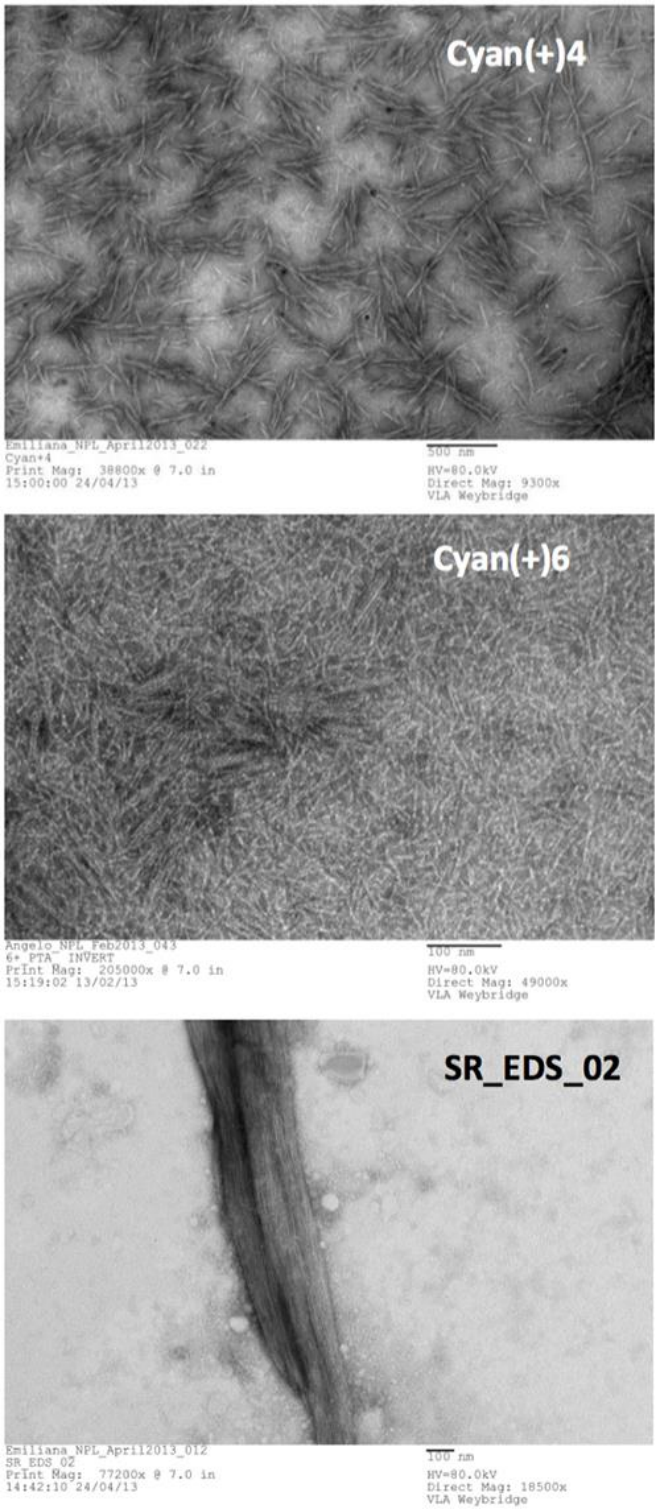

Figure 96: SEM images of the three different fibres supplied by Dr Ryadnov's group. According to their SEM data, cyan(+)4 fibres are between 90 and 500 nm in length, with a thickness of 5 – 25 nm. Cyan(+)6 has a length between 70 and 90 nm with a thickness of 4 – 6 nm. SR_EDS_02 has a length in the µm range with a thickness of approximately 300 nm. This data was supplied by Dr Ryadnov's group, as measured using imageJ from multiple SEM experiments.

Table 19: A table describing the characteristics of Dr Ryadnov's group's fibre-forming peptides. Three different self assembling peptides known as cyan(+)4, cyan(+)6, and SR_EDS_02 were provided.

Peptide	Amino acid composition	Amino Acid Length	Molecular Weight	pI
Cyan(+)4	A (8), E (4), K (5), L (4),Q (2), I (4), Y (1)	28	3069	9.5
Cyan(+)6	A (12), E (6), K (7), L (6),Q (4), I (6), Y (1)	42	4573	9.4
SR_EDS_02	A (12), E (6), K (6), L (12),Q (3), W (3)	42	4713	7.1

5.2. Experimental

5.2.1. FLCS measurements

Before FLCS measurements, the substrate surface was fluorescently imaged to identify both the presence of the fluorescently-labelled lipid and fluorescently-labelled fibres. The actin fibres were fluorescently-labelled with phalloidin-TRITC, while the Ryadnov group's fibres were fluorescently-labelled with sulfo-rhodamine B. Confocal images were collected using a MicroTime 200 fluorescence lifetime microscope system. Fluorophores were excited with 532 nm PicoTA or 640 nm light from a LDH-P-C-640B diode laser. The laser was directed toward a z532/635rpc dichroic mirror and focused on a water immersion objective (NA 1.2 UPlanSApo 60 x 1.2 water/ CC1.48, Olympus). The sample fluorescence was collected through the same objective and filtered by the aforementioned dichroic mirror, as well as by an HQ550lp AHF/Chroma filter (Olching, Germany) for the 532 nm laser, or a BLP01-635R-25 Semrock filter (New York, USA) for the 640 nm laser. Finally, the sample fluorescence was passed through a 50 mm pinhole onto a MPD SPAD detector. The ability to locate the various filamentous proteins on the substrate surface allowed for the positioning of point measurements above both actin and Ryadnov group fibres. The Z-position was firstly roughly tuned using the built-in CCD camera of the microscope. This allowed us to identify the approximate Z-position of planar substrates. To fine-tune this position to the lipid bilayer, a Z-scan was then performed to locate the point of highest fluorescence intensity due to the presence of fluorescently-labelled lipid and protein. Due to drift within the system the Z-position was recalibrated between each point measurement.

Diffusion coefficients for labelled lipid or fibres were obtained using FLCS. The autocorrelation functions obtained using FLCS are less prone to noise and distortion caused by scattered excitation light, detector thermal noise and detector

afterpulsing than conventional FCS.[67] FLCS measurements were performed using a MicroTime 200 confocal fluorescence lifetime microscope system. For FLCS experiments, the fluorophores were excited and the sample fluorescence was also collected as described for confocal microscopy. The autocorrelation functions (ACF) were fit using SymphoTime software (PicoQuant GmbH, Berlin, Germany):

$$G(\tau) = 1 + \left[\frac{1}{N}\right]\left[\frac{1}{1 + (\tau/\tau_D)^{\alpha}}\right]$$

For simple single component diffusion, or in the case of the presence of a triplet state:

$$G(\tau) = 1 + [1 - T + Texp(-\tau/\tau_T)]\left[\frac{1}{N(1-T)}\right]\left[\frac{1}{1 + (\tau/\tau_D)^{\alpha}}\right]$$

where G(τ) is the autocorrelation function of fluorescence fluctuations; N is the number of fluorophores in the effective volume; T is the fraction of the molecules in the triplet state; τ_T is the relaxation time for the singlet–triplet crossing; α is the anomalous parameter; and τ_D is the diffusion time, which is related to the lateral diffusion coefficient (D) of the labelled tracer by the expression:

$$\tau_D = \frac{\omega^2}{4D}$$

In the latter equation, the radius ω_0 is the distance at which the excitation intensity profile decreases to e^{-2} of its maximum value. This parameter was determined experimentally, by measuring the translational diffusion of Rhodamine 6G (532 nm laser) and Atto655 (640 nm laser) in water at room temperature (approximately 21 °C).[137] These dyes, have well characterized diffusion coefficients and so were used as standards to determine the working confocal volume for FLCS measurements.

5.2.2. STED imaging

STED imaging was performed with a Leica SP8 TCS STED 3X microscope using a Leica HC PL APO 100x/1.40 oil immersion objective designed for STED imaging. The labelled fibres were excited at the desired wavelength using the microscopes white light laser which had a tuning range between 470 and 670 nm in 1 nm intervals. Laser power and gain was adjusted as required. The instrument utilised hybrid detectors and/or PMTs to detect fluorescence. Again this detection window may be tuned to nanometer accuracy. Before STED imaging began, fibres were firstly identified via standard confocal microscopy. STED imaging was then performed at the same location using a suitable depletion laser (for example 660 nm for TRITC) to obtain a super resolution image.

5.2.3. PDMS cell construction

For these preliminary cytoskeleton-SLB-based experiments we utilised planar, super-hydrophillic glass as the underlying substrate. This was achieved through the plasma-treatment of glass coverslips (Harrick PDC-002 plasma cleaner at 1000 mT for 5 minutes). In a similar set-up our group have previously shown that ozone treatment of glass reduced the contact angle of a water droplet from 50° to 0°, thus rendering the glass superhydrophillic.[137] The experiments were conducted using a simple PDMS flow cell constructed around the glass coverslip. The structure of the cell was a simplified version of the cavity array cell, but the lipid interface was built at glass. Briefly, 10 parts PDMS elastomer to 1 part PDMS curing agent (w/w) were mixed to form the PDMS solution. The PDMS was thoroughly mixed and then placed in a vacuum desiccator for 30 minutes to ensure that all air bubbles were removed. Meanwhile a thin piece of freshly cleaved mica was glued to a glass slide to provide a raised platform and an aluminium foil “boat” was folded around the mica-glass

slide platform. Once the PDMS solution was bubble free the solution was gently poured into the foil (approximately 3 g per aluminium foil "boat"). The array was then placed on hotplate which had been preheated to 150 °C and cured over a 15-minute period. Once complete the PDMS piece was removed and left to cool before the aluminium foil was peeled from the substrate. Using a scalpel, the PDMS was then cut from the glass-mica platform to yield a PDMS piece with a lowered imprint which had been created by the raised mica. Two holes were punched at the extremities of the PDMS to provide an inlet and outlet for flow-through and Teflon tubing was attached to either end. Prior the beginning of an experiment, a glass coverslip was plasma treated in a Harrick PDC-002 plasma cleaner at 1000 mT for 5 minutes. The coverslip was then glued to the PDMS piece to provide a sealed chamber for later experimentation. Figure 97 shows a schematic of the PDMS cell. In contrast to the majority of chapter 4, which primarily focused on bilayer formation on the PDMS side of a similar cell set-up, this chapter focused on the near glass side of the PDMS cell where bilayers and cytoskeletal proteins were examined.

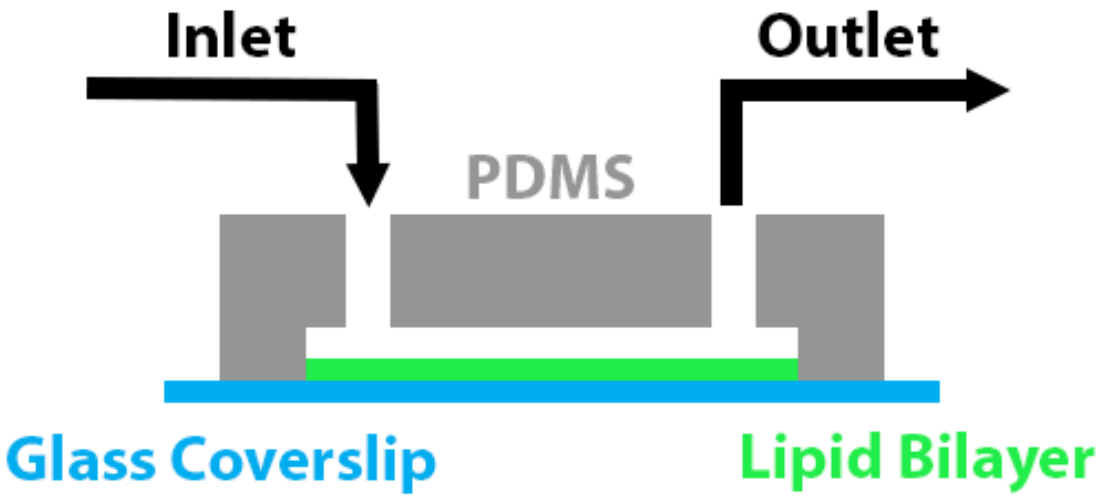

Figure 97: A schematic of the constructed PDMS cell used for cytoskeleton and SLB-based experiments. The glued PDMS cell provided a chamber containing inlets and outlets for flow through of buffers, lipids, and proteins used during the experiments.

5.2.4. Cytoskeletal fibres

In order to create a cytoskeletal mimic for our SLB system, a number of filamentous structures were examined. The first category of these were the actins; bovine actin, rabbit actin, and human platelet actin. The second category of fibres were self-assembling peptide fibres designed to mimic the cell cytoskeleton. These fibres were supplied by the Ryadnov group and known as cyan(+)4, cyan(+)6, and SR_EDS_02.

Actin polymerization

In order to form filamentous actin, frozen aliquots of actin (bovine, rabbit, or platelet) were thawed and placed on ice for 1 hour to depolymerize any F-actin filaments that may have been present. This defrosted actin was in general actin buffer of 5 mM Tris-HCl, 0.2 mM $CaCl_2$, 0.2 mM ATP, pH 8. In order to polymerise actin, $1/10^{th}$ of the volume of a 10x actin polymerization buffer was added to the globular actin. This 10x actin polymerization buffer was composed of 100 mM Tris, 500 mM KCl, 20 mM $MgCl_2$, 10 mM ATP, pH 7.5. The actin was incubated at room temperature for 1 hour to allow for F-actin to form. The concentration of actin was kept above 0.1 mg/ml throughout. This is because the propensity of actin to polymerize is dependent upon the affinity of actin monomers for filament ends. Thus, there is an actin monomer concentration below which actin will not polymerize. This value has been termed the Critical Concentration (CC). The exact CC varies with ionic type and strength. Keeping the actin concentration above 0.1 mg/ml was suitable for the nucleation step to begin. In order to fluorescently stain actin filaments, phalloidin-TRITC was used. Phalloidin is a mushroom toxin with strong binding affinity for actin filaments and is thus an excellent marker for actin visualization when conjugated to a fluorescent probe. Stock solutions of phalloidin-TRITC were stored in the fridge in methanol at 0.1 mg/ml. F-actin was diluted to 0.01 mg/ml (approximately 240 nM). Phalloidin-TRITC was added at a final concentration of approximately 24 nM and left to incubate for 1 hour. Labelled F-actin was then flushed through the PDMS flow cell.

Ryadnov group's fibres

Peptides provided by Dr Ryadnov's group are referred to as as cyan(+)4, cyan(+)6 and SR_EDS_02 and were each provided as lyophilised powders and stored at – 20 °C until required. Stock solutions were prepared to a concentration of 2 mM using dH_2O. Working samples were prepared by diluting the peptides to 100 μM using a buffer of 10 mM HEPES at pH7.4. It was important to limit the concentration of salts used as fibre assembly is stabilised by electrostatic interactions and thus improper buffer preparation could prevent assembly or promote disassembly. The thawed peptides were left to self-assemble overnight at room temperature. Before use, the fibres were gently mixed with a pipette to re-suspend them. In order to fluorescently label the fibres, the electrostatic dye sulfo-rhodamine B was used. Lyophilised sulfo-rhodamine B was re-suspended in methanol to make a stock concentration of 10 mM. This could be aliquoted and frozen for later use. For the working concentration this solution was diluted to 1 μM in the working buffer, in this case 10 mM HEPES, pH 7.4. The dye was then added to the peptides at a final concentration of 100 nM and left to incubate at room temperature for one hour. The fibres were then flushed through the PDMS flow cell.

5.2.5. Substrate Functionalization

In later experiments we sought to increase the surface coverage of immobilised fibres via modification of the glass substrate. Two different methods were explored.

Poly-L-Lysine coating

Poly-L-Lysine is a positively-charged synthetic polymer that facilitates the attachment of proteins and cells to solid surfaces for biological applications. Here it was used to increase the surface coverage of F-actin on a glass substrate. Poly-L-lysine (PLL) coating was carried out on the day of the experiment. The PLL was firstly diluted to 0.1 mg/ml in dH_2O for the working concentration. It was then pipetted onto a plasma-cleaned glass coverslip and incubated for 1 hour at room

temperature. dH_2O was then flushed across the coverslip to remove an excess PLL. This protocol was suitable to render the coverslip positively charged.

APTMS/GA coating

As an alternative to poly-L-lysine, a two-step functionalization of glass substrates was explored using 3-aminopropyl trimethoxysilane (APTMS) and glutaraldehyde (GA). Glass coverslips were firstly plasma-treated as normal. The surface was then modified with APTMS by attachment to the substrate's hydroxyl functional groups. This was achieved by incubating the coverslips for 3 hours with 5 mM APTMS dissolved in acetone. The coverslips were then dried under nitrogen to remove any remaining solvent. Directly before use the coverslips were incubated in a 10 % GA in dH_2O solution (v/v) for 1 hour. Following this the substrate was gently washed in dH_2O to leave behind an amine-reactive surface. An F-actin-containing solution could then be flushed across the surface in order to yield an actin coated surface. This two-step coating process has previously been used in microfluidic cells for the immobilisation of proteins.[212]

5.3. Results

5.3.1. Fibres below the SLB

Initial experiments were designed to measure the diffusion dynamics of fibre-spanning lipid membranes (Figure 98). Our objective was to investigate the relative ability of each actin and fibrous peptide type to form filaments at the glass interface, to investigate if the lipid bilayer spanned across these structures and to determine whether these filamentous structures were capable of altering the diffusion co-efficient of the spanning lipid bilayer. The use of these filamentous proteins within the SLB system was designed to better mimic the environmental conditions encountered by the lipid membrane within the cell. To date, the majority of existing work within the literature, as well as the platforms used in this thesis, have utilised a lipid bilayer in contact with buffers or solid substrates rather than a cytoskeletal cushion found below the cell membrane. Therefore, our inclusion of cytoskeleton proteins aimed to create a more accurate biomimetic model than what currently exists within the literature. To act as cytoskeleton mimics we used 6 different fibres: bovine actin, rabbit actin, human platelet actin, cyan(+)4, cyan(+)6, and SR_EDS_02.

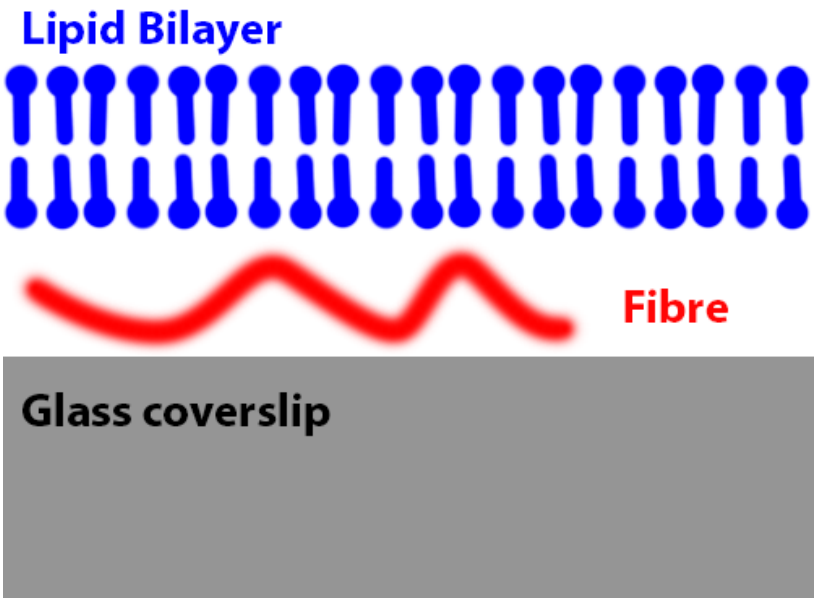

Figure 98: A schematic of the proposed system where a lipid bilayer is formed above nanometer wide and micrometer length polypeptide filaments. It was hoped that these fibres would act as a sufficient barrier to lipid mobility that would be reflected in the diffusional characteristics of the spanning lipid molecules.

F-actin polymerisation above bare glass

Following formation of F-actin according to the protocol described in experimental section, the labelled actin filaments were flushed across a superhydrophillic coverslip using the PDMS flow cell and imaged via confocal microscopy to determine whether actin fibres had formed and bound to the surface. Figure 99 demonstrates that using this approach we succeeded in achieving bovine F-actin polymerisation and that these filaments bind to the superhydrophillic glass slide. We therefore used analogous polymerisation conditions for the other actins as a routine method for formation of F-actin, and this lead to high levels of fibre assembly at the glass interface. The next step was to assemble a supported DOPC lipid bilayer above the actin modified interface. This was achieved via the addition of extruded DOPC LUVs which were introduced into the flow cell. Here the vesicles were left to disrupt over a 30-minute period in order to form a lipid bilayer above the actin filaments. Following SLB formation this cell was flushed with buffer to remove any loosely bound actin and undisrupted vesicles. The coverslip surface was once again imaged to locate the actin filaments. Figure 100 shows that following the various buffer flushes used in the bilayer formation step, much of the actin filaments had been

washed away from the surface narrowing the number of locations available for upcoming diffusion measurements. Nonetheless, enough F-actin remained below the lipid bilayer for some point measurements to be recorded. Figure 101 shows DOPE-Atto655 within a spanning DOPC bilayer. As can be seen, forming a spanning SLB above actin fibres did not result in any obvious defects to the lipid membrane where the SLB looked no different than the creation of a bilayer above plasma treated glass in the absence of actin.

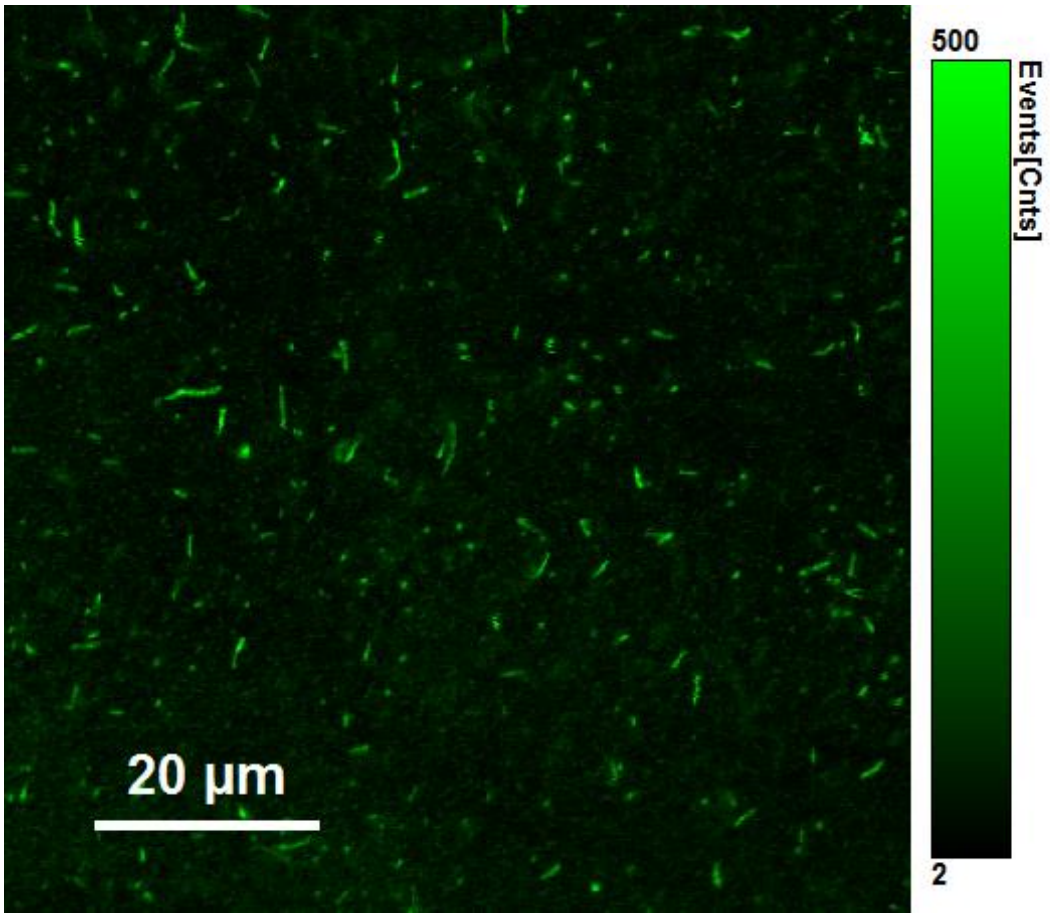

Figure 99: Phalloidin-TRITC stained bovine actin filaments assembled on a glass surface as seen via confocal microscopy. F-actin filaments readily formed under the polymerisation conditions used and surface coverage of the glass substrate was extremely good. The experiment was carried out at room temperature in a PDMS cell. Phalloidin TRITC labelled actin was excited by a 532 nm laser line and fluorescence was passed through a 550LP filter onto the SPAD detectors.

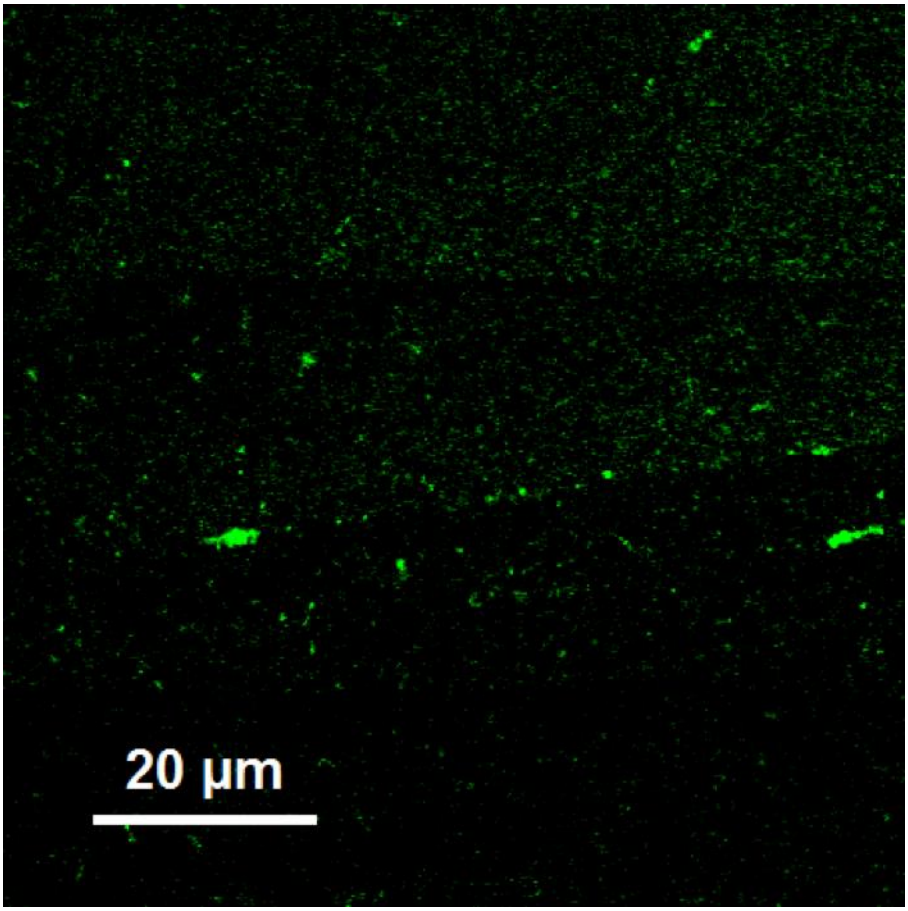

Figure 100: Bovine actin on plasma-treated glass following the addition and disruption of DOPC lipid vesicles. During the disruption process, which features a number of buffer flushes through the cell, the vast majority of actin was washed away from the glass. The experiment was carried out at room temperature in a PDMS cell. Phalloidin-TRITC labelled actin was excited by a 532 nm laser line and fluorescence was passed through a 550LP filter onto the SPAD detectors.

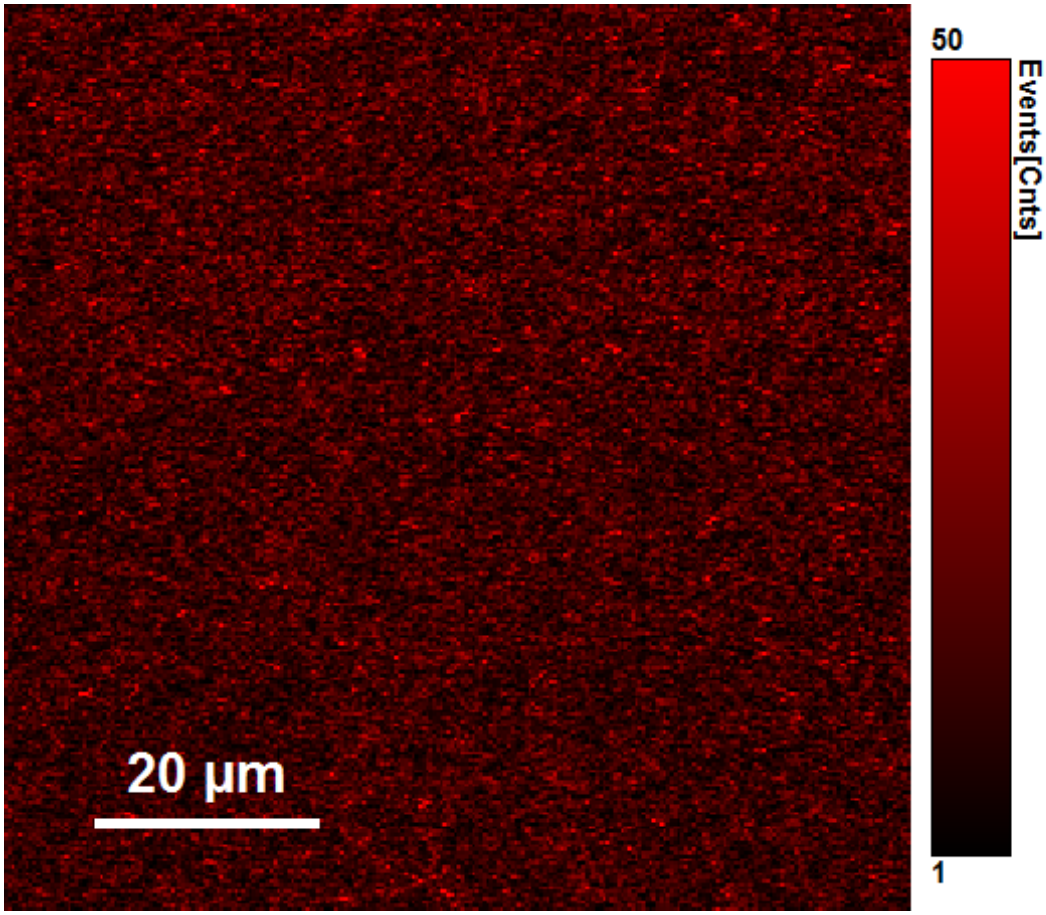

Figure 101: A DOPC bilayer formed above F-actin filaments. DOPE-Atto655 was used as the lipid probe. The bilayer appeared formed homogeneously with no defects visible due undisrupted vesicles and no perturbation caused by the presence of some underlying actin filaments. The experiment was carried out at room temperature in a PDMS cell. DOPE-Atto655 was excited by a 640 nm laser line and fluorescence was passed through a 635R filter onto the SPAD detectors.

Following imaging of both the F-actin and the lipid bilayer it was possible to begin point measurements for lipid (DOPE-Atto655) diffusion directly above actin filaments using the confocal image of phalloidin-TRITC as a reference. A typical ACF trace of lipid diffusion above an actin filament is given in Figure 102. In all cases the diffusional data was easily obtained in the ACF traces where the data fit well to single component two-dimensional diffusional model. Point measurements were carried out for lipid diffusion above all three actin types; bovine, rabbit, and platelet. A control sample was prepared in the absence of actin to provide a baseline diffusion co-efficient. In the actin free control the calculated lipid diffusion co-efficient (DOPE-Atto655) was found to be 3.82 ± 0.29 $\mu m^2/s$. Above bovine actin filaments this was found to be 3.92 ± 0.26 $\mu m^2/s$. Measurements above rabbit actin

provided a lipid diffusion co-efficient of 4.00 ± 0.31 $\mu m^2/s$, while above human platelet actin the lipid diffusion co-efficient was found to be 3.99 ± 0.20 $\mu m^2/s$. A one-way ANOVA and post-hoc Bonferroni test was performed on all the data-sets which found that these diffusion co-efficients did not significantly differ from one another, where $F(3, 76) = 1.71$, $p > 0.05$. The alpha value was shown to be 1 in all cases, indicating Brownian diffusion. Based on this data, it can therefore be stated that actin filaments failed to alter the diffusion co-efficient of a spanning DOPC bilayer, indicating that they were not a sufficient barrier to membrane fluidity. Between 5 and 10 measurements were performed above 10 different actin filaments to obtain this diffusion data. This was repeated across 3 different flow cells. This diffusional data is summarised in Figure 103.

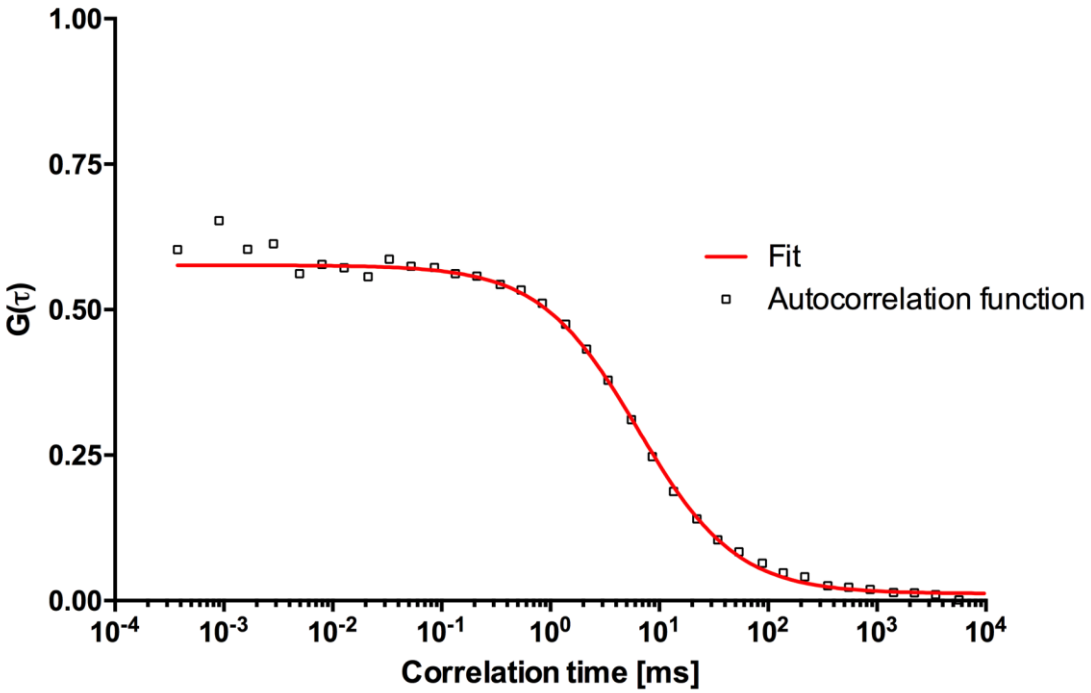

Figure 102: A typical ACF of DOPE-Atto655 diffusion in a DOPC bilayer located above a filamentous bovine actin. The fits to a single component model were good, and no other diffusing species were evident within the trace. Analogous behaviour was observed for lipid above the other actin fibres in rabbit actin and human platelet actin, where ACF data could be routinely obtained. The experiment was carried out at room temperature in a PDMS cell. DOPE-Atto655 was excited by a 640 nm laser line and fluorescence was passed through a 635R filter onto the SPAD detectors. Point measurements were performed for between 1 and 3 minutes.

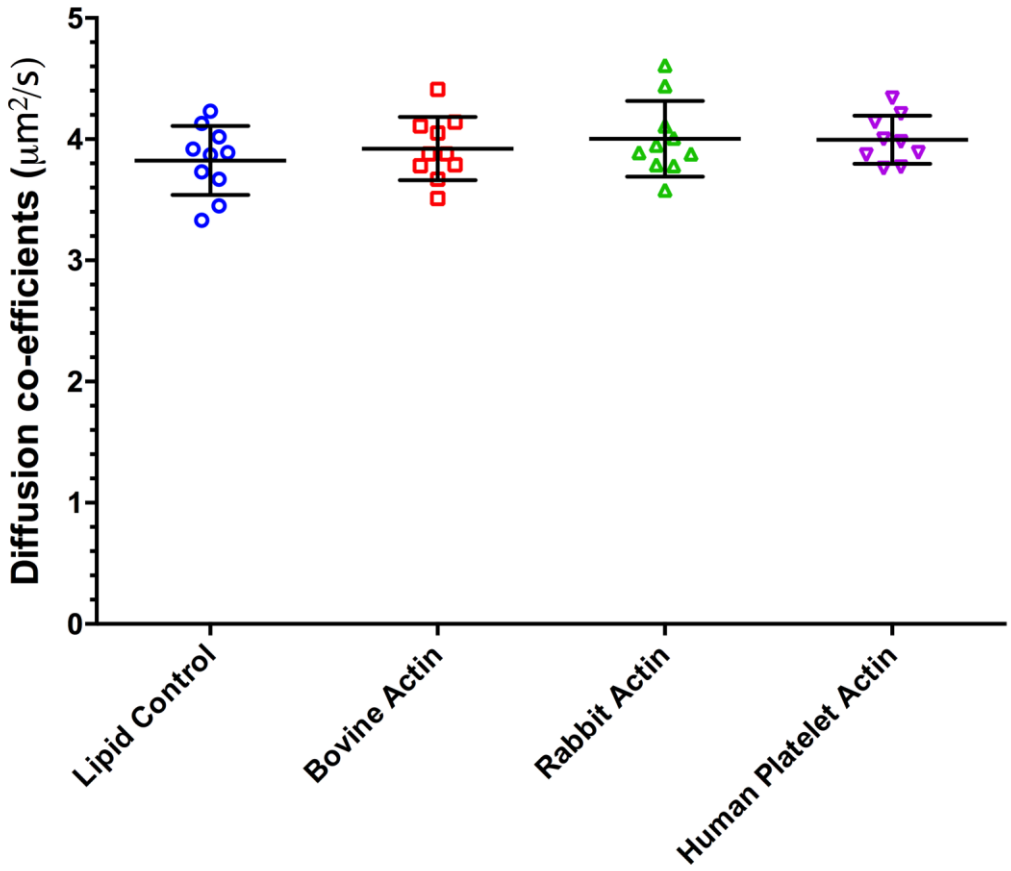

Figure 103: A summary of DOPE-Atto655 diffusion co-efficients in a DOPC bilayer above various actin filaments and a lipid only control fitted using a two-dimensional single species model. Diffusion of lipid above bovine, rabbit, or human platelet actin failed to alter the diffusion co-efficient when compared to lipid diffusion above plasma-cleaned glass. This was confirmed via a one-way ANOVA analysis. Each point refers to the average lipid diffusion co-efficient over an individual actin fibre, or in the case of the control, above planar glass. The experiment was repeated in triplicate using three separate PDMS flow cells. Standard deviation was used to represent the error.

STED imaging of F-actin

In order to identify actin fibres for point measurement experiments, standard confocal microscopy was described above. However, confocal microscopy is limited by the diffraction limit of light which means that structures separated by less than about 250 nm nm are not resolvable. Due to the fact that actin fibres have a diameter between 7 and 10 nm these filaments fall well below the diffraction limit. Indeed, if there are several filaments group together, for example, these cannot be distinguished from single fibres.[189] Therefore, to ensure the positioning of the point

measurements to obtain diffusion data directly above individual filaments we use STED microscopy, which allows for the collection of super-resolution images with a resolution of approximately 20 to 50 nm. Phallodin-TRITC stained actin fibres were firstly imaged by standard confocal imaging before STED images were obtained using the 660 nm depletion laser. A typical confocal image and corresponding STED image is shown in Figure 104. STED imaging (right) shows a significant increase in optical resolution when compared to confocal microscopy (left) under experimental conditions. Using this super-resolution image allowed us to better position the location of diffusion measurements to more accurately target actin filaments. These point measurements were carried out as before; however, again, no change in diffusion data was obtained when compared to using confocal microscopy images as reference.

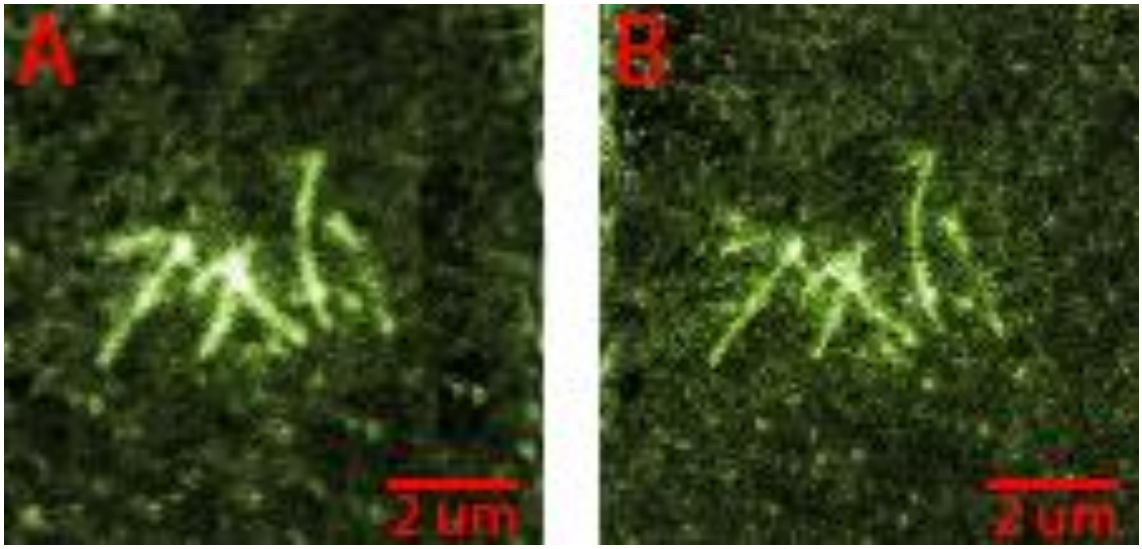

Figure 104: Confocal and STED imaging of phalloidin-TRITC labelled human-platelet actin. A) A standard confocal image which was routinely used to position point measurements above actin filaments. B) A complementary STED image of the same actin filaments. STED imaging provided an improvement in resolution when compared with confocal imaging. Increased accuracy in positioning point measurements above actin filaments did not alter obtained diffusion data. Phalloidin-TRITC was excited by the white light laser at 542 nm. Fluorescence was detected between 560 and 700 nm. The experiment was carried out at room temperature in a PDMS flow cell.

F-actin polymerisation above PLL coated glass

It was rather surprising that DOPC diffusion was unaffected by assembly over actin filaments. For example, *Sterling et al.* reported a reduction in the diffusion co-efficient of a G-actin-spanning SLB.[206] However in their experimental setup, their substrate surface was described as "fully coated with actin monomers". We therefore speculated that our unchanged lipid diffusion co-efficients were a result of the low surface coverage of F-actin. For example, single actin filaments of between 7 and 10 in diameter make up a relatively small barrier to diffusion of the lipid bilayer within the focal volume's cross-sectional area.[49,189] As such it was hoped that increasing the surface coverage of actin on the glass surface after bilayer formation would mean that multiple actin filaments would be present within the focal volume during point measurements. Thus, the actin bundles would be more likely to act as a hindrance to lipid bilayer mobility.

The first and simplest method to increase actin surface coverage utilised the positively charged amino acid polymer poly-L-lysine. This polymer is widely used to promote cell adhesion to solid substrates and it was hoped that coating the the glass substrate with PLL prior to actin addition would promote immobilisation of the negatively charged cytoskeletal protein. The actins were polymerised as before and flushed across the PLL coated surface before being imaged by confocal microscopy. This is shown in Figure 105 where phalloidin-TRITC was used to stain bovine actin. It was immediately evident that the PLL-coating had dramatically improved the surface of coverage of actin before the lipid bilayer was formed (compared to Figure 99 on bare glass). Extruded DOPC LUVs were subsequently introduced to the cell and allowed to disrupt over a 30-minute period to yield an actin-spanning SLB. The surface was then flushed with buffer to remove excess lipid and the PLL-coated surface was once again imaged for actin via confocal microscopy. Figure 106 shows phalloidin-TRITC labelled bovine actin following the formation of the SLB. It can clearly be seen that much of the F-actin filaments remained on the PLL-coated surface after the bilayer formation process. This is in contrast to the earlier observations on bare glass where the SLB formation step washed the vast majority of actin filaments from the substrate (Figure 100). After establishing the presence of

actin on the surface, attention was turned to the spanning lipid bilayer itself, which after assembly was also imaged via confocal microscopy as can be seen in Figure 107. Although the DOPE-Atto655 containing DOPC bilayer was definitely present and the surface coverage was good, careful examination of the bilayer shows that bilayer was not continuous. These defects are visible as fluorescently labelled lipid-free regions within the bilayer. This is in contrast to the construction of actin-spanning bilayer on bare glass as in Figure 101 where the bilayer appears homogeneous throughout.

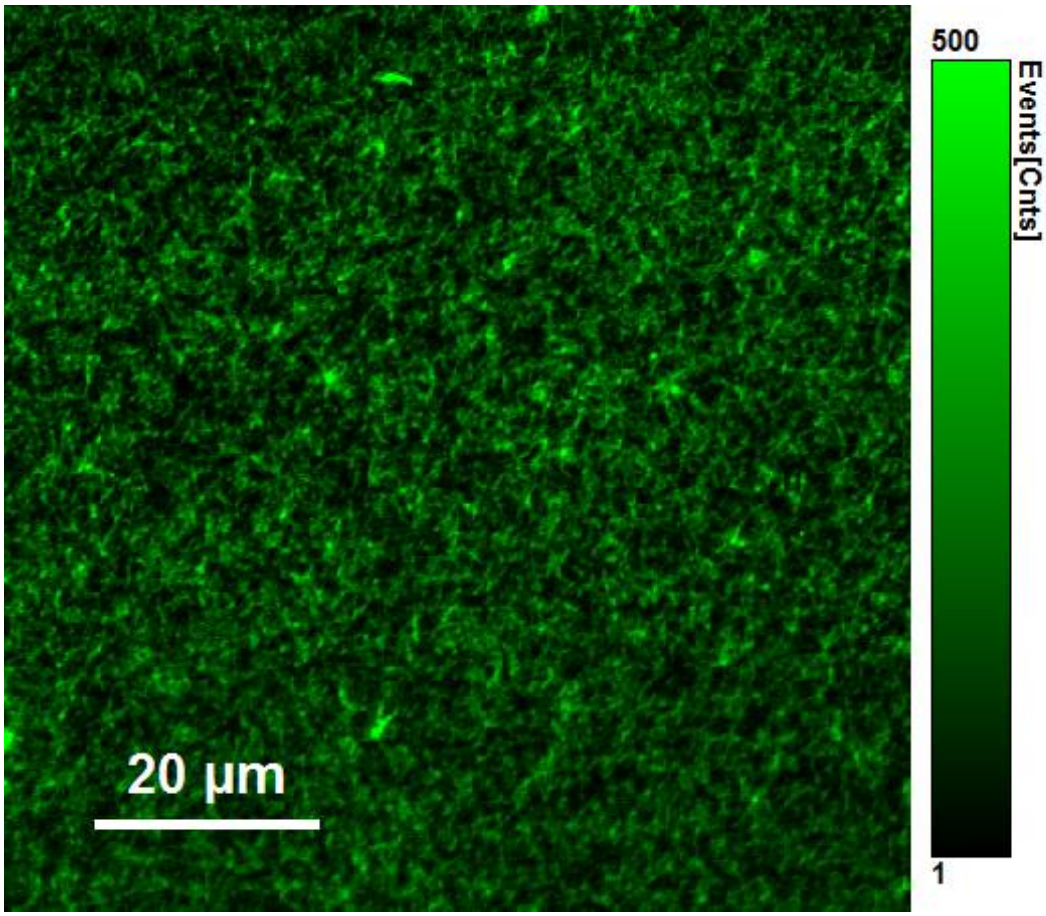

Figure 105: Phalloidin-TRITC stained bovine actin filaments on a PLL-coated glass coverslips before bilayer formation. The use of PLL coating massively increased the number of actin filaments present on the glass substrate when compared to bare glass. The experiment was carried out at room temperature in a PDMS cell. Phalloidin-TRITC-labelled actin was excited by a 532 nm laser line and fluorescence was passed through a 550LP filter onto the SPAD detectors.

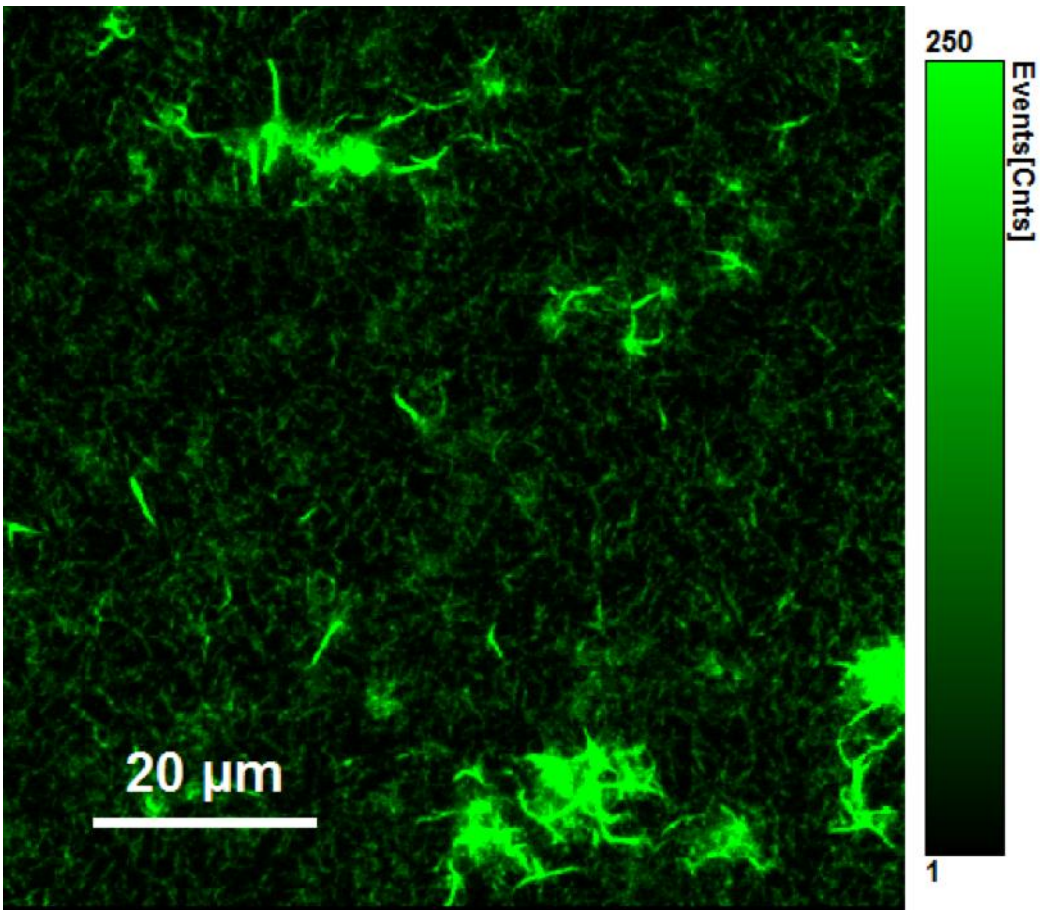

Figure 106: Phalloidin-TRITC-stained bovine actin filaments on a PLL-coated glass coverslips following the formation of a spanning DOPC SLB. Unlike non-PLL-coated glass the vast majority of the F-actin remained on the substrate following bilayer formation. The SLB was created via vesicle disruption. The experiment was carried out at room temperature in a PDMS cell. Phalloidin-TRITC-labelled actin was excited by a 532 nm laser line and fluorescence was passed through a 550LP filter onto the SPAD detectors.

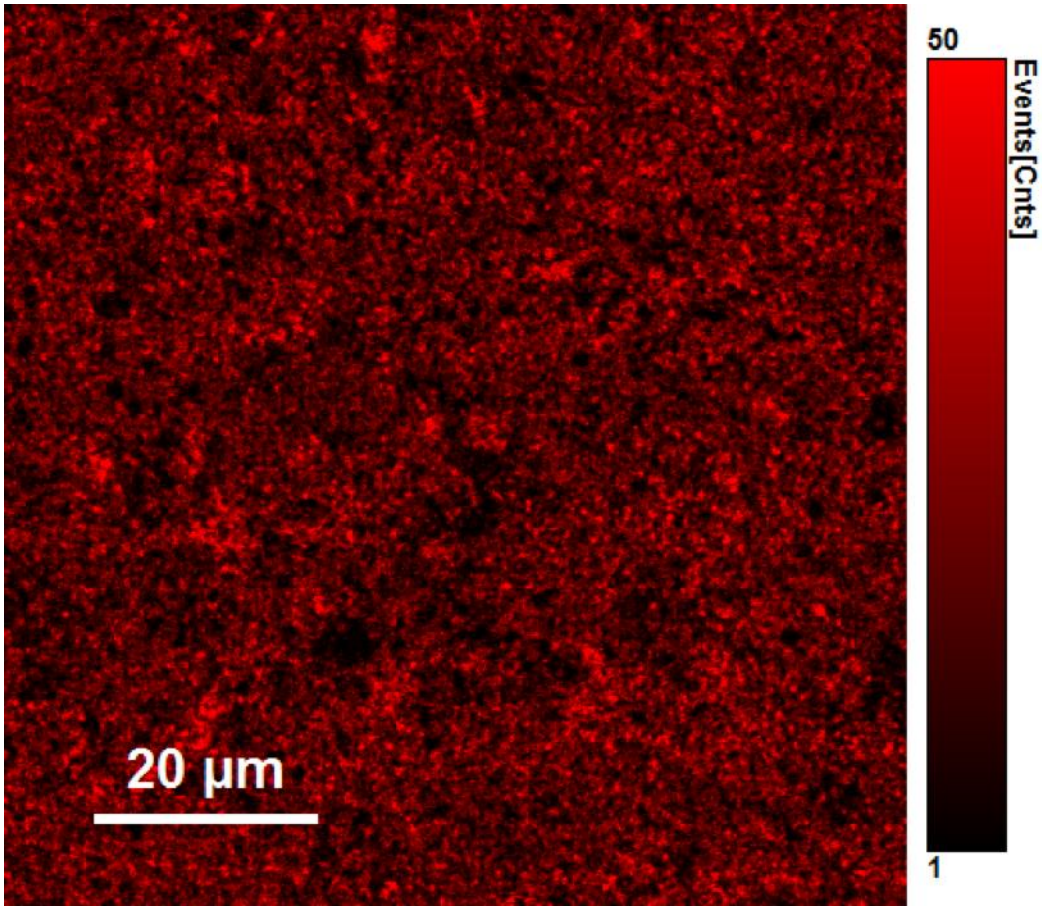

Figure 107: DOPE-Atto655 in a DOPC bilayer that spanned PLL-immobilised F-actin filaments. The lipid coverage was high but relatively heterogeneous, as some lipid-free defects can be seen on the surface. It was hoped that these defects would not negatively influence the fluidity of the lipid bilayer. The experiment was carried out at room temperature in a PDMS cell. DOPE-Atto655 was excited by a 640 nm laser line and fluorescence was passed through a 635R filter onto the SPAD detectors.

Despite the presence of these defects within the SLB, the high surface coverage of actin filaments provided an opportunity to attempt to study lipid diffusion above these fibres. To do so, further confocal images were taken at higher magnifications, in order to accurately position the point measurements directly above actin filaments. Once individual filaments or filamentous bundles were identified in the XY direction, and Z-scans performed to position the Z-direction, point measurements of the spanning lipid bilayer could be performed with accuracy. Figure 108 shows the location and MCS trace of a point measurement for the lipid bilayer above a single actin filament. Figure 109 shows the location and MCS trace of a point measurement for the lipid bilayer above a bundle of actin filaments. Interestingly in both cases it

was found that the lipid bilayer was immobile. This can be seen in the MCS traces where photobleaching is immediately evident. Thus no ACF trace of lipid diffusion could be calculated.

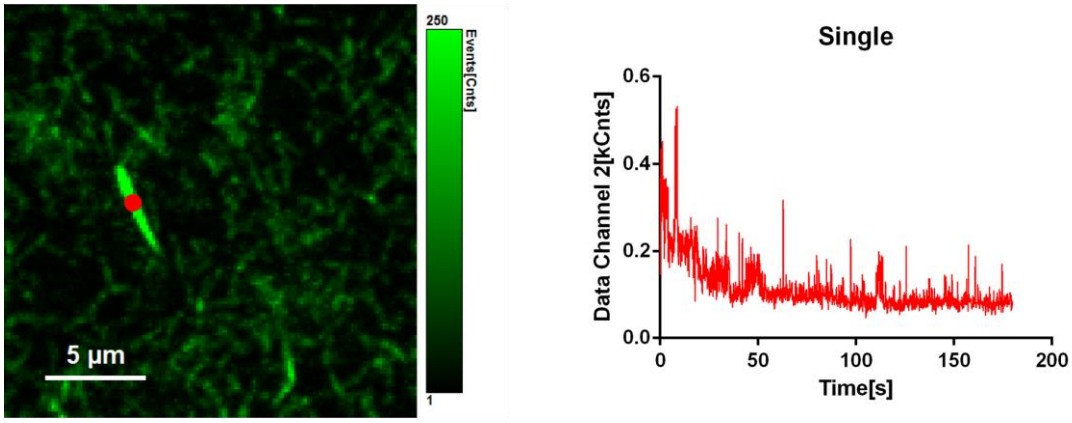

Figure 108: MCS trace of lipid above an actin filament. The image on the left shows separate actin filaments immobilised on PLL-coated glass. The red dot shows the exact location of the point measurement. This point measurement was used to determine the diffusion co-efficient of the lipid bilayer above the actin filament. The MCS trace on the right shows the photobleaching of DOPE-Atto655 at this location showing that no lipid diffusion was apparent above this single actin filament. The experiment was carried out at room temperature in a PDMS cell. DOPE-Atto655 was excited by a 640 nm laser line and fluorescence was passed through a 635R filter onto the SPAD detectors.

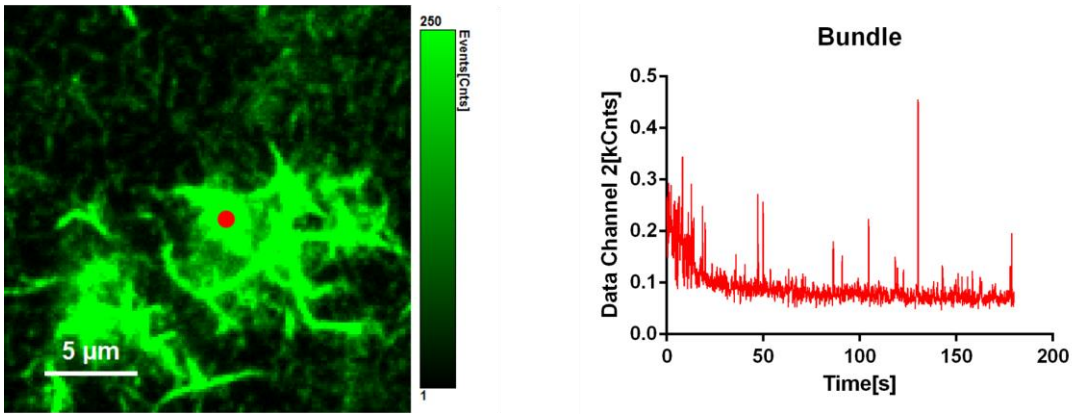

Figure 109: MCS trace of lipid above an actin bundle. The image on the left shows a bundle of F-actin filaments immobilised on PLL-coated glass. The red dot shows the exact location of the point measurement. Again this point measurement was used to determine the diffusion co-efficient of the lipid bilayer above the actin filament. As was the case above a single actin filament, the MCS trace on the right shows that photobleaching of DOPE-Atto655 was occurring. Therefore, once again the lipid bilayer appeared to be immobile. The experiment was carried out at room temperature in a PDMS cell. DOPE-Atto655 was excited by a 640 nm laser line and fluorescence was passed through a 635R filter onto the SPAD detectors.

Thus, the defects visible in the confocal image of the actin-spanning bilayer on PLL glass were reflected in the point measurements, where no lipid mobility was present. It was initially unclear whether this lipid immobility was due to the actin filaments themselves or the PLL treatment of the glass substrate. In order to determine this, a control was prepared where a lipid bilayer was formed above PLL-coated glass in the absence of actin filaments. A confocal image of this PLL-spanning bilayer is shown in Figure 110 where DOPE-Atto655 was included as lipid probe. As was the case of the PLL and F-actin sample, some defects are seen in the lipid bilayer where lipid free regions and lipid aggregates are visible within the SLB. This suggests that the lack of lipid fluidity in the previous sample as a result of the PLL coating rather than the high actin surface coverage. To confirm this, FLCS measurements were taken for the lipid bilayer at various locations in the bilayer. An MCS trace of one such point measurement is given in Figure 111. Again, photobleaching was observed showing that the lipid was immobile even in the absence of actin. Thus, it appeared that the PLL-coating was responsible for immobilising the lipid molecules on the surface. The PLL is expected to be polycationic at the pH used here and it is likely that they have a strong interaction with the anionic phosphates of the zwitterionic lipids used here. PLL has been used to coat vesicles, and thereby stabilise them, though there are few reports on the mobility of the lipid in such work. It has been been shown however that addition of PLL to SLBs comprised of DPPC, and particularly those of DOPS/DOPC leads to lipid removal and aggregation.[213,214] Therefore, despite the excellent immobilisation of actin with high surface coverage on PLL, the immobility of the lipid bilayer meant that the polymer coating was unsuited for our spanning lipid bilayer experiments.

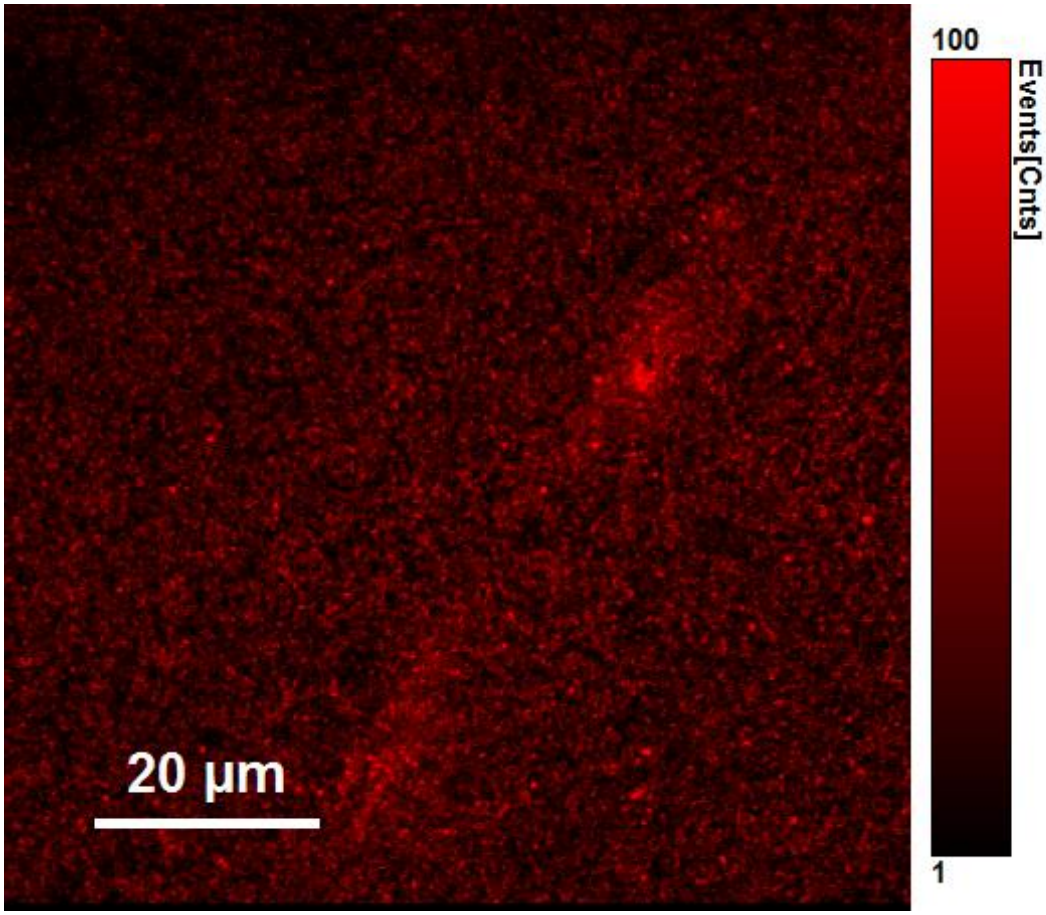

Figure 110: A DOPC bilayer formed above PLL coated glass. DOPE-Atto655 was used as the lipid probe. No actin was present these experiments. Despite this, the homogeneity of the bilayer is less than typically observed on glass alone and a number of defects were apparent in the bilayer. The experiment was carried out at room temperature in a PDMS cell. DOPE-Atto655 was excited by a 640 nm laser line and fluorescence was passed through a 635R filter onto the SPAD detectors.

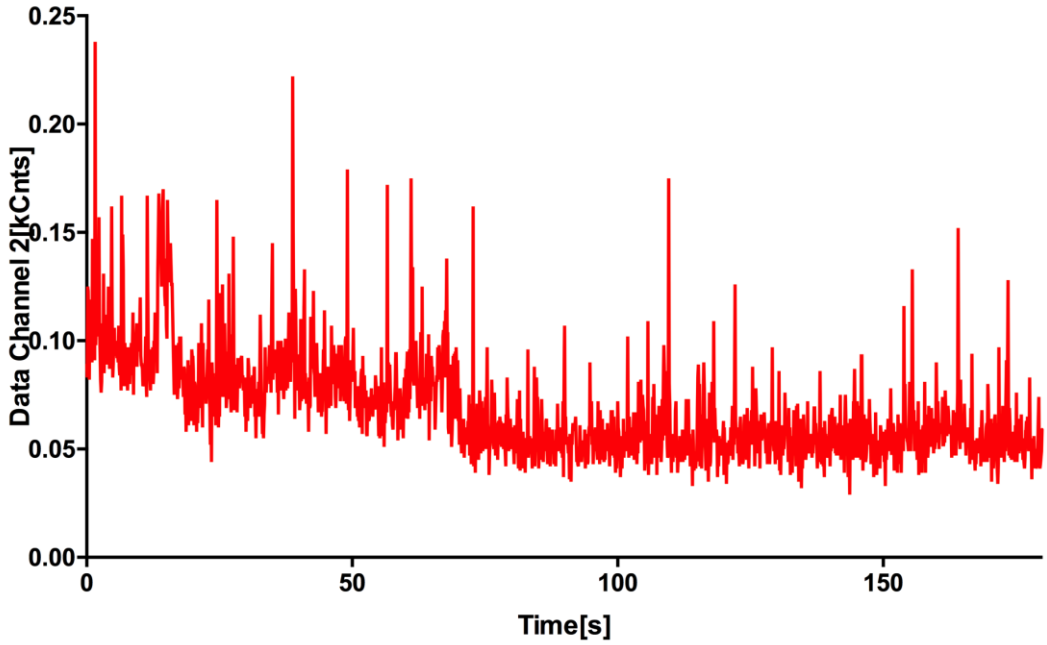

Figure 111: An MCS trace of DOPE-Atto655 in a DOPC bilayer on PLL-coated glass. As with the PLL immobilised actin on glass, photobleaching of lipid probe was evident. This data shows that PLL coating, while an excellent coating to increase actin surface coverage, was a poor choice of substrate for an SLB system. The experiment was carried out at room temperature in a PDMS cell. DOPE-Atto655 was excited by a 640 nm laser line and fluorescence was passed through a 635R filter onto the SPAD detectors.

F-actin polymerisation above APTMS/GA-coated glass

As an alternative to PLL coating, we modified the glass substrate with gluteraldehde (GA). This was achieved in a two-step coating of (3-aminopropyl)trimethoxysilane (APTMS) followed by GA. This protocol has previously been used to modify glass surfaces with APTMS in order to provide an amine terminated group on the substrate, and then the use of GA as a crosslinker between the amine on the surface and amines of the protein.[206,212] As previously described, F-actin was polymerised as normal and flushed across the APTMS/GA coated surface. The surface imaged for the phalloidin-TRITC stained F-actin via confocal microscopy as shown in Figure 112 where rabbit actin was used. As was the case in PLL-coated glass, APTMS/GA provided excellent surface coverage of actin filaments. A spanning SLB was formed by flushing extruded DOPC LUVs across the substrate and incubating them for 30 minutes to allow for a lipid bilayer to form from vesicle disruption. After the elapsed time the surface was once again imaged via confocal microscopy and a

representative image of the resulting surface is shown in Figure 113. This image clearly shows that the vast majority of rabbit actin filaments remained immobilised on the glass surface after SLB formation. This result is similar to observations with PLL-functionalised glass (Figure 106), but contrasts with bare glass, where few actin filaments remained adhered to the surface (Figure 100). A confocal image of the bilayer above F-actin on APTMS/GA glass is given in Figure 114 where DOPE-Atto655 was used as the lipid probe. It can clearly be seen that the bilayer is very heterogeneous with both lipid aggregates and contrasting lipid free areas visible on the coverslip. For comparison, a defect-free bilayer can be seen in Figure 101. Despite the heterogeneity of bilayer assembly, the high surface coverage of actin provided an attempt to obtain point measurements for DOPE-Atto655 above filaments was made. Figure 115 shows an MCS trace of one such point measurement. Unfortunately, again, it is evident that the lipid bilayer was not mobile as evident from the photobleaching of the lipid probe within the focal volume, indicating, as was the case for PLL-coated glass, that lipid adsorption was occurring at the interface and a fluid bilayer was not being established (Figure 108 and Figure 109). At this stage it was unclear whether the lack of bilayer fluidity was due to the high surface coverage of actin filaments themselves or instead due to the APTMS/GA coating.

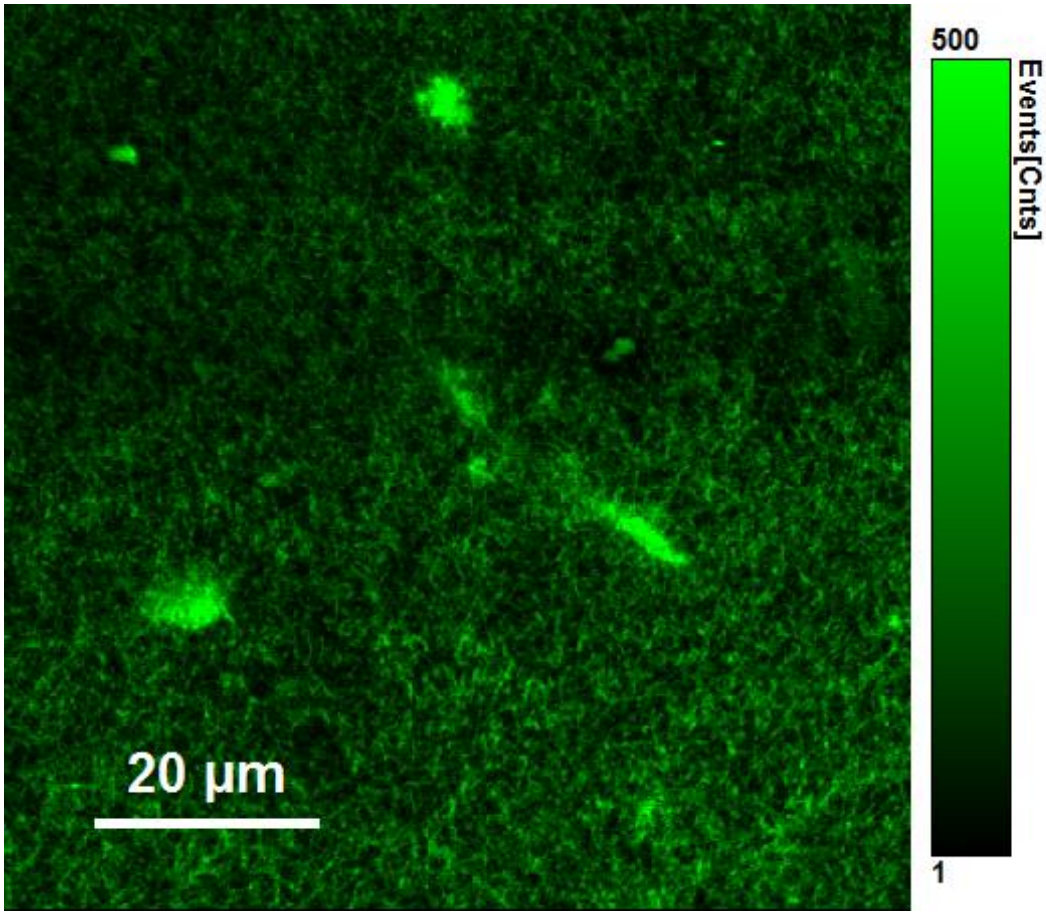

Figure 112: Rabbit actin filaments on APTMS/GA-coated glass before the addition of extruded lipid vesicles in order to form a spanning lipid bilayer. As was the case with PLL coating, APTMS/GA massively increased the concentration of actin filaments present on the glass substrate when compared to bare glass. The experiment was carried out at room temperature in a PDMS cell. Phalloidin TRITC-labelled actin was excited by a 532 nm laser line and fluorescence was passed through a 550LP filter onto the SPAD detectors.

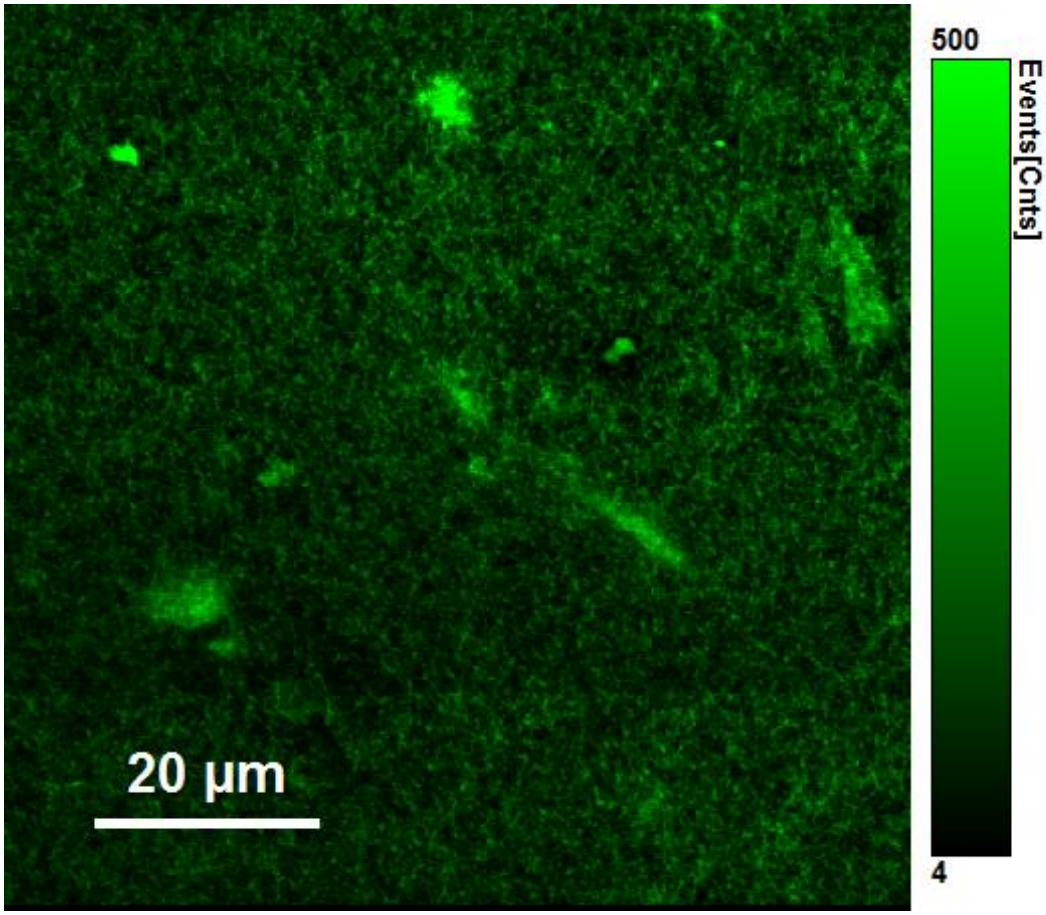

Figure 113: Rabbit actin filaments on APTMS/GA-coated glass directly after bilayer formation at the same location. Extruded DOPC vesicles were added to the cell and incubated above the actin covered glass substrate and allowed to rupture over a 30-minute period. The APTMS/GA coating meant that the majority of actin filaments remained adhered to the glass with little variation between the before and after bilayer formation images. The experiment was carried out at room temperature in a PDMS cell. Phalloidin TRITC-labelled actin was excited by a 532 nm laser line and fluorescence was passed through a 550LP filter onto the SPAD detectors.

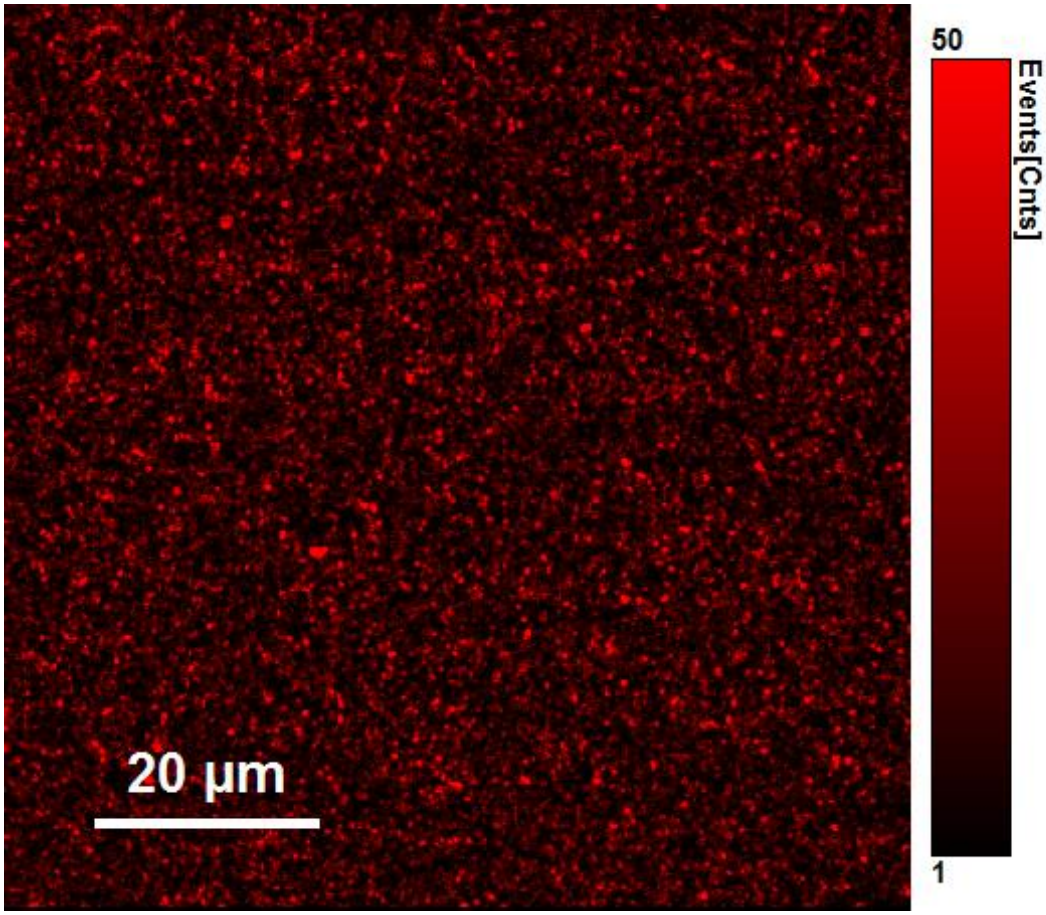

Figure 114: Confocal luminescence image of DOPE-Atto655 in a DOPC bilayer formed above actin, immobilised on a APTMS/GA-coated glass substrate. In contrast to the formation of a lipid bilayer above plasma-cleaned glass, the emission was considerably less homogeneous. This can be seen where the lipid probe appears to be excluded from certain regions and aggregated in others in a patchwork fashion. The experiment was carried out at room temperature in a PDMS cell. DOPE-Atto655 was excited by a 640 nm laser line and fluorescence was passed through a 635R filter onto the SPAD detectors.

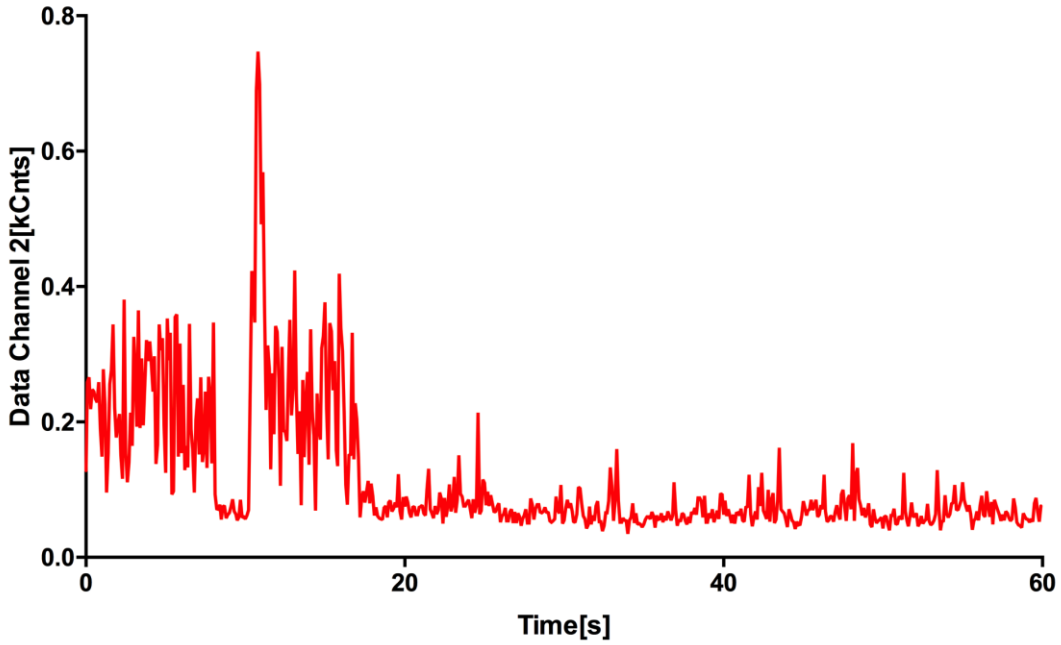

Figure 115: Photobleaching of DOPE-Atto655 in a DOPC bilayer above actin immobilised on glass via an APTMS/GA coating. This bleaching means that the lipid bilayer was not diffusive in this sample. At this stage it was unclear whether this was due to the actin filaments or the APTMS/GA treatment. The experiment was carried out at room temperature in a PDMS cell. DOPE-Atto655 was excited by a 640 nm laser line and fluorescence was passed through a 635R filter onto the SPAD detectors.

In order to determine whether the photobleaching was a result of the APTMS/GA coating (as was the case with PLL), or due to the actin filaments themselves, a control was setup whereby the glass substrate was coated with APTMS/GA and a bilayer assembled at this interface in the absence of actin above the functionalized surface. Figure 116 shows the confocal image of the resulting SLB where DOPE-Atto655 was included as a lipid probe. As for the PLL layer it is clear that the APTMS/GA coating prevented the formation of a continuous and defect free lipid bilayer. In fact, in this particular case the bilayer failed to form in large areas of the coverslip as can be seen in the lower right of image where the surface is devoid of DOPE-Atto655. Even where DOPE-Atto655 was present, such as the top left of the image, the bilayer appeared patchy and full of defects. Thus, it appeared that the APTMS/GA coating was responsible for the failure of a continuous and fluid lipid bilayer to form. To confirm this, point measurements were undertaken in areas that did feature some degree of labelled lipid. Figure 117 shows an MCS trace of one such measurement. Once again bleaching of the lipid probe was evident suggesting the lipid was adsorbing onto the substrate. This bilayer immobility is perhaps

surprising given the fact that an APTMS/GA coating has previously been used below a lipid bilayer with not mention of lipid immobility.[206] In that case *Sterling et al.* were able to produce a G-actin-coated (not F-actin) surface via APTMS/GA surface functionalization and subsequently create a spanning diffusive DMPC bilayer. However, in their case, they describe their glass surface as "fully coated with actin monomers" as described by immunochemical staining. This may suggest that their lipid bilayer is fully cushioned by G-actin monomers while our lipid bilayer is cushioned by a combination of narrow actin filaments and surrounding APTMS/GA coated glass.

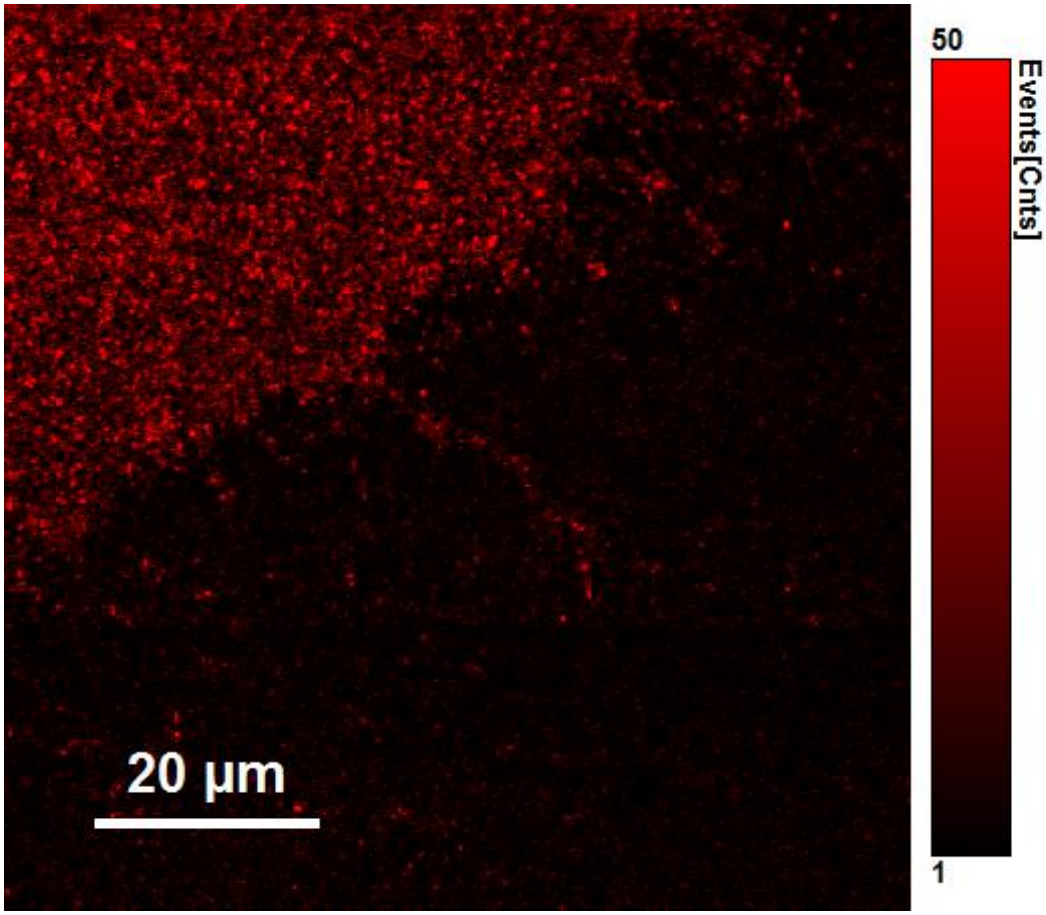

Figure 116: DOPE-Atto655 in a DOPC bilayer above APTMS/GA-coated glass. No actin filaments were present in this sample. The lipid bilayer was again not continuous. This can clearly be seen where much of the probe was excluded from the lower right of the image. Even where the probe was present in the upper left its coverage appears patchy when compared to plasma-cleaned glass. The experiment was carried out at room temperature in a PDMS cell. DOPE-Atto655 was excited by a 640 nm laser line and fluorescence was passed through a 635R filter onto the SPAD detectors.

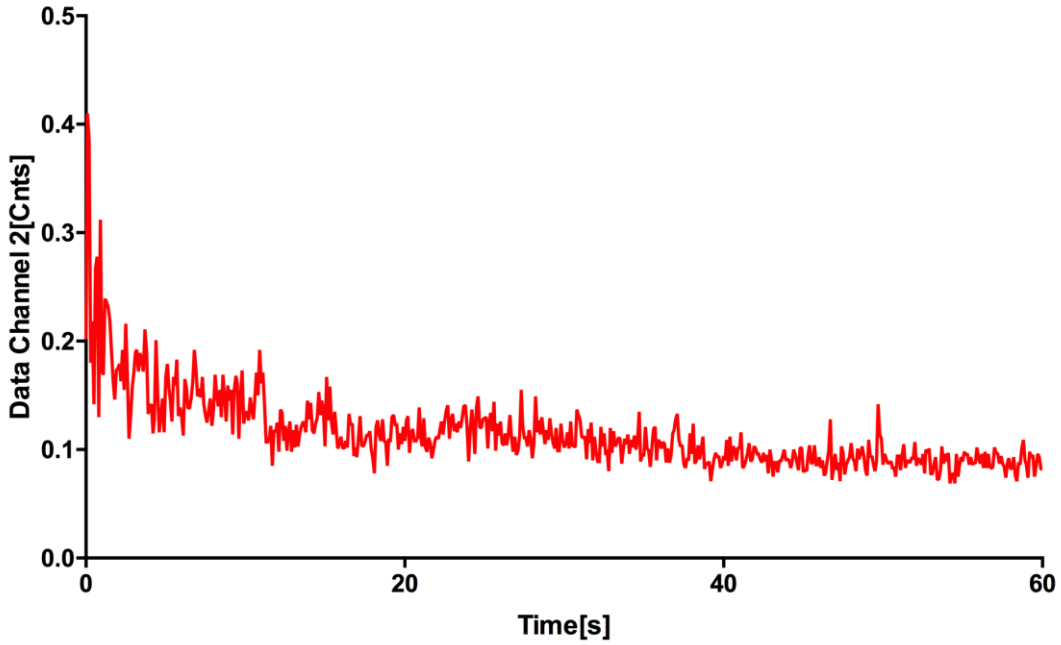

Figure 117: Photobleaching of DOPE-Atto655 in a DOPC bilayer above APTMS/GA coated glass. No actin was present in this sample, yet the lipid bilayer was not diffusive. This suggests that the APTMS/GA coating was responsible for the immobilisation of the lipid molecules. The experiment was carried out at room temperature in a PDMS cell. DOPE-Atto655 was excited by a 640 nm laser line and fluorescence was passed through a 635R filter onto the SPAD detectors.

Ryadnov group fibre polymerisation on bare glass

Under our experimental conditions, the isolated actin fibres (bovine, rabbit and human platelet) were not observed to hinder the diffusion of a lipid bilayer on bare glass. Furthermore, attempts to immobilize more densely packed actin on PLL or ATPMS/GA-coated glass rendered the lipid molecules immobile, indicating the lipid/dye was adsorbing onto the structures rather than forming a bilayer. Therefore, attention then turned to the peptide fibres supplied by the Ryadnov group. These fibres known as cyan(+)4, cyan(+)6 and SR_EDS_02 were formed in low salt buffers as described (section 5.2.4) and labelled with sulforhodmaine B, before being incubated with a plasma-cleaned glass coverslip. Each fibre possesses different dimensions and PI, and so we were interested to see if these parameters influenced lipid diffusion of lipid in contact with the fibres. A lipid bilayer was formed as normal be injecting extruded DOPC LUVs across the surface and

incubating them for 30 minutes. After washing out excess lipid the fibres and bilayer were imaged via confocal microscopy. Figure 118 shows a representative image of sulfo-rhodmaine B labelled cyan(+)4 after the formation of a spanning DOPC SLB. As was the case with actin filaments the various wash steps involved in bilayer formation meant that high surface coverage of filaments was difficult to achieve. Nonetheless, a sufficient number of fibres remained on the surface for FCS point measurements to be undertaken. Figure 119 shows a corresponding confocal image of the bilayer itself at the same location where DOPE-Atto655 was used as a lipid dye. Consistent with SLB formation, the lipid bilayer appeared homogeneously fluorescent across the substrate with no evidence for lipid aggregates or luminophore (lipid bilayer) free regions. Using both images, from lipid and fibre fluorescence, in combination, it was possible to perform point measurements on lipid diffusing above the fibres. Figure 120 shows a typical ACF and its single component two-dimensional fit for lipid diffusion above a cyan(+)4 filament. The model fit well to the ACF trace with no obvious second component present in the data.

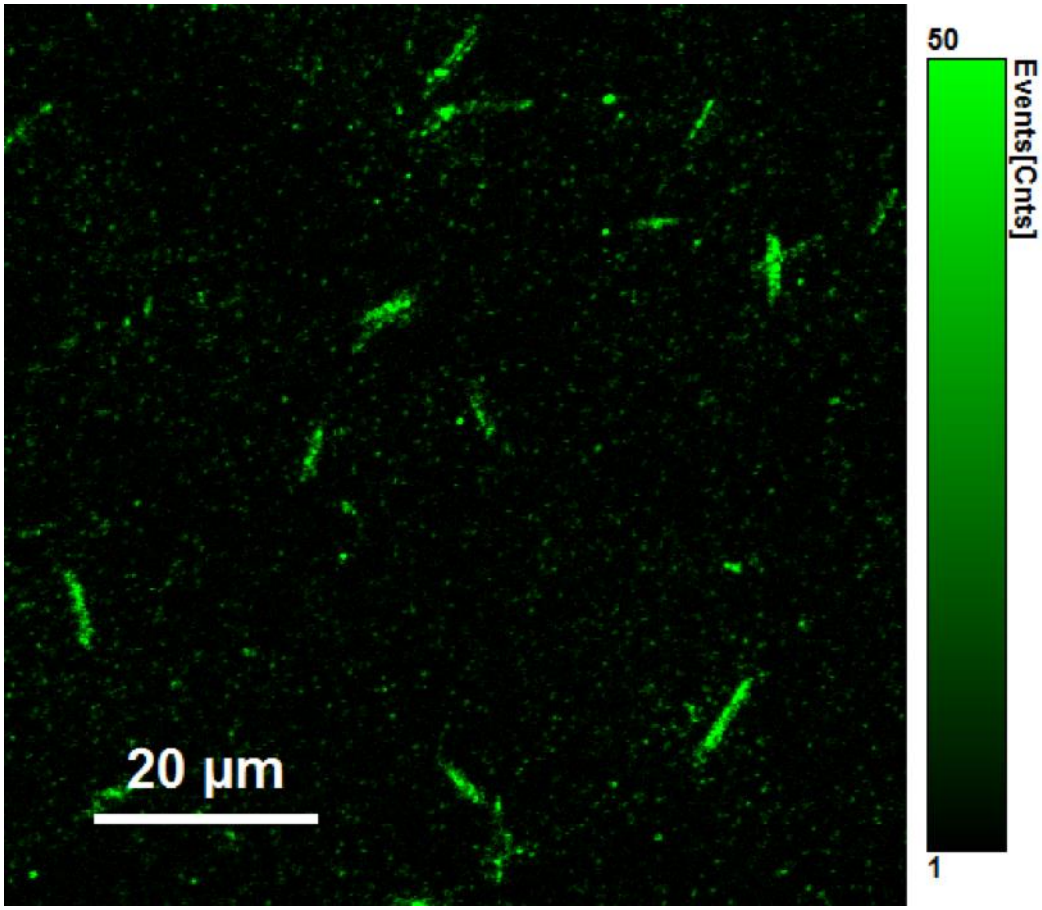

Figure 118: Sulfo-rhodamine B-labelled cyan(+)4 below a DOPC SLB. Some cyan(+)4 filaments remained adhered to the glass during the vesicle disruption process and thus were present below the lipid bilayer. This allowed the bilayer to be probed for changes in fluidity directly above individual fibres. The experiment was carried out at room temperature in a PDMS cell. Sulfo-rhodamine B-labelled cyan(+)4 was excited by a 532 nm laser line and fluorescence was passed through a 550LP filter onto the SPAD detectors.

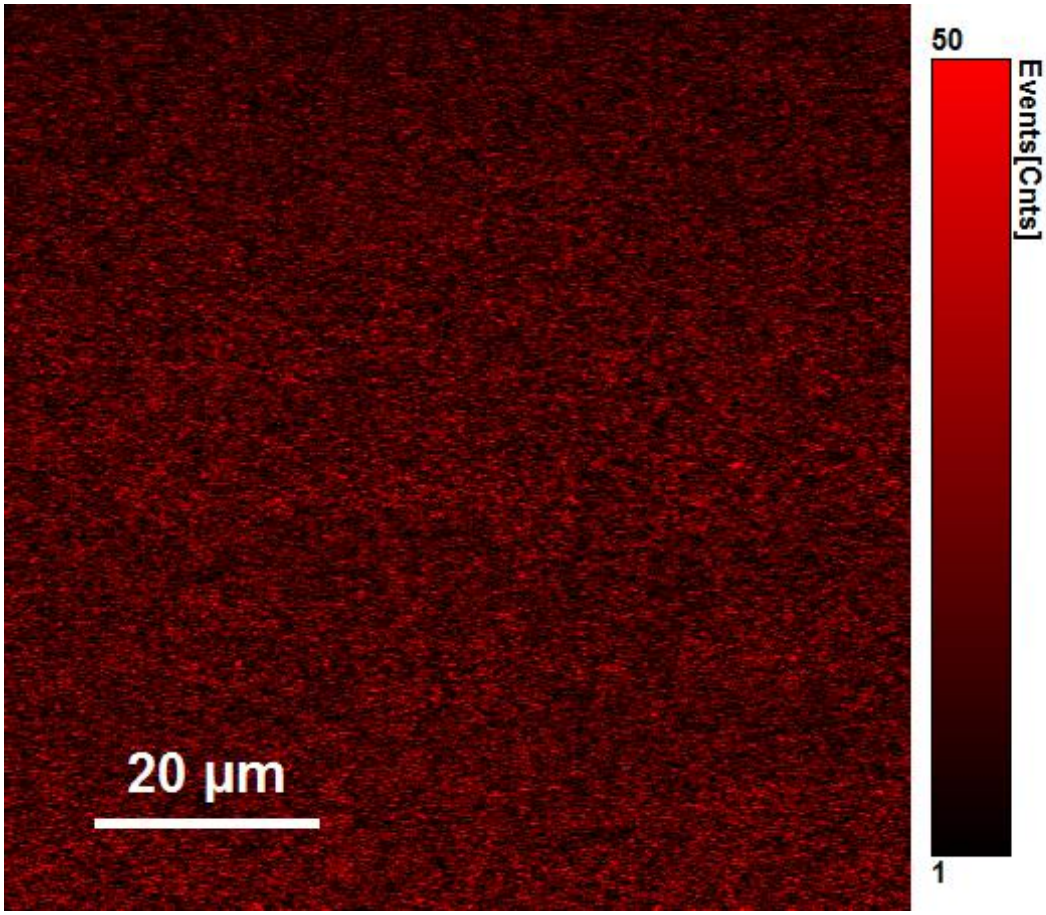

Figure 119: DOPE-Atto655 in a DOPC bilayer-spanning above cyan(+)4 fibres on plasma-cleaned glass. The bilayer was formed by flushing extruded LUVs across the surface and allowing the vesicles to rupture over a 30-minute period. The resultant bilayer appeared to form without any defects. Knowing the locations of the fibres it was then possible to perform point measurements of the lipid bilayer above the peptides. The experiment was carried out at room temperature in a PDMS cell. DOPE-Atto655 was excited by a 640 nm laser line and fluorescence was passed through a 635R filter onto the SPAD detectors.

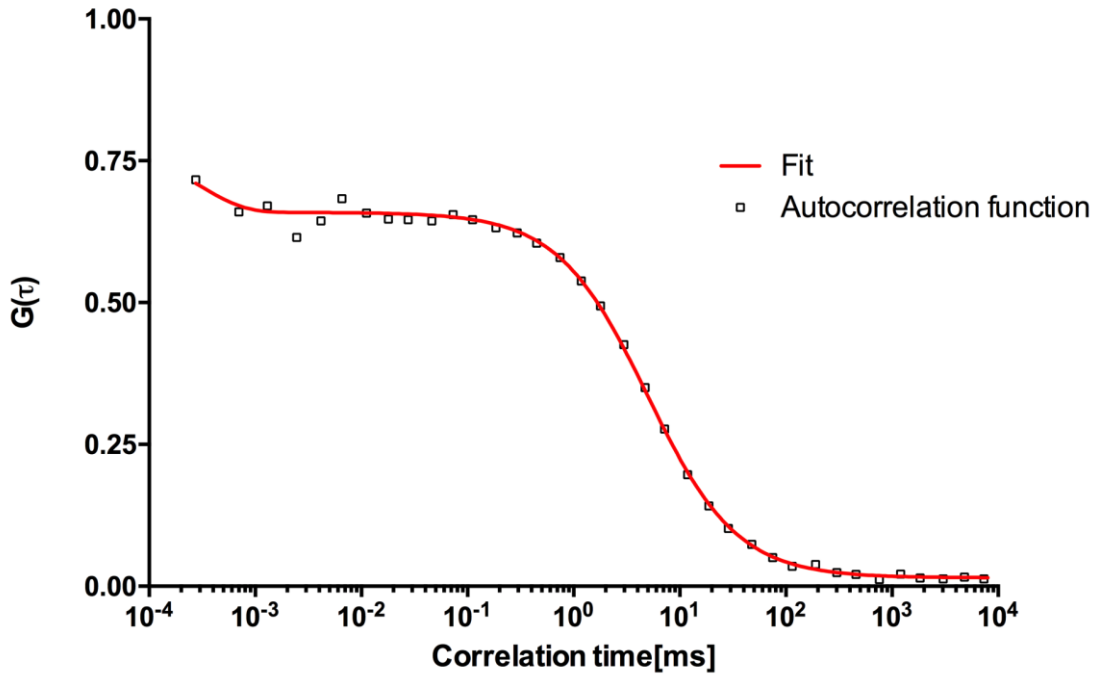

Figure 120: A typical ACF of DOPE-Atto655 diffusion in a DOPC bilayer above cyan(+)4. The fits to a single component model were good and no other species were obvious within the trace. The experiment was carried out at room temperature in a PDMS cell. DOPE-Atto655 was excited by a 640 nm laser line and fluorescence was passed through a 635R filter onto the SPAD detectors. Point measurements were carried out above filaments for between 1 and 3 minutes.

The same protocol was also carried out for the other fibres supplied by the Ryadnov group. For example, Figure 121 shows polymerised cyan(+)6 on plasma-cleaned glass following the formation of a spanning DOPC SLB, while Figure 122 shows polymerised SR_EDS_02 on plasma-cleaned glass following the formation of a spanning DOPC SLB. Once again surface coverage of fibres was low after the formation of a traversing lipid bilayer. While cyan(+)6 size and surface coverage was comparable to that of cyan(+)4, SR_EDS_02 was difficult to form and was only found below the lipid bilayer on a single occasion, and at extremely sparse levels. Nonetheless, the identification of individual fibres allowed us to subsequently perform point measurements at these locations. As was the case with cyan(+)4 experiments, the ACF trace fitted well to a its single-component two-dimensional fit with no obvious second component present in the data.

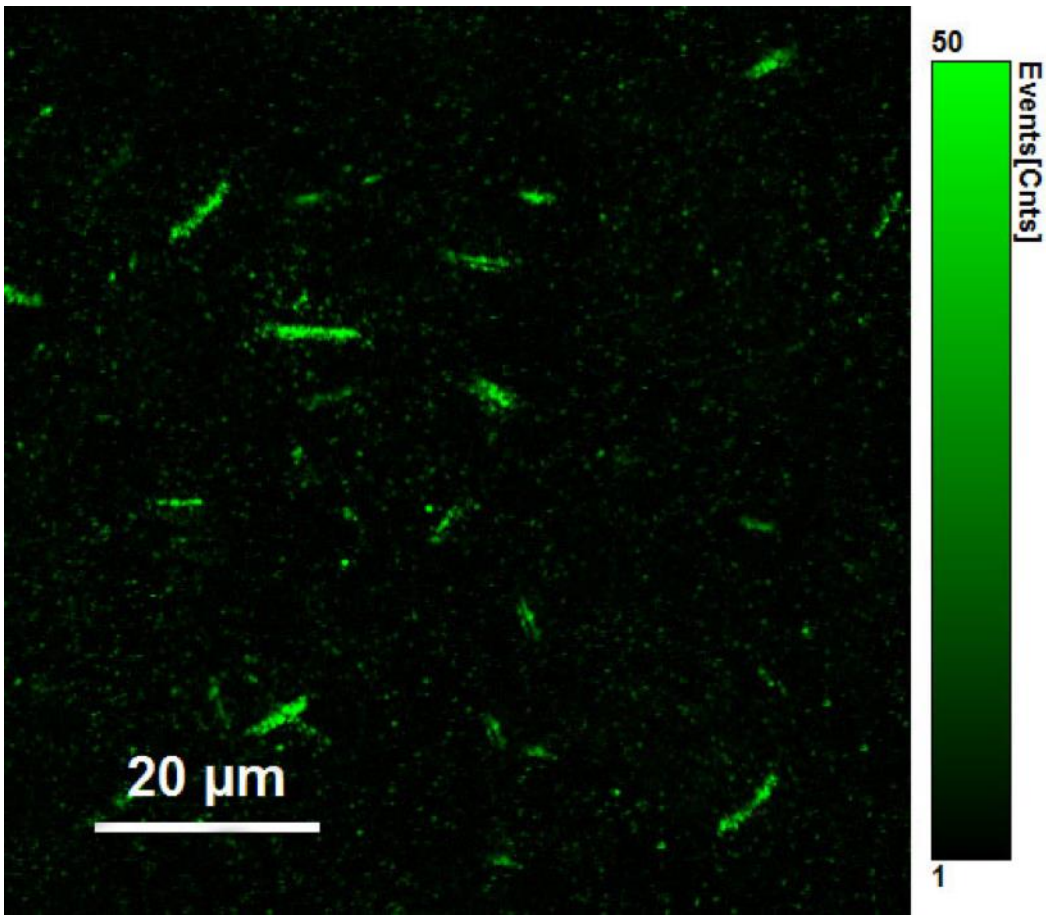

Figure 121: Sulfo-rhodamine B-labelled cyan(+)6 below a DOPC SLB. Some cyan(+)6 filaments remained adhered to the glass during the vesicle disruption process and thus were present below the lipid bilayer. This allowed the bilayer to be probed for changes in fluidity directly above individual fibres. The experiment was carried out at room temperature in a PDMS cell. Sulfo-rhodamine B labelled cyan(+)6 was excited by a 532 nm laser line and fluorescence was passed through a 550LP filter onto the SPAD detectors. Point measurements for the lipid diffusion co-efficients were then carried out above these filaments for between 1 and 3 minutes.

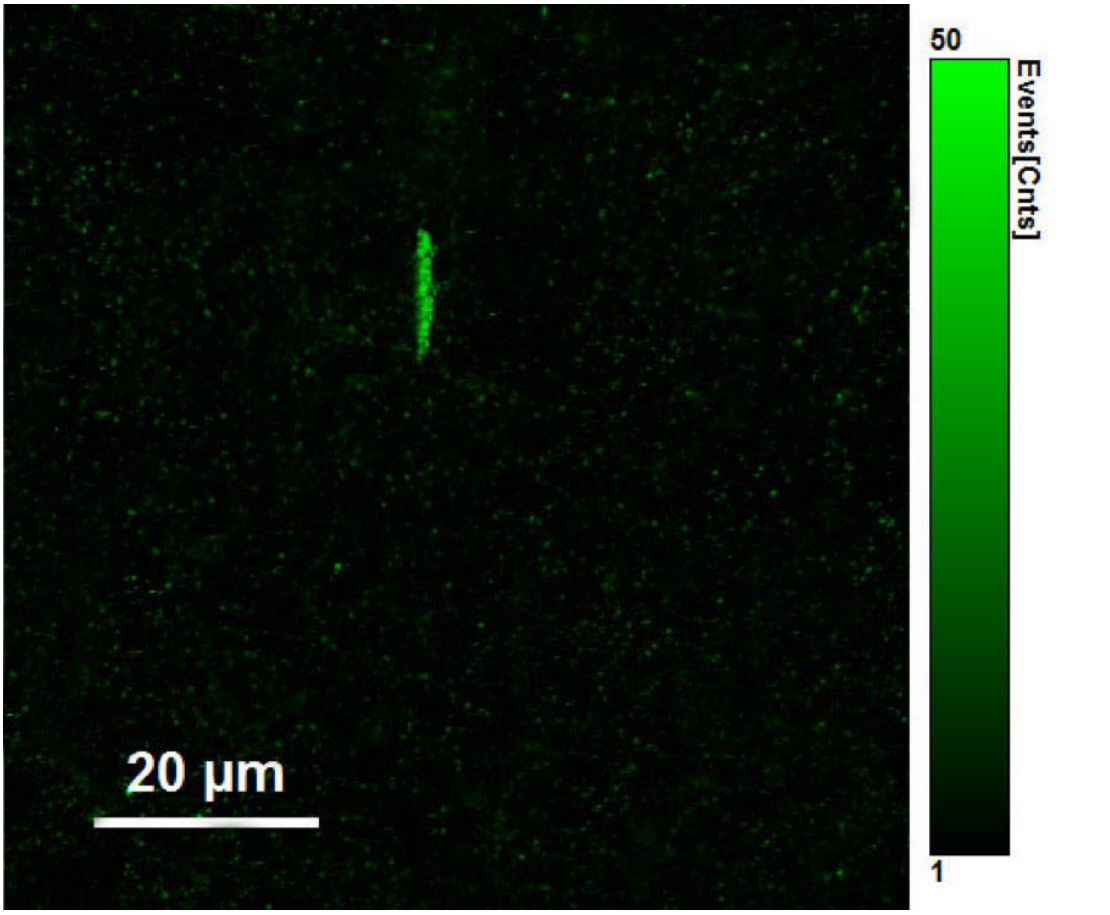

Figure 122: Sulfo-rhodamine B-labelled SR_EDS_02 below a DOPC SLB. SR_EDS_02 was extremely difficult to polymerise and was only once immobilised on a glass slide below a lipid bilayer. Despite this low surface coverage, this again allowed the bilayer to be probed for changes in fluidity directly above individual fibres. The experiment was carried out at room temperature in a PDMS cell. Sulfo-rhodamine B-labelled SR_EDS_02 was excited by a 532 nm laser line and fluorescence was passed through a 550LP filter onto the SPAD detectors. Point measurements for the lipid diffusion co-efficients were then carried out above these filaments for between 1 and 3 minutes.

It was calculated that DOPE-Atto655 in a DOPC bilayer above cyan(+)4 fibres diffused at 3.98 ± 0.28 $\mu m^2/s$. Above cyan(+)6, DOPE-Atto655 diffused at 3.84 ± 0.28 $\mu m^2/s$, while above SR_EDS_02 the diffusion co-efficient was found to be 3.81 ± 0.17 $\mu m^2/s$. Alongside these fibre-containing samples, a fibre free control was prepared that featured a DOPC bilayer with DOPE-Atto655 above plasma-cleaned glass. In this case the diffusion co-efficient was determined to be 3.81 ± 0.29 $\mu m^2/s$. This data is summarised in Figure 123. In all cases the alpha value was 1 showing that the diffusion was Brownian. A one-way ANOVA and post-hoc Bonferroni test was

performed on the diffusion values under each condition and found that there was no significant difference between each data set, where $F(3, 73) = 2.40$, $p > 0.05$. Therefore, this data shows that none of the Ryadnov group's fibres, within experimental error affected diffusion of a spanning DOPC bilayer and this is line with our earlier actin-spanning results.

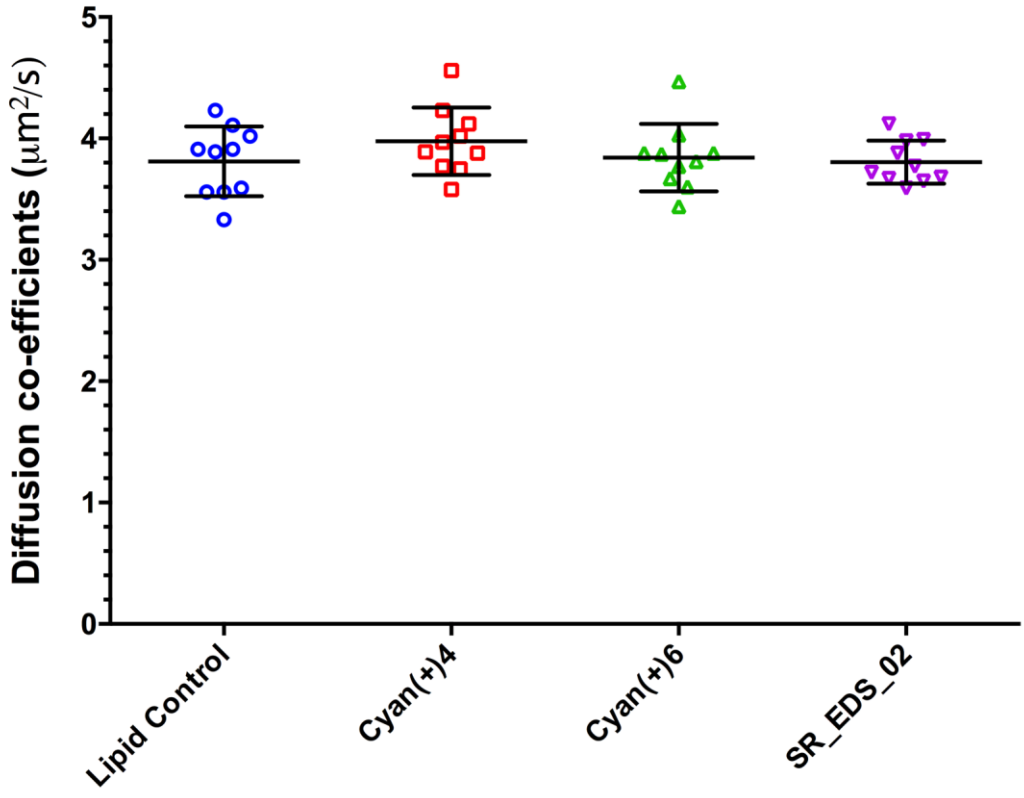

Figure 123: A summary of DOPE-Atto655 diffusion co-efficients in a DOPC bilayer above cyan(+)4, cyan(+)6 and SR_EDS_02, as well a lipid only control. Data was fitted using a two-dimensional single species model. None of the fibres lead to a change in the diffusivity of the spanning lipid bilayer when compared to a fibre free control. This was confirmed by one-way ANOVA anlysis. Each point represents the average diffusion co-efficient of 5 to 10 measurements above an individual filament. The experiment was performed in triplicate using three separate flow cells, except for SR_EDS_02 where data was obtained from a single experiment. Standard deviation was used to represent the error.

5.3.2. Fibres above the SLB

Polymerized actin has been shown to bind to phospholipid monolayers and bilayers in liposomes at physiological pH. Binding occurs to a range of lipids irrespective of the charge at the lipid, which suggests the interactions are multi-sited and non-specific.[215] However, to date there have been no studies reported on the diffusion of actin filaments at fluid lipid bilayers so this was investigated here by reversing the previous setup and adding polymerised fibres above a pre-constructed lipid bilayer as shown in Figure 124. For comparison, we used the same actin filament structures in; bovine actin, rabbit actin, human platelet actin, as well as the synthetic fibrous peptides; cyan(+)4, cyan(+)6, and SR_EDS_02.

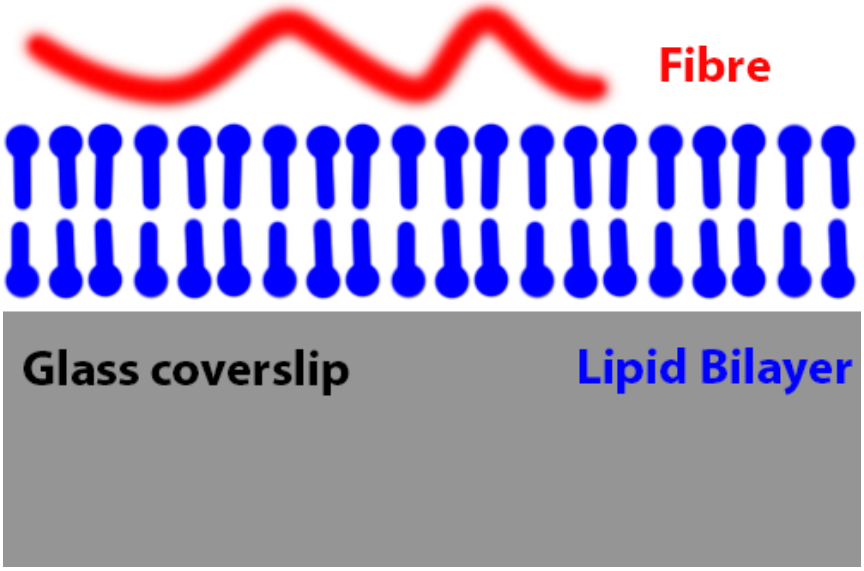

Figure 124: In a reversal of the earlier experimental set-up, the various fibre-forming polypeptides were added above an already formed DOPC lipid bilayer. This was due to the fact that creating a lipid bilayer above immobilised fibres had failed to alter the diffusional characteristics of the SLB.

Actin polymerisation above the lipid bilayer

To investigate the binding of actins to a pre-assembled lipid bilayer polymerised actins; bovine, rabbit and human platelet were each separately studied by

incubating them with a DOPC SLB. The bilayer was formed, by flushing extruded DOPC LUVs above a plasma-cleaned glass coverslip, followed by 30-minute incubation, and then removing excess lipid via a buffer flush. The already polymerised F-actin was then flushed across the lipid membrane with the intention of performing point measurements for the lipid membrane at locations below these actin filaments. However, by collecting confocal images over time it was clear that the actin filaments themselves were highly mobile above the lipid. This mobility of actin can be seen in Figure 125 where pholloidin-TRITC-stained bovine actin which is shown at 5 minute intervals. Confocal images of pholloidin-TRITC-stained rabbit actin and human platelet actin are shown in Figure 126 and Figure 127, respectively. All of the actin filaments, regardless of origin were not only found to bind to the bilayer but also to be highly mobile at this bilayer.

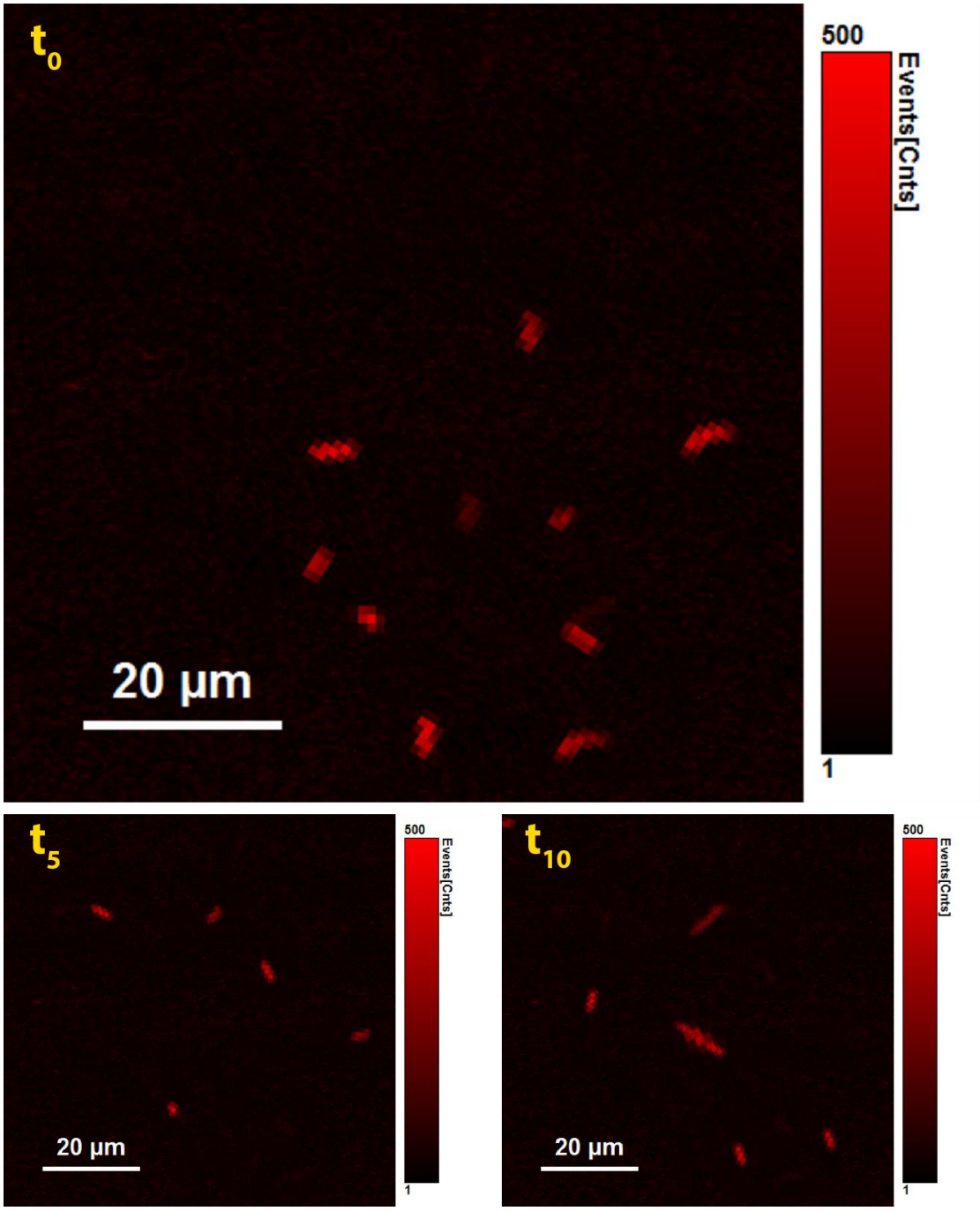

Figure 125: Phalloidin-TRITC-labelled bovine actin above a DOPC bilayer on plasma-cleaned glass. Top shows the initial confocal image of the area. Bottom left shows the same area 5 minutes later, while bottom right shows the same area 10 minutes later. It can clearly be seen that the labelled actin is mobile atop the SLB. The experiment was carried out at room temperature in a PDMS cell. Phallodin-TRITC was excited by a 532 nm laser line and fluorescence was passed through a 550LP filter onto the SPAD detectors. Point measurements were performed for between 12 and 20 minutes to build ACF data.

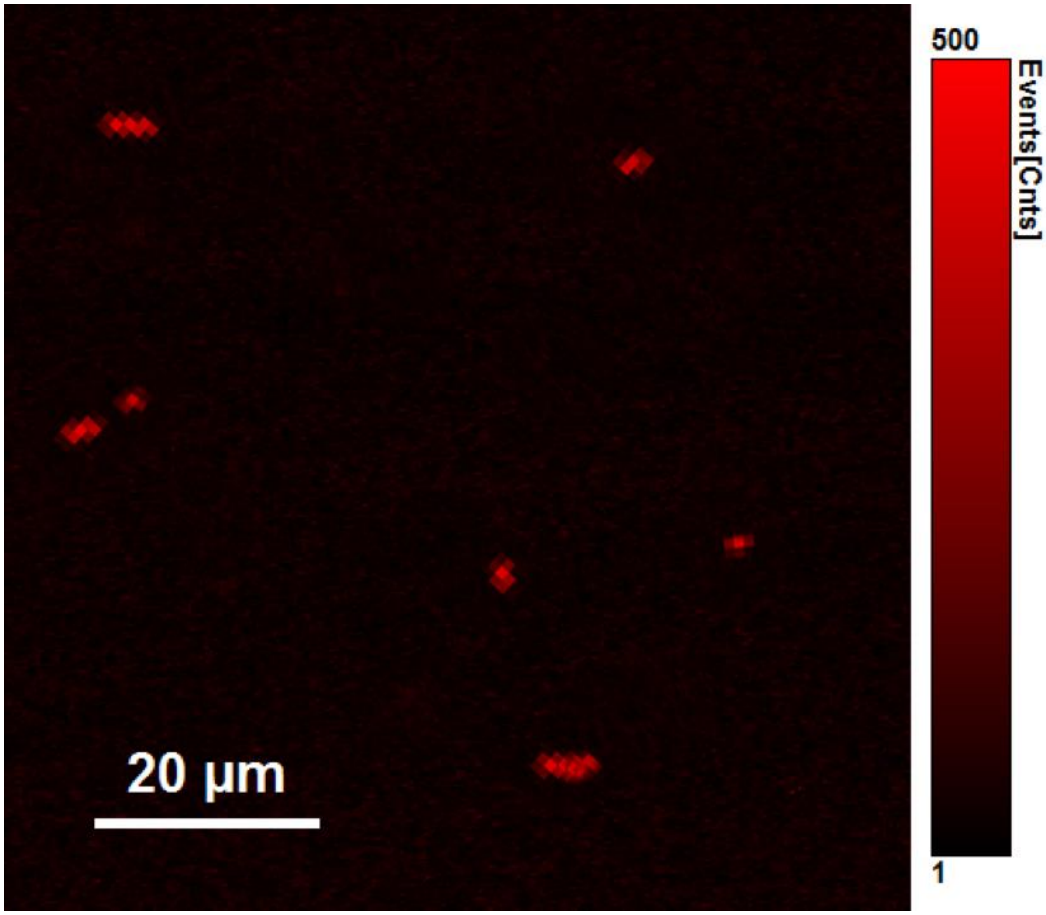

Figure 126: Pholloidin-TRITC-labelled rabbit actin above a DOPC bilayer formed on plasma-cleaned glass. As was the case with bovine actin these actin filaments were mobile atop the SLB and thus only low resolution images could be obtained. The experiment was carried out at room temperature in a PDMS cell. Phallodin-TRITC was excited by a 532 nm laser line and fluorescence was passed through a 550LP filter onto the SPAD detectors.

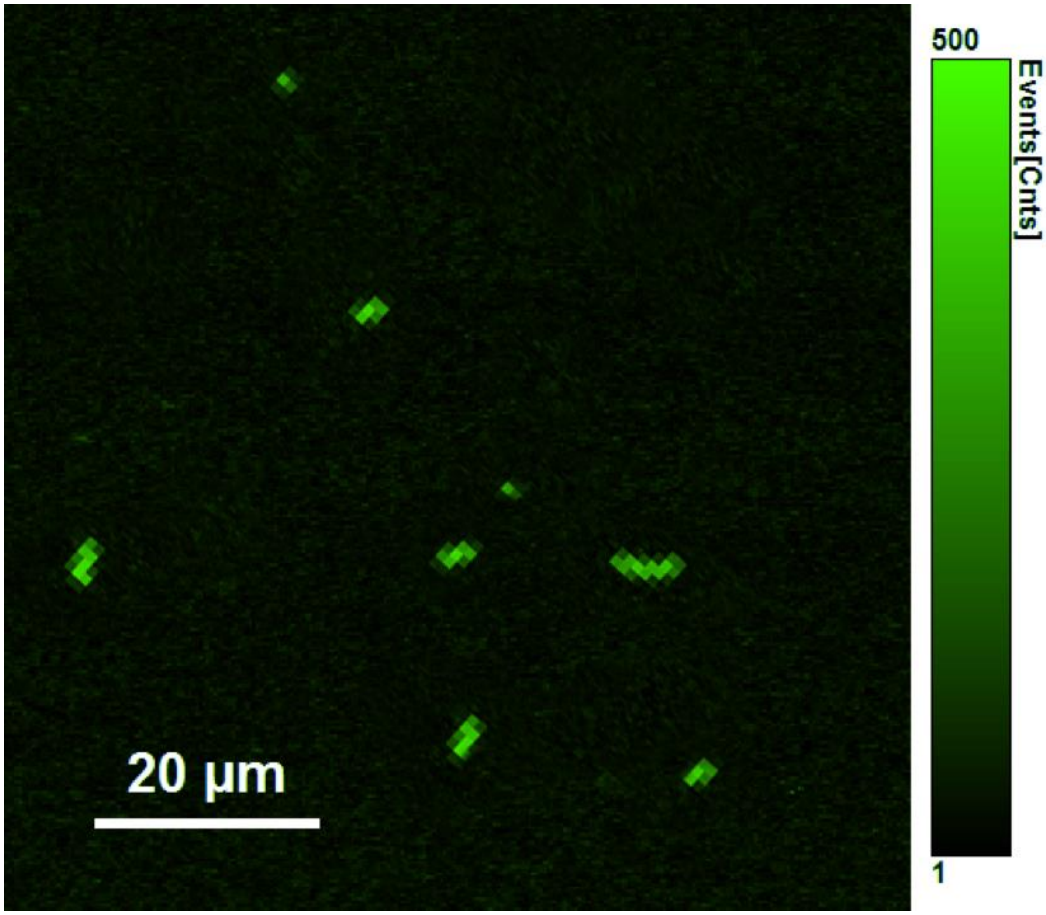

Figure 127: Pholloidin-TRITC-labelled human platelet actin above a DOPC bilayer formed on plasma-cleaned glass. In agreement with our bovine and rabbit actin results, human platelet F-actin was mobile on top of a SLB and once again only low resolution images could be obtained. The experiment was carried out at room temperature in a PDMS cell. Phalloidin-TRITC was excited by a 532 nm laser line and fluorescence was passed through a 550LP filter onto the SPAD detectors.

To measure the diffusion of the actin filaments, point measurements were performed detecting at the wavelength of the TRITC-labelled actin filaments at random locations on the bilayer. Initially this proved difficult due to the sparse nature of the F-actin filaments atop the SLB and what was evidently relatively slow diffusion. In order to overcome this limitation, the concentration of the actin was increased and the length scale of the point measurements were increased to a 12 to 20-minute window in order to gain diffusional data. A typical ACF of phalloidin-TRITC-labelled rabbit actin diffusing atop a DOPC SLB is shown in Figure 128. Fitting of this ACF data was more challenging than unhindered Brownian diffusion for lipid diffusion. The most obvious feature of these fits for actin filament was the much

more gradual decay of the curve, an indication of a sub 1 alpha value and thus hindered diffusion.

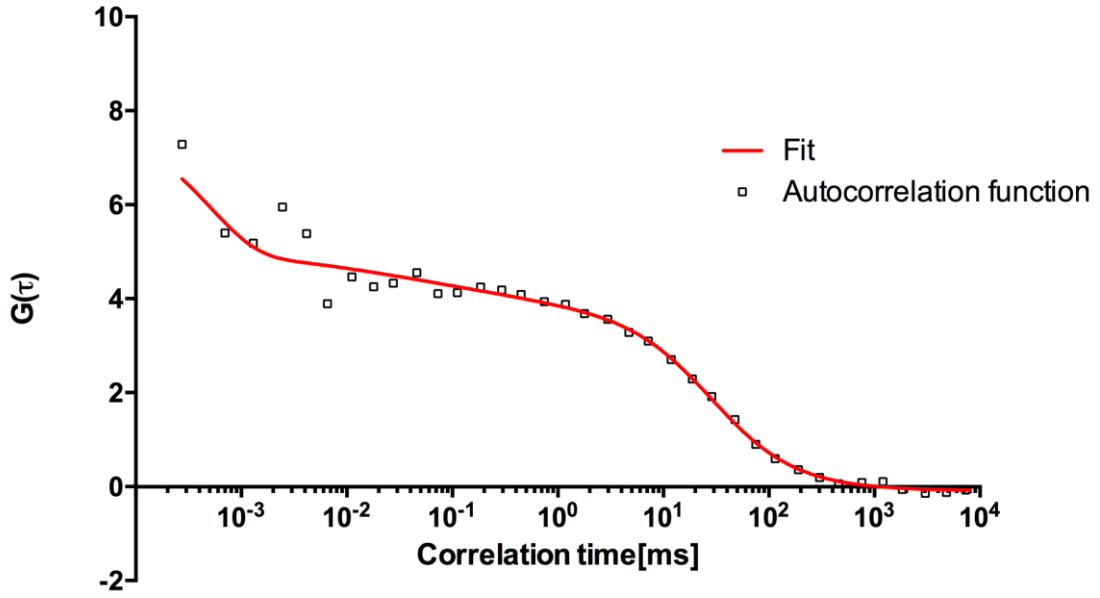

Figure 128: A representative ACF of phalloidin-TRIC-labelled rabbit actin diffusing above a DOPC bilayer. Fits to ACF trace were often difficult when compared to the ease at which lipid data was routinely fitted. Nonetheless diffusion co-efficients could be obtained for actin filaments above a DOPC bilayer. The experiment was carried out at room temperature in a PDMS cell. Phallodin-TRITC was excited by a 532 nm laser line and fluorescence was passed through a 550LP filter onto the SPAD detectors. Point measurements were performed for between 12 and 20 minutes to build ACF data.

Fitting the ACF data to a two-dimensional model, the diffusion co-efficient was calculated for all three actin types as well as the underlying lipid bilayer. By this stage the lipid bilayer diffusive properties had been well characterised and this was not altered by the presence of mobile actin filaments above. Here the lipid diffusion co-efficient was determined to be 3.69 ± 0.22 $\mu m^2/s$ and the alpha was 1. Fitting the bovine actin to a single-component two-dimensional model the diffusion co-efficient was determined to be 1.18 ± 0.43 $\mu m^2/s$, while the alpha value was 0.77 ± 0.11. Rabbit actin was found to diffuse at 1.54 ± 0.50 $\mu m^2/s$, while the alpha value was 0.78 ± 0.09. Finally, human platelet actin was determined to diffuse at 1.26 ± 0.56 $\mu m^2/s$, with an alpha value of 0.68 ± 0.12. These diffusion co-efficients are summarized in Figure 129. A one-way ANOVA found the difference between these diffusion co-efficients to be significant, where $F(3, 60) = 128.50$, < 0.001. A post-hoc

Bonferroni test found this significance to lie between the lipid value and all three actin fibres ($p < 0.001$). There are several points to note; firstly these diffusion co-efficients are at least an order of magnitude lower than reported for actin filaments in free aqueous media.[216] Secondly, these actin diffusion values are 2 to 3 times slower than the surrounding lipid values. Recalling our earlier integrin reconstitution data, we had previously seen that protein that was loosely associated with the lipid bilayer diffused faster than the bilayer itself (section 4.3.6). Only properly inserted integrin diffused slower than the surrounding lipid bilayer (section 4.3.7). Therefore the fact that the actin proteins diffused well below the lipid diffusion co-efficient suggests that the protein fibres are not merely loosely bound to the lipid membrane. This was the case for all three actin fibres.

As seen in Figure 129, the distribution of the diffusion values varies widely, where the range of the values is used as the experimental standard deviation. However, this is probably not appropriate as the breadth of the SD, particularly compared with the lipid diffusion is likely due to variation in length distributions of the filaments which are evidently variable from visual examination of the confocal images. However, in two-dimensional diffusion, it is the membrane incorporated volume of the protein which is regarded to dictate the diffusion rate, and the slow rate of diffusion here suggests that there is either some intercalation of the actin filaments into the bilayer and that there is muli-point attachment of the actin to the bilayer. The actin, which has a PI of approximately 4.8[210], is anionic at the pH used here, and zwitterionic, electrostatic interactions between the actin and ammonium group of DOPC may promote binding. Furthermore, that the actin does diffuse indicates that it is not penetrating through the membrane, i.e. and interacting with the underlying substrate. The alpha values are notable in that in all cases the filaments they are found to be below 0.80. As described, where the anomalous exponent is below 1, this indicates that sub-diffusion is occurring. This value, not found in the lipid data, shows that the movement of the actin filaments is anomalous and thus hindered. Again multipoint attachment to the lipid is the most likely explanation for this behaviour. Overall, to our knowledge this is the first report on the interaction and

diffusion of actin filaments with the lipid bilayer and they may be a useful analogue for peripheral protein interactions with bilayers.

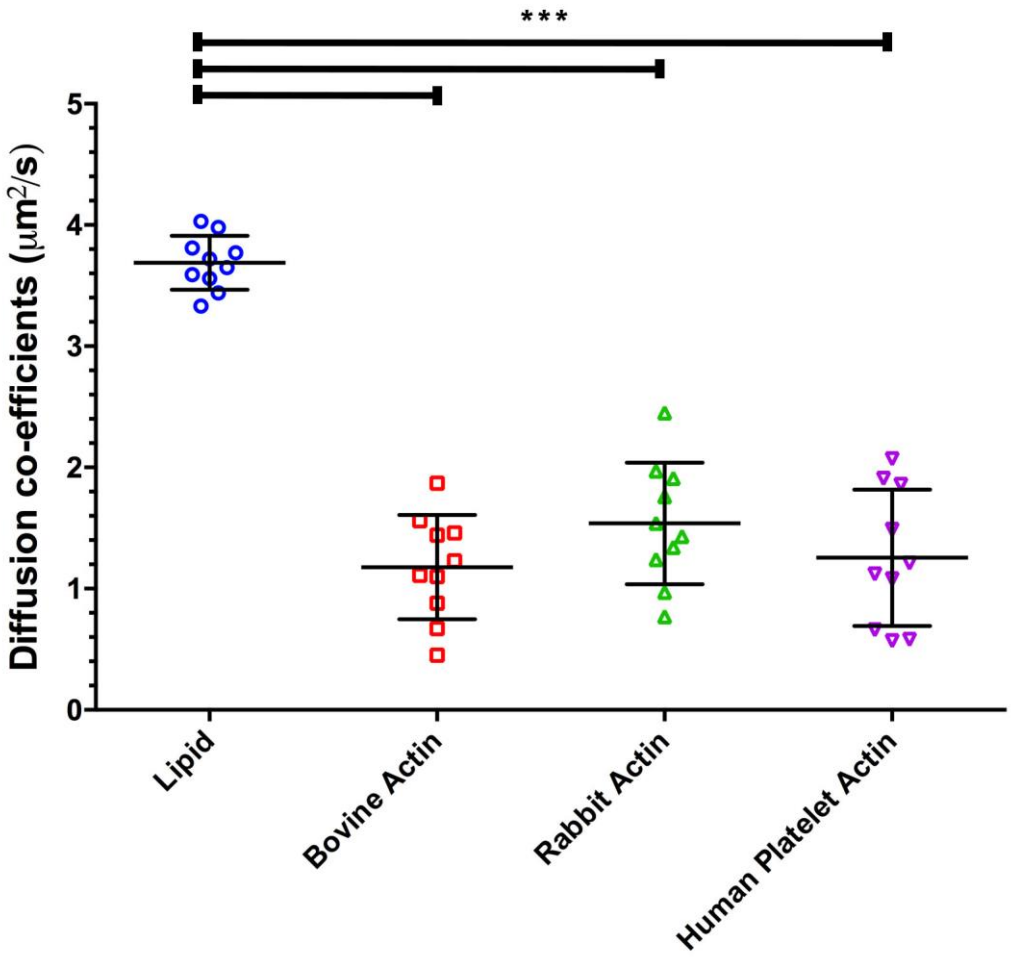

Figure 129: A summary of actin diffusion co-efficients above a DOPC SLB. The actin was labelled with phalloidin-TRITC and flushed on top of a preformed lipid bilayer. Point measurements were then performed over a 12 to 20 minute period and the ACF data was fitted to a two-dimensional model. A lipid probe was also included in the form of DOPE-Atto655 to determine whether actin presence altered the bilayer's diffusive properties. It was found that the actin filaments diffused much slower than the SLB, while the lipid itself behaved as normal with no change in the diffusion co-efficients when compared to previous actin free experiments. Standard deviation was used to represent the error.

Ryadnov group fibre polymerisation above the lipid bilayer

We then compared the interaction of the actin filaments with the filament forming peptides provided by Dr Ryadnov's group. Here, the DOPC lipid bilayer was formed via the same method as before and self-assembled fibres (cyan(+)4, cyan(+)6 and SR_EDS_02) were each flushed across the SLB in separate experiments. The surface

was then imaged by confocal fluorescence microscopy to confirm assembly had occurred prior to the initiation of point FCS measurements. As before, cyan(+)4 fibres could be routinely formed. However, interestingly, unlike the actin fibres above the lipid bilayer we observed that the cyan(+)4 fibres were completely immobilized at the bilayer. For reference, the lipid bilayer remained completely mobile. This fibre immobility is shown in Figure 130 where sulfo-rhodamine B labelled cyan(+)4 was was imaged three times over a 30 minute period at the same location. In contrast to the actin observations, the movement between frames was negligible showing that the fibres were stationary above the SLB. Owing to this immobility it was not possible to perform the anticipated diffusion measurements on the fluorescently labelled fibres as achieved in the actin-based experiments.

This same protocol was repeated on the cyan(+)6 peptide where the self-assembled fibres were incubated with the pre-formed DOPC SLB. The sulfo-rhodamine B labelled fibres were then imaged via confocal microscopy to determine their polymerisation state, and subsequently imaged 10 and 30 minutes later to determine whether the fibres were mobile like actin, or stationary as in the case of cyan(+)4. A typical confocal image of cyan(+)6 is shown in Figure 131. Interestingly, it was evident that like cyan(+)4, cyan(+)6 was immobile over the time-course of the experiment.

Finally, attempts were made to repeat this experiment with the final Ryadnov group fibre-forming peptide; SR_EDS_02. The fibre was allowed to self-assemble overnight as prescribed before being flushed across the pre-formed DOPC SLB. Previously we had found it difficult to assemble this fibre directly above a glass substrate and this difficulty continued where no SR_EDS_02 was successfully found atop the lipid bilayer despite multiple attempts.

As a whole both cyan(+)4 and cyan(+)6 were found to be immobile over multiple measurements when introduced onto a DOPC SLB. This was unexpected given that the fibres were atop a mobile freely diffusing lipid plane and also given that their positive charge. Logically it would be expected that any fibres interacting with the

bilayer would also be mobile, as had been our experience with fluorescently labelled bovine, rabbit, and human platelet actin. This contrasting observation with these cytoskeletal mimics is an interesting feature of the Ryadnov group's fibres. To help explain this, it is speculated that these cytoskeletal mimics are capable of penetrating though the lipid bilayer in order to interact with the underlying stationary glass substrate, giving the impression of immobility atop the SLB. However, to confirm such a hypothesis, further experimentation will be necessary.

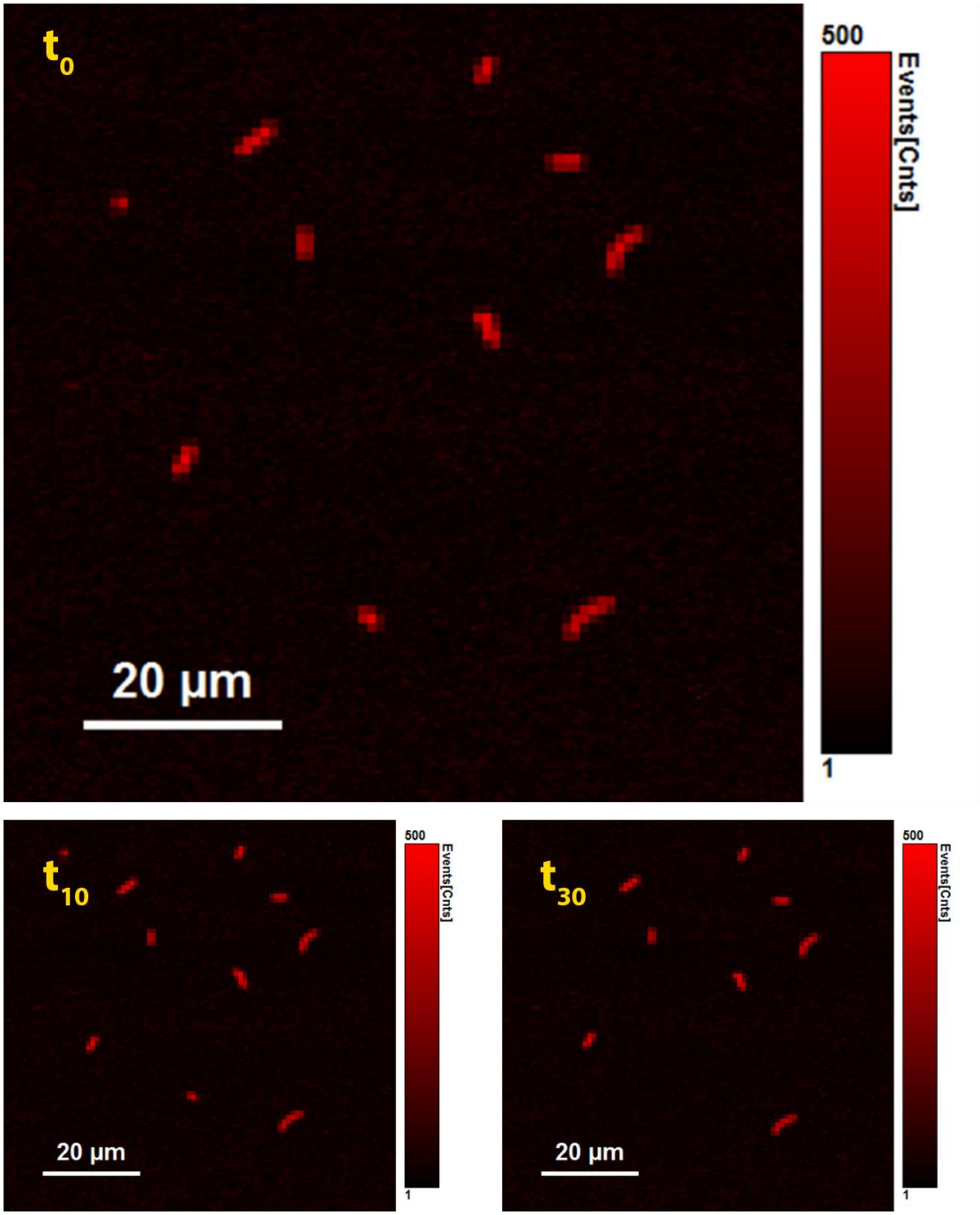

Figure 130: Sulfo-rhodamine B-labelled cyan(+)4 on top of a DOPC SLB. Top shows cyan(+)4 after flushing the fibres across the bilayer. Bottom left shows the fibres 10 minutes later, while bottom right shows the fibres 30 minutes later. The movement of the fibres was negligible over the course of the experiment. Sulfo-rhodamine B-labelled fibres were excited with a 532 nm laser line and fluorescence was passed through a 550LP filter onto the SPAD detectors.

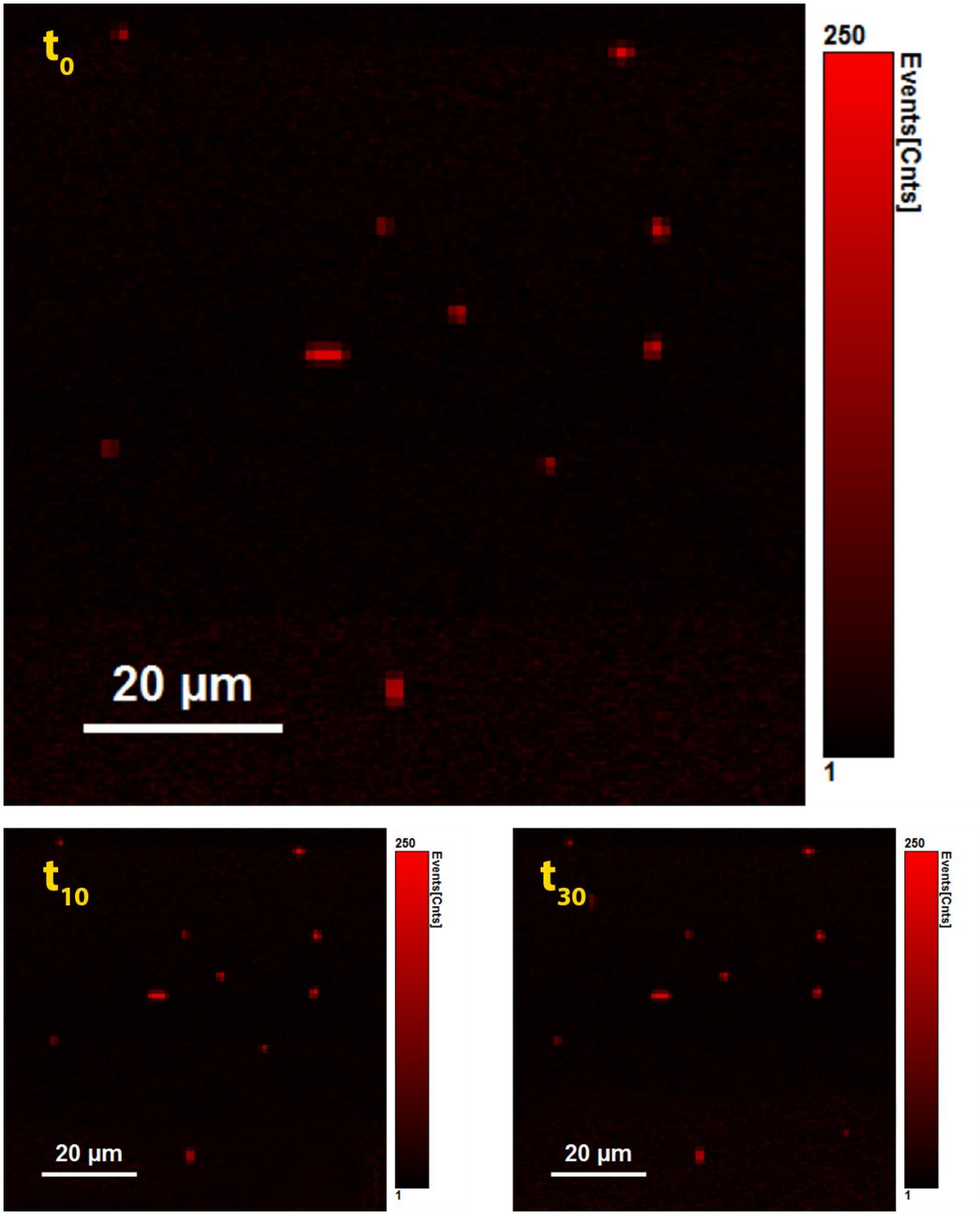

Figure 131: Sulfo-rhodamine B-labelled cyan(+)6 on top of a DOPC SLB. Top shows cyan(+)6 after flushing the fibres across the bilayer. Bottom left shows the fibres 10 minutes later, while bottom right shows the fibres 30 minutes later. As was the case with cyan(+)4, the movement of the cyan(+)6 was negligible over the course of the experiment. Sulfo-rhodamine B labelled fibres were excited with a 532 nm laser line and fluorescence was passed through a 550LP filter onto the SPAD detectors.

Although it was not confirmed whether the Ryadnov group's fibres had penetrated below the bilayer or were actually stationary above the SLB, we decided to carry out

point measurements on the under/overlying lipid regardless, to see whether the fibres had any influence on bilayer diffusion. We had previously carried out similar experiments where the Ryadnov group's fibres were known to be below the bilayer (section 5.3.1).

To examine the influence of overlying cyan(+)4 and cyan(+)6 on the DOPC SLB, confocal imaging was used to image the sulfo-rhodamine fibres and locate them for point measurements in order to determine whether the immobile fibres provided any barrier to the fluidity of the bilayer. A typical ACF of lipid diffusion below a stationary cyan(+)4 fibre is shown in Figure 132. In this case the data fitted well to a single-component two-dimensional fit with no obvious defects. The same protocol was also carried out for cyan(+)6 where similar ACF data was obtained. In order to provide a baseline diffusion rate, a fibre free control was prepared in tandem. Using DOPE-Atto655 as the lipid probe this control was determined to diffuse at 3.89 ± 0.34 $\mu m^2/s$. Below cyan(+)4 the diffusion co-efficient was 3.91 ± 0.23 $\mu m^2/s$. Below cyan(+)6 the diffusion co-efficient was 3.92 ± 0.25 $\mu m^2/s$. In all cases the alpha value was determined to be 1, indicating unhindered Brownian diffusion. This data is summarised in Figure 133. As a whole this data shows that the addition of cyan(+)4 and cyan(+)6 fibres above a DOPC SLB had no influence on the diffusion co-efficient of the lipid membrane. However, this observation presumes that fibres are stationary above the diffusing lipid membrane. This may suggest that the fibres are somehow immobilising a thin nanometer wide stretch of underlying lipid. On the other hand it can be speculated that the fibres are no longer situated above the lipid membrane but have penetrated through the lipid film to the underlying glass substrates. If this were the case then the previous lipid diffusion measurements were merely measuring the diffusional characteristics of the surrounding intact lipid membrane, rather than the influence of fibres on an underlying lipid bilayer.

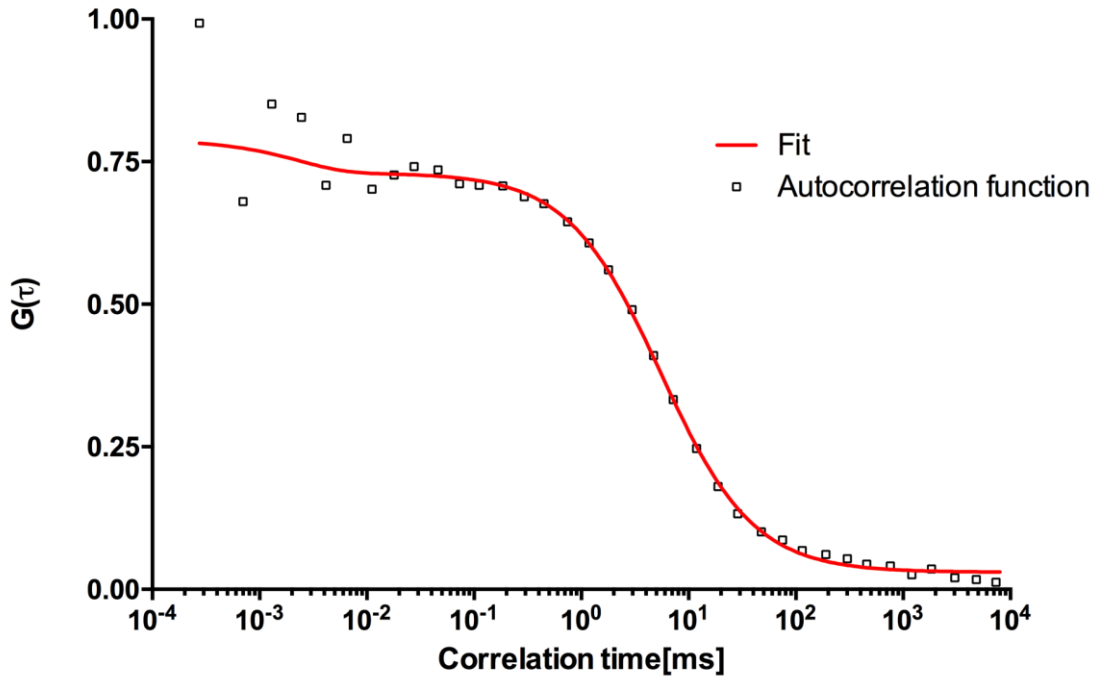

Figure 132: A typical ACF and its two-dimensional single component fit for DOPE-Atto655 in a DOPC bilayer "below" a cyan(+)4 fibre. The immobility of the cyan(+)4 (and cyan(+)6) fibres may suggest that the filaments are not in fact resting above the lipid bilayer but rather have penetrated through the membrane to interact with the underlying glass substrate. On the other hand the fibres may immobilise a thin length of underlying lipid molecules to remain stationary above the SLB.

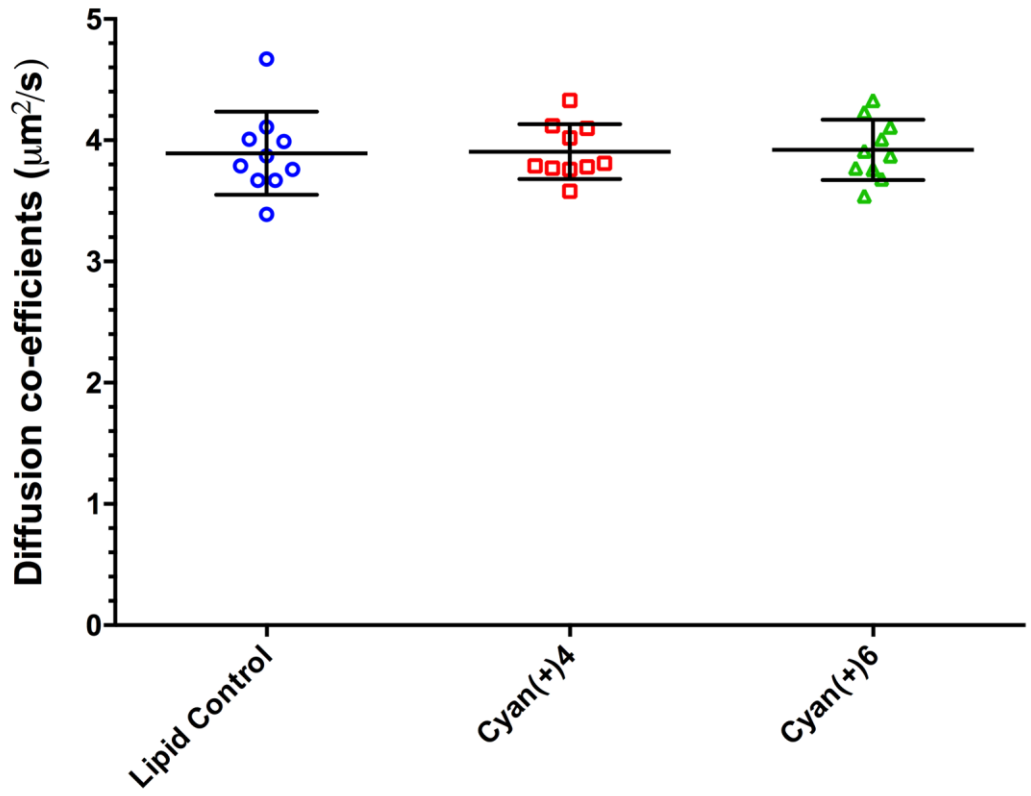

Figure 133: A summary of lipid diffusion co-efficients for DOPE-Atto655 in a DOPC SLB "below" cyan(+)4 and cyan(+) 6 fibres, as well as a fibre-free control. The fact that the fibres remained stationary rather than diffusion in tandem with the lipid suggests that the fibres have penetrated through the lipid bilayer to interact with the underlying substrate. Nonetheless the fibre's presence does not appear to provide a sufficient barrier to lipid diffusion to alter DOPE-Atto655 mobility when compared to a lipid only control.

This work highlights contrasting lipid-fibre interactions between actin filaments and the Rydnov group's cytoskeletal mimics. Further work will be needed to characterise this contrasting interaction above the lipid bilayer. All of this work was carried out in pure DOPC membranes and in the future we would like to expand this to include a variety of lipid compositions to determine the controlling factor in these lipid-fibre interactions. For example, the inclusion of charged lipids (eg the negatively charged DOPS) at varying concentrations may provide alternative observations. Likewise, the use of ordered domain-forming lipids such as cholesterol and sphingomyelin is another avenue of approach. Furthermore, we have yet to incorporate these cytoskeletal mimics with our biologically-relevant nature's own composition. Ideally we would also like to combine this cytoskeletal work with our novel PDMS arrays (chapter 4). For example, by assembling both classes of filamentous mimics above

our microcavity-containing arrays we could eliminate the concern of the underlying stationary substrate. Our microcavity system has also been shown to be an ideal platform for the reconstitution of transmembrane proteins and given the role of actin in integrin function[199,203,217] it would therefore be extremely desirable to combine these two proteins in a platform such as ours. For example, if F-actin could be formed across our mircocavities in a mesh we could monitor integrin diffusion and function while in contact with cytoskeletal proteins alone, away from the constraints of a planar substrate. This proposed experiment is sketched in Figure 134.

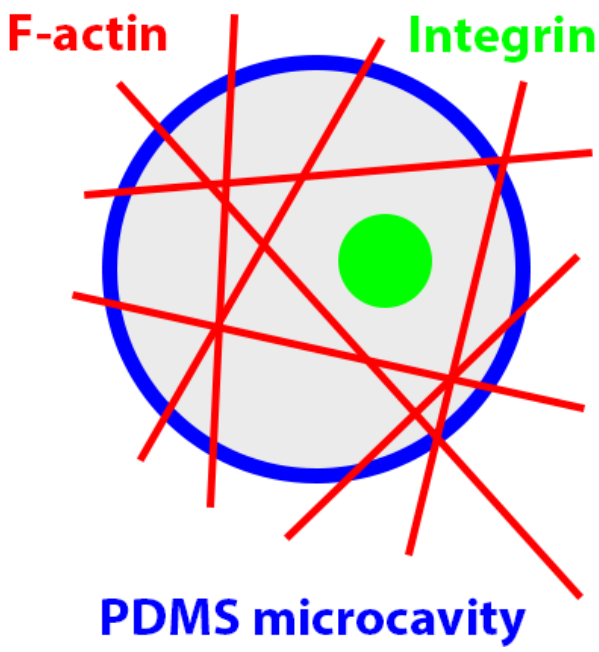

Figure 134: By combining cytoskeletal structures with our PDMS cavity arrays we would hope to more accurately reflect the cell membrane in an artificial lipid model. This top down sketch of one such proposed experiment would involve the formation of a cytoskeletal mesh (such as actin) across buffer-filled microcavites. By spanning a protein inserted (such as integrin) SLB across the microcavity we could better mimic the cell membrane. Here membrane proteins could be examined in a biologically-relevant environment.

6. Conclusions and future work

We have shown that artificial mimics of the cell membrane are insightful models to better understand the complex nature of the cell's lipid bilayer and its interactions with transmembrane and membrane associating proteins. As described, these models may take various forms, each with their own advantages and disadvantages. These models can be roughly divided into two main categories, namely free-standing vesicle systems and planar supported bilayers. This thesis has focused on both of these categories and has sought to advance upon what currently exists within the literature to better model the cell membrane.

One of the main focuses of this thesis has been on a transmembrane protein integrin $\alpha_{IIb}\beta_3$ within lipid bilayer models. Therefore, the study began with the characterisation of $\alpha_{IIb}\beta_3$ in its native environment, the platelet (chapter 2). Physiologically $\alpha_{IIb}\beta_3$ remains constrained in its low-affinity form within the resting discoid platelet. $\alpha_{IIb}\beta_3$ activation to its high affinity ligand binding form occurs in response to platelet activation. Here, platelet agonists interact with their respective receptors leading to intracellular signalling processes and culminating in a pro-aggregatory response. $\alpha_{IIb}\beta_3$ is one of the key mediators of the response and its inside out activation leads to structural changes within the integrin protein which allow for ligand binding. While such an activation process is beyond the scope of an artificial membrane system it is possible to mimic this $\alpha_{IIb}\beta_3$ activation process using artificial integrin activators. Therefore, before we began to investigate artificial integrin activation in our lipid vesicles and planar lipid bilayer, we first attempted to characterise activation in platelets. The two artificial integrin activators were DTT and Mn^{2+}. Both have been widely used in the literature to initiate integrin-ligand binding both *in vivo* and *in vitro*.[104,109,110,112,113,117,119,218,219] The investigation began with platelet aggregometry experiments, where the ability of DTT and Mn^{2+} to initiate platelet aggregation was examined. While TRAP, a physiological agonist and positive control was a potent activator, the platelet response to DTT and Mn^{2+} was noticeably different. Firstly, DTT was noted to have a concentration dependent lag time. For example, at 0.5 mM DTT, the lag-phase lasted over 13 minutes, while at 5 mM, the lag phase lasted nearly 4 minutes. This was in contrast to the almost

immediate response using TRAP. On the other hand, Mn^{2+} initially appeared to have no ability to initiate platelet aggregation in a washed platelet population. In order to promote an aggregatory response it was required that the platelets were supplemented with additional fibrinogen to mediate platelet bridging. From this data we were able to conclude that Mn^{2+} was a weaker activator than DTT, but with the caveat that DTT possess an inherent lag-phase that must be taken into account for upcoming experiments (section 2.3.1). Flow cytometry was later used to characterise the influence of DTT and Mn^{2+} on $\alpha_{IIb}\beta_3$ in isolation. Here we found that although both DTT and Mn^{2+} lead to a change in integrin conformation (PAC-1 binding), only DTT lead to a measurable degree of fibrinogen binding (OgFg binding). This again highlights Mn^{2+} as a weak integrin activator (section 2.3.2). The bidirectional signalling ability of $\alpha_{IIb}\beta_3$ was also taken into account where assays for alpha and dense granule release were performed. While, as expected, the positive control of TRAP lead to P-selectin presentation and ATP/ADP release, DTT and Mn^{2+} failed to initiate these responses. From this we were able to conclude that these artificial activators were unable to promote a whole-platelet response. Therefore, whatever activating ability possessed by DTT and Mn^{2+} is limited to the integrin protein (section 2.3.3). From this data we were able conclude that both of these activators were candidates for use in our upcoming reconstituted lipid systems, although DTT seemed a more potent activator as long as its lag-phase is accounted for.

The next chapter focused on lipid vesicles and in particular GUVs as a model for studying reconstituted $\alpha_{IIb}\beta_3$ (chapter 3). Here various methods of vesicle formation were explored and refined including sonication (SUVs), extrusion (LUVs), and electroformation (GUVs). While these techniques are relatively common, one of the striking features of the available literature is the reliance on relatively simple unary and binary lipid compositions.[33,53,126,142,150,220] Therefore, one of the key goals of this refinement stage was the development of a more accurate physiological mimic of the cell membrane. To this end, we adopted a lipid composition known as nature's own from the Lentz group at the University of North Carolina at Chapel Hill. The Lentz group had been using this composition for some time in their SUV-based

experiments, but the lipid mixture had yet to be used in larger vesicles or planar lipid bilayer systems. We found that the nature's own composition was compatible with electroformation and could be routinely used to create complex and physiologically-relevant GUVs (section 3.3.1). Parallel to this development process, we also explored methods of integrin $\alpha_{IIb}\beta_3$ reconstitution into lipid vesicles. To do so, a number of approaches were possible, using varying vesicle sizes, detergents, and detergent removal methods. We utilised two separate insertion methods, one based on Dennison *et al.*[27], and the other based on Müller *et al*.[34] The Dennison method used partial solubilisation of sonicated SUVs and slow detergent removal, while the Müller method used complete solubilisation of extruded LUVs and fast detergent removal. Both of these methods yielded integrin-containing proteoliposomes (section 3.3.3). As our goal was to study $\alpha_{IIb}\beta_3$ in GUVs, we then developed a method of converting these small proteoliposomes into giant vesicles, well suited to microscopy-based experiments. It was found that a two-step procedure of 1) ultracentrifugation, and 2) electroformation of a proteoliposomes pellet, could successfully produce such $\alpha_{IIb}\beta_3$-reconstituted GUVs. Combining the two strands of the chapter it was therefore possible to produce nature's own GUVs containing reconstituted $\alpha_{IIb}\beta_3$ (section 3.3.4). FLCS was then used to examine the diffusion co-efficients of the lipid and integrin molecules. The lipid diffusion co-efficients were in-line with literature values for such free-standing structures.[53] The $\alpha_{IIb}\beta_3$ diffusion co-efficient was found to be well below the lipid value, indicating that $\alpha_{IIb}\beta_3$ had been fully inserted into the nature's own GUVs and was not simply membrane-associated. This is particularly relevant given the fact that $\alpha_{IIb}\beta_3$ has been highlighted as associating with the lipid bilayer in other reconstitution experiments, particularly in the absence of the lipid DMPC.[29,34] Another key point is that GUV systems are free-standing and are immune from the immobilisation of reconstituted proteins on a substrate surface, as is normally the case in planar bilayer systems.[221] Therefore $\alpha_{IIb}\beta_3$ was capable of diffusing freely without being encumbered, as has previously been the case in other $\alpha_{IIb}\beta_3$-containing systems.[31] This means that our GUV work is the first such setup to confirm full $\alpha_{IIb}\beta_3$ insertion into a non DMPC-based composition, the first to provide diffusion co-efficients for $\alpha_{IIb}\beta_3$ in a vesicle-based

system, and the first artificial lipid system to show fully mobile $\alpha_{IIb}\beta_3$ (section 3.3.5). After establishing that $\alpha_{IIb}\beta_3$ could be routinely inserted into GUVs we later sought to determine whether activation induced structural changes in the integrin protein would bring about a change in the diffusion co-efficient. The use of DTT and Mn^{2+} as integrin activators failed to alter the mobility of $\alpha_{IIb}\beta_3$. However, when DTT and Mn^{2+} were used as integrin activators in the presence of fibrinogen, a large change in the mobility of $\alpha_{IIb}\beta_3$ became apparent. Here the diffusion co-efficient of $\alpha_{IIb}\beta_3$ fell to approximately 60 % of its original value. This reduction was identical for either activator. Importantly, the use of fibrinogen alone failed to alter the diffusion co-efficient showing that the reconstituted $\alpha_{IIb}\beta_3$ was in its resting low-affinity conformation following reconstitution. Such a large reduction in the diffusion co-efficient could only be brought about massive integrin-fibrinogen conglomerates.[55] To the best of our knowledge this is the first work to show how protein-protein interaction may bring about a change in the diffusion co-efficient of protein in GUVs, and the first to utilise FLCS to show this in any artificial lipid system (section 3.3.6). We later used domain-forming GUVs to determine whether $\alpha_{IIb}\beta_3$ had affinity for either the liquid order or liquid disordered phase of the giant vesicles. Here, we found that $\alpha_{IIb}\beta_3$ preferentially associates with the phospholipid rich, cholesterol poor, liquid disordered phase of GUVs, regardless of activation state. Interestingly this is in contrast to other members of the integrin family (section 3.3.7).[35]

Armed with the knowledge gained from GUV studies, we next sought to combine the advantages of free-standing vesicle systems with those of existing SLB models. To provide this platform our group has developed a novel cavity array system (chapter 4). This was achieved using polystyrene beads and PDMS to create optically transparent cavity arrays with pore sizes with well-defined dimensions.[175] This was done using beads with diameters ranging from hundreds of nanometres to 8 μm, although this thesis focuses on PDMS arrays constructed using 2.88 μm spheres. Such beads were capable of constructing cavity sizes well suited to FLCS-based experiments. It was found that by plasma treating the PDMS surface to render it hydrophilic, and sonicating it in buffer, it was possible to produce buffer-filled

cavities. The next step was to form a spanning lipid bilayer across these cavities. It was immediately clear that SUVs and LUVs were too small to span the dimensions of our cavities and so GUVs were explored as the lipid source in our SLB system. Unlike smaller vesicles, GUVs do not readily rupture to form planar bilayer so this disruption was promoted by the use of high concentrations of calcium within the buffer. Via this method an SLB was formed, but the bilayer did not span the cavities. As such an alternative method to create a spanning bilayer was investigated. It was found that a two-step protocol of 1) LB transfer of a lipid monolayer, and 2) SUV/LUV rupture lead to formation of a lipid bilayer. Confocal microscopy and point measurements were able to show that this SLB spanned the buffer-filled microcavities. We were able to achieve this spanning with a multitude of lipid compositions, including the physiologically-relevant nature's own mixture. Importantly, point measurements showed that the lipid diffused at values comparable with GUV systems and away from the non-specific interactions normally associated with SLBs. In fact, diffusion values above cavities were approximately three-fold higher than diffusion co-efficients on planar PDMS regions (section 4.3.3). The next step in our development of the PDMS array was to reconstitute membrane proteins into the SLB, with particular emphasis on integrin $\alpha_{IIb}\beta_3$. Given that liposomes were required for completion of the lipid bilayer, and given the fact that we had already created $\alpha_{IIb}\beta_3$-containing proteoliposomes in the previous chapter, it at first appeared straightforward to create an integrin-reconstituted cavity-spanning SLB. However, the disruption of the $\alpha_{IIb}\beta_3$-containing proteoliposomes atop the LB monolayer yielded a lipid bilayer where reported integrin diffusion co-efficients were well in excess of lipid diffusion co-efficients. In fact, this protein value was approximately twice that of the lipid bilayer value (section 4.3.6). This was in contrast to our experience in $\alpha_{IIb}\beta_3$-reconstituted GUVs. Combined with the knowledge $\alpha_{IIb}\beta_3$ has a tendency to associate with lipid membranes in non-DMPC-containing compositions, such high diffusion co-efficients suggested that $\alpha_{IIb}\beta_3$ was not correctly inserted into the lipid bilayer in our cavity-spanning system. In the search for a solution we looked to our earlier GUV-based work. There, we had shown proper integrin reconstitution into GUVs. As such, we decided to utilise these

giant vesicles to complete the lipid bilayer in our cavity-spanning system, rather than the smaller proteoliposomes. Using these GUVs as an intermediate, and calcium to promote vesicle rupture, it was possible to create a cavity-spanning lipid bilayer. Under these conditions point measurements were able to show integrin diffusion co-efficients well below the lipid bilayer values and in line with our earlier experience in GUVs. From this we were able to conclude that the protein was properly inserted via this method. This suggests that the two-step combination of ultracentrifugation and electroformation was required to produce properly reconstituted $\alpha_{IIb}\beta_3$ into DMPC-free lipid compositions (section 4.3.7). Interestingly, we were not able to accurately mirror ligand binding experiments when compared to our GUV system. In GUVs, the addition of fibrinogen leads to a measurable decrease in the diffusion co-efficient of the integrin protein. Here, above cavities, no such reduction in integrin diffusion was noted. However, we were able to observe large scale aggregation of $\alpha_{IIb}\beta_3$ on planar regions of the PDMS. Dual colour experiments were able to show that these integrin clusters aligned with the locations of labelled fibrinogen molecules. This shows that fibrinogen was responsible for the aggregation process (section 4.3.9). As a whole, our PDMS arrays provide a low cost and straightforward means of creating cavity-spanning lipid bilayers that alleviate the primary drawback of planar systems, namely non-specific interactions between the bilayer and the underlying substrates. Much of the existing work in the literature that has attempted to do so has produced nanocavity scale systems unsuited to FCS-based measurements, or used complex surface modifications to improve bilayer mobility. Indeed, even these surface modifications do not fully decoupled the two interfaces, where lipid and, in particular, protein immobility is still observed. To the best of our knowledge this work is the first to fully reconstitute $\alpha_{IIb}\beta_3$ into a DMPC-free planar bilayer system, and the first to measure $\alpha_{IIb}\beta_3$ diffusion in any planar bilayer system via FCS. Another key aspect to our cavity system is the fact that 100 % of our $\alpha_{IIb}\beta_3$ molecules were mobile. Existing setups within the literature have reported that 40 – 84 % of the integrin protein was immobile even where polymer cushions were utilised.[30,31,43,44] This shows the power of our novel system. Furthermore, our system has been shown to be compatible

wide other membrane proteins such as annexin V and glycophorin.[153] Such flexibility means that potentially any membrane protein could be studied using our platform.

Much of the previous work had focused on the lipid bilayer and the membrane proteins within the bilayer but the final experimental chapter concentrated on the cell cytoskeleton, the protein backbone of the cell's lipid membrane (chapter 5).[191] We had initially hoped that actin filaments or cytoskeletal mimics would be capable of bringing about a change in the diffusion co-efficient of a spanning lipid bilayer by acting as a barrier to lipid mobility. While it was possible to assemble these various actin proteins and cytoskeletal peptide mimics, we could not identify any alterations to the lipid bilayer's diffusive properties. Much of this was put down to the low surface coverage of the fibres. While initially the concentration of said fibres on the substrate was good, the creation of a spanning lipid bilayer meant that much of these fibres were removed from the surface. While it was possible to vastly increase the surface coverage of the fibres by immobilising them on the substrate, this process had the unfortunate side-effect of also rendering the lipid bilayer immobile (section 5.3.1). Because of these difficulties, the experimental set-up was reversed and the fibres were instead added atop a pre-formed SLB. In this case we found two diverging observations between the actin proteins and the cytoskeletal mimics. While the actins were highly mobile above the lipid bilayer, the cytoskeletal mimics were completely immobile. Interestingly, the diffusion co-efficient of the actin proteins were well below the value for the supporting SLB. Additionally, this diffusion was hindered, as shown by the low alpha value. This data suggests that the actin proteins were not merely associated with the bilayer but rather embedded somehow within the SLB. On the other hand, the immobility of the cytoskeletal mimics when added above a mobile bilayer suggests that fibres were penetrating through the SLB and interacting with the stationary underlying substrates. Such differing protein-lipid interactions are sure to require further investigation (section 5.3.2).

Throughout this thesis, one of the main objectives has been to increase the complexity of existing artificial lipid bilayer systems to more accurately mimic the

native cell membrane environment. Both the platelet-based chapter and GUV-based chapter served as a precursor for our novel PDMS cavity arrays. Going forward, one of the key goals would be to combine our existing PDMS cavity arrays with cytoskeletal structures such as actin in order to achieve even more physiological relevance. While currently, our PDMS arrays allow for the diffusion of membrane proteins above buffer-filled cavities, in the future it would be desirable to examine diffusion values over an actin (or other cytoskeletal protein) mesh. The cytoskeleton is of course not merely an inert structure within the cell. Instead it provides a platform for cell-cell interactions and functions as a base for signal transduction. It is a dynamic assembly that interacts with a wide array of binding proteins as well as having a role in the formation of lipid rafts. The fact that our PDMS arrays facilitate access to the intracellular regions of any transmembrane protein means that these actin-transmembrane protein interactions can be studied in greater detail. Indeed, one of the avenues of investigation proposed has been the controlled release of transmembrane binding proteins from the inside of buffer-filled cavities. Using $\alpha_{IIb}\beta_3$ as a model protein, for example, this hypothetical experiment could involve the release of talin, or another intracellular protein with a role in integrin activation, to the cytoplasmic tail end of membrane-reconstituted $\alpha_{IIb}\beta_3$. In such a set-up, this controlled release of binding proteins could perhaps be governed via electrorelease or the use of magnetically functionalised proteins. Perhaps the strongest feature of our PDMS array system is the fact that the platform may be applicable to a wide range of membrane proteins. It has already be used to host three un-related proteins ($\alpha_{IIb}\beta_3$, annexin V, and glycophorin), each inserted via a different reconstitution method. This versatility is combined with a low cost, straightforward, highly reproducible means of creating cavity-containing arrays. The platform is ideal for studying biological molecules as the system is completely surrounded by buffer unlike many existing systems. It also allows for the study of membrane proteins away from harsh solvents, while their optical transparency is well suited to microscopy experiments. The PDMS arrays provide an extremely stable means of study where lipid bilayer diffusion values were unchanged days after construction. This stability is improved in comparison to GUVs. The other massive improvement when compared to GUV is the spatial stability of our cavity-spanning system. Due to

the free-standing nature of GUVs, vesicle movement meant that point measurements were often difficult to perform. The stationary nature of our PDMS arrays meant that the acquisition of data is greatly improved. Finally, the fact that our cavity arrays are part of a flow cell setup means that buffer, drugs, proteins, and other molecules may be freely exchanged. Therefore, our PDMS arrays provide an excellent and versatile means of mimicking the native cell environment. By combining this platform with cytoskeletal structure and other membrane and membrane interacting proteins we hope to further mimic the physiology of the cell.

7. References

1. Eeman, M. & Deleu, M. From biological membranes to biomimetic model membranes. *Biotechnol. Agron. Société Environ.* **14,** 719–736 (2010).

2. Singer, S. J. & Nicolson, G. L. The fluid mosaic model of the structure of cell membranes. *Science* **175,** 720–31 (1972).

3. Kusumi, A., Fujiwara, T. K., Chadda, R., Xie, M., Tsunoyama, T. a, Kalay, Z., Kasai, R. S. & Suzuki, K. G. N. Dynamic organizing principles of the plasma membrane that regulate signal transduction: commemorating the fortieth anniversary of Singer and Nicolson's fluid-mosaic model. *Annu. Rev. Cell Dev. Biol.* **28,** 215–50 (2012).

4. Pike, L. J. The challenge of lipid rafts. *J. Lipid Res.* **50 Suppl,** S323–8 (2009).

5. Lindner, R. & Naim, H. Y. Domains in biological membranes. *Exp. Cell Res.* **315,** 2871–8 (2009).

6. Lajoie, P., Goetz, J. G., Dennis, J. W. & Nabi, I. R. Lattices, rafts, and scaffolds: domain regulation of receptor signaling at the plasma membrane. *J. Cell Biol.* **185,** 381–5 (2009).

7. Lodish, H., Berkman, A. & Zipursky, S. *Molecular Cell Biology (Fourth Edition)*. (W. H. Freeman, 2000). at <http://www.ncbi.nlm.nih.gov/books/NBK21493/>

8. Rawicz, W., Olbrich, K. C., McIntosh, T., Needham, D. & Evans, E. Effect of chain length and unsaturation on elasticity of lipid bilayers. *Biophys. J.* **79,** 328–39 (2000).

9. Dickson, R. C. Sphingolipid functions in Saccharomyces cerevisiae: comparison to mammals. *Annu. Rev. Biochem.* **67,** 27–48 (1998).

10. Pucadyil, T. J. & Chattopadhyay, A. Role of cholesterol in the function and organization of G-protein coupled receptors. *Prog. Lipid Res.* **45,** 295–333 (2006).

11. Alberts, B., Johnson, A., Lewis, J., Raff, M., Roberts, K. & Walter, P. in *Mol. Biol. Cell* (Garland Science, 2002). at <http://www.ncbi.nlm.nih.gov/books/NBK26878/>

12. Anthis, N. J. & Campbell, I. D. The tail of integrin activation. *Trends Biochem. Sci.* **36,** 191–198 (2011).

13. Arnaout, M. A., Mahalingam, B. & Xiong, J.-P. Integrin structure, allostery, and bidirectional signaling. *Annu. Rev. Cell Dev. Biol.* **21,** 381–410 (2005).

14. Cox, D., Brennan, M. & Moran, N. Integrins as therapeutic targets: lessons and opportunities. *Nat. Rev. Drug Discov.* **9,** 804–820 (2010).

15. Owen, J. S., Hutton, R. a, Day, R. C., Bruckdorfer, K. R. & McIntyre, N. Platelet lipid composition and platelet aggregation in human liver disease. *J. Lipid Res.* **22,** 423–30 (1981).

16. Hamid, M. A., Kunicki, T. J. & Aster, R. H. Lipid composition of freshly prepared and stored platelet concentrates. *Blood* **55,** 124–30 (1980).

17. Marcus, A. J., Ullman, H. L. & Safier, L. B. Lipid composition of subcellular particles of human blood platelets. *J. Lipid Res.* **10,** 108–14 (1969).

18. Rigaud, J. L., Pitard, B. & Levy, D. Reconstitution of membrane proteins into liposomes: application to energy-transducing membrane proteins. *Biochim. Biophys. Acta* **1231,** 223–246 (1995).

19. Scotto, a. W. & Zakim, D. Reconstitution of membrane proteins. Spontaneous incorporation of integral membrane proteins into preformed bilayers of pure phospholipid. *J. Biol. Chem.* **263,** 18500–18506 (1988).

20. Szoka, F. & Papahadjopoulos, D. Procedure for preparation of liposomes with large internal aqueous space and high capture by reverse-phase evaporation. *Proc. Natl. Acad. Sci. U. S. A.* **75,** 4194–8 (1978).

21. Darszon, A., Vandenberg, C. A., Ellisman, M. H. & Montal, M. Incorporation of membrane proteins into large single bilayer vesicles. Application to rhodopsin. *J. Cell Biol.* **81,** 446–52 (1979).

22. Rigaud, J. L., Bluzat, A. & Buschlen, S. Incorporation of bacteriorhodopsin into large unilamellar liposomes by reverse phase evaporation. *Biochem. Biophys. Res. Commun.* **111,** 373–82 (1983).

23. Riquelme, G., Lopez, E., Garcia-Segura, L. M., Ferragut, J. A. & Gonzalez-Ros, J. M. Giant liposomes: a model system in which to obtain patch-clamp recordings of ionic channels. *Biochemistry* **29,** 11215–22 (1990).

24. Darszon, A., Vandenberg, C. A., Schönfeld, M., Ellisman, M. H., Spitzer, N. C. & Montal, M. Reassembly of protein-lipid complexes into large bilayer vesicles: perspectives for membrane reconstitution. *Proc. Natl. Acad. Sci. U. S. A.* **77,** 239–43 (1980).

25. Lapinski, M. M., Castro-Forero, A., Greiner, A. J., Ofoli, R. Y. & Blanchard, G. J. Comparison of liposomes formed by sonication and extrusion: rotational and translational diffusion of an embedded chromophore. *Langmuir* **23,** 11677–83 (2007).

26. Kasahara, M. & Hinkle, P. C. Reconstitution and Purificaton of the {D}-Glucose Transporter from Human Erythrocytes. *J. Biol. Chem.* **252,** 7384–7390 (1977).

27. Dennison, S. M., Bowen, M. E., Brunger, A. T. & Lentz, B. R. Neuronal SNAREs do not trigger fusion between synthetic membranes but do promote PEG-mediated membrane fusion. *Biophys. J.* **90,** 1661–75 (2006).

28. Tunuguntla, R., Bangar, M., Kim, K., Stroeve, P., Ajo-Franklin, C. M. & Noy, A. Lipid bilayer composition can influence the orientation of proteorhodopsin in artificial membranes. *Biophys. J.* **105,** 1388–96 (2013).

29. Erb, E. M. & Engel, J. Reconstitution of functional integrin into phospholipid vesicles and planar lipid bilayers. *Methods Mol. Biol.* **139,** 71–82 (2000).

30. Erb, E. M., Tangemann, K., Bohrmann, B., Müller, B. & Engel, J. Integrin alphaIIb beta3 reconstituted into lipid bilayers is nonclustered in its activated state but clusters after fibrinogen binding. *Biochemistry* **36,** 7395–402 (1997).

31. Goennenwein, S., Tanaka, M., Hu, B., Moroder, L. & Sackmann, E. Functional incorporation of integrins into solid supported membranes on ultrathin films

of cellulose: impact on adhesion. *Biophys. J.* **85,** 646–55 (2003).

32. Gassmann, O., Kreir, M., Ambrosi, C., Pranskevich, J., Oshima, A., Röling, C., Sosinsky, G., Fertig, N. & Steinem, C. The M34A mutant of Connexin26 reveals active conductance states in pore-suspending membranes. *J. Struct. Biol.* **168,** 168–76 (2009).

33. Kreir, M., Farre, C., Beckler, M., George, M. & Fertig, N. Rapid screening of membrane protein activity: electrophysiological analysis of OmpF reconstituted in proteoliposomes. *Lab Chip* **8,** 587–95 (2008).

34. Müller, B., Zerwes, H. G., Tangemann, K., Peter, J. & Engel, J. Two-step binding mechanism of fibrinogen to alpha IIb beta 3 integrin reconstituted into planar lipid bilayers. *J. Biol. Chem.* **268,** 6800–8 (1993).

35. Hussain, N. F., Siegel, A. P., Ge, Y., Jordan, R. & Naumann, C. a. Bilayer asymmetry influences integrin sequestering in raft-mimicking lipid mixtures. *Biophys. J.* **104,** 2212–21 (2013).

36. Kahya, N., Brown, D. A. & Schwille, P. Raft partitioning and dynamic behavior of human placental alkaline phosphatase in giant unilamellar vesicles. *Biochemistry* **44,** 7479–89 (2005).

37. Rigaud, J.-L. & Lévy, D. Reconstitution of membrane proteins into liposomes. *Methods Enzymol.* **372,** 65–86 (2003).

38. Racker, E., Chien, T.-F. & Kandrach, A. A cholate-dilution procedure for the reconstitution of the Ca++ pump, 32Pi—ATP exchange, and oxidative phosphorylation. *FEBS Lett.* **57,** 14–18 (1975).

39. Jackson, M. L. & Litman, B. J. Rhodopsin-egg phosphatidylcholine reconstitution by an octyl glucoside dilution procedure. *Biochim. Biophys. Acta - Biomembr.* **812,** 369–376 (1985).

40. Plasencia, I., Survery, S., Ibragimova, S., Hansen, J. S., Kjellbom, P., Helix-Nielsen, C., Johanson, U. & Mouritsen, O. G. Structure and stability of the spinach aquaporin SoPIP2;1 in detergent micelles and lipid membranes. *PLoS One* **6,** e14674 (2011).

41. Ramadurai, S., Duurkens, R., Krasnikov, V. V. & Poolman, B. Lateral diffusion of membrane proteins: Consequences of hydrophobic mismatch and lipid composition. *Biophys. J.* **99,** 1482–1489 (2010).

42. Parise, L. V & Phillips, D. R. Platelet membrane glycoprotein IIb-IIIa complex incorporated into phospholipid vesicles. Preparation and morphology. *J. Biol. Chem.* **260,** 1750–6 (1985).

43. Purrucker, O., Förtig, A., Jordan, R. & Tanaka, M. Supported membranes with well-defined polymer tethers - Incorporation of cell receptors. *ChemPhysChem* **5,** 327–335 (2004).

44. Purrucker, O., Förtig, A., Jordan, R., Sackmann, E. & Tanaka, M. Control of frictional coupling of transmembrane cell receptors in model cell membranes with linear polymer spacers. *Phys. Rev. Lett.* **98,** 1–4 (2007).

45. Ye, F., Hu, G., Taylor, D., Ratnikov, B., Bobkov, A. a, McLean, M. a, Sligar, S. G., Taylor, K. a & Ginsberg, M. H. Recreation of the terminal events in physiological integrin activation. *J. Cell Biol.* **188,** 157–73 (2010).

46. Streicher, P., Nassoy, P., Bärmann, M., Dif, A., Marchi-Artzner, V., Brochard-Wyart, F., Spatz, J. & Bassereau, P. Integrin reconstituted in GUVs: A biomimetic system to study initial steps of cell spreading. *Biochim. Biophys. Acta - Biomembr.* **1788,** 2291–2300 (2009).

47. Sloan, S. M., Brown, E. B., Liu, Q. & Frojmovic, M. M. Glycoprotein IIb-IIIa-liposomes bind fibrinogen but do not undergo fibrinogen-mediated aggregation. *Platelets* **11,** 99–110 (2000).

48. Machán, R. & Hof, M. Lipid diffusion in planar membranes investigated by fluorescence correlation spectroscopy. *Biochim. Biophys. Acta* **1798,** 1377–91 (2010).

49. Basit, H., Lopez, S. G. & Keyes, T. E. Fluorescence correlation and lifetime correlation spectroscopy applied to the study of supported lipid bilayer models of the cell membrane. *Methods* (2014). doi:10.1016/j.ymeth.2014.02.005

50. Machán, R. & Hof, M. Lipid diffusion in planar membranes investigated by fluorescence correlation spectroscopy. *Biochim. Biophys. Acta* **1798,** 1377–91 (2010).

51. Saffman, P. G. & Delbrück, M. Brownian motion in biological membranes. *Proc. Natl. Acad. Sci. U. S. A.* **72,** 3111–3 (1975).

52. Weiß, K., Neef, A., Van, Q., Kramer, S., Gregor, I. & Enderlein, J. Quantifying the diffusion of membrane proteins and peptides in black lipid membranes with 2-focus fluorescence correlation spectroscopy. *Biophys. J.* **105,** 455–62 (2013).

53. Ramadurai, S., Holt, A., Krasnikov, V., van den Bogaart, G., Killian, J. A. & Poolman, B. Lateral Diffusion of Membrane Proteins. *J. Am. Chem. Soc.* **131,** 12650–12656 (2009).

54. Quemeneur, F., Sigurdsson, J. K., Renner, M., Atzberger, P. J., Bassereau, P. & Lacoste, D. Shape matters in protein mobility within membranes. *Proc. Natl. Acad. Sci. U. S. A.* **111,** 5083–7 (2014).

55. Gambin, Y., Lopez-Esparza, R., Reffay, M., Sierecki, E., Gov, N. S., Genest, M., Hodges, R. S. & Urbach, W. Lateral mobility of proteins in liquid membranes revisited. *Proc. Natl. Acad. Sci. U. S. A.* **103,** 2098–102 (2006).

56. Naji, A., Levine, A. J. & Pincus, P. A. Corrections to the Saffman-Delbruck mobility for membrane bound proteins. *Biophys. J.* **93,** L49–51 (2007).

57. Guigas, G. & Weiss, M. Influence of hydrophobic mismatching on membrane protein diffusion. *Biophys. J.* **95,** L25–7 (2008).

58. Lichtman, J. W. & Conchello, J.-A. Fluorescence microscopy. *Nat. Methods* **2,** 910–919 (2005).

59. Berezin, M. Y. & Achilefu, S. Fluorescence lifetime measurements and biological imaging. *Chem. Rev.* **110,** 2641–84 (2010).

60. García-Sáez, A. J. & Schwille, P. Single molecule techniques for the study of membrane proteins. *Appl. Microbiol. Biotechnol.* **76,** 257–66 (2007).

61. Siegel, A. P., Hays, N. M. & Day, R. N. Unraveling transcription factor interactions with heterochromatin protein 1 using fluorescence lifetime imaging microscopy and fluorescence correlation spectroscopy. *J. Biomed. Opt.* **18,** 25002 (2013).

62. Brown, M. & Wittwer, C. Flow cytometry: principles and clinical applications in hematology. *Clin. Chem.* **46,** 1221–9 (2000).

63. Webb, R. Confocal optical microscopy. *Reports Prog. Phys.* **59,** 427–471 (1999).

64. Hell, S. W. & Wichmann, J. Breaking the diffraction resolution limit by stimulated emission: stimulated-emission-depletion fluorescence microscopy. *Opt. Lett.* **19,** 780 (1994).

65. Klar, T. A., Jakobs, S., Dyba, M., Egner, A. & Hell, S. W. Fluorescence microscopy with diffraction resolution barrier broken by stimulated emission. *Proc. Natl. Acad. Sci.* **97,** 8206–8210 (2000).

66. Neupane, B., Ligler, F. S. & Wang, G. Review of recent developments in stimulated emission depletion microscopy: applications on cell imaging. *J. Biomed. Opt.* **19,** 080901 (2014).

67. Kapusta, P., Macháň, R., Benda, A. & Hof, M. Fluorescence Lifetime Correlation Spectroscopy (FLCS): Concepts, Applications and Outlook. *Int. J. Mol. Sci.* **13,** 12890–910 (2012).

68. Scherfeld, D., Kahya, N. & Schwille, P. Lipid dynamics and domain formation in model membranes composed of ternary mixtures of unsaturated and saturated phosphatidylcholines and cholesterol. *Biophys. J.* **85,** 3758–68 (2003).

69. Banks, D. S. & Fradin, C. Anomalous diffusion of proteins due to molecular crowding. *Biophys. J.* **89,** 2960–71 (2005).

70. LaRochelle, J. R., Cobb, G. B., Steinauer, A., Rhoades, E. & Schepartz, A. Fluorescence Correlation Spectroscopy Reveals Highly Efficient Cytosolic Delivery of Certain Penta-Arg Proteins and Stapled Peptides. *J. Am. Chem. Soc.*

137, 2536–2541 (2015).

71. Basford, C., Forraz, N. & McGuckin, C. Optimized multiparametric immunophenotyping of umbilical cord blood cells by flow cytometry. *Nat. Protoc.* **5,** 1337–46 (2010).

72. Vahabi, S., Nazemi Salman, B. & Javanmard, A. Atomic force microscopy application in biological research: A review study. *Iran. J. Med. Sci.* **38,** 76–83 (2013).

73. Alessandrini, A. & Facci, P. AFM: a versatile tool in biophysics. *Meas. Sci. Technol.* **16,** R65–R92 (2005).

74. Jalili, N. & Laxminarayana, K. A review of atomic force microscopy imaging systems: Application to molecular metrology and biological sciences. *Mechatronics* **14,** 907–945 (2004).

75. Kroll, M. H. & Afshar-Kharghan, V. Platelets in pulmonary vascular physiology and pathology. *Pulm. Circ.* **2,** 291–308 (2012).

76. Rivera, J., Lozano, M. L., Navarro-Núñez, L. & Vicente, V. Platelet receptors and signaling in the dynamics of thrombus formation. *Haematologica* **94,** 700–711 (2009).

77. Kamath, S. Platelet activation: assessment and quantification. *Eur. Heart J.* **22,** 1561–1571 (2001).

78. McEwan, P. A., Andrews, R. K. & Emsley, J. Glycoprotein Ibalpha inhibitor complex structure reveals a combined steric and allosteric mechanism of von Willebrand factor antagonism. *Blood* **114,** 4883–5 (2009).

79. Ruggeri, Z. M. The role of von Willebrand factor in thrombus formation. *Thromb. Res.* **120 Suppl ,** S5–9 (2007).

80. Savage, B., Saldívar, E. & Ruggeri, Z. M. Initiation of platelet adhesion by arrest onto fibrinogen or translocation on von Willebrand factor. *Cell* **84,** 289–97 (1996).

81. Bye, A. P., Unsworth, A. J. & Gibbins, J. M. Platelet signaling: a complex

interplay between inhibitory and activatory networks. *J. Thromb. Haemost.* (2016). doi:10.1111/jth.13302

82. Gibbins, J. M. Platelet adhesion signalling and the regulation of thrombus formation. *J. Cell Sci.* **117,** 3415–25 (2004).

83. Varga-Szabo, D., Braun, A. & Nieswandt, B. Calcium signaling in platelets. *J. Thromb. Haemost.* **7,** 1057–66 (2009).

84. Harper, M. T. & Poole, A. W. Isoform-specific functions of protein kinase C: the platelet paradigm. *Biochem. Soc. Trans.* **35,** 1005–8 (2007).

85. Nieswandt, B. & Watson, S. P. Platelet-collagen interaction: is GPVI the central receptor? *Blood* **102,** 449–61 (2003).

86. Nakahata, N. Thromboxane A2: physiology/pathophysiology, cellular signal transduction and pharmacology. *Pharmacol. Ther.* **118,** 18–35 (2008).

87. De Candia, E. Mechanisms of platelet activation by thrombin: a short history. *Thromb. Res.* **129,** 250–6 (2012).

88. Offermanns, S. Activation of Platelet Function Through G Protein-Coupled Receptors. *Circ. Res.* **99,** 1293–1304 (2006).

89. Li, Z., Delaney, M. K., O'Brien, K. A. & Du, X. Signaling during platelet adhesion and activation. *Arterioscler. Thromb. Vasc. Biol.* **30,** 2341–9 (2010).

90. Soulet, C., Hechler, B., Gratacap, M.-P., Plantavid, M., Offermanns, S., Gachet, C. & Payrastre, B. A differential role of the platelet ADP receptors P2Y1 and P2Y12 in Rac activation. *J. Thromb. Haemost.* **3,** 2296–306 (2005).

91. Flaumenhaft, R., Dilks, J. R., Rozenvayn, N., Monahan-Earley, R. a, Feng, D. & Dvorak, A. M. The actin cytoskeleton differentially regulates platelet alpha-granule and dense-granule secretion. *Blood* **105,** 3879–87 (2005).

92. Mizuno, Y., Isotani, E., Huang, J., Ding, H., Stull, J. T. & Kamm, K. E. Myosin light chain kinase activation and calcium sensitization in smooth muscle in vivo. *Am. J. Physiol. Cell Physiol.* **295,** C358–64 (2008).

93. Crittenden, J. R., Bergmeier, W., Zhang, Y., Piffath, C. L., Liang, Y., Wagner, D.

D., Housman, D. E. & Graybiel, A. M. CalDAG-GEFI integrates signaling for platelet aggregation and thrombus formation. *Nat. Med.* **10,** 982–6 (2004).

94. Legate, K. R. & Fässler, R. Mechanisms that regulate adaptor binding to beta-integrin cytoplasmic tails. *J. Cell Sci.* **122,** 187–98 (2009).

95. Radomski, M. W., Palmer, R. M. & Moncada, S. Characterization of the L-arginine:nitric oxide pathway in human platelets. *Br. J. Pharmacol.* **101,** 325–8 (1990).

96. Wang, G. R., Zhu, Y., Halushka, P. V, Lincoln, T. M. & Mendelsohn, M. E. Mechanism of platelet inhibition by nitric oxide: in vivo phosphorylation of thromboxane receptor by cyclic GMP-dependent protein kinase. *Proc. Natl. Acad. Sci. U. S. A.* **95,** 4888–93 (1998).

97. Geiger, J. Inhibitors of platelet signal transduction as anti-aggregatory drugs. *Expert Opin. Investig. Drugs* **10,** 865–90 (2001).

98. Stalker, T. J., Wu, J., Morgans, A., Traxler, E. A., Wang, L., Chatterjee, M. S., Lee, D., Quertermous, T., Hall, R. A., Hammer, D. A., Diamond, S. L. & Brass, L. F. Endothelial cell specific adhesion molecule (ESAM) localizes to platelet-platelet contacts and regulates thrombus formation in vivo. *J. Thromb. Haemost.* **7,** 1886–96 (2009).

99. Lam, F. W., Vijayan, K. V. & Rumbaut, R. E. Platelets and Their Interactions with Other Immune Cells. *Compr. Physiol.* **5,** 1265–80 (2015).

100. Hantgan, R. R., Stahle, M. C., Connor, J. H., Horita, D. A., Rocco, M., McLane, M. A., Yakovlev, S. & Medved, L. Integrin alphaIIbbeta3:ligand interactions are linked to binding-site remodeling. *Protein Sci.* **15,** 1893–906 (2006).

101. Sánchez-Cortés, J. & Mrksich, M. The platelet integrin alphaIIbbeta3 binds to the RGD and AGD motifs in fibrinogen. *Chem. Biol.* **16,** 990–1000 (2009).

102. Nguyen-Ho, P. & Lakkis, N. M. Platelet glycoprotein IIb/IIIa receptor antagonists and coronary artery disease. *Curr. Atheroscler. Rep.* **3,** 139–48 (2001).

103. Hantgan, R. R., Lyles, D. S., Mallett, T. C., Rocco, M., Nagaswami, C. & Weisel, J. W. Ligand binding promotes the entropy-driven oligomerization of integrin alpha IIb beta 3. *J. Biol. Chem.* **278,** 3417–26 (2003).

104. Ye, F., Liu, J., Winkler, H. & Taylor, K. A. Integrin alpha IIb beta 3 in a membrane environment remains the same height after Mn2+ activation when observed by cryoelectron tomography. *J. Mol. Biol.* **378,** 976–86 (2008).

105. Shimaoka, M. & Springer, T. A. Therapeutic antagonists and conformational regulation of integrin function. *Nat. Rev. Drug Discov.* **2,** 703–16 (2003).

106. Harburger, D. S. & Calderwood, D. A. Integrin signalling at a glance. *J. Cell Sci.* **122,** 1472–1472 (2009).

107. Kanchanawong, P., Shtengel, G., Pasapera, A. M., Ramko, E. B., Davidson, M. W., Hess, H. F. & Waterman, C. M. Nanoscale architecture of integrin-based cell adhesions. *Nature* **468,** 580–4 (2010).

108. Michelson, A. D., Barnard, M. R., Krueger, L. A., Frelinger, A. L. & Furman, M. I. Evaluation of platelet function by flow cytometry. *Methods* **21,** 259–70 (2000).

109. Yan, B. & Smith, J. W. Mechanism of Integrin Activation by Disulfide Bond Reduction. *Biochemistry* **40,** 8861–8867 (2001).

110. Takagi, J., Petre, B. M., Walz, T. & Springer, T. a. Global conformational rearrangements in integrin extracellular domains in outside-in and inside-out signaling. *Cell* **110,** 599–11 (2002).

111. Mersmann, H. J., Goodman, J. R. & Brown, L. J. Guidelines on platelet function testing. *J. Clin. Pathol.* **41,** 1322–1330 (1988).

112. Yan, B., Hu, D. D., Knowles, S. K. & Smith, J. W. Probing chemical and conformational differences in the resting and active conformers of platelet integrin alpha(IIb)beta(3). *J. Biol. Chem.* **275,** 7249–60 (2000).

113. Kamata, T., Handa, M., Sato, Y., Ikeda, Y. & Aiso, S. Membrane-proximal / Stalk Interactions Differentially Regulate Integrin Activation. *J. Biol. Chem.*

280, 24775–24783 (2005).

114. Luo, B.-H., Karanicolas, J., Harmacek, L. D., Baker, D. & Springer, T. a. Rationally designed integrin beta3 mutants stabilized in the high affinity conformation. *J. Biol. Chem.* **284,** 3917–24 (2009).

115. Rosano, C. & Rocco, M. Solution properties of full-length integrin alpha(IIb)beta3 refined models suggest environment-dependent induction of alternative bent /extended resting states. *FEBS J.* **277,** 3190–202 (2010).

116. Bennett, J. S., Berger, B. W. & Billings, P. C. The structure and function of platelet integrins. *J. Thromb. Haemost.* **7 Suppl 1,** 200–5 (2009).

117. Zhang, K., Pan, Y., Qi, J., Yue, J., Zhang, M., Xu, C., Li, G. & Chen, J. Disruption of disulfide restriction at integrin knees induces activation and ligand-independent signaling of $\alpha_4\beta_7$. *J. Cell Sci.* **126,** 5030–41 (2013).

118. Ni, H. Integrin Activation by Dithiothreitol or Mn2+ Induces a Ligand-occupied Conformation and Exposure of a Novel NH2-terminal Regulatory Site on the beta 1 Integrin Chain. *J. Biol. Chem.* **273,** 7981–7987 (1998).

119. Ye, F., Kim, C. & Ginsberg, M. H. Reconstruction of integrin activation. *Blood* **119,** 26–33 (2012).

120. BioLegend. FITC Anti-human CD41/CD61 Antibody Anti-CD41/CD61 - PAC-1. at <http://www.biolegend.com/fitc-anti-human-cd41-cd61-antibody-10179.html>

121. Bennett, J. The structure and function of platelet integrins. *J. Thromb. Haemost.* **7 Suppl 1,** 200–5 (2009).

122. Yokoyama, K., Zhang, X. P., Medved, L. & Takada, Y. Specific binding of integrin alpha v beta 3 to the fibrinogen gamma and alpha E chain C-terminal domains. *Biochemistry* **38,** 5872–7 (1999).

123. Kim, M., Carman, C. V & Springer, T. A. Bidirectional transmembrane signaling by cytoplasmic domain separation in integrins. *Science* **301,** 1720–5 (2003).

124. Wonerow, P., Obergfell, A., Wilde, J. I., Bobe, R., Asazuma, N., Brdicka, T., Leo,

A., Schraven, B., Horejsí, V., Shattil, S. J. & Watson, S. P. Differential role of glycolipid-enriched membrane domains in glycoprotein VI- and integrin-mediated phospholipase Cgamma2 regulation in platelets. *Biochem. J.* **364,** 755–65 (2002).

125. Jesorka, A. & Orwar, O. Liposomes: technologies and analytical applications. *Anal. Chem.* **1,** 801–832 (2008).

126. Aimon, S., Manzi, J., Schmidt, D., Poveda Larrosa, J. A., Bassereau, P. & Toombes, G. E. S. Functional reconstitution of a voltage-gated potassium channel in giant unilamellar vesicles. *PLoS One* **6,** e25529 (2011).

127. Milhiet, P.-E., Gubellini, F., Berquand, A., Dosset, P., Rigaud, J.-L., Le Grimellec, C. & Lévy, D. High-resolution AFM of membrane proteins directly incorporated at high density in planar lipid bilayer. *Biophys. J.* **91,** 3268–75 (2006).

128. Olson, F., Hunt, C. A., Szoka, F. C., Vail, W. J. & Papahadjopoulos, D. Preparation of liposomes of defined size distribution by extrusion through polycarbonate membranes. *Biochim. Biophys. Acta - Biomembr.* **557,** 9–23 (1979).

129. Ingolia, T. D. & Koshland, D. E. The role of calcium in fusion of artificial vesicles. *J. Biol. Chem.* **253,** 3821–9 (1978).

130. Karlsson, M., Nolkrantz, K., Davidson, M. J., Strömberg, A., Ryttsén, F., Åkerman, B. & Orwar, O. Electroinjection of Colloid Particles and Biopolymers into Single Unilamellar Liposomes and Cells for Bioanalytical Applications. *Anal. Chem.* **72,** 5857–5862 (2000).

131. Angelova, M. I. & Dimitrov, D. S. Liposome electroformation. *Faraday Discuss. Chem. Soc.* **81,** 303–311 (1986).

132. Angelova, M., Soléau, S., Méléard, P., Faucon, F. & Bothorel, P. in *Trends Colloid Interface Sci. VI* (eds. Helm, C., Lösche, M. & Möhwald, H.) **89,** 127–131 (Springer Berlin / Heidelberg, 1992).

133. Politano, T. J., Froude, V. E., Jing, B. & Zhu, Y. AC-electric field dependent

electroformation of giant lipid vesicles. *Colloids Surf. B. Biointerfaces* **79,** 75–82 (2010).

134. Pott, T., Bouvrais, H. & Méléard, P. Giant unilamellar vesicle formation under physiologically relevant conditions. *Chem. Phys. Lipids* **154,** 115–9 (2008).

135. Méléard, P. & Bagatolli, L. in *Methods Enzymol.* **465,** 161–176 (2009).

136. Avanti Polar Lipids. Extruder Assembly. at <http://www.avantilipids.com/index.php?option=com_content&view=article&id=532&Itemid=296>

137. Tabarin, T., Martin, A., Forster, R. J. & Keyes, T. E. Poly-ethylene glycol induced super-diffusivity in lipid bilayer membranes. *Soft Matter* **8,** 8743–8751 (2012).

138. Estes, D. J. & Mayer, M. Giant liposomes in physiological buffer using electroformation in a flow chamber. *Biochim. Biophys. Acta* **1712,** 152–60 (2005).

139. Juhasz, J., Davis, J. H. & Sharom, F. J. Fluorescent probe partitioning in giant unilamellar vesicles of 'lipid raft' mixtures. *Biochem. J.* **430,** 415–23 (2010).

140. Popov, J., Vobornik, D., Coban, O., Keating, E., Miller, D., Francis, J., Petersen, N. O. & Johnston, L. J. Chemical mapping of ceramide distribution in sphingomyelin-rich domains in monolayers. *Langmuir* **24,** 13502–8 (2008).

141. Scherfeld, D., Kahya, N. & Schwille, P. Lipid dynamics and domain formation in model membranes composed of ternary mixtures of unsaturated and saturated phosphatidylcholines and cholesterol. *Biophys. J.* **85,** 3758–68 (2003).

142. Doeven, M. K., Folgering, J. H. a, Krasnikov, V., Geertsma, E. R., van den Bogaart, G. & Poolman, B. Distribution, lateral mobility and function of membrane proteins incorporated into giant unilamellar vesicles. *Biophys. J.* **88,** 1134–42 (2005).

143. Rocco, M., Spotorno, B. & Hantgan, R. Modeling the alpha iib beta 3 integrin

solution conformation. *Protein Sci.* **141,** 1685–95 (1993).

144. Bacia, K., Schuette, C. G., Kahya, N., Jahn, R. & Schwille, P. SNAREs prefer liquid-disordered over 'raft' (liquid-ordered) domains when reconstituted into giant unilamellar vesicles. *J. Biol. Chem.* **279,** 37951–5 (2004).

145. Kahya, N. Protein-protein and protein-lipid interactions in domain-assembly: lessons from giant unilamellar vesicles. *Biochim. Biophys. Acta* **1798,** 1392–8 (2010).

146. Siegel, A. P., Kimble-Hill, A., Garg, S., Jordan, R. & Naumann, C. a. Native ligands change integrin sequestering but not oligomerization in raft-mimicking lipid mixtures. *Biophys. J.* **101,** 1642–50 (2011).

147. Leitinger, B. & Hogg, N. The involvement of lipid rafts in the regulation of integrin function. *J. Cell Sci.* **115,** 963–72 (2002).

148. Castellana, E. & Cremer, P. Solid supported lipid bilayers: From biophysical studies to sensor design. *Surf. Sci. Rep.* **61,** 429–444 (2006).

149. Tamm, L. K. & McConnell, H. M. Supported phospholipid bilayers. *Biophys. J.* **47,** 105–113 (1985).

150. Hamai, C., Cremer, P. S. & Musser, S. M. Single giant vesicle rupture events reveal multiple mechanisms of glass-supported bilayer formation. *Biophys. J.* **92,** 1988–99 (2007).

151. Hussain, M. A., Agnihotri, A. & Siedlecki, C. A. AFM Imaging of Ligand Binding to Platelet Integrin A2bB3 Receptors Reconstituted into Planar Lipid Bilayers. *Langmuir* **21,** 6979–6986 (2005).

152. Tero, R. Substrate effects on the formation process, structure and physicochemical properties of supported lipid bilayers. *Materials (Basel).* **5,** 2658–2680 (2012).

153. Basit, H., Gaul, V., Maher, S., Forster, R. & Keyes, T. Aqueous-filled polymer microcavity arrays: versatile and stable lipid bilayer platforms offering high lateral mobility to incorporated membrane proteins. *Analyst* 3012–3018

(2015). doi:10.1039/C4AN02317J

154. Sinner, E.-K., Reuning, U., Kök, F. N., Saccà, B., Moroder, L., Knoll, W. & Oesterhelt, D. Incorporation of integrins into artificial planar lipid membranes: characterization by plasmon-enhanced fluorescence spectroscopy. *Anal. Biochem.* **333,** 216–24 (2004).

155. Puu, G. & Gustafson, I. Planar lipid bilayers on solid supports from liposomes – factors of importance for kinetics and stability. *Biochim. Biophys. Acta - Biomembr.* **1327,** 149–161 (1997).

156. in *Nanobiotechnology Biomim. Membr.* (ed. Martin, D. K.) **1,** (Springer US, 2007).

157. Kalb, E., Frey, S. & Tamm, L. K. Formation of supported planar bilayers by fusion of vesicles to supported phospholipid monolayers. *Biochim. Biophys. Acta - Biomembr.* **1103,** 307–316 (1992).

158. Montero, M. T., Pijoan, M., Merino-Montero, S., Vinuesa, T. & Hernández-Borrell, J. Interfacial membrane effects of fluoroquinolones as revealed by a Combination of fluorescence binding experiments and atomic force microscopy observations. *Langmuir* **22,** 7574–7578 (2006).

159. Richter, R. P., Maury, N. & Brisson, A. R. On the effect of the solid support on the interleaflet distribution of lipids in supported lipid bilayers. *Langmuir* **21,** 299–304 (2005).

160. Mingeot-Leclercq, M.-P., Deleu, M., Brasseur, R. & Dufrêne, Y. F. Atomic force microscopy of supported lipid bilayers. *Nat. Protoc.* **3,** 1654–9 (2008).

161. Munro, J. C. & Frank, C. W. In situ formation and characterization of poly(ethylene glycol)-supported lipid bilayers on gold surfaces. *Langmuir* **20,** 10567–10575 (2004).

162. Nirasay, S., Badia, A., Leclair, G., Claverie, J. & Marcotte, I. Polydopamine-Supported Lipid Bilayers. *Materials (Basel).* **5,** 2621–2636 (2012).

163. Wagner, M. L. & Tamm, L. K. Tethered polymer-supported planar lipid bilayers

for reconstitution of integral membrane proteins: silane-polyethyleneglycol-lipid as a cushion and covalent linker. *Biophys. J.* **79,** 1400–14 (2000).

164. Yoshina-Ishii, C. & Boxer, S. G. Arrays of mobile thethered vesicles on supported bilayers. *J. Am. Chem. Soc.* **125,** 3696 (2003).

165. Svedhem, S., Pfeiffer, I., Larsson, C., Wingren, C., Borrebaeck, C. & Höök, F. Patterns of DNA-labeled and scFv-antibody-carrying lipid vesicles directed by material-specific immobilization of DNA and supported lipid bilayer formation on an Au/SiO2 template. *ChemBioChem* **4,** 339–343 (2003).

166. Römer, W. & Steinem, C. Impedance analysis and single-channel recordings on nano-black lipid membranes based on porous alumina. *Biophys. J.* **86,** 955–965 (2004).

167. Kumar, K., Isa, L., Egner, A., Schmidt, R., Textor, M. & Reimhult, E. Formation of nanopore-spanning lipid bilayers through liposome fusion. *Langmuir* **27,** 10920–10928 (2011).

168. Urban, M., Kleefen, A., Mukherjee, N., Seelheim, P., Windschiegl, B., Vor Der Brüggen, M., Koçer, A. & Tampé, R. Highly parallel transport recordings on a membrane-on-nanopore chip at single molecule resolution. *Nano Lett.* **14,** 1674–1680 (2014).

169. Im, H., Wittenberg, N. J., Lesuffleur, A., Lindquist, N. C. & Oh, S.-H. Membrane protein biosensing with plasmonic nanopore arrays and pore-spanning lipid membranes. *Chem. Sci.* **1,** 688 (2010).

170. Simon, A., Girard-Egrot, A., Sauter, F., Pudda, C., Picollet D'Hahan, N., Blum, L., Chatelain, F. & Fuchs, A. Formation and stability of a suspended biomimetic lipid bilayer on silicon submicrometer-sized pores. *J. Colloid Interface Sci.* **308,** 337–43 (2007).

171. Stimberg, V. C., Bomer, J. G., van Uitert, I., van den Berg, A. & Le Gac, S. High Yield, Reproducible and Quasi-Automated Bilayer Formation in a Microfluidic Format. *Small* **9,** 1076–1085 (2013).

172. Nussio, M. R., Oncins, G., Ridelis, I., Szili, E., Shapter, J. G., Sanz, F. & Voelcker,

N. H. Nanomechanical Characterization of Phospholipid Bilayer Islands on Flat and Porous Substrates: A Force Spectroscopy Study. *J. Phys. Chem. B* **113,** 10339–10347 (2009).

173. Hennesthal, C., Drexler, J. & Steinem, C. Membrane-suspended nanocompartments based on ordered pores in alumina. *Chemphyschem* **3,** 885–9 (2002).

174. Jönsson, P., Jonsson, M. P. & Höök, F. Sealing of submicrometer wells by a shear-driven lipid bilayer. *Nano Lett.* **10,** 1900–6 (2010).

175. Mallon, C. T., Forster, R. J. & Keyes, T. E. Fabrication of gold sphere to cuboid nanoarrays using PDMS templates. *Chem. Commun. (Camb).* **47,** 7605–7607 (2011).

176. van Zoelen, E. J., Verkleij, A. J., Zwaal, R. F. & van Deenen, L. L. Incorporation and asymmetric orientation of glycophorin in reconstituted protein-containing vesicles. *Eur. J. Biochem.* **86,** 539–46 (1978).

177. Isas, J. M., Cartailler, J. P., Sokolov, Y., Patel, D. R., Langen, R., Luecke, H., Hall, J. E. & Haigler, H. T. Annexins V and XII insert into bilayers at mildly acidic pH and form ion channels. *Biochemistry* **39,** 3015–22 (2000).

178. Lizarbe, M. A., Barrasa, J. I., Olmo, N., Gavilanes, F. & Turnay, J. *Annexin-phospholipid interactions. Functional implications. Int. J. Mol. Sci.* **14,** (2013).

179. Gerke, V., Creutz, C. E. & Moss, S. E. Annexins: linking Ca2+ signalling to membrane dynamics. *Nat. Rev. Mol. Cell Biol.* **6,** 449–61 (2005).

180. Moss, S. E. & Morgan, R. O. The annexins. *Genome Biol.* **5,** 219 (2004).

181. Diaz, A. J., Albertorio, F., Daniel, S. & Cremer, P. S. Double cushions preserve transmembrane protein mobility in supported bilayer systems. *Langmuir* **24,** 6820–6 (2008).

182. Richter, R., Mukhopadhyay, A. & Brisson, A. Pathways of lipid vesicle deposition on solid surfaces: a combined QCM-D and AFM study. *Biophys. J.* **85,** 3035–47 (2003).

183. Purrucker, O., Gonnenwein, S., Fortig, A., Jordan, R., Rusp, M., Barmann, M., Moroder, L., Sackmann, E. & Tanaka, M. Polymer-tethered membranes as quantitative models for the study of integrin-mediated cell adhesion. *Soft Matter* **3,** 333 (2007).

184. Cézanne, L., Lopez, a, Loste, F., Parnaud, G., Saurel, O., Demange, P. & Tocanne, J. F. Organization and dynamics of the proteolipid complexes formed by annexin V and lipids in planar supported lipid bilayers. *Biochemistry* **38,** 2779–86 (1999).

185. Saurel, O., Cézanne, L., Milon, a, Tocanne, J. F. & Demange, P. Influence of annexin V on the structure and dynamics of phosphatidylcholine/phosphatidylserine bilayers: a fluorescence and NMR study. *Biochemistry* **37,** 1403–10 (1998).

186. Wagner, M. L. & Tamm, L. K. Reconstituted syntaxin1a/SNAP25 interacts with negatively charged lipids as measured by lateral diffusion in planar supported bilayers. *Biophys. J.* **81,** 266–75 (2001).

187. Fletcher, D. A. & Mullins, R. D. Cell mechanics and the cytoskeleton. *Nature* **463,** 485–492 (2010).

188. Alberts, B., Johnson, A., Lewis, J., Raff, M., Roberts, K. & Walter, P. in *Mol. Biol. Cell* (Garland Science, 2002). at <http://www.ncbi.nlm.nih.gov/books/NBK26809/>

189. Barfoot, R. J., Sheikh, K. H., Johnson, B. R. G., Colyer, J., Miles, R. E., Jeuken, L. J. C., Bushby, R. J. & Evans, S. D. Minimal F-actin cytoskeletal system for planar supported phospholipid bilayers. *Langmuir* **24,** 6827–6836 (2008).

190. Dominguez, R. & Holmes, K. C. Actin Structure and Function. *Annu. Rev. Biophys.* **40,** 169–186 (2011).

191. Blanchoin, L., Boujemaa-Paterski, R., Sykes, C. & Plastino, J. Actin dynamics, architecture, and mechanics in cell motility. *Physiol. Rev.* **94,** 235–63 (2014).

192. Cooper, G. M. *Intermediate Filaments*. (Sinauer Associates, 2000). at <http://www.ncbi.nlm.nih.gov/books/NBK9834/>

193. Lodish, H. *Molecular Cell Biology*. (W. H. Freeman, 2008). at <https://books.google.com/books?id=K3JbjG1JiUMC&pgis=1>

194. Gómez-Llobregat, J., Buceta, J. & Reigada, R. Interplay of cytoskeletal activity and lipid phase stability in dynamic protein recruitment and clustering. *Sci. Rep.* **3,** 2608 (2013).

195. Dinic, J., Ashrafzadeh, P. & Parmryd, I. Actin filaments attachment at the plasma membrane in live cells cause the formation of ordered lipid domains. *Biochim. Biophys. Acta - Biomembr.* **1828,** 1102–1111 (2013).

196. Chichili, G. R. & Rodgers, W. Clustering of Membrane Raft Proteins by the Actin Cytoskeleton. *J. Biol. Chem.* **282,** 36682–36691 (2007).

197. Chubinskiy-Nadezhdin, V. I., Efremova, T. N., Khaitlina, S. Y. & Morachevskaya, E. a. Functional impact of cholesterol sequestration on actin cytoskeleton in normal and transformed fibroblasts. *Cell Biol. Int.* **37,** 617–623 (2013).

198. Geiger, B., Spatz, J. P. & Bershadsky, A. D. Environmental sensing through focal adhesions. *Nat. Rev. Mol. Cell Biol.* **10,** 21–33 (2009).

199. Wiesner, S., Legate, K. R. & Fässler, R. Integrin-actin interactions. *Cell. Mol. Life Sci.* **62,** 1081–99 (2005).

200. Head, B. P., Patel, H. H. & Insel, P. a. Interaction of membrane/lipid rafts with the cytoskeleton: Impact on signaling and function: Membrane/lipid rafts, mediators of cytoskeletal arrangement and cell signaling. *Biochim. Biophys. Acta - Biomembr.* **1838,** 532–545 (2014).

201. Hartwig, J. H. Mechanisms of actin rearrangements mediating platelet activation. *J. Cell Biol.* **118,** 1421–1441 (1992).

202. Bearer, E. L., Prakash, J. M. & Li, Z. Actin dynamics in platelets. *Int. Rev. Cytol.* **217,** 137–182 (2002).

203. Bennett, J. S., Zigmond, S., Vilaire, G., Cunningham, M. E. & Bednar, B. The platelet cytoskeleton regulates the affinity of the integrin alpha(IIb)beta(3) for fibrinogen. *J. Biol. Chem.* **274,** 25301–25307 (1999).

204. Han, J., Lim, C. J., Watanabe, N., Soriani, A., Ratnikov, B., Calderwood, D. a, Puzon-McLaughlin, W., Lafuente, E. M., Boussiotis, V. a, Shattil, S. J. & Ginsberg, M. H. Reconstructing and deconstructing agonist-induced activation of integrin alphaIIbbeta3. *Curr. Biol.* **16,** 1796–806 (2006).

205. Yi, F., Xu, J., Smith, a. M., Parikh, A. N. & LaVan, D. A. Nanofiber-supported phospholipid bilayers. *Soft Matter* **5,** 5037 (2009).

206. Sterling, S. M., Dawes, R., Allgeyer, E. S., Ashworth, S. L. & Neivandt, D. J. Comparison of Actin- and Glass-Supported Phospholipid Bilayer Diffusion Coefficients. *Biophys. J.* **108,** 1946–1953 (2015).

207. Heath, G. R., Johnson, B. R. G., Olmsted, P. D., Connell, S. D. & Evans, S. D. Actin assembly at model-supported lipid bilayers. *Biophys. J.* **105,** 2355–2365 (2013).

208. Honigmann, A., Sadeghi, S., Keller, J., Hell, S. W., Eggeling, C. & Vink, R. A lipid bound actin meshwork organizes liquid phase separation in model membranes. *Elife* **2014,** 1–16 (2014).

209. Perrin, B. J. & Ervasti, J. M. The actin gene family: function follows isoform. *Cytoskeleton* **67,** 630–4 (2010).

210. Collins, J. H. & Elzinga, M. The primary structure of actin from rabbit skeletal muscle. Completion and analysis of the amino acid sequence. *J. Biol. Chem.* **250,** 5915–20 (1975).

211. De Santis, E., Faruqui, N., Noble, J. E. & Ryadnov, M. G. Exploitable length correlations in peptide nanofibres. *Nanoscale* **6,** 11425–11430 (2014).

212. Kim, D. & Herr, A. E. Protein immobilization techniques for microfluidic assays. *Biomicrofluidics* **7,** 1–47 (2013).

213. Hong, S., Leroueil, P. R., Janus, E. K., Peters, J. L., Kober, M.-M., Islam, M. T., Orr, B. G., Baker, J. R. & Banaszak Holl, M. M. Interaction of polycationic polymers with supported lipid bilayers and cells: nanoscale hole formation and enhanced membrane permeability. *Bioconjug. Chem.* **17,** 728–34 (2006).

214. Spurlin, T. A. *Investigation of Phospholipid Bilayer Interactions with Substrates, Polymers, and Nanoparticles*. **4,** (ProQuest, 2007).

215. Bessonov, A. N., Gur'nev, F. A., Kuznetsova, I. M., Takemoto, J. Y., Turoverov, K. K., Malev, V. V & Shchagina, L. V. [Interaction between filamentous actin and lipid bilayer causes the increase of syringomycin E channel-forming activity]. *Tsitologiia* **46,** 628–33 (2004).

216. Wang, Y. L., Lanni, F., McNeil, P. L., Ware, B. R. & Taylor, D. L. Mobility of cytoplasmic and membrane-associated actin in living cells. *Proc. Natl. Acad. Sci. U. S. A.* **79,** 4660–4 (1982).

217. Brakebusch, C. & Fässler, R. The integrin-actin connection, an eternal love affair. *EMBO J.* **22,** 2324–2333 (2003).

218. Adamson, K., Dolan, C., Moran, N., Forster, R. J. & Keyes, T. E. RGD labeled Ru(II) polypyridyl conjugates for platelet integrin αIIbβ3 recognition and as reporters of integrin conformation. *Bioconjug. Chem.* **25,** 928–44 (2014).

219. Litvinov, R. I., Nagaswami, C., Vilaire, G., Shuman, H., Bennett, J. S. & Weisel, J. W. Functional and structural correlations of individual alphaIIbbeta3 molecules. *Blood* **104,** 3979–85 (2004).

220. Heinemann, F., Betaneli, V., Thomas, F. A. & Schwille, P. Quantifying lipid diffusion by fluorescence correlation spectroscopy: a critical treatise. *Langmuir* **28,** 13395–404 (2012).

221. Tanaka, M. & Sackmann, E. Polymer-supported membranes as models of the cell surface. *Nature* **437,** 656–63 (2005).